Doctoral Dissertation
Doctoral Program in Physics (32$^{\text{nd}}$ cycle)

Miscibility properties of bosonic binary mixtures in ring lattices

Andrea Richaud

* * * * * *

Supervisor
Prof. Vittorio Penna

Doctoral Examination Committee:
Prof. Francesco Minardi, *Referee*, LENS, Firenze
Prof. Andrea Trombettoni, *Referee*, SISSA, Trieste
Prof. Emilio N. M. Cirillo, *External Member*, Sapienza Università di Roma
Prof. Giuseppe Gonnella, *External Member*, Università di Bari
Prof. Alessandro Pelizzola, *Internal Member*, Politecnico di Torino

Politecnico di Torino
October 30, 2019

Declaration

I hereby declare that the contents and organisation of this dissertation constitute my own original work and does not compromise in any way the rights of third parties, including those relating to the security of personal data.

. . . .

Andrea Richaud
Turin, October 30, 2019

---

[*] This dissertation is presented in partial fulfillment of the requirements for **Ph.D. degree** in the Graduate School of Politecnico di Torino (ScuDo).

Acknowledgements

This Thesis is just the final landmark of a three-year travel, during which I have started walking along the endless, but fascinating, path of Scientific Research.

This scientific hiking would have never started without the constant and irreplaceable presence of a great guide: Prof. Vittorio Penna. To him goes my most sincere gratitude and thanks for supporting, helping, and teaching me how to be a good researcher, something that I will definitely (try to) be in my future.

I would like to thank also my friends and colleagues, Davide, Serena, Fabio, Lucrezia, Angelo, Mirko, Giovanni, Daniele, Fabrizio, and all the other guys with which I have worked, eaten, laughed and spent three happy and fruitful years of my life.

I am in debt with Magnus Ögren and Muntsa Guilleumas, who invited me, respectively, to Sweden and to Catalonia, two places where I learned a lot, but also where I had a lot of fun!

I am grateful to my experimental friend Alessandro Zenesini, who presented me the experimental side of ultracold atoms, showing the limitations, but also the considerable possibilities offered by these amazing experimental apparatuses.

A special thank goes to my dear friend and older colleague, Luca Tocchio, not only for our happy lunches at the local Crocetta market, but also for always reminding me that there is a whole *fermionic* world to explore!

Talking about friends, I would need a whole chapter of this Thesis to thank them all for their constant presence, support, and the good times that we always have together. Thanks a lot!

I thank my parents and my family, the people who make my life great and complete. Franci, Nemanja, Paola and Gionni, consider yourself part of it! In particular, I thank Marianna, the person who is and will be the constant of motion of my life.

Publications

1. A. Richaud and V. Penna, “Quantum dynamics of bosons in a two-ring ladder: Dynamical algebra, vortexlike excitations, and currents”. Phy. Rev. A **96**, 013620 (2017);
2. V. Penna and A. Richaud, “Two-species boson mixture on a ring: A group theoretic approach to the quantum dynamics of low-energy excitations”. Phys. Rev. A **96**, 053631 (2017);
3. F. Lingua, A. Richaud, and V. Penna, “Residual entropy and critical behavior of two interacting boson species in a double well”. Entropy, **20**, 84 (2018);
4. V. Penna and A. Richaud, “The phase-separation mechanism of a binary mixture in a ring trimer”. Sci. Rep. **8**, 10242 (2018);
5. A. Richaud and V. Penna, “Phase separation can be stronger than chaos”. New J. Phys. **20**, 105008 (2018);
6. V. Penna and A. Richaud, “Spatial phase separation of a binary mixture in a ring trimer”. J. Phys. Conf. Ser. **1206**, 012011 (2019);
7. A. Richaud, A. Zenesini, and V. Penna, “The mixing-demixing phase diagram of ultracold heteronuclear mixtures in a ring trimer”. Sci. Rep. **9**, 6908 (2019);
8. A. Richaud and V. Penna, “Pathway toward the formation of supermixed states in ultracold boson mixtures loaded in ring lattices”. Phys. Rev. A **100**, 013609 (2019);
9. A. Richaud, V. Penna, R. Mayol and M. Guilleumas, “Vortices with massive cores in a binary mixture of Bose-Einstein condensates”. ArXiv: 1908.06668 (2019).
10. A. Richaud and V. Penna, “Quantum-granularity effect in the formation of supermixed solitons in ring lattices”. Cond. Matt. **5**, 2 (2020).

Summary

The purpose of this PhD thesis is to investigate the miscibility properties of bosonic binary mixtures in ring-lattice and few-site potentials. To this end, a number of different research topics are explored: on one hand, the study of the low energy-excitations of a mixed and uniformly distributed mixture, whose dynamical properties are investigated within a group-theoretic approach based on the application of the dynamical-algebra method; on the other hand, the systematic analysis of the mixing-demixing quantum phase transitions that can occur in these systems, and the introduction of suitable quantum indicators to characterize them. The latter are employed, among other things, to quantify the degree of entanglement between different bosonic modes, but also the degree of mixing and localization of the two quantum fluids. This analysis results in rather rich mixing-demixing phase diagrams, which capture the impact of *spatial fragmentation* onto the miscibility properties of the components. Our analysis indeed takes into account the possible asymmetry between the atomic species and, going also beyond the pointlike approximation of potential wells (by means of a suitable Gross-Pitaevskii treatment), constitutes an effective springboard towards an actual experimental realization. In this regard, we remark that a part of our study has been developed in strict collaboration with the experimental group from Hannover University, with which we have demonstrated that the investigated mixing-demixing quantum phase transitions are within the reach of modern experimental setups. Our analysis has touched, also, on excited states, as it has highlighted several *dynamical* properties of phase-separated states, evidencing, among various aspects, that demixing can be robust and persistent even in the presence of chaos. Eventually, we have have focused on *attractive* interspecies interactions and on the emergence of a rather general mechanism of formation of supermixed solitons.

Contents

Chapter 1

Introduction

In this Chapter, we give an historical perspective and review the most relevant theoretical and experimental advances in the field of Bose-Bose mixtures in optical lattices, a class of particularly versatile model systems which offers the possibility to probe a number of fundamental phenomena and quantum effects, including but not limited to, nonlinear dynamics, entanglement, and strongly correlated phases of matter. Then, we give some motivations behind the studies collected in this PhD Thesis and sketch its outline.

1.1 Historical perspective and Physics of Bose-Bose mixtures

1.1.1 Bose-Einstein condensation

The theoretical prediction of Bose-Einstein condensation dates back to 1925 when Albert Einstein, on the basis of a publication by the Indian physicist Satyendra Nath Bose, envisaged the possibility of the occurrence of a phase transition in a dilute gas of noninteracting ultracold atoms. The basic idea was that, due to their bosonic quantum statistics, atoms, in particular conditions, could *condense* in the lowest energy state [1]. More specifically, at temperatures T below a certain critical temperature T_c (tipically of the order 100 nK - 10 μK), the characteristic width of the atomic wave functions approaches the typical interparticle distance (recall that the thermal de Broglie wavelength reads $\lambda_{dB} = h/\sqrt{2\pi m k_B T}$, where m

is the atomic mass). As a consequence, below T_c, the wave packets of the individual atoms start to overlap and the influence of quantum statistics force the system to Bose condense.

For many years, this theory had no significant impact in the community of theoretical physicists and lacked of any experimental validation. Only in 1938, after the discovery of superfluidity in liquid helium, did Fritz London guess that superfluidity could be intimately linked to Bose-Einstein condensation. Later on, in 1947, Nikolay Bogoliubov extended the concept of Bose-Einstein condensation to weakly interacting Bose gases and proposed the first microscopic theory for this phenomenon. Subsequently, a series of papers by Landau, Lifshitz, Penrose and Onsager introduced the concept of nondiagonal long-range order and clarified the role thereof in Bose-Einstein condensates and superfluids [2]. This is a particularly important point, as it provides the way to understand the spatial coherence of an atomic cloud (i.e. the fact that distant portions of the same sample exhibit correlated properties) [3]. To better explain this key concept, let us introduce the particle creation and annihilation field operators $\hat{\Psi}^\dagger(\vec{r})$ and $\hat{\Psi}(\vec{r})$ and the one-body density matrix

$$\rho(\vec{r},\,\vec{r}') = \langle \hat{\Psi}^\dagger(\vec{r})\hat{\Psi}(\vec{r}')\rangle, \tag{1.1}$$

expressing the probability amplitude to annihilate a particle at location $\vec{r}'$ and to create one at location $\vec{r}$. Notice that, for $\vec{r} = \vec{r}'$, it corresponds to local density of the system

$$n(\vec{r}) = \rho(\vec{r},\,\vec{r}) = \langle \hat{\Psi}^\dagger(\vec{r})\hat{\Psi}(\vec{r})\rangle$$

which is indeed well normalized to the number of particles present in the system, N, that means that $\int \rho(\vec{r},\,\vec{r})\,\mathrm{d}\vec{r} = N$. In general, the symbol $\langle\cdot\rangle$ in expression (1.1) represents, for a pure state, an usual quantum-mechanical expectation value, namely:

$$\rho(\vec{r},\,\vec{r}') = N\int \Psi^*(\vec{r},\,\vec{r}_2,\,\ldots,\,\vec{r}_N)\,\Psi(\vec{r}',\,\vec{r}_2,\,\ldots,\,\vec{r}_N),$$

while, in the case of a statistical mixture, the average is meant to be an *ensemble average*, which therefore incorporates the probability of occupation of a certain state. If one considers a homogeneous, noninteracting quantum gas at $T = 0$, with N particles confined in a volume V and takes the thermodynamic limit ($N,\,V \to +\infty$, with $N/V = n = \text{const}$), one obtains a translation-invariant system [a circumstance which implies that the one-body density matrix depends only on the *distance* between the considered points, i.e. it is of the type $\rho(\vec{r}, \vec{r}') = \rho(|\vec{r} - \vec{r}'|)$]. In such a system, all N particles occupy the single-particle wave function $|\psi\rangle$ and, therefore, the system itself is described by the properly-symmetrized many-body wave function $\psi(\vec{r}) = \sqrt{N}\langle\vec{r}|\psi\rangle$. The associated one-body density matrix is such that all the matrix elements are equal to the constant value N/V. If one switches on the interactions between bosons, even at $T = 0$, only $N_0 < N$ atoms will be in the ground state, because of the quantum depletion and, as a consequence, the one-body density matrix $\rho(|\vec{r} - \vec{r}'|)$ will decay to the constant value N_0/V for large $|\vec{r} - \vec{r}'|$ (over a length scale given by λ_{dB}). Both in the noninteracting and in the interacting case, the system is said to exhibit an off-diagonal long-range order. This is directly related to the macroscopic occupation of a single-particle state (e.g., the $k = 0$ momentum mode). Conversely, in the absence of condensation, no single-particle state is macroscopically occupied, and the elements of the one-body density matrix $\rho(|\vec{r} - \vec{r}'|)$ will decay to zero for large distances $|\vec{r} - \vec{r}'|$.

The experimental interest toward ultracold atomic gases came years later the theoretical foundations were laid. In the 1970s, thanks to the advent of new techniques for cooling and trapping atoms, some experimental groups started trying to Bose condense some chemical elements. Initially, special attention was devoted to hydrogen, in view of its very light mass but, despite the combined use of dilution refrigeration and evaporation cooling, Bose-Einstein condensation was not achieved. In the 1980s, experimental physicist developed powerful and versatile laser-based cooling techniques (see References [4, 5] for reviews) in order to trap and cool neutral atoms (especially alkali atoms). The time was then ripe for the observation of the first Bose-Einstein condensates: in 1995, the research group of Eric Allin Cornell and Carl Wieman [6] and the one of Wolfgang Ketterle [7] managed to observe Bose-Einstein condensation in gases of, respectively, ^{87}Rb and ^{23}Na. From that moment on, several other elements were successfully condensed, e.g. ^{7}Li [8], spin-polarized hydrogen [9], metastable ^{4}He [10, 11], and ^{41}K [12]. It is important to remember that, in the conditions of temperature and density normally available in modern experimental apparatuses, the equilibrium state of the atomic system would be the solid phase. Therefore, in order to observe Bose-Einstein condensation, one has to keep the system in a metastable gas phase for a sufficiently long time. This is indeed possible because three-body losses [13] constitute rare events in an ultracold dilute gas, whose typically lifetime is hence long enough to perform experiments. The latter usually involve $10^3 - 10^7$ atoms confined in harmonic potentials, whose trapping frequency ω_{ho} sets the characteristic length scale $a_{\text{ho}} = \sqrt{\hbar/(m\omega_{\text{ho}})}$ of the atomic cloud, which generally turns out to be of the order of $10^{-6} - 10^{-5}$ m (notice that this length scale can significantly increase in the presence of interactions).

The experimental achievements of 1995, celebrated by the award of the Nobel Prize in Physics in 2001 [14], opened the door to a number of theoretical and experimental studies in the field of quantum gases, posed new fundamental questions and stimulated the curiosity of generations of young scientists. Some of these problems have already been addressed and solved: there is now a very rich and established literature on Bose-Einstein condensation (References [1, 15–19] represent actual milestones). Nevertheless, many questions concerning the Physics of ultracold quantum matter remain unanswered and many areas of this research field are still uncharted [20–24].

1.1.2 Mixtures of Bose-Einstein condensates

Mixtures of two spin states. The first bosonic binary mixture was produced in 1997 by the research team of Wieman [25] and it consisted of two different spin states ($|F = 2, m = 2\rangle$ and $|F = 1, m = -1\rangle$) of ^{87}Rb. This pioneering experiment showed that the rich scenario of phenomena, phase transitions and dynamical regimes envisaged by Vijay Shenoy the year before (see Reference [26]) was within the reach of experimental setups. A number of experiments based on mixtures of atoms in different spin states immediately followed, which showed the intriguing dynamics of component separation [27], the formation of spin domains [28], the possibility of confining the bosons in optical dipole traps [29], and their collective oscillations [30]. It is important to remark that special attention has been paid to the miscibility of these different components: at the theoretical level, after the seminal work of Shenoy [26], a three-dimensional Hartree-Fock treatment to describe the coupled condensates observed by Wieman [25] was described [31], different kinds of spatial phase separations were predicted [32], and the associated wave functions numerically determined [33]. On the experimental side, the Feshbach resonances between internal spin states have been used to control the phase separation of different spin states of ^{87}Rb atoms [34].

Mixtures of two atomic species. The second class of bosonic binary mixture is represented by systems where two different atomic species are Bose condensed. In 2002, the research group from Firenze (LENS), reported, for the first time, the realization of a mixture of Bose-Einstein condensates of different atomic species, namely ^{41}K and ^{87}Rb [35], opening also the door to the formation of ultracold heteronuclear molecules (which are now a reality [36–38]). This simultaneous condensation of potassium and rubidium atoms, together with the possibility of tuning the interspecies interactions [39], paved the way to a series of experimental and theoretical investigations. In 2011, a research group from Innsbruck (Austria) managed to produce a dual-species Bose-Einstein condensate of rubidium and cesium, and a striking phase separation thereof, revealing the mixture to be immiscible, was also observed [40]. Two years later, in 2013, again in Innsbruck, a quantum degenerate mixture of strontium and rubidium atoms was obtained [41], reaching more than 10^5 condensed atoms per element and thus constituting an important step toward the formation of a quantum gas of polar RbSr molecules. Notice, in this regard, that heteronuclear molecules such as KRb, RbCs and RbSr, can exhibit rather big permanent electric dipole moments [42–45], which, in turn, when subjected to an external polarizing electric field, can be responsible for long-range and anisotropic dipole-dipole interactions. Consequently, at the conditions of densities and temperatures normally present in modern experimental setups [46], dipolar effects are expected to dominate over scattering and reaction dynamics [47] and to give place to intriguing many-body phenomena [48–50]. More recently, there has been increasing interest in the experimental investigation of the Feshbach resonance spectrum of the bosonic pair $^{23}\mathrm{Na} + {}^{39}\mathrm{K}$. The measurements of these resonances and the subsequent creation of a two-species Bose-Einstein condensate of $^{23}\mathrm{Na} + {}^{39}\mathrm{K}$ atoms have been reported by the Hannover group [51] in 2018.

This specific bosonic binary mixture plays an important role in this Thesis, not only because the combination of two intra- and two inter-species resonances allow for a smooth tuning of the scattering lengths, but also because the numerical simulations described in Chapter 4 involve coefficients and model parameters directly linked with the measurements of the Hannover group.

Mixtures of two isotopes. The third way to realize a bosonic binary mixture is to employ different isotopes of the same chemical element (see Reference [52] for a review). In 2008, the research group led by Wieman published the observation of controlled phase separation in a dual-species Bose-Einstein condensate made of ^{85}Rb and ^{87}Rb atoms [53] and, three years later, a mixture of ^{168}Yb - ^{174}Yb atoms was Bose condensed in Japan [54], a demonstration that encouraged the study of Bose-Einstein condensation in radioactive atoms.

Phenomenology of bosonic binary mixtures. Over the last two decades, two-species Bose-Einstein condensates have been employed in the exploration of several different phenomena, ranging from various dynamical phase-separation mechanisms and modulation instabilities [55–58], to the presence of persistent currents (see Reference [59] for an experimental realization and References [60–66] for extended theoretical investigations) and collective excitations [30, 67, 68]. In particular, the conditions under which spatial phase separation (also called "demixing") takes place have been thoroughly analized within mean-field treatments at zero [26, 32, 33, 69–71] and finite [72] temperature, and also by means of Quantum Monte Carlo simulations in the case of hardcore repulsions [73, 74] and dipolar interactions [75].

The basic rule when dealing with harmonically-confined condensates in the mean-field approximation is that, if intra- and interspecies scattering lengths a_{ij} verify the condition $a_{12} < \sqrt{a_{11}a_{22}}$, then the two quantum fluids are miscible [76–80]. Conversely, if the interspecies repulsion $\propto a_{12}$ gets bigger than the (geometric average of the) intraspecies repulsions $\propto \sqrt{a_{11}a_{22}}$, then, already in the rather simple case of bosonic binary mixture trapped in a harmonic potential, two phase separation mechanisms are available, depending on the ratio of the atomic masses and of the interaction strengths: either a two-asymmetric-blob configuration, or in-out spherical separation.

A particular and noticeable class of phase-separated systems is the one where a bosonic binary mixture features dark-bright soliton configurations [57, 81, 82]. These structures, first predicted in Reference [83], are frequently termed as "symbiotic solitons" [84] because the bright component, being endowed with repulsive intraspecies interaction, could not exist if the dark component did not play the role of an effective confining potential. The same symbiotic relationship was shown to constitute the mechanism underlying the robustness of vortex-bright soliton complexes [85], i.e. the topological extension of the dark-bright soliton configuration to the case where a component hosts one or more vortices. The aforementioned study paved the way to a series of further investigations which highlighted, among various aspects, the spontaneous generation of vortex-bright soliton structures [86], a rich dynamical scenario for the bright-solitary component [87], and for the massive vortices [88].

Eventually, it is worth mentioning that considerable attention has been recently paid to quantum liquid droplets [89, 90], a particular class of quantum fluids whose existence is due to the balance between attractive forces, which hold them together, and repulsive ones, that prevent them from collapsing. In ultracold atomic droplets, part of this repulsion originates from a beyond-mean-field effect, well described (to the first order) by the Lee-Huang-Yang repulsive energy [91, 92]. Leaving aside the early works on helium nanodroplets (see References [93, 94] for a review), in 2016, the groups of Tilman Pfau [95–99] and Francesca Ferlaino [100] reported the observation of droplets in quantum gases featuring repulsive contact interactions and dipolar attraction. The following year, the group of Leticia Tarruell published the observation of droplets in a confined system with pure isotropic contact interactions [24] and, soon after, the Firenze group reported the formation of droplets in a homonuclear bosonic binary mixture in free space [46]. The latter experiment opened the door to the study of other important properties, such as self-evaporation, energy dissipation, effect of reduced dimensionality, excitation spectra, etc.

1.1.3 Ultracold atoms in optical lattices

The possibility of storing ultracold atoms in artificial periodic potentials of light, allowed by the unprecedented controllability of matter at the nanoscale, has paved the way to the direct probing of fundamental condensed-matter physics problems [101]. Ultracold quantum gases in optical lattices represent, in fact, quantum simulators, i.e. highly controllable quantum systems that can be employed to mimic and simulate the static or dynamical behavior of other complex quantum systems. Proposed by Richard Feynman [102, 103] in 1985, quantum simulators give a particularly pristine access to several classes of Hamiltonians (some of them coming from solid state physics, atomic physics, quantum optics, or quantum information theory) and therefore constitute almost ideal systems where to test fundamental theoretical concept and to observe quantum many-body effects.

Optical lattices can be produced simply by superimposing two counter- propagating laser beams, whose interference gives place to an optical standing wave which, in turn, can trap atoms. Depending on the number of laser beams used, it is possible to obtain 1D, 2D, or 3D optical periodic potentials, whose sites can be effectively modeled as tight harmonic wells. The striking feature of these experimental apparatuses is that the properties of the resulting periodic potential (geometry and depth) are under the complete control of the experimentalist (the tuning being both static and dynamic). As a consequence of the lattice structure, the motion of single particles in such potentials is usually described in terms of Bloch waves, following the same well-known methodologies used to describe electrons in crystalline structures. In this regard, it is important to remark that, when the interactions in a Bose-Einstein condensate (confined in an optical lattice) get high enough, the particles description in terms of Bloch waves gives way to collective behaviors ruled by nonlinearity. The ensuing phenomenology can be well captured by a description in terms of arrays of bosonic Josephson Junctions [104]. In the context of ultracold atoms, the most essential example of bosonic Josephson Junction is represented by a double-well potential [105]. Observed for the first time by the group of Markus Oberthaler in 2005, but already theoretically extensively studied within different approximation schemes [106–112], this rather simple system discloses a very peculiar and intriguing dynamics, featuring anharmonic Josephson oscillations if the initial population imbalance of the two wells is below a certain critical value, and macroscopic quantum self-trapping (a regime where large-amplitude Josephson oscillations are inhibited) for initial population differences above the critical threshold.

Weakly and strongly interacting regimes. One of the most important features of ultracold atomic systems trapped in optical lattices is the possibility to generate and observe strongly correlated quantum regimes (in spite of their ultralow densities, which is more than five orders of magnitude lower than that of the air around us). We recall, in this regard, that a quantum many-body system featuring *weak* interactions, can be effectively described by a macroscopic wave function, whose time evolution is ruled by a suitably-modified version of the well-known Schrödinger equation, namely the Gross-Pitaevskii equation [1], which does include a nonlinear term incorporating the interaction between particles. Conversely, in the presence of *strong* interactions (compared to the kinetic energy), the system cannot be described in terms of a simple matter wave, its state being ultraquantum and highly correlated [113]. The investigation of this kind of states represents a theoretical and computational challenge in condensed-matter Physics. A typical example of such a transition from the weakly to the strongly interacting regime is represented by the superfluid-to-Mott-insulating quantum phase transition. Firstly predicted to occur in liquid helium [114] and, subsequently, in ultracold atom systems [115], this zero-temperature phase transition has been observed in 2002 by the group of Immanuel Bloch [116]. It can be easily understood by resorting to the Bose-Hubbard Hamiltonian, a second-quantized model which well describes interacting bosons in an optical potential (whose energies are such that only the first band is occupied):

$$\hat{H} = -J \sum_{\langle i,j \rangle} \left(\hat{a}_i^\dagger \hat{a}_j + \text{h.c.} \right) + \frac{U}{2} \sum_i \hat{n}_i (\hat{n}_i - 1) \tag{1.2}$$

The first part constitutes the kinetic energy term, incorporating the tunnel coupling J between adjacent sites and including operators $\hat{a}_i^\dagger$ and $\hat{a}_i$ which, respectively, create and destroy a boson at site i. The second part represents the onsite repulsive energy term U and includes operator $\hat{n}_i$, which counts the number of particles at site i. According to which of the two terms prevails in the energy competition, one can observe two different kinds of ground states: for $U/J \ll 1$ (weakly interacting regime), each atom is delocalized over the entire lattice and one has an actual Bose-Einstein condensate, a phase of matter which can be described by a macroscopic wave function and such that the atom number per well follows a poissonian statistics. Conversely, for $U/J \gg 1$ (strongly interacting regime), the system is a Mott insulator, a phase of matter where bosons are localized to single lattice sites and that cannot be described in terms of a coherent matter wave: phase coherence gives the way to a complete correlation in the particle numbers per site.

Since the experimental observation of the superfluid-Mott insulator transition [116], ultracold atoms have increasingly become a tool to study and probe strongly interacting quantum systems, problems that are so complex that cannot be solved not even by the most powerful supercomputer on Earth. Nowadays, due to their extreme controllability, ultracold atomic and molecular systems are considered to be the best platform where to study several important problems of condensed-matter physics, statistical physics, quantum chemistry and high energy physics. [22, 113, 117]. Among the rest, an important class of quantum simulators is employed to mimic and study magnetic systems and the associated intriguing phenomenology, part of which is still not fully understood. Classical frustrated magnets, for example, can indeed be realized in the context of ultracold atom systems by trapping bosons in an elliptically shaken triangular optical lattice (as the shaking induces controlled complex tunneling processes between the different sites of the triangular plaquettes) and taking the local *phase* of the bosons as a classical spin orientation. Quantum Ising-like magnets, on the other hand, can be realized encoding two-state spin variables in the occupation difference between two neighboring sites [118].

Ultracold atoms in optical lattices allow to explore, also, fundamental phenomena in statistical physics. In this regard, there is a remarkable interest in understanding whether a closed quantum system always thermalizes after a long quantum evolution [119–121], and the impact of disorder on its thermalization and localization properties [122]. It is strongly believed that quantum simulation with ultracold atoms will probably open new research branches in the field of quantum electrodynamics, quantum chromodynamics, and quantum chemistry, possibly leading to the discovery of new phases of matter.

1.1.4 Binary mixtures in optical lattices

The first experimental observation of a Bose-Bose mixture in an optical lattice dates back to 2008 and was reported by the Firenze group [123], which managed to produce a degenerate mixture of ^{87}Rb and ^{41}K atoms in a 3D optical lattice. In the same article, it was shown that, despite the reduced overlap of the two atomic clouds, the presence of superfluid ^{41}K atoms affects the phase coherence of the ^{87}Rb atoms. This effect was possibly interpreted in terms of generation of polarons [124], quasiparticles which, in this context, are composed by localized atoms (^{87}Rb), plus a cloud of superfluid ^{41}K atoms. Polarons hinder the tunneling processes in a twofold way: at zero temperature they simply make what they dress (^{87}Rb atoms) heavier; at finite temperature they undergo incoherent scattering, further damaging the hopping properties of ^{87}Rb atoms.

This is just an example of the the incredibly rich scenario of physical phenomena offered by bosonic binary mixtures in optical lattices. Already in 2003, the group of Peter Zoller envisaged the possibility of creating a molecular dipolar superfluid by means of two-atom processes occurring in an optical lattice [125]. More specifically, starting from a Mott-insulator phase with exactly one atom of each species per lattice site and resorting to a photoassociation process, they showed that one heteronuclear dipolar molecule could be produced in each lattice site, effectively constituting a molecular Mott insulator, whose melting, in turn, could result in a polar molecular superfluid. Always in 2003, Kuklov and Svistunov [126] discussed the possibility of counterflow superfluidity in a two-species ultracold atom system, i.e. the possible existence of two equal and opposite currents of the two atomic species such that the net number-of-atoms transport is zero. This kind of combined flow is made possible by the presence of *two* species in the optical lattice since, in the Mott phase of *single*-species atoms, any low-energy transport process is well known to be suppressed [114]. Interestingly enough, the same paper by Kuklov and Svistunov also highlighted the possibility of writing, in the strong-coupling regime, the effective Hamiltonian for the super-counter fluids in terms of $s = n/2$ isospin operator (the integer n is the filling factor) with ferromagnetic coupling, thus giving the possibility to interpret critical phenomena of spin system within boson system.

The coupling between two different species can be conveniently exploited in order to build cooling schemes that can be used to damp the motional state of neutral atoms encoding a series of entangled qubits in a non-destructive way [127]. The idea is that the atom carrying the (quantum) information dissipates its motional excitations by creating excitations in the superfluid it is immersed in. So, if one has an array of (possibly entangled) atoms, trapped in the sites of an optical lattice, it is indeed possible to keep them into their ground motional state whilst preserving their initial internal state (and their possible entanglement) by submerging them in a superfluid.

Strongly interacting bosonic binary mixtures in optical lattices can also give place to metastable quantum emulsions featuring the properties of a Bose glass [128, 129]. This particular kind of states exhibits finite compressibility (in absence of superfluidity) and *microscopic* phase separation, a circumstance which is reminiscent of emulsions in immiscible fluids. The basic principle is that the presence of a barely-hopping second bosonic species (prepared in a random configuration) produces an effective quasi static disorder potential [130, 131] which, in turn, triggers the emergence of a Bose glass [114, 132] (or Anderson localization [133]) in the first species.

At the theoretical level, bosonic binary mixtures in optical lattices can be conveniently described by means of a two-species Bose-Hubbard Hamiltonian [134], a generalization of the already introduced single-species Bose-Hubbard Hamiltonian (1.2) which incorporates the density-density coupling U_{ab} between the two bosonic species:

$$\begin{aligned} \hat{H} = -J_a \sum_{\langle i,j\rangle} \left(\hat{a}_i^\dagger \hat{a}_j + \text{h.c.}\right) + \frac{U_a}{2} \sum_i \hat{n}_i(\hat{n}_i - 1) + \\ -J_b \sum_{\langle i,j\rangle} \left(\hat{b}_i^\dagger \hat{b}_j + \text{h.c.}\right) + \frac{U_b}{2} \sum_i \hat{m}_i(\hat{m}_i - 1) + \\ + U_{ab} \sum_i \hat{n}_i \hat{m}_i. \end{aligned} \tag{1.3}$$

This kind of Hamiltonian has been used, also, to model spin exchange interactions [135], to investigate the system phase diagram in extended lattices [136–139], to determine the properties of the model at unitary filling [140], to study the superfluid-Mott insulator phase transition of both spin-1 bosons with (anti)ferromagnetic interactions [141] and homonuclear mixtures [142], and to highlight the presence of phases including charge and spin density wave orders [143]. Moreover, Hamiltonian (1.3) has been extended in order to include non-local dipole-dipole interactions [144], to model the formation of polar molecules [145], to investigate the Ising antiferromagnetic phase [146], and it was employed to explore mixing-demixing transitions [147].

The latter aspect has recently received considerable attention in extended lattices both at zero [75, 139, 147–149] and finite [150, 151] temperature, and, more recently, in the simplest possible lattice, i.e. the two well-potential. The dynamical properties of two-species ultracold atoms in a double well have been studied by means of a semiclassical approach that allowed one to map the quantum system into a classical model and hence to investigate the stability of fixed point solutions [152], the presence of symmetry-breaking [153] and symmetry-restoring [154] dynamical regimes, and its possible description in terms of two-species atomic Josephson junctions [155, 156]. The presence of Josephson-like oscillations has been evidenced also in spin-orbit coupled [157–160] and spinor [161] Bose-Einstein condensates, both in the two-mode approximation [162] and in the full framework of the Gross-Pitaevskii equation [1].

1.2 Motivations and Outline

For a number of reasons, a fully-quantum approach to bosonic binary mixtures in few-site potentials deserves a treatment too. First, because when the number of trapped bosons is low enough, a mean-field Gross-Pitaevskii treatment is *not* justified, and neither is its semiclassical description in terms of discrete nonlinear Schrödinger equations. If one aims at a realistic description of microscopic processes occurring in the system at essentially zero temperature, one indeed needs to formulate the model in terms of second-quantized space modes. Second, because even the rather simple models consisting of mixtures trapped in few-site potentials can disclose complex dynamical behaviors and non-trivial quantum effects originating from the competition among tunneling processes and intraspecies and interspecies interactions. Such a competition has an impact, not only on strongly-excited states, but also on weakly-excited ones, including the ground state. It is therefore interesting to revisit symmetry-breaking phenomena and nonlinear behaviors, originally explored within a not-too-problematic mean-field treatment, by means of a fully-quantum approach. In this regard, several well-known methods, both theoretical and computational, seem to be applicable to study few-site Bose-Hubbard models. Despite such circumstances, a rather small attention has been focused on genuinely quantum properties of these systems [163–167]. All these studies, published between 2010 and 2017, are restricted to the two-well system (also known as "dimer") and touched on different aspects, such as the determination of energy eigenvalues and eigenstates by means of perturbation theory [163], the huge number fluctuations (of particles belonging to the different gas components) present in the system ground state in the vicinity of the mixing-demixing phase transition [164], the link between the presence of singularities in the entanglement entropy, the onset of phase separation and the collapse of the energy levels [165, 166] and the analytical determination of the latter [167].

In this Thesis, we investigate the miscibility properties of bosonic binary mixtures loaded in ring lattices, paying particular attention to the simplest possible closed circuit, i.e. the three-well potential (also known as “trimer”). Although it is well known that the competition between intra- and interspecies interactions underpins the rich phenomenology exhibited by bosonic binary mixtures, in this Thesis we point out that there is another key aspect that must be considered when studying the miscibility of quantum fluids: the fragmented character of the confining potential. We show that it is indeed the *discreteness* ensuing from the presence of some (or many) lattice sites that gives place to a rich scenario of quantum phases differing in the degree of mixing and localization.

The latter are evaluated in a *quantitative* way by means of suitable indicators [168] imported from Statistical Thermodynamics, but, so far, never employed in the realm of ultracold atoms. The various quantum phase transitions that have been found (i.e. transitions from phase-separated regimes to uniform and homogeneous configurations and, then, to states where a localized soliton begins to emerge) are, among the rest, characterized in terms of *entanglement* between the species [169] and shown to be related to the emergence of particular types of Schrödinger-cat-like states [170–172]. Within a semiclassical framework [173–175], we investigate a number of dynamical regimes, both regular and chaotic, showing that demixing can persist even in the presence of chaos. Interestingly, a considerable part of the models and physical phenomena theoretically analyzed in this Thesis have been shown to be within the reach of modern experimental apparatuses (see Reference [176], published in collaboration with the experimental group of the Institute of Quantum Optics of Hannover University).

With this Thesis, we sincerely hope we have collected, summarized and properly linked the results of a three-year study which, although it touched on different problems and theoretical aspects (e.g. the formation of currents in ring geometries, entanglement properties, quantum phase transitions involving spatial phase separation of the quantum fluids, dynamical simulations, emergence of solitons), should provide new and original insights in the field of bosonic binary mixtures and some links among different view points. Eventually, we recall that other two published studies (see References [177] and [88] concerning, respectively, ring-ladder and massive-vortex systems), have not been included in this Thesis.

The outline of this manuscript is the following:

- In Chapter 2, we investigate the low-energy excitations of a miscible binary mixture uniformly distributed in a Bose-Hubbard ring. The model Hamiltonian, after a suitable approximation, is recognized to be an element of a 10-dimensional Lie algebra. This uncommon property allows one to shine light on important microscopic processes occurring in the system, and to make use of a group-theoretic approach consisting in the application of the dynamical-algebra method. We therefore find an important conserved quantity (corresponding to the Casimir operator of the algebra), we determine the time evolution of many meaningful physical observables (in particular, we evidence the possibility of angular-momentum transfer between the two fluids and vortex formation), and compute the energy spectrum. The latter, derived in a fully-analytic way, is compared with exact numerical results, and shown to collapse when the interspecies interaction exceeds a precise critical value, a circumstance which heralds the onset of a mixing-demixing quantum phase transition.

- Chapter 3 is devoted to the analysis of a genuinely quantum indicator, the bipartite Von Neumann entanglement entropy, in the different phases exhibited by a bosonic binary mixture trapped in a two-well potential. The critical character of this indicator, i.e. its effectiveness in capturing quantum phase transitions is therefore pointed out in the simplest possible lattice geometry and investigated according to different partition schemes. Moreover, a fully-analytic computation based on the coherent-state approach is presented in order to gain further physical insights into the problem.

- In Chapter 4, we determine the mixing-demixing phase diagram of a repulsive bosonic binary mixture confined in a three-well potential. We show that, in spite of the rather large number of parameters characterizing the model, such a diagram is naturally spanned by only two effective variables, incorporating the possible asymmetry between the two species and the ratio between inter- and intraspecies interactions. The four possible phases are characterized in terms of the Entropy of Mixing, both at a semiclassical and at a fully-quantum level, i.e. analyzing the tomography of the ground state. Several quantum indicators are also employed to evidence the occurrence of quantum phase transitions, including but not limited to, the Entanglement Entropy, the energy fingerprint and the ground-state energy. The experimental feasibility of the system and the observability of the phenomena associated to it are carefully discussed, also thanks to a mean-field Gross-Pitaevskii treatment, which allows one to go beyond the pointlike approximation of potential wells.

- Chapter 5 is focused on some dynamical properties of a repulsive mixture trapped in a three-well potential. We investigate the system dynamics resorting to a suitable set of discrete nonlinear Schrödinger equations and discuss the properties of several dynamical regimes. The energetic and dynamical stability of whole classes of fixed points are analyzed and extended sets of trajectories are numerically simulated. Interestingly, we show that the onset of chaos (i.e. the presence of a non-zero Lyapunov exponent) does not necessarily involve the mixing of the two species. Conversely, because of either energetic or dynamical constraints, phase separation is shown to be a possibly robust and persistent property.

- Chapter 6 is devoted to the analysis of ring-lattice systems featuring *attractive* interspecies coupling. We show that, irrespective of the number of lattice sites, supermixed solitons (i.e. solitons composed of both species) emerge in a rather universal way upon increasing the interspecies attraction. More specifically, we recognize three different quantum phases differing in the degree of miscibility and localization of the two quantum fluids.

- Eventually, Chapter 7 is devoted to an overview of the experimental setups that could be employed in order to probe the effects described in the previous chapters of this manuscript. Part of the developed discussion is the fruit of the collaboration with the experimental team of the Institute of Quantum Optics of Hannover University.

Each chapter is self-readable, although the numerous links with aspects discussed in other chapters are properly pointed out.

Chapter 2

Low-energy excitations of a miscible binary mixture

2.1 Introduction

In this Chapter[1], we investigate the low-energy excitations of a miscible binary mixture uniformly distributed in a Bose-Hubbard ring. To develop our analysis, we move from the site-mode picture (where the expectation values of operators are *local* order parameters of the lattice sites), to the momentum-mode picture (where the expectation values of operators are *collective* order parameters in momentum space). In the momentum domain, we perform the well-known Bogoliubov procedure, assuming that momentum mode $k = 0$ is the one macroscopically occupied for both atomic species. The resulting model Hamiltonian is thus shown to decouple into many sub-Hamiltonians $\hat{H}_k$, one for each *pair* of momentum modes. Each sub-Hamiltonian $\hat{H}_k$ is then proved to belong to the dynamical Lie algebra so(2,3). The presence of a certain dynamical algebra in a physical model is an important and uncommon property, which has been used to find dynamical invariants, the spectrum and the time evolution of several quantum systems [112, 179–184]. In our case, once again, the dynamical algebra proves to be the key-element for the analytic solution of the model under scrutiny. The remarkable importance

---

[1] Note to the reader: part of the content of this Chapter has been published in [178], while further details on the Dynamical Algebra Method have been discussed in [177].

of this abstract mathematical property is that it provides an effective diagonalization scheme and helps to find conserved quantities. Moreover, as it allows one to recognize the important microscopic processes occurring in the system, the time evolution of several meaningful observables belonging to the dynamical algebra can be obtained by solving a linear system of ordinary differential equations.

The solution scheme presented for a generic many-site Bose-Hubbard ring is then applied to the simplest closed circuit: the trimer (a three-site Bose-Hubbard ring). Within a fully-analytic treatment, we compute the low-energy spectrum of this specific system as a function of model parameters. The quantum dynamics of the two-species-trimer low-energy excitations (corresponding to weak currents) is then explored by taking into account different initial conditions (corresponding to simple but significant rotational states) and by solving the relevant system of Heisenberg equations. Interestingly, we observe that angular momentum can indeed be transferred between the two condensed species and we point out the condition under which this phenomenon occurs. Eventually, we focus our attention on the stability of the system and derive an inequality in the parameters' space giving the condition under which the spectrum is well defined and the mixed phase is stable. Approaching the border of this stability region, the energy levels collapse and many physical observables feature a diverging behavior, a circumstance which heralds the onset of a mixing-demixing quantum phase transition (see Chapter 4 for an exhaustive description thereof).

2.2 Model presentation

The Hamiltonian describing a mixture of two condensates loaded in a $L-$site ring lattice and coupled by an interspecies repulsive term is given, in the formalism of second-quantization, by

$$\hat{H} = \frac{U_a}{2}\sum_{j=1}^{L} N_j(N_j-1) - T_a\sum_{j=1}^{L}\left(A_{j+1}^\dagger A_j + A_j^\dagger A_{j+1}\right)$$

$$+\frac{U_b}{2}\sum_{j=1}^{L} M_j(M_j-1) - T_b\sum_{j=1}^{L}\left(B_{j+1}^\dagger B_j + B_j^\dagger B_{j+1}\right)$$

$$+\,W\sum_{j=1}^{L} N_j\, M_j, \tag{2.1}$$

where T_a and T_b represent the hopping amplitudes, U_a and U_b the *intra*-species repulsive interactions, and W is the *inter*-species repulsion (labels a and b are indeed referred to the two species that make up the mixture). A_j and B_j are standard bosonic annihilation operators, which respectively destroy a species-a and a species-b boson in the j-th site. They feature commutators $[A_j, A_k^\dagger] = \delta_{j,k} = [B_j, B_k^\dagger]$, and $[A_j, B_k^\dagger] = 0$. The total number of particles $N = \sum_j^L N_j$ (for species a) and $M = \sum_j^L M_j$ (for species b) are both conserved. $N_j = A_j^\dagger A_j$ and $M_j = B_j^\dagger B_j$ are number operators which count the number of species-a and species-b bosons in the j-th site. Parameter L is the number of sites in the ring lattice and $L+1 \equiv 1$ due to the periodic boundary conditions associated to the ring geometry.

We assume that T_a (T_b) is sufficiently larger than U_a (U_b) in order to avoid the emergence of Mott-insulator states; we also assume that W is sufficiently smaller than U_a and U_b in such a way that the two quantum fluids are miscible. These assumptions not only imply that the system's ground state is superfluid, but also that the two components are completely mixed and delocalized among all the available L sites (see, for example, [139]). This uniform boson distribution (among the lattice sites) entails the macroscopic occupation of momentum modes with $k = 0$ for both species, a circumstance which suggests, in turn, the application of the Bogoliubov approximation scheme. In order to properly enact it, we take advantage of the ring-structure of the system, and move to momentum-mode basis. *Momentum*-mode operators, a_k and b_k, (which, respectively, annihilate a species-a and a species-b boson in momentum mode k) can be defined in terms of the already presented *site*-mode operators

$$A_j = \sum_{k=1}^{L} \frac{a_k}{\sqrt{L}} e^{+i\tilde{k}aj}, \qquad B_j = \sum_{k=1}^{L} \frac{b_k}{\sqrt{L}} e^{+i\tilde{k}aj},$$

with $\tilde{k} = (2\pi/d)k$ and $d = La$. Parameter a is the lattice constant, d is the ring circumference, N (M) is the number of atoms of atomic species a (b) and the summations are restricted to the first Brillouin zone. Momentum-mode operators a_k and b_k are also characterized by standard bosonic commutators $[a_j, a_k^\dagger] = \delta_{j,k}$, $[b_j, b_k^\dagger] = \delta_{j,k}$ and $[a_j, b_k^\dagger] = 0$. In view of the ring geometry, number operators

$n_k = a_k^\dagger a_k$ and $m_k = b_k^\dagger b_k$ count the number of bosons having (angular) momentum equal to $\hbar\tilde{k}$ and therefore taking part to a *current*. After this change of basis, which leads one from the *site*-mode picture to the *momentum*-mode picture, the model Hamiltonian (2.1) can be recast into the form

$$\hat{H} = \frac{U_a}{2L} \sum_{p,q,k=1}^{L} a_{q+k}^\dagger a_{p-k}^\dagger a_q a_p - 2T_a \sum_{k=1}^{L} a_k^\dagger a_k \, \cos(a\tilde{k})$$

$$+\frac{U_b}{2L} \sum_{p,q,k=1}^{L} b_{q+k}^\dagger b_{p-k}^\dagger b_q b_p - 2T_b \sum_{k=1}^{L} b_k^\dagger b_k \, \cos(a\tilde{k})$$

$$+\frac{W}{L} \sum_{p,q,k=1}^{L} a_{p+k}^\dagger \, b_{q-k}^\dagger \, a_p \, b_q .$$

If the system is in the superfluid phase (T_ν/U_ν, $\nu = a, b$ large enough) and both species are uniformly distributed in the lattice ($W/U_\nu, \nu = a, b$ small enough in order to fulfill the miscibility condition), both atomic species are characterized by a macroscopically occupied momentum mode, namely $k = 0$, and the Bogoliubov procedure [185, 186] can be easily enacted.

2.2.1 The Bogoliubov procedure

The two terms corresponding to intraspecies interactions and the term corresponding to the interspecies interaction can be simplified neglecting those addends that include less than two r-mode operators (recall that mode $r = 0$ is the one macroscopically occupied).

$$\sum_{p,q,k=1}^{L} a_{q+k}^\dagger a_{p-k}^\dagger a_q a_p \approx n_0(n_0 - 1) + 4n_0 \sum_{k\neq 0} n_k + (a_0)^2 \sum_{k\neq 0} a_k^\dagger a_{-k}^\dagger + \left(a_0^\dagger\right)^2 \sum_{k\neq 0} a_k a_{-k}$$

Of course, the same is true also for the second atomic species. The interspecies repulsion term can be simplified as follows

$$\sum_{p,q,k=1}^{L} a_{p+k}^\dagger \, b_{q-k}^\dagger \, a_p \, b_q \approx n_0 m_0 + n_0 \sum_{k\neq 0} m_k + m_0 \sum_{k\neq 0} n_k +$$

$$a_0^\dagger b_0^\dagger \sum_{k\neq 0} a_{-k} b_k + a_0^\dagger b_0 \sum_{k\neq 0} a_{-k} b_{-k}^\dagger + a_0 b_0^\dagger \sum_{k\neq 0} a_k^\dagger b_k + a_0 b_0 \sum_{k\neq 0} a_k^\dagger b_{-k}^\dagger$$

The Bogoliubov approximation is based on the identification of the most populated mode. Such mode is then made semiclassical and the relevant operator turned into a complex order parameter (the phase is usually chosen to be null). After enacting the substitutions $a_0^\dagger \to \sqrt{n_0}$, $a_0 \to \sqrt{n_0}$, $b_0^\dagger \to \sqrt{m_0}$, $b_0 \to \sqrt{m_0}$ and writing n_0 as $N - \sum_{k\neq 0} n_k$ and m_0 as $M - \sum_{k\neq 0} m_k$, the Hamiltonian can be written in the following form:

$$\hat{H} = \hat{H}_a + \hat{H}_b + \hat{H}_{ab}$$

where

$$\hat{H}_a = -2T_a\left[N + \sum_{k\neq 0}\Big(\cos(a\tilde{k}) - 1\Big)\, n_k\right] +$$

$$\frac{U_a N}{2L}\left[N - 1 + \sum_{k\neq 0}\Big(n_k + n_{-k} + a_k^\dagger a_{-k}^\dagger + a_k a_{-k}\Big)\right]$$

$$\hat{H}_b = -2T_b\left[M + \sum_{k\neq 0}\Big(\cos(a\tilde{k}) - 1\Big)\, m_k\right] +$$

$$\frac{U_b M}{2L}\left[M - 1 + \sum_{k\neq 0}\Big(m_k + m_{-k} + b_k^\dagger b_{-k}^\dagger + b_k b_{-k}\Big)\right]$$

$$\hat{H}_{ab} = \frac{U_{ab}}{2L} NM +$$

$$\frac{U_{ab}}{2L}\sqrt{NM}\sum_{k>0}\left[a_k b_{-k} + a_{-k} b_k + a_k^\dagger b_{-k}^\dagger + a_{-k}^\dagger b_k^\dagger + a_k^\dagger b_k + a_{-k}^\dagger b_{-k} + a_k b_k^\dagger + a_{-k} b_{-k}^\dagger\right]$$

2.2.2 Effective Hamiltonian

The resulting Hamiltonian

$$\hat{H} = E_0 + \sum_{k>0} \hat{H}_k, \tag{2.2}$$

can be written as the sum of an unessential constant term

$$E_0 = u_a(N-1)/2 - 2NT_a + u_b(M-1)/2 - 2MT_b + w\sqrt{NM} - \sum_{k>0}(\gamma_{k,a} + \gamma_{k,b}),$$

and $(L-1)/2$ decoupled (and therefore independent) Hamiltonians $\hat{H}_k$, each one involving just one *pair* of opposite momentum modes,

$$\begin{aligned} \hat{H}_k &= 2(\gamma_{k,a}A_3 + \gamma_{k,b}B_3) + u_a\,(A_+ + A_-) \\ &+ u_b\,(B_+ + B_-) + w(K_+ + K_- + S_+ + S_-). \end{aligned} \tag{2.3}$$

In the latter expression, two-boson operators

$$\begin{aligned} A_+ &= a_k^\dagger a_{-k}^\dagger, & B_+ &= b_k^\dagger b_{-k}^\dagger, \\ A_- &= a_k a_{-k}, & B_- &= b_k b_{-k}, \\ A_3 &= \frac{n_k + n_{-k} + 1}{2}, & B_3 &= \frac{m_k + m_{-k} + 1}{2}, \\ S_+ &= a_k^\dagger b_k + a_{-k}^\dagger b_{-k}, & K_+ &= a_{-k}^\dagger b_k^\dagger + a_k^\dagger b_{-k}^\dagger. \\ S_- &= a_k b_k^\dagger + a_{-k} b_{-k}^\dagger, & K_- &= a_{-k} b_k + a_k b_{-k} \end{aligned} \tag{2.4}$$

and effective parameters

$$\gamma_{k,a} = u_a - 2T_a\,(c_k - 1)\,, \quad \gamma_{k,b} = u_b - 2T_b\,(c_k - 1)\,,$$

$$u_a = \frac{U_a N}{L}, \qquad u_b = \frac{U_b M}{L}, \qquad w = \frac{W\sqrt{NM}}{L},$$

where $c_k = \cos(a\tilde{k})$, have been introduced to lighten the notation.

2.3 The dynamical algebra method

In general, a dynamical algebra $\mathcal{A}$ is a Lie algebra, i.e. $n-$dimensional vector space spanned by n generators (operators) $\hat{e}_1, \hat{e}_2, \ldots, \hat{e}_n$ closed under commutation (see Figure 2.1 for a pictorial representation). The closure property means that the commutator of any two algebra elements is again an algebra element. A Lie algebra is univocally specified once all the commutators $[\hat{e}_j, \hat{e}_k] = i\sum_m f_{jkm}\,\hat{e}_m$ are given, namely when the set of the so called "structure constants" $\{f_{jkm}\}$ is specified [180]. A model Hamiltonian $\hat{H}$ belongs to a dynamical algebra $\mathcal{A} = \mathrm{span}\{\hat{e}_1, \hat{e}_2, \ldots, \hat{e}_n\}$ whenever $\hat{H}$ can be expressed as a linear combination $\hat{H} = \sum_j h_j \hat{e}_j$ of the generators

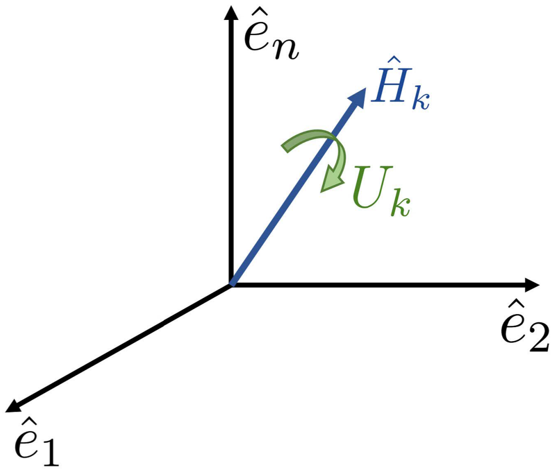

Figure 2.1: Pictorial representation of the dynamical algebra as a vector space. Hamiltonians (2.3) and (2.5) corresponds to vectors and unitary transformations (2.6) correspond to rotations.

of $\mathcal{A}$. The important consequences of this property are that

(a) Conserved physical quantities correspond to algebra's invariants,

(b) The diagonalization process of $\hat{H}$ becomes straightforward,

(c) The Heisenberg equations can be shown to form a simple linear system of ordinary differential equations.

Hamiltonian $\hat{H}_k$ [see formula (2.3)] is recognized to be an element of the dynamical algebra $\mathcal{A} = \text{so}(2,3)$, a 10−dimensional Lie algebra spanned by operators (2.4) where operators $\{A_+,\ A_-,\ A_3\}$, associated to species a, generate a su(1,1) algebra marked by the well-known commutators $[A_+, A_-] = -2A_3$, $[A_3, A_\pm] = \pm A_\pm$, and operators $\{B_+,\ B_-,\ B_3\}$, relevant to species b, feature the same su(1,1) structure (an application of this dynamical algebra can be found in [187] for a trapped condensate).

However, the important term in $\hat{H}_k$ is the inter-species interaction term which is responsible for an algebraic structure considerably more complex than the simple direct sum of two su(1,1) algebras. The defining commutators of this 2-boson realization of algebra so(2,3) are given in Figure 2.2.

Interestingly, the same algebra was found to feature the completely different model of a single condensate trapped in a two-ring ladder [177]. In that model,

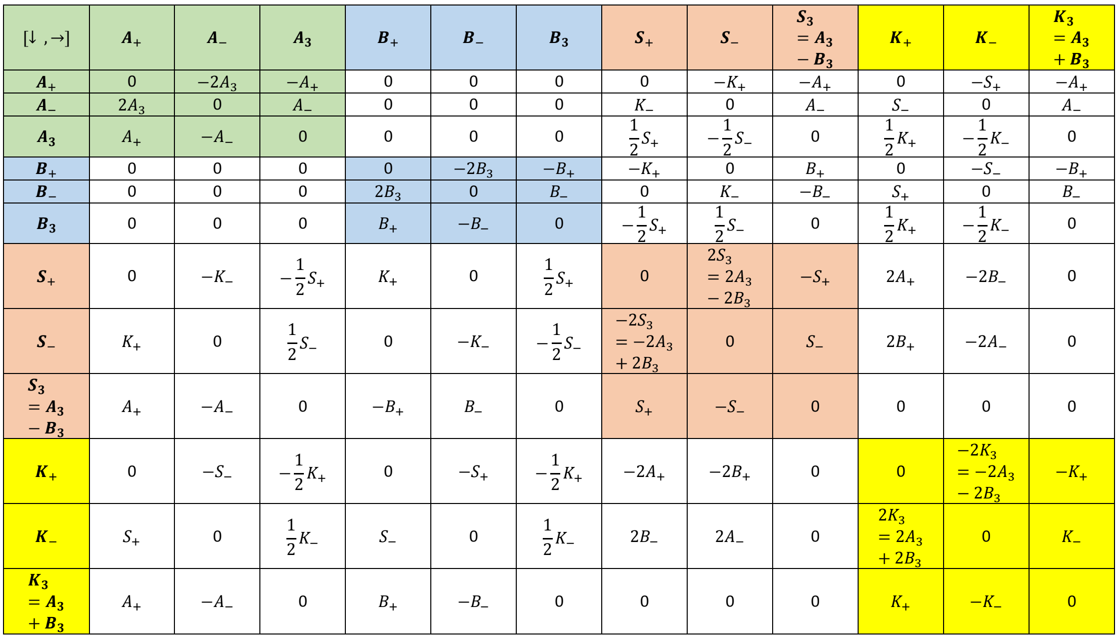

[↓ ,→]	**A_+**	**A_-**	**A_3**	**B_+**	**B_-**	**B_3**	**S_+**	**S_-**	**$S_3 = A_3 - B_3$**	**K_+**	**K_-**	**$K_3 = A_3 + B_3$**
A_+	0	$-2A_3$	$-A_+$	0	0	0	0	$-K_+$	$-A_+$	0	$-S_+$	$-A_+$
A_-	$2A_3$	0	A_-	0	0	0	K_-	0	A_-	S_-	0	A_-
A_3	A_+	$-A_-$	0	0	0	0	$\frac{1}{2}S_+$	$-\frac{1}{2}S_-$	0	$\frac{1}{2}K_+$	$-\frac{1}{2}K_-$	0
B_+	0	0	0	0	$-2B_3$	$-B_+$	$-K_+$	0	B_+	0	$-S_-$	$-B_+$
B_-	0	0	0	$2B_3$	0	B_-	0	K_-	$-B_-$	S_+	0	B_-
B_3	0	0	0	B_+	$-B_-$	0	$-\frac{1}{2}S_+$	$\frac{1}{2}S_-$	0	$\frac{1}{2}K_+$	$-\frac{1}{2}K_-$	0
S_+	0	$-K_-$	$-\frac{1}{2}S_+$	K_+	0	$\frac{1}{2}S_+$	0	$2S_3 = 2A_3 - 2B_3$	$-S_+$	$2A_+$	$-2B_-$	0
S_-	K_+	0	$\frac{1}{2}S_-$	0	$-K_-$	$-\frac{1}{2}S_-$	$-2S_3 = -2A_3 + 2B_3$	0	S_-	$2B_+$	$-2A_-$	0
$S_3 = A_3 - B_3$	A_+	$-A_-$	0	$-B_+$	B_-	0	S_+	$-S_-$	0	0	0	0
K_+	0	$-S_-$	$-\frac{1}{2}K_+$	0	$-S_+$	$-\frac{1}{2}K_+$	$-2A_+$	$-2B_+$	0	0	$-2K_3 = -2A_3 - 2B_3$	$-K_+$
K_-	S_+	0	$\frac{1}{2}K_-$	S_-	0	$\frac{1}{2}K_-$	$2B_-$	$2A_-$	0	$2K_3 = 2A_3 + 2B_3$	0	K_-
$K_3 = A_3 + B_3$	A_+	$-A_-$	0	B_+	$-B_-$	0	0	0	0	K_+	$-K_-$	0

Figure 2.2: Characteristic commutators of the dynamical algebra so(2,3). The various sub-algebras discussed in the main text are evidenced with different colors. The presence of two extra rows and columns (the ones corresponding to S_3 and K_3, which are not linearly independent generators) is indeed intended to highlight the presence of the sub-algebras. Notice that this table is antisymmetric because, in general $[\mathcal{O}_1, \mathcal{O}_2] = -[\mathcal{O}_2, \mathcal{O}_1]$, for any pair of operators $\mathcal{O}_1$, $\mathcal{O}_2$.

terms $S_\pm$ described the angular-momentum transfer between two coupled rings via tunnelling effect. In the present model, in addition to terms $S_\pm$, the new operators $K_\pm$ appear, and they correspond to two-boson creation and destruction processes that were absent in the two-ring model. This difference comes from the density-density inter-species coupling term characterizing the current model which replaces the inter-ring tunneling term of the two-ring model (compare term $W \sum_{j=1}^{L} N_j\, M_j$ in (2.1) with term $-T \sum_{j=1}^{L} \left(A_j B_j^\dagger + B_j A_j^\dagger \right)$ in [177]).

Concluding, we note that this approximation scheme, based on the macroscopic occupation of momentum modes $k = 0$, is valid also in the case $U_a, U_b < 0$, describing attractive interactions among bosons of the same species, provided that *i)* the ratio $T_\nu/|U_\nu|$ ($\nu = a, b$) is sufficiently large, in order to guarantee a superfluid phase, and *ii)* the ratio $W/|U_\nu|$ is small enough to determine uniform boson distributions [188].

2.4 Diagonalization of the model

In order to diagonalize our model, we choose the set $\{|n_k,\, n_{-k},\, m_k,\, m_{-k}\rangle\}$ as a basis of the Hilbert space of states associated to sub-Hamiltonian $\hat{H}_k$. The four quantum numbers $n_{\pm k}$ and $m_{\pm k}$ which label a basis vector, correspond to the numbers of bosons endowed with angular momentum $\pm k$ in either the condensed species. Since the numbers of particles in each species are conserved, the number of bosons in momentum modes $r = 0$ (modes that have been made semiclassical) are

$$n_0 = N - \sum_{k\neq 0} n_k, \qquad m_0 = N - \sum_{k\neq 0} m_k.$$

2.4.1 Energy eigenstates and eigenvalues

The information that a Hamiltonian belongs to a certain dynamical algebra allows one to calculate its spectrum in a straightforward way. In general, one can exploit the algebra structure to numerically diagonalize the Hamiltonian. In the particular but significant case where $u_a = u_b =: u$ and $T_a = T_b =: T$, the diagonalization process is fully analytic, and sub-Hamiltonian

$$\hat{H}_k = 2\gamma_k\,(A_3 + B_3) + u\,(A_+ + A_- + B_+ + B_-) \\ + w(K_+ + K_- + S_+ + S_-) \tag{2.5}$$

can be put in diagonal form (see Appendix A for detailed calculations) by making use of a unitary transformation U_k belonging to group SO(2,3)

$$U_k = e^{\frac{\varphi}{2}(S_- - S_+)} e^{\frac{\theta_a}{2}(A_- - A_+)} e^{\frac{\theta_b}{2}(B_- - B_+)}. \tag{2.6}$$

A proper choice of angles φ, θ_a and θ_b, allows one to get rid of those operators which are not diagonal in the Fock-state basis. By choosing

$$\varphi = \frac{\pi}{2}, \qquad \operatorname{th}\theta_a = \frac{u+w}{\gamma_k + w}, \qquad \operatorname{th}\theta_b = \frac{u-w}{\gamma_k - w}, \tag{2.7}$$

one obtains the diagonal Hamiltonian

$$\hat{\mathcal{H}}_k = U_k^{-1}\,\hat{H}_k\,U_k = 2A_3\sqrt{(\gamma_k - u)(\gamma_k + u + 2w)}$$

$$+\, 2B_3\sqrt{(\gamma_k - u)(\gamma_k + u - 2w)} \tag{2.8}$$

in which operators A_3 and B_3 are linear combinations of number operators [see formulas (2.4)], and thus are diagonal in the Fock-state basis. Since $\hat{H} = \sum_k \hat{H}_k$, then the energy spectrum of $\hat{H}$ takes the form

$$E(\{n_k, n_{-k}, m_k, m_{-k}\}) =$$

$$-4TN + \frac{U}{L}(N^2 - N) + \frac{W}{L}N^2 + \sum_{k>0}\Big[4T(c_k - 1) - 2u$$

$$+\hbar\omega_k(n_k + n_{-k} + 1) + \hbar\Omega_k(m_k + m_{-k} + 1)\Big] \tag{2.9}$$

where $\tilde{k} = 2\pi k/(aL)$ in $c_k = \cos(a\tilde{k})$, $k \in [1, (L-1)/2]$ is an integer index, and

$$\omega_k = \frac{1}{\hbar}\sqrt{2T(1-c_k)[2T(1-c_k) + 2u + 2w]}, \tag{2.10}$$

$$\Omega_k = \frac{1}{\hbar}\sqrt{2T(1-c_k)[2T(1-c_k) + 2u - 2w]}. \tag{2.11}$$

are characteristic frequencies associated to each Hamiltonian $\hat{H}_k$ together with quantum numbers $n_{\pm k}$ and $m_{\pm k}$.

Comparison with matrix method. Hamiltonian (2.5) can be diagonalized also by means of a different approach, which bypasses the recognition of the underlying dynamical algebra. This Hamiltonian, in fact, can be regarded as a quadratic form of boson operators [recall definitions (2.4)], and, as such, it can be diagonalized in a straightforward way according to the general scheme discussed in reference [189].

Preliminary, Hamiltonian (2.5) can be written (up to an additive constant C_0 which affects the zero-point energy but *not* the characteristic frequencies) in the form

$$\hat{H}_k = C_0 + (a_k^\dagger,\, a_{-k}^\dagger,\, b_k^\dagger,\, b_{-k}^\dagger,\, a_k,\, a_{-k},\, b_k,\, b_{-k})\,\mathbb{M}\,(a_k,\, a_{-k},\, b_k,\, b_{-k},\, a_k^\dagger,\, a_{-k}^\dagger,\, b_k^\dagger,\, b_{-k}^\dagger)^t \tag{2.12}$$

where matrix

$$\mathbb{M} = \begin{pmatrix} \frac{\gamma_k}{2} & 0 & \frac{w}{2} & 0 & 0 & \frac{u}{2} & 0 & \frac{w}{2} \\ 0 & \frac{\gamma_k}{2} & 0 & \frac{w}{2} & \frac{u}{2} & 0 & \frac{w}{2} & 0 \\ \frac{w}{2} & 0 & \frac{\gamma_k}{2} & 0 & 0 & \frac{w}{2} & 0 & \frac{u}{2} \\ 0 & \frac{w}{2} & 0 & \frac{\gamma_k}{2} & \frac{w}{2} & 0 & \frac{u}{2} & 0 \\ 0 & \frac{u}{2} & 0 & \frac{w}{2} & \frac{\gamma_k}{2} & 0 & \frac{w}{2} & 0 \\ \frac{u}{2} & 0 & \frac{w}{2} & 0 & 0 & \frac{\gamma_k}{2} & 0 & \frac{w}{2} \\ 0 & \frac{w}{2} & 0 & \frac{u}{2} & \frac{w}{2} & 0 & \frac{\gamma_k}{2} & 0 \\ \frac{w}{2} & 0 & \frac{u}{2} & 0 & 0 & \frac{w}{2} & 0 & \frac{\gamma_k}{2} \end{pmatrix} \tag{2.13}$$

encodes the coefficients of the quadratic form (2.5). Notice, in passing, that $\mathbb{M}$ is Hermitian and that, due to the bosonic characters of the associated operators, it features the following block structure:

$$\mathbb{M} = \begin{pmatrix} A & B \\ B^* & A^* \end{pmatrix}$$

where A and B are suitable matrices.

After introducing matrix

$$\mathbb{E} = \begin{pmatrix} 1 & 0 & 0 & 0 & 0 & 0 & 0 & 0 \\ 0 & 1 & 0 & 0 & 0 & 0 & 0 & 0 \\ 0 & 0 & 1 & 0 & 0 & 0 & 0 & 0 \\ 0 & 0 & 0 & 1 & 0 & 0 & 0 & 0 \\ 0 & 0 & 0 & 0 & -1 & 0 & 0 & 0 \\ 0 & 0 & 0 & 0 & 0 & -1 & 0 & 0 \\ 0 & 0 & 0 & 0 & 0 & 0 & -1 & 0 \\ 0 & 0 & 0 & 0 & 0 & 0 & 0 & -1 \end{pmatrix}, \tag{2.14}$$

the characteristic frequencies of Hamiltonian (2.5) can be easily found by computing the eigenvalues λ_i (with $i = 1, \ldots, 8$) of matrix $2\mathbb{E}\mathbb{M}$. Among the 8 eigenvalues output by this procedure, one focuses just on the 4 λ_i's which are *positive*. Eventually, one can easily notice that these 4 positive eigenvalues are pairwise equal. So, one remains with just two independent characteristic frequencies, which perfectly correspond to frequencies ω_k and Ω_k, obtained, in turn, within the dynamical-algebra method [see equations (2.10) and (2.11), where the extra factor $\hbar^{-1}$ therein simply comes from the way these frequencies are defined in equation (2.9)].

Comparison with numerics. We have compared the results obtained within the Bogoliubov approximation scheme with the exact results obtained by means of exact numerical diagonalization of Bose-Hubbard Hamiltonian (2.1). As Figure 2.3 clearly illustrates, the agreement between analytic and numerical results is very good, particularly for the ground state and for the first excited states. Notice that the numerical diagonalization has been performed with a relative low number of bosons ($N = M = 10$) and that, increasing the number of particles, Bogoliubov approximation scheme gets more and more valid and accurate. The discussion relevant to the degeneracy of the eigenlevels can be found in [177].

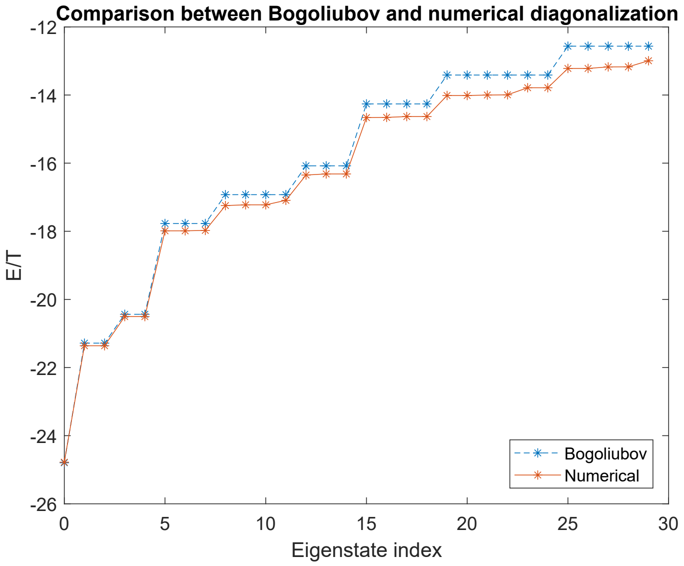

Figure 2.3: Comparison between the spectrum obtained via Bogoliubov approximation scheme [see formulas (2.9)-(2.11)] with the exact spectrum of Hamiltonian (2.1) obtained via exact numerical diagonalization for $L = 3$, $T = 3$, $U = 1$, $W = 0.5$ and $N = M = 10$.

2.4.2 Time-evolution of physical observables and microscopic processes

The knowledge of the dynamical algebra of an Hamiltonian allows one to represent it as a linear combination $\hat{H} = \sum_i h_i \hat{e}_i$ of the algebra generators $\hat{e}_k$. For our effective model [see Hamiltonian (2.3)], these coincide with the two-mode operators (2.4) of the set $\mathcal{A}$. Thanks to the characteristic commutators of the algebra (see Figure 2.2), the Heisenberg equation of any $\hat{e}_k$ is readily found to be

$$i\hbar\frac{\mathrm{d}}{\mathrm{d}t}\hat{e}_k = [\hat{e}_k, \hat{H}] = i\sum_m \rho_{km}\hat{e}_m, \tag{2.15}$$

Then, the time evolution of any observable $\mathcal{O}$ belonging to the algebra (i.e. that can be written in the form $\mathcal{O} = \sum_k o_k \hat{e}_k$) is easily determined within the algebra. For example, from Equation (2.15) one easily discovers that operator $C_k = n_k - n_{-k} + m_k - m_{-k}$ (the angular momentum carried by bosons populating the momentum modes $\pm k$) is a constant of motion. Another example concerns the number of bosons $N_* = A_3 + B_3 = n_k + n_{-k} + m_k + m_{-k}$ with angular momentum (proportional to) $\pm k$, whose equation is

$$\begin{aligned} i\hbar\frac{\mathrm{d}N_*}{\mathrm{d}t} &= -2u\left(A_+ - A_- + B_+ - B_-\right) - 2w\left(K_+ - K_-\right) \\ &= -2u\left(a_k^\dagger a_{-k}^\dagger - a_k a_{-k} + b_k^\dagger b_{-k}^\dagger - b_k b_{-k}\right) \\ &\quad - 2w\left(a_k^\dagger b_{-k}^\dagger + a_{-k}^\dagger b_k^\dagger - a_k b_{-k} - a_{-k} b_k\right). \end{aligned} \tag{2.16}$$

This equation shows how the time evolution of N_* depends on and implicitly defines two generalized currents of boson-pairs whose distinctive trait is to flow from the macroscopic modes[2] a_0 and b_0 to the excited modes $a_{\pm k}$ and $b_{\pm k}$. Remarkably, while the intraspecies repulsive interaction u accounts for the creation of opposite-momentum boson pairs within the *same* atomic species through the terms $A_\pm$ and $B_\pm$, the interspecies coupling w causes the formation of opposite-momentum boson pairs in a twisted fashion (i.e. one boson in an atomic species and one in the other) through the terms $K_\pm$. We remark that this second process is due to operators $K_\pm$ which were absent in the two-ring model [177]. Some of these microscopic processes are illustrated in Figure 2.4.

---

[2] One should remember that, in the Bogoliubov scheme, a_0 and b_0 have been incorporated in the effective interaction strengths u, w in terms of the parameters $\sqrt{N}$ and $\sqrt{M}$.

A bigger algebra for finer-grained observables. Another application of formula (2.15) consists in computing the dynamical equations of finer-grained observables such as the single-mode number operators $n_{\pm k}$ and $m_{\pm k}$ related to excited modes. To this end, one must consider the enlarged dynamical algebra so(2,4) [including so(2,3)] in which $n_{\pm k}$ and $m_{\pm k}$ can be seen as algebra elements. The 15 generators constituting the two-boson realization of so(2,4) are given below:

$$A_+ = a_k^\dagger a_{-k}^\dagger, \qquad A_- = A_+^\dagger, \qquad A_3 = \frac{1}{2}(n_k + n_{-k} + 1),$$

$$B_+ = b_k^\dagger b_{-k}^\dagger, \qquad B_- = B_+^\dagger, \qquad B_3 = \frac{1}{2}(m_k + m_{-k} + 1),$$

$$Q_+ = a_k^\dagger b_k, \quad Q_- = Q_+^\dagger, \quad G_+ = a_{-k}^\dagger b_k^\dagger, \quad G_- = G_+^\dagger$$

$$H_+ = a_k^\dagger b_{-k}^\dagger, \quad H_- = H_+^\dagger, \quad R_+ = a_{-k}^\dagger b_{-k}, \quad R_- = R_+^\dagger,$$

$$T = \frac{1}{2}\left[(n_k - n_{-k}) - (m_k - m_{-k})\right].$$

Within this wider algebraic framework, the equation of motion for the excited-mode number operator n_k therefore reads

$$i\hbar\dot{n}_k = [u\, a_k^\dagger a_{-k}^\dagger + w(a_k^\dagger b_{-k}^\dagger + a_k^\dagger b_k)] - H.C. \tag{2.17}$$

A similar equation holds for operators m_k in which operators a_k and b_k are exchanged. This equation clearly shows that a time variation of n_k is caused both by intraspecies ($u \neq 0$) and by interspecies ($w \neq 0$) interaction processes. Such processes are depicted in Figure 2.4.

2.5 Dynamics on a ring trimer

The theory and the formulas we have discussed so far are valid for a ring having an arbitrary site number L. In the present section, we investigate the simple model with $L = 3$, the so-called two-species ring trimer. This particular geometry has been thoroughly analyzed in the last decade, because of the rich scenario of nonlinear phenomena triggered by the non-integrable character of a system featuring three spatial modes [175, 183, 190–200]. In the trimer case, k takes just three values, namely, ±1, and 0 (whose relevant momentum mode will be made semiclassical

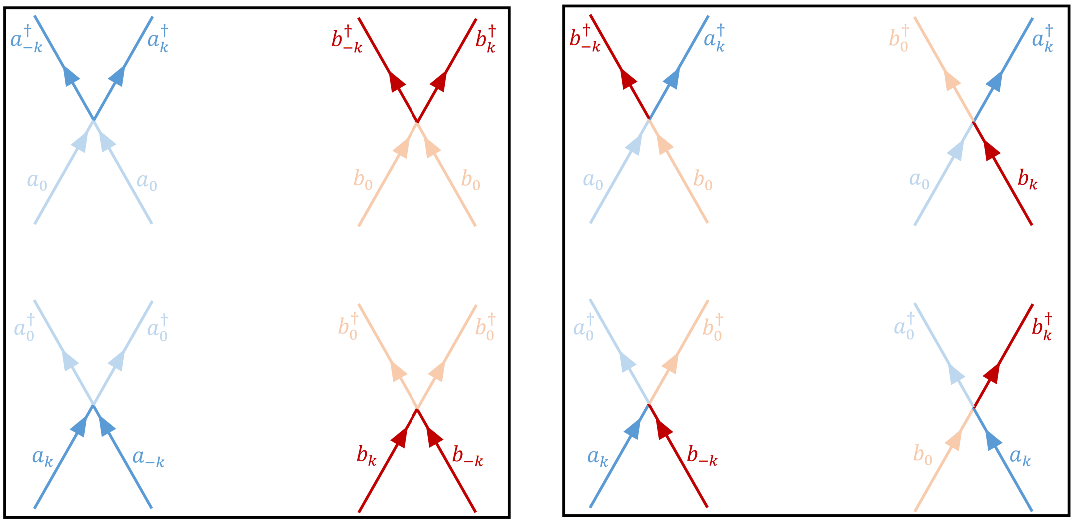

U W

Figure 2.4: Some important microscopic processes that occur in the mixture. Blue and red colors are used to distinguish the two species. Faded colors denote particles that belong to the two macroscopic modes, a_0 and b_0, that have been made semiclassical. Left panel: U determines the creation and annihilation of excited boson-pairs within the same species. Right panel: W determines the creation and annihilation of twisted boson-pairs (left side) and is responsible for scattering processes between particles of different species (right side).

in the Bogoliubov picture). Therefore, the only sub-Hamiltonian is $\hat{H}_k = \hat{H}_1$ [see (2.3)], associated to parameter

$$\gamma_1 = 2T\left[1 - \cos\left(2\pi/3\right)\right] + u.$$

To diagonalize $\hat{H}_1$, the proper choice of generalized angles is $\mathrm{th}\theta_a = (u+w)(\gamma_1+w)$, $\mathrm{th}\theta_b = (u-w)/(\gamma_1-w)$ and $\varphi = \pi/2$ which gives $\hat{\mathcal{H}} = E_0 + 2\hbar\omega\ A_3 + 2\hbar\Omega\ B_3$ with the two characteristic frequencies

$$\omega = \sqrt{3T(3T+2u+2w)}/\hbar, \tag{2.18}$$

$$\Omega = \sqrt{3T(3T+2u-2w)}/\hbar. \tag{2.19}$$

The energy eigenvalues then read

$$E(n_{\pm 1}, m_{\pm 1}) = E_g + \hbar\omega(n_1 + n_{-1}) + \hbar\Omega(m_1 + m_{-1}) \tag{2.20}$$

where $E_g = E_0 + \hbar(\omega + \Omega)$. The good agreement of eigenvalues (2.20) with the numerically computed spectrum of Hamiltonian (2.1) is illustrated in Figure 2.3.

The frequencies (2.18) and (2.19), and the expressions of angles θ_a and θ_b are correctly defined only in a portion of the three-dimensional parameter space (T, U, W). This region of the parameter space, where the spectrum is discrete, classically corresponds to the region where the system exhibits a stable dynamics. At the border of such stability region, the energy cost to create excitations tends to zero and the system manifest unstable behaviors. From the point of view of the dynamics, in fact, one can observe the divergence of many physical observables. This aspect will be resumed in Section 2.6.

2.5.1 Time evolution of excitations

In the same spirit of reference [177], it is possible to describe the dynamics of the momentum mode operators in terms of their expectation values. The latter are represented by the four (complex) order parameters

$$a_{\pm 1} = \sqrt{n_{\pm 1}} e^{i\phi_{\pm 1}}, \qquad b_{\pm 1} = \sqrt{m_{\pm 1}} e^{i\psi_{\pm 1}}.$$

Over the remainder of this subsection, we will show that one can trigger different dynamical regimes by performing different choices both for the initial state (i.e. the complex order parameter at $t = 0$), and for the Hamiltonian parameters T, u, and w. The plots that we present below correspond to the analytic solutions of the dynamical equations (2.17) for the excited populations $n_{\pm 1}(t)$ and $m_{\pm 1}(t)$ for four different choices of initial conditions. Note that the excitation of angular-momentum modes corresponds to excite weakly-populated vortices.

(1) Absence of excitations at $t = 0$. Although, at the beginning of the dynamics, none of the condensates feature any excitation, the presence of interactions $w \neq 0$ and $u \neq 0$ causes the periodic formation of excited bosons within the mixture, according to the formula

$$n_{\pm 1}(t) = m_{\pm 1}(t) =$$

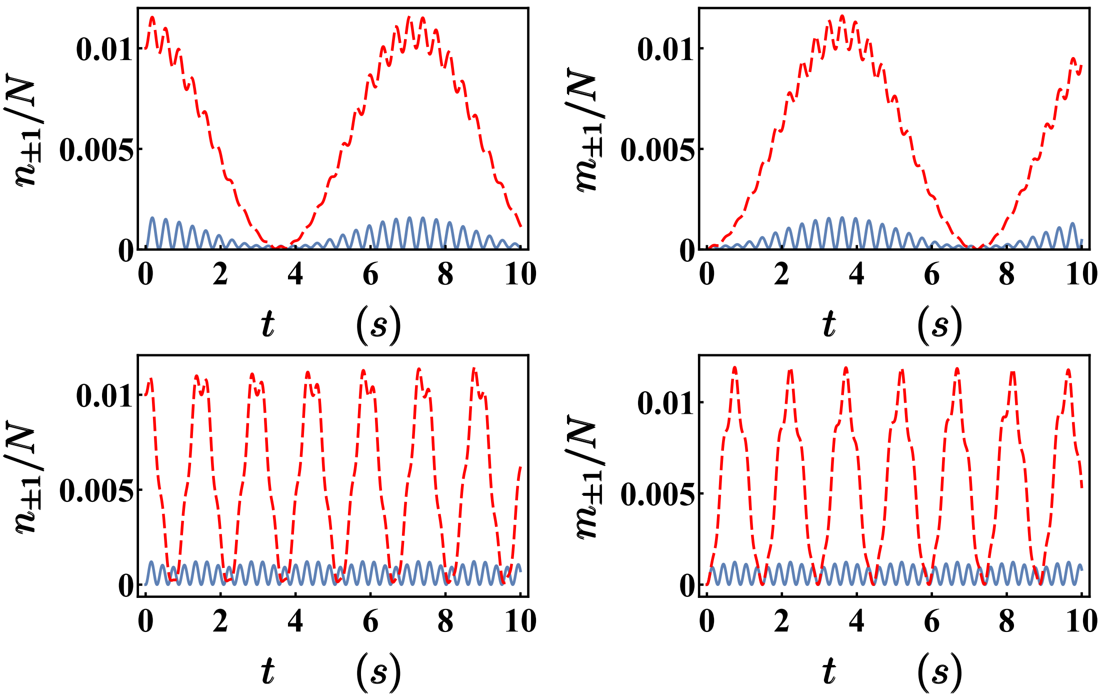

Figure 2.5: Dynamics of excitations for $n_1(0) = 10$, $n_{-1}(0) = m_{\pm1}(0) = 0$ and $W/U = 0.19$ (upper panels) and $W/U = 0.9$ (lower panels), with $T = 2$, $U = 0.01$, $N = 1000$ and $\hbar = 1$. Left (right) panel concerns atomic species A (B). Red dashed (blue) color corresponds to bosons with $k = +1$ $(k = -1)$. The fact that $n_1(t)$ features a maximum when $m_1(t)$ is zero and vice-versa entails the periodic and complete angular momentum transfer between the two species. Increasing W strongly changes the time scale of population oscillations.

$$\frac{1}{2\hbar^2}\left[\frac{(u-w)^2}{\Omega^2}\sin^2(\Omega t)+\frac{(u+w)^2}{\omega^2}\sin^2(\omega t)\right].$$

In other words, the fact that interactions u and w are non zero causes fluctuations in the vacuum state $|n_1, n_{-1}, m_1, m_{-1}\rangle = |0, 0, 0, 0\rangle$.

(2) Vortex-like excitation in condensate A, no excitations in condensate B. If, at time $t = 0$, one of the two atomic species exhibits a non-zero population (e.g. $n_1 \neq 0$, namely a vortex excitation with $k = +1$), one observes, apart form minor quantum fluctuations (the high-frequency ripple in the figure), a periodic transfer of angular momentum between the two atomic species. This effect is illustrated in Figure 2.5 for $W << U$ (upper panels) and $W \simeq U$ (lower panels). Of course, this case is equivalent to the case with condensate B excited and condensate A unexcited at $t = 0$.

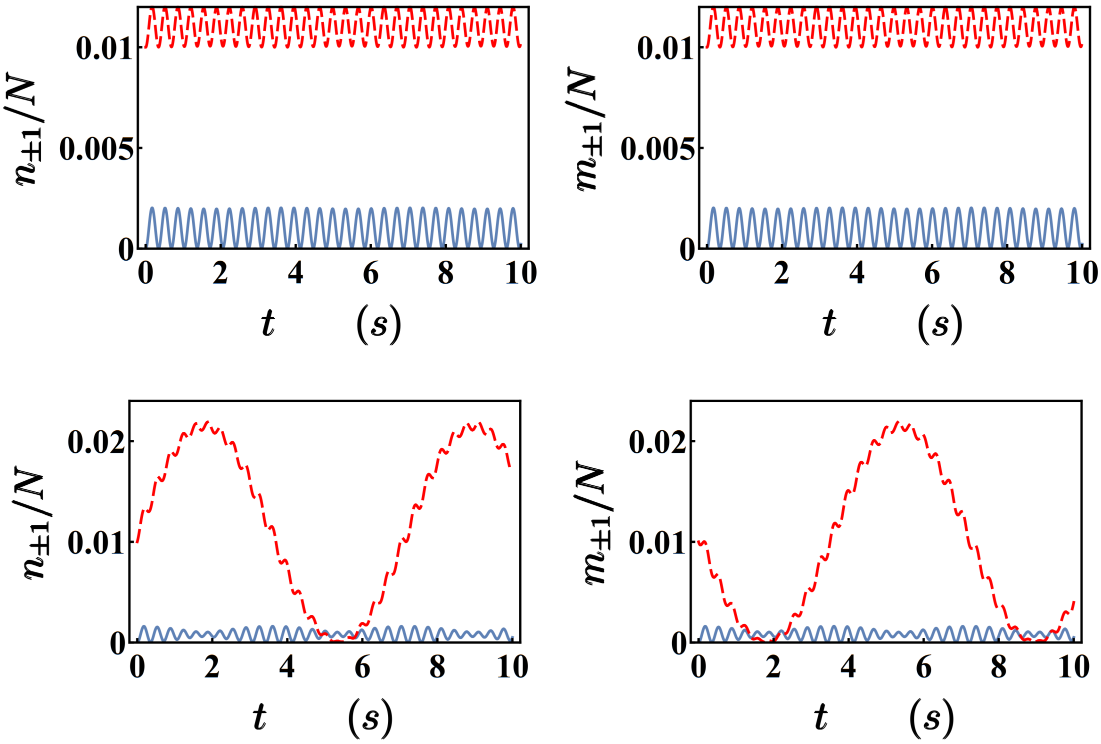

Figure 2.6: Dynamics of excitations for $n_1(0) = m_1(0) = 10$, $n_{-1}(0) = m_{-1}(0) = 0$, and $T = 2$, $U = 0.01$, $W/U = 0.19$, $N = 1000$ and $\hbar = 1$. Left (right) panels concern species A (B). Red dashed (blue) color is used to depict $n_1(t)$ and $m_1(t)$ ($n_{-1}(t)$ and $m_{-1}(t)$). Upper panels: for an initial phase difference $\phi_1(0) - \psi_1(0) = 0$ the system features a trivial dynamics, entailing that the inter-species angular-momentum transfer is suppressed. Lower panels: Conversely, the periodic angular-momentum transfer is active if $\phi_1(0) - \psi_1(0)$ is non-zero (e.g. equal to $\pi/2$).

The relevance of the inter-species parameter on the population dynamics is highlighted in the lower panels of Figure 2.5: Increasing W clearly shows how the periodic collapse and revival of populations n_{-1}, m_{-1} is replaced by an essentially regular oscillation while the oscillation of n_{+1}, m_{+1} as well as the angular-momentum transfer take place on a much smaller time scale. The same periodic angular-momentum transfer is also observed when, in addition to a vortex, the initial configuration includes an anti-vortex in the same species.

(3) Vortex in condensate A and equal vortex in condensate B. Let us assume that, at $t = 0$, species A exhibits a weakly-populated vortex while an equal vortex is present in species B. This is an interesting situation, because different initial

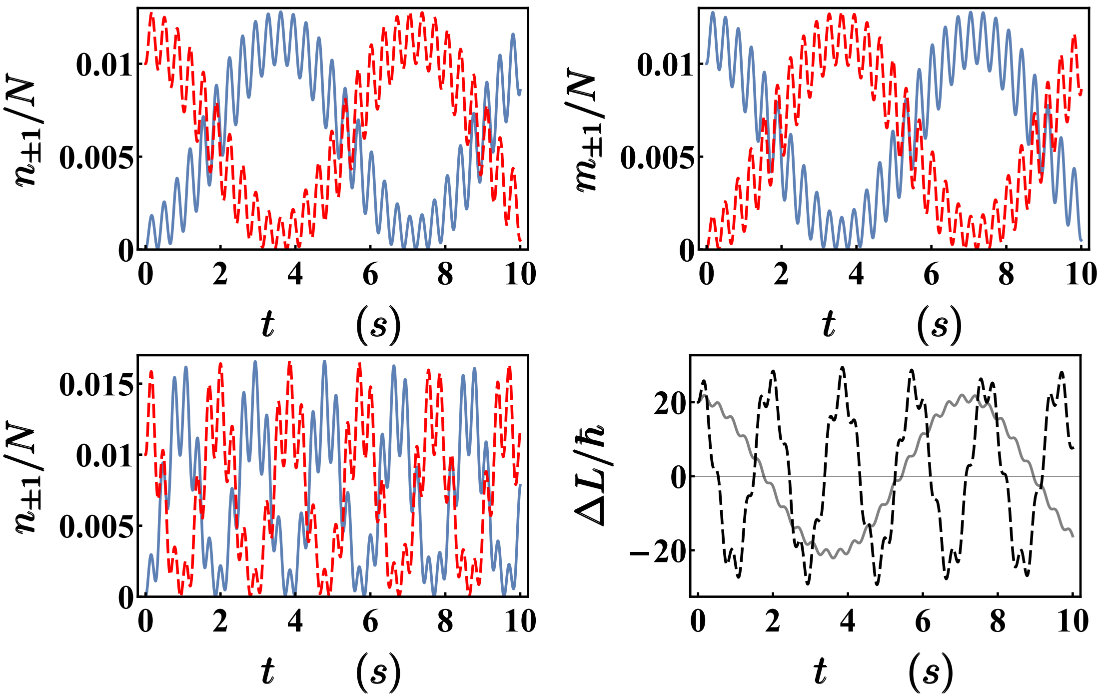

Figure 2.7: Upper panels: Dynamics of excitations for $n_1(0) = m_{-1}(0) = 10$, $n_{-1}(0) = m_1(0) = 0$ and $W/U = 0.19$, $T = 2$, $U = 0.01$, $N = 1000$ and $\hbar = 1$. The left (right) panel concerns species A (B). Red dashed (blue) color corresponds to bosons with $k = +1$ $(k = -1)$. Note, up to quantum fluctuations (high frequency ripple), the periodic and complete transfer of excitations between the two species. Lower left panel: for $W/U = 0.9$ the frequency of oscillations increases (the color code is the same as in the upper panels). Right lower panel: Gray (dashed black) lines describes the time evolution of the inter-species angular-momentum difference for $W/U = 0.19$ $(W/U = 0.9)$.

phase differences $\phi_1(0) - \psi_1(0)$ can trigger different dynamical regimes. Namely, if the complex quantities a_1 and b_1 are *in phase* at $t = 0$, the two condensates seem to be decoupled and just feature quantum fluctuations (upper panels of Figure 2.6). Conversely, an initial non-zero phase difference allows for a periodic angular-momentum exchange between the two condensates (lower panels of Figure 2.6). Once more, we note that the same dynamics is observed by exchanging A and B at $t = 0$.

(4) Vortex excitation in condensate A, and equal anti-vortex in condensate B. Finally, let us consider the case where a weakly-populated vortex of species A $(n_1 \neq 0)$ is superimposed to an equal but counter-propagating anti-vortex of species

B ($m_{-1} \neq 0$). It turns out that the two kinds of excitations are periodically transferred from a species to the other (see upper panels of Figure 2.7). The left lower panel of Figure 2.7 confirms the relevance of parameter W: As discussed in the case (*2*), increasing W implies that the population oscillations and the angular-momentum transfer take place on a much smaller time scale. In particular, the right lower panel of Figure 2.7 illustrates the angular-momentum transfer through the quantity $\Delta L = n_{+1} - n_{-1} - (m_{+1} - m_{-1})$ where the signs ± in front of the mode population takes into account the clockwise (or anti-clockwise) rotations of bosons.

It is important to note that the equation governing the dynamics of the angular-momentum transfer ΔL in the cases (*2*)-(*4*)

$$i\hbar \frac{d\Delta L}{dt} = 2w(a_k^\dagger b_{-k}^\dagger + a_{-k} b_k + a_k^\dagger b_k + a_{-k} b_{-k}^\dagger - H.C.)$$

clearly shows how the microscopic processes involved by operators $S_\pm$ and $K_\pm$ both contribute to activate the angular-momentum transfer. This circumstance is due to the fact that, unlike the two-ring ladder model [177], where the transfer is controlled by the inter-ring tunneling, in the current model the transfer is triggered by the inter-species interaction.

2.6 Towards dynamical instability

In this section we resume the discussion on the diagonalization procedure of Section 2.4 and comment on the stability of the system. One can observe that the angles associated to generalized rotations, θ_a and θ_b, [see Equations (2.7)] are subject to some *constraints*. The same constrains can also be found in relation to the diagonal Hamiltonian (2.8), i.e., in the expressions of characteristic frequencies (2.10) and (2.11). Recalling that T, U and W have been assumed to be non-negative, all the dynamical results and the solution scheme that we have discussed up to now are valid provided that

$$w < T(1 - c_k) + u. \tag{2.21}$$

When w approaches this upper limiting value, the energy spectrum collapses, i.e., the energy difference between two adjacent energy levels tends to vanish (Figure 2.8 well illustrates the collapse). As a consequence, each $\hat{H}_k$ is associated to a specific limiting value for w, namely $T(1-c_k)+u$. Recalling that $1-c_k = 1-\cos(a\tilde{k})$ is an increasing function in the interval $k \in [0,(L-1)/2]$, the global limiting value is always found at the smallest momentum, i.e., for $k=1$, irrespective of site number L. In other words, increasing w, the sub-Hamiltonian which could first be affected by the spectral collapse is $\hat{H}_1$, no matter the number of ring-lattice sites L.

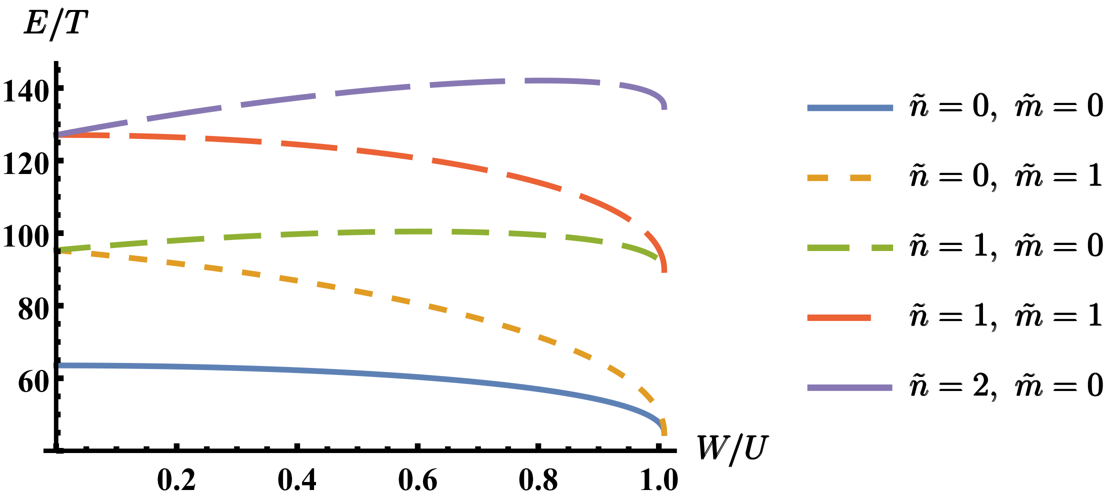

Figure 2.8: Energy levels vs interspecies interaction W for a trimer. If the two atomic species do not interact ($W=0$), the two characteristic frequencies ω_1 and Ω_1 coincide. When W/U approaches the limiting value 1.009, one can observe the collapse of the energy spectrum relevant to the second generalized harmonic oscillator. Parameters $T=2$, $U=1$, $N=1000$ have been chosen.

With reference to the most elementary closed circuit, the trimer, the stability condition becomes

$$w < \frac{3}{2}T + u, \tag{2.22}$$

or, in other words,

$$\frac{W}{U} < 1 + \frac{9}{2}\frac{T}{UN}, \tag{2.23}$$

an inequality which guarantees the correctness of formulas (2.18), (2.19) and (2.20). As far as excited populations, they reveal a *diverging* evolution when one approaches the border of the stability region. Figure 2.9 clearly depicts this situation. In view

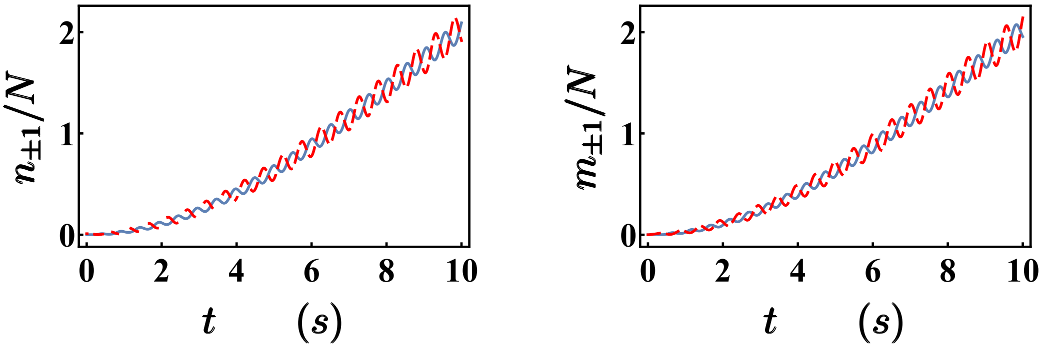

Figure 2.9: Time evolution of populations for $U = 0.01$, $T = 2$, $W/U = 1.895$, $\hbar = 1$, $N = 1000$, $n_1(0) = 10$ and $n_{-1}(0) = m_{\pm 1}(0) = 0$. Notice that W is close to the critical value W_c, i.e. $W/W_c = 0.997$. $n_1(t)$ and $m_1(t)$ are depicted in red, while $n_{-1}(t)$ and $m_{-1}(t)$ are represented in blue. All the excited boson populations quickly grow and soon get unphysical.

of this, the inequality (2.22) is particularly significant in that, in addition to setting the limits of validity for our model, it can be seen as the hallmark of a quantum phase transition [188], [183]. Finally, we note how the more general inequality (2.21) reproduces, for a generic ring lattice, the *spectral-collapse conditions* related to the demixing effect for a mixture in a 2-well potential [167].

2.7 Conclusions

In this Chapter, we have studied the weak excitations of a two-species bosonic mixture uniformly distributed in a L-site Bose-Hubbard ring. In Section 2.2, we proved that, after enacting the well-known Bogoliubov approximation scheme (justified by the fact that the two species are *miscible* and *uniformly* distributed in the ring lattice), the model Hamiltonian reduces to the sum of $(L-1)/2$ independent sub-Hamiltonians $\hat{H}_k$ involving *pairs* of (opposite) momentum modes. In particular, we showed that each $\hat{H}_k$ belongs to a specific dynamical algebra, the algebra so(2,3). Thanks to the knowledge of the dynamical algebra, in Section 2.4, we diagonalized the effective Hamiltonian, determined the energy spectrum, found the conserved quantities, computed the Heisenberg equations for various physical observables, and highlighted several microscopic processes characterizing the mixture.

In Section 2.5, we applied the proposed solution scheme to the simplest but non trivial ring, the Bose-Hubbard trimer, featuring $k = 0$ as macroscopically occupied momentum mode. The corresponding energy spectrum was determined and shown not only to provide the two frequencies that characterize the trimer dynamics, but also to well match the one computed via exact numerical diagonalization. We computed the time evolution of excited populations for different choices of model parameters and different values of initial conditions. More specifically, we pointed out the presence of fluctuations in the vacuum state, the possible coherent periodic transfer of angular momentum between the two species and its relation with their initial *phase difference*. Also, we emphasized the influence of the interspecies interaction W on the population dynamics by comparing the population oscillations in the case when W is smaller than the intraspecies coupling U and when $W \simeq U$. We showed that an increase of W makes the angular momentum transfer faster and more efficient.

As a conclusion, in Section 2.6, we identified the region where the mixed phase is stable, and observed that, for $W \to U + 9T/(2N)$, the system approaches instability, a possible signature of the mixing-demixing quantum phase transition [167]. The latter issue will be analyzed in Chapter 4 while the analysis of attractive interactions will be considered in Chapter 6.

Chapter 3

Entanglement entropy and mixing-demixing transitions

3.1 Introduction

In this Chapter[1], we study the behavior of the bipartite Von Neumann entanglement entropy (EE) as a function of the interspecies coupling in a system where two condensed species are confined in a two-well potential (dimer). Depending on the magnitude and on the sign of the interspecies coupling W, this system is known to feature three different quantum phases, which differ in the degree of mixing and spatial localization of the two quantum fluids: mixed, demixed and supermixed [165, 167]. In this regard, making the coupling W more *repulsive*, drives the mixture from the uniform and delocalized configuration (mixing) to a state exhibiting a macroscopic spatial separation of the two species (demixing). On the attractive side, instead, making W more *attractive*, the uniform ground state gives the way to a configuration where atoms of different components tend to occupy the same well (supermixing). The two-species dimer can be conveniently described in terms of a four-mode Bose-Hubbard Hamiltonian (a spatial mode per species per site) which, in addition to single-component interwell tunnelling processes and onsite intraspecies interactions, also incorporates a density-density interaction between atoms of different species.

---

[1] Note to the reader: part of the content of this Chapter has been published in [201].

In order to characterize the macroscopic changes in the ground-state structure upon a variation of W, we present different kinds of entanglement entropies, each one associated to a different way of partitioning the system. We indeed show that they all strictly depend on the specific quantum phase exhibited by the mixture, a circumstance which corroborates their role of critical indicators in detecting quantum phase transitions (in view of this, the entanglement entropy will be conveniently used as a critical indicator to characterize the quantum phase transitions described in Chapters 4 and 6).

Our analysis is based on the exact numerical diagonalization of extended sets of Bose-Hubbard Hamiltonians (which share the same structure but differ in the values of model parameters). The obtained ground states are then used to construct the associated density matrices which, in turn, offer the possibility to enact the chosen partition scheme. Eventually, the quantum correlation between the two identified partitions is quantified by computing the Von Neumann entropy of the reduced density matrix of the sub-system obtained after tracing out the degrees of freedom of the other one. Eventually, to provide a deeper physical insight into the relationship between entanglement and quantum phase transitions, we apply a fully-analytical variational approach based on su(2) coherent states, showing that it can provide a considerably good approximation of these entanglement entropies.

3.2 The model and the ground-state properties

As already discussed in Section 2.2 of Chapter 2, an effective description of ultracold bosons trapped in homogeneous arrays of potential wells is provided by the Bose-Hubbard model [114] in which local boson operators A_i and A_i^+ represent the microscopic annihilation and creation processes, respectively, at the ith well. In the simplest possible case of a two-site lattice (a double-well potential), the Bose-Hubbard Hamiltonian is given by

$$H_a = \frac{U_a}{2}\Big[A_L^\dagger A_L^\dagger A_L A_L + A_R^+ A_R^+ A_R A_R\Big] - J_a\Big(A_L^+ A_R + A_R^+ A_L\Big),$$

where L and R refers to the left and right well, respectively, U_a is the boson-boson interaction and J_a is the hopping amplitude controlling interwell boson exchange. Boson operators A_L, A_L^+, A_R, and A_R^+ satisfy the standard commutator $[A_\sigma, A_\sigma^+]$

= 1 with $\sigma = L, R$. If, in addition to species A, a second species B is introduced, the spatial modes become four, A_L, A_R, and B_L, B_R, for the species A and B, respectively. The resulting mixture is thus described by the two-species dimer Hamiltonian [165]

$$H = H_a + H_b + W\Big(N_L M_L + N_R M_R\Big) \tag{3.1}$$

in which, apart from the single-species Bose-Hubbard Hamiltonians H_a and H_b, a term proportional to the density-density interspecies interaction is present. This term couples the two species through the local boson populations described by the number operators $N_\sigma = A_\sigma^+ A_\sigma$ and $M_\sigma = B_\sigma^+ B_\sigma$ with $\sigma = L, R$.

When the interspecies interaction $|W|$ is low enough, the two quantum fluids are equally distributed in the two wells (mixing) [165, 167]. Conversely, when $|W|$ becomes sufficiently strong, the two species give place to macroscopic localization effects. In particular, a repulsive interaction $W > 0$ tends to spatially separate the species into different wells (demixing) while an attractive $W < 0$ interaction tends to gather both species in the same well (supermixing). These effects constitute delocalization-localization (DL) transitions [165, 167].

The deep change in the ground state properties across these DL transitions is confirmed by the numerical calculation of the ground state of Hamiltonian (3.1) for different values of W. To illustrate this, we decompose the energy eigenstates in the basis of space-mode Fock states:

$$|n_L, m_L, n_R, m_R\rangle := |i, j\rangle_L |N-i, M-j\rangle_R, \qquad i \in [0, N],\ j \in [0, M], \tag{3.2}$$

where labels n_σ and m_σ, describing the local boson populations, are the eigenvalues of number operators N_σ and M_σ, respectively. The parametrization $n_L = i$, $m_L = j$, $n_R = N - i$ and $m_R = M - j$ has been assumed to include the property that both operator $N = N_L + N_R$ and operator $M = M_L + M_R$ (representing the total boson numbers of the two species) commute with Hamiltonian H and thus are conserved quantities. The factorized form of (3.2) aims to better distinguish left-well from right-well populations. A generic quantum state of Hamiltonian (3.1) can be therefore written as

$$|\Psi\rangle = \sum_{i=0}^{N}\sum_{j=0}^{M} w_{i,j}\,|i,j\rangle_L|N-i,M-j\rangle_R \tag{3.3}$$

Determining the energy eigenstates thus amounts to calculating coefficients $w_{i,j}$ for which the eigenvalue equation $H|E\rangle = E|E\rangle$ is fulfilled. For values of $|W|$ small enough, the ground state $|E_0\rangle$ is approximated in terms of su(2) coherent states [202]

$$|E_0\rangle \simeq \frac{1}{2^{(N+M)/2}\sqrt{N!M!}}\left(A_L^+ + A_R^+\right)^N \left(B_L^+ + B_R^+\right)^M |0,0\rangle_L|0,0\rangle_R$$

whose dominating components $|i,j\rangle$ can be shown to feature $i \simeq N/2$, $j \simeq M/2$, namely, boson populations equally distributed in the two wells (delocalized ground state). For large values of $|W|$, $|E_0\rangle$ can be approximated by

$$|E_0\rangle \simeq \frac{1}{\sqrt{2}}\Big(|N,0\rangle_L|0,M\rangle_R + |0,M\rangle_L|N,0\rangle_R\Big) \tag{3.4}$$

$$|E_0\rangle \simeq \frac{1}{\sqrt{2}}\Big(|N,M\rangle_L|0,0\rangle_R + |0,0\rangle_L|N,M\rangle_R\Big), \tag{3.5}$$

in the repulsive and attractive regime, respectively. The latter states constitute Schrödinger cats whose constituting components exhibit strong localization.

Figure 3.1, obtained by numerically calculating the ground state of Hamiltonian (3.1) for different values of W, allows one to appreciate the occurrence of a DL transition by illustrating the macroscopic changes occurring in the ground-state structure.

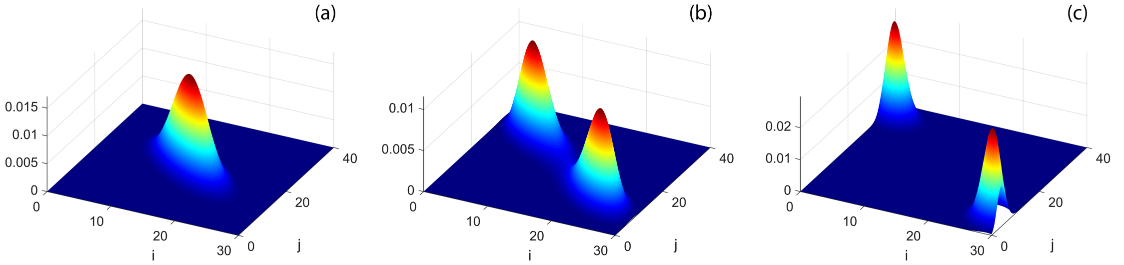

Figure 3.1: Ground-state probabilities $|w_{i,j}|^2$ vs i (left occupation number of species A) and j (left occupation number of species B) associated to space-mode Fock states $|i,j\rangle_L|N-i,M-j\rangle_R$ of equation (3.3) for boson numbers $N=30$, $M=40$, $J=1$ and $U=0.1$. Panel (**a**) (obtained for $W/J=0.15$), features delocalized populations; Panel (**b**), obtained for $W/J=0.168$, shows the germ of localization; Panel (**c**), obtained for $W/J=0.2$, corresponds to full localization and demixing. A similar behavior characterize the DL transition in the attractive regime ($W<0$), but the two emerging peaks finally localize around $i=j=0$ an $i=30$, $j=40$.

The critical behavior of the DL transition has been studied analytically by resorting to the semiclassical approach where boson number operators are approximated in terms of continuous variables [167]. This method (see Chapter 4 for a detailed description) has provided the critical value of W at which the transition takes place in the case of twin species ($J_a=J_b=J$, $U_a=U_b=U$). In this approach, the Fock states essentially become wave functions depending on the new continuous variables while, for energies low enough, the energy-eigenvalue equation takes the form of the Schrödinger problem for a multidimensional harmonic-oscillator Hamiltonian. The extremal points of the associated effective potential allow one to determine the ground-state configurations, and, in particular, to find the formula

$$\frac{W}{U}=1+\frac{2J}{UN} \tag{3.6}$$

defining, for large boson numbers ($N=M\gg 1$), the transition critical point in the parameter space. Interestingly, when W approaches this critical value, the energy spectrum of Hamiltonian (3.1) has been shown to undergo a collapse in which the inter-level separation tends to zero [167]. This spectral collapse can be seen as the hallmark of the transition corresponding to the macroscopic change in the structure of the ground state and of the relevant low-energy excitations [167]. Notice that the generalized version of formula (3.6) for a mixture loaded in a L-well ring lattice has been derived Chapter 2 [see formula (2.21)] within the Bogoliubov approximation scheme.

3.2.1 Quasi-degeneracy of the ground-state

As already mentioned, if ratio $|W|/J$ is big enough, the system ground state approaches cat-like states of the type (3.4) or (3.5) depending on the sign of the iterspecies interaction W. In parallel, the system spectrum may appear quasi-degenerate, due to the quasi-collapse of the energy levels [165, 167].

However, the degeneracy of the ground-state is only apparent, as Hamiltonian (3.1) is always non-degenerate [203, 204] (provided that ratios J_a/N and J_b/M are non-zero). As shown in Figure 3.2, in fact, the energy gap between the ground-state energy E_0 and the first excited level, E_1, rapidly diminishes if one increases the number of particles per species (N and M) but remains finite. This has been verified in Figure 3.2 down to computational limit fixed by the machine precision.

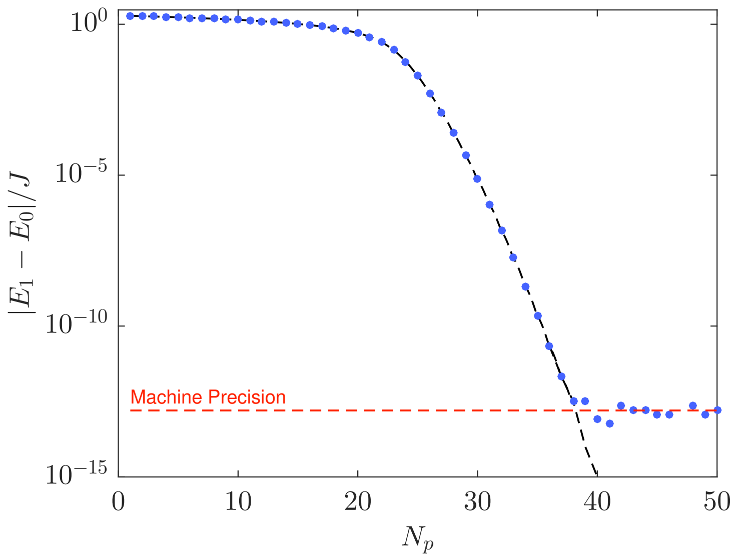

Figure 3.2: Energy gap between the ground state energy E_0 and the first excited level E_1, as function of the number of particles per species ($N = M = N_p$), $J = 1$, $U = 0.1$, $W = 0.2$.

3.3 Bipartite Von Neumann entanglement entropy as a critical indicator

3.3.1 A standard way to quantify the entanglement

A standard indicator to quantify entanglement in a many-body quantum pure state is the Von Neumann entropy of either the reduced density matrices of the subsystems. Given $\hat{\rho}$, the density matrix corresponding to a pure state of the quantum system, and having defined two partitions A and B of the relevant Hilbert space $\mathcal{H}$ such that $\mathcal{H} = \mathcal{H}_A \bigotimes \mathcal{H}_B$, the bipartite Von Neumann entanglement entropy (EE) is defined as [205]

$$EE_{A-B} = S(\hat{\rho}_A) = -\mathrm{Tr}_A(\ \hat{\rho}_A\ \log_2\ \hat{\rho}_A), \tag{3.7}$$

where $\hat{\rho}_A = \mathrm{Tr}_B(\ \hat{\rho})$ ($\hat{\rho}_B = \mathrm{Tr}_A(\ \hat{\rho})$) is the reduced density matrix of partition A (B) obtained tracing out the degrees of freedom of B (A). Notice that, in principle, there exists infinitely many possible ways to partition the same Hilbert space $\mathcal{H}$ into two parts.

Although the partition of the Hilbert space is obviously independent from the choice of the basis in which the density operator is represented (i.e. $S(\rho) = S(U\rho U^\dagger)$ for any unitary transformation U which enacts the change of basis), to perform calculation (3.7), it is convenient to represent the density operator associated to the system ground state

$$\hat{\rho}_0 = |E_0\rangle\langle E_0| \tag{3.8}$$

in a basis which is suitable to enact the chosen partition A-B. In other words, a suitable choice of the basis can give easy access to a partition that, in another basis, would be hard to computationally handle. An example of this is shown in Section 3.3.3, where we consider the partition between momentum modes.

In practice, one can start with expanding the ground-state

$$|E_0\rangle = \sum_i \sum_j w_{i,j}\ |\phi_i\rangle_A |\phi_j\rangle_B\ , \tag{3.9}$$

with respect to a basis $\{|\phi_i\rangle\}$ which is convenient for the enacting of the partition.

The corresponding density operator (3.8) therefore reads

$$\hat{\rho}_0 = \sum_i \sum_j \sum_{i'} \sum_{j'} C_{i,j,i',j'} |\phi_i\rangle_A |\phi_j\rangle_B \, {}_B\langle\phi_{j'}| {}_A\langle\phi_{i'}| \ , \tag{3.10}$$

where

$$C_{i,j,i',j'} = w_{i,j} w^*_{i'j'} \ . \tag{3.11}$$

One can then trace away the degrees of freedom of a subsystem and plug the resulting reduced density matrix into formula (3.7) to obtain the entanglement in quantum state $|E_0\rangle$ with respect to the partition A-B.

In the sequel, we will consider three different kinds of EEs, each one associated to a different way of partitioning the system. First, we consider the quite natural partition in terms of left-well bosons and right-well bosons, suggested by the representation of physical states in the space-mode Fock basis (3.2). Then, by representing physical states in the momentum-mode Fock basis, we partition the system in terms of zero-momentum and non-zero-momentum bosons. Finally, we consider the partition of the system distinguishing species-A from species-B bosons, which is again suggested by definition (3.2) where populations n_L, n_R and m_L, m_R refer to species A and B, respectively.

3.3.2 Entanglement entropy for a partition characterized by spatial modes

Let us start by computing the EE by considering the partition of the system ground state in terms of left-well bosons and right-well bosons. Given the system ground state

$$|E_0\rangle = \sum_{i=0}^{N} \sum_{j=0}^{M} \ w_{i,j} \ |i,j\rangle_L \ |N-i, \, M-j\rangle_R \tag{3.12}$$

and the corresponding density operator

$$\hat{\rho}_0 = |E_0\rangle\langle E_0| =$$

$$= \sum_{i=0}^{N} \sum_{j=0}^{M} \sum_{i'=0}^{N} \sum_{j'=0}^{M} \ w_{i,j} w^*_{i',j'} \ |i,j\rangle_L \ |N-i, \, M-j\rangle_R \, {}_R\langle N-i', \, M-j'| \ \ {}_L\langle i',j'| \tag{3.13}$$

where

$$w_{i,j} = \langle i, j, N-i, M-j|E_0\rangle,$$

the reduced density matrix relevant to the right-well bosons, is obtained tracing out the degrees of freedom of the left-well bosons:

$$\hat{\rho}_R = \sum_{k=0}^{N}\sum_{l=0}^{M} {}_L\langle k,l|\hat{\rho}_0|k,l\rangle_L = \sum_{i=0}^{N}\sum_{j=0}^{M} \;|w_{i,j}|^2\;\; |N-i,\, M-j\rangle_R\; {}_R\langle N-i,\, M-j|.$$

The latter is diagonal, and one can therefore easily compute the EE [see formula (3.7)] as

$$EE_{L-R} = S(\hat{\rho}_R) = -\sum_{i=0}^{N}\sum_{j=0}^{M} \;|w_{i,j}|^2 \log_2 |w_{i,j}|^2. \tag{3.14}$$

The solid line in Figure 3.3 illustrates the functional dependence of indicator (3.14) on ratio W/J which, in turn, determines the degree of localization and mixing of the two quantum fluids. This plot exhibits two sharp peaks where the DL transitions occur. The emergence of the two peaks in the proximity of the W/J critical values is, in fact, caused by the bigger and bigger number of Fock states which have a non-zero weight $w_{i,j}$ in decomposition (3.12). In this regard, looking at Figure 3.1b, one can appreciate the fact that the two Gaussian-like distributions involve the maximum number of Fock states when they are about to merge and the transition takes place. In the region between the two peaks, bosons are delocalized and the quantum fluids fully mixed; the left tail corresponds to supermixed states (states where both species are localized in a single well); eventually, the right tail is the region where the two species localize in different wells (demixing). Both tails feature a genuinely quantum character because the relevant ground states correspond to Schrödinger cats, in which the species localization gets more and more pronounced as $|W|/J$ increases [see Formulas (3.4) and (3.5)]. In fact, the entanglement entropy asymptotically tends to 1, a value which is reminiscent of the double-faced structure of cat states (3.4) and (3.5) because both their components contribute to Formula (3.14) with $\frac{1}{2}\log_2 2$. It is worth noticing that EE_{L-R} is always different from zero in that, even for noninteracting species ($W=0$), the presence of a non-zero J couples the left and right modes of either species. As expected, one can show numerically that the height of the central minimum of EE_{L-R} decreases more and more (tending to zero) as the interwell hopping J becomes smaller and smaller.

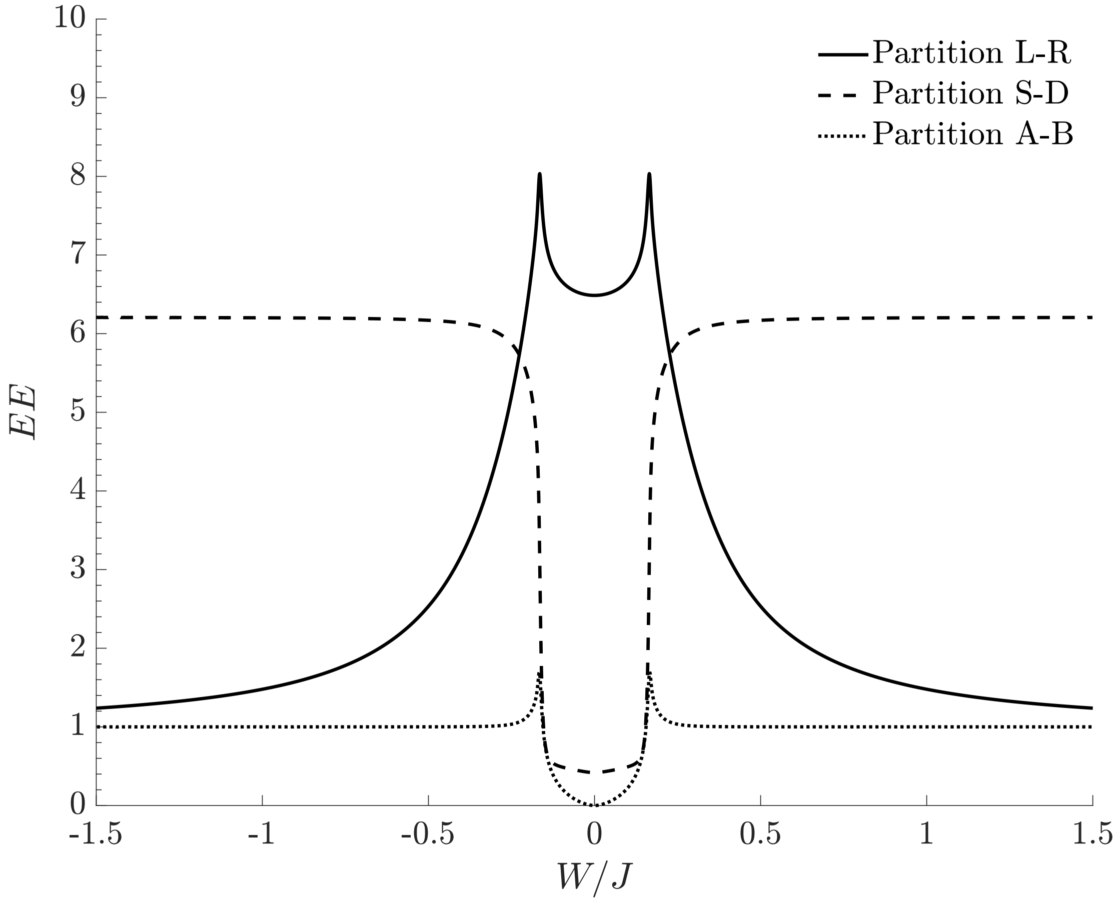

Figure 3.3: EEs as a function of W/J for three different partitions of the Hilbert space: partition L-R [continuous line, see formula (3.14)], partition S-D [dashed line, see formula (3.15)], and partition A-B [dotted line, see formula (3.16)]. $N = 30$, $M = 40$, $J = 1$, $U = 0.1$.

3.3.3 Entanglement entropy for a partition characterized by momentum modes

Let us introduce the following momentum-mode operators obtained summing and subtracting usual site-mode operators

$$S_a = \frac{1}{\sqrt{2}}(A_L + A_R), \qquad D_a = \frac{1}{\sqrt{2}}(A_L - A_R),$$

$$S_b = \frac{1}{\sqrt{2}}(B_L + B_R), \qquad D_b = \frac{1}{\sqrt{2}}(B_L - B_R),$$

together with the corresponding number operators

$$N_S = S_a^\dagger S_a, \qquad N_D = D_a^\dagger D_a, \qquad M_S = S_b^\dagger S_b, \qquad M_D = D_b^\dagger D_b,$$

which count the number of bosons having vanishing (S) or non-vanishing (D) momentum in the two species. The momentum-mode Fock basis $\{|N_S,\, N-N_S,\, M_S,\, M-M_S\rangle\}$ can be chosen as a new basis against which it is possible to expand the system ground state

$$|E_0\rangle = \sum_{n_S=0}^{N}\sum_{m_S=0}^{M} w_{n_S,m_S}\, |n_S, m_S\rangle_S |N-n_S, M-m_S\rangle_D,$$

where we have set $|n_S, N-n_S, m_S, M-m_S\rangle = |n_S, m_S\rangle_S |N-n_S, M-m_S\rangle_D$ in order to emphasize the difference between zero and non-zero momentum quantum numbers. As a consequence, the density matrix relevant to the ground state reads

$$\hat{\rho}_0 = |E_0\rangle\langle E_0| = \sum_{n_S=0}^{N}\sum_{m_S=0}^{M}\sum_{n'_S=0}^{N}\sum_{m'_S=0}^{M} w_{n_S,m_S} w^*_{n'_S,m'_S} \cdot$$

$$\cdot |n_S, m_S\rangle_S |N-n_S, M-m_S\rangle_D \;{}_D\langle N-n'_S, M-m'_S|\;{}_S\langle n'_S, m'_S|.$$

The reduced density matrix relevant to the sub-system of bosons having non-vanishing momentum (modes D's) is obtained by tracing out the degrees of freedom relevant to the sub-system of bosons having zero momentum (modes S's)

$$\hat{\rho}_D = \sum_{n_S=0}^{N}\sum_{m_S=0}^{M} {}_S\langle n_S, m_S|\hat{\rho}_0|n_S, m_S\rangle_S =$$

$$= \sum_{n_S=0}^{N}\sum_{m_S=0}^{M} |w_{n_S,m_S}|^2\, |N-n_S, M-m_S\rangle_D \;{}_D\langle N-n_S, M-m_S|.$$

Since the obtained reduced density matrix $\hat{\rho}_D$ is diagonal, the associated Von Neumann entropy simply reads

$$EE_{S-D} = S(\hat{\rho}_D) = -\sum_{n_S=0}^{N}\sum_{m_S=0}^{M} |w_{n_S,m_S}|^2\, \log_2 |w_{n_S,m_S}|^2. \tag{3.15}$$

The dashed line in Figure 3.3 shows the EE associated to the partition between still and circulating bosons as a function of the ratio W/J. This plot (black dashed line) exhibits two sharp discontinuities at the two values of W/J for which the DL phase transitions occur. Such discontinuities separate three quasi-plateaus corresponding to supermixed, mixed and demixed phases.

The central region (mixed species) features a quite small entanglement between circulating and still bosons. In fact, if the interspecies coupling W is small compared to the tunneling J and if the ratio U/J is small enough to guarantee superfluid and delocalized bosons, momentum modes S_a and S_b are macroscopically occupied, while D_a and D_b are poorly populated. If the intraspecies repulsion U tends to zero, one can show that the latter momentum modes are not populated at all and that the EE vanishes for $W/J = 0$.

3.3.4 Entanglement entropy for a partition characterized by boson species

A third way to compute the EE consists in partitioning the system in terms of species-A and species-B bosons. We use the representation in terms of space-mode Fock states, although the momentum-mode Fock basis is equally convenient to the job. Starting from density matrix (3.13), the reduced density matrix relevant to species-B sub-system is obtained by tracing out the degrees of freedom relevant to species-A sub-system

$$\hat{\rho}_B = \sum_{k=0}^{N} {}_L\langle k| \; {}_R\langle N-k|\hat{\rho}_0|k\rangle_L |N{-}k\rangle_R = \sum_{j=0}^{M}\sum_{j'=0}^{M} C_{j,j'} \;\; |j\rangle_L |M{-}j\rangle_R \;\; {}_L\langle j'| \;\; {}_R\langle M-j'|,$$

where we have defined

$$C_{j,j'} = \sum_{k=0}^{N} w_{k,j} w^*_{k,j'}.$$

The diagonalization of $\hat{\rho}_B$ provides the eigenvalues $\{\lambda_j\}$ necessary to compute the relevant Von Neumann entropy

$$EE_{A-B} = S(\hat{\rho}_B) = -\sum_{j=1}^{M+1} \lambda_j \, \log_2 \lambda_j. \tag{3.16}$$

The dotted line in Figure 3.3 represents the bipartite Von Neumann entanglement entropy relevant to species-mode partition scheme as a function of W/J.

As in the case of the L-R partition, two sharp peaks, at which the DL transitions occur, separate the three regions corresponding to the supermixed, mixed and demixed phase. Also in the present case, the outer regions consist of two quasi-plateaus whose height quickly converges to 1, a limiting value which is, once again, reminiscent of the two-faced character of cat states (3.4) and (3.5) (recall that $1 = 2 \times \left(-\frac{1}{2}\log_2 \frac{1}{2}\right)$). As noted in the previous Subsections, where we showed that the EE relevant to partition L-R and to partition S-D features a central minimum tending to zero for $J \to 0$ and $U \to 0$, respectively, in the current case, where the species-mode separation is adopted, the vanishing of the minimum of indicator (3.16) is obtained when the two species are non interacting, namely, for $W = 0$.

3.4 Calculation of the entanglement entropy in the coherent-state picture

The coherent-state variational approach has found large application in the study of many-body quantum systems [180] since, due to their semi-classical character, they provide an effective description of physical systems and allow one to gain insights into their properties. Also, from the experimental point of view, coherent states have an important role since their semi-classical character enables one to achieve a realistic approximation of the quantum state describing the real system.

An su(2) coherent state describing single condensate trapped in a dimer is given by [202]

$$|\xi_L, \xi_R\rangle = \frac{1}{\sqrt{N!}} \left(\xi_L A_L^\dagger + \xi_R A_R^\dagger\right)^N |0\rangle, \tag{3.17}$$

where $|0\rangle = |0, 0\rangle$ is the boson vacuum state and the normalization condition $|\xi_L|^2 + |\xi_R|^2 = 1$ must be assumed. Since $\langle\psi_a|A_\sigma^\dagger A_\sigma|\psi_a\rangle = N|\xi_\sigma|^2$, with $\sigma = R, L$, is the expectation value of number operator $N_\sigma = A_\sigma^\dagger A_\sigma$ then $|\xi_\sigma|^2$ represents the fraction of bosons in the well σ. In the following, we employ combinations of coherent states (3.17) (for a single species in a double well) to approximate the cat structure of the ground state relevant to the two-species dimer in the strong-interaction regime, both for $W/J > 0$ and for $W/J < 0$.

1. Supermixing (attractive cat). If the interspecies attraction ($W/J < 0$) is large enough, the two species aggregate together in the same well. Since none of the two wells is privileged with respect to the other, quantum mechanically both configurations are equally probable, and the system lives in both states at the same time. By using the notation of Formula (3.17), the resulting cat state can be written as

$$|\Psi\rangle = \frac{1}{\sqrt{2}}\Big[|\mathrm{Loc}\rangle_{a,L}|\mathrm{Loc}\rangle_{b,L} + |\mathrm{Loc}\rangle_{a,R}|\mathrm{Loc}\rangle_{b,R}\Big] =$$
$$= \frac{1}{\sqrt{2}}\Big[|\lambda_a,\eta_a\rangle|\lambda_b,\eta_b\rangle + |\eta_a,\lambda_a\rangle|\eta_b,\lambda_b\rangle\Big],$$

where "Loc" stands for "localized" and entails the fact that $|\eta_c|^2 \ll |\lambda_c|^2$. Following the scheme discussed in Reference [193], one can show that the expectation value of the model Hamiltonian reduces to

$$E(\lambda_a,\eta_a,\lambda_b,\eta_b) = \frac{U}{2}N(N-1)\left(|\lambda_a|^4 + |\eta_a|^4\right) - 2JN(\mathrm{Re}\{\lambda_a\eta_a\})$$
$$+\frac{U}{2}M(M-1)\left(|\lambda_b|^4 + |\eta_b|^4\right) - 2JM(\mathrm{Re}\{\lambda_b\eta_b\}) + W\left(|\lambda_a|^2|\lambda_b|^2 + |\eta_a|^2|\eta_b|^2\right)$$

where the local order parameters λ_a, λ_b, η_a, and η_b are complex quantities defined as

$$\lambda_a = \sqrt{1-x_a}e^{i\theta_a}, \qquad \eta_a = \sqrt{x_a}e^{i\phi_a}, \qquad \lambda_b = \sqrt{1-x_b}e^{i\theta_b}, \qquad \eta_b = \sqrt{x_b}e^{i\phi_b}.$$

After these substitutions, the variational energy reads:

$$E(x_a,\theta_a,\phi_a,x_b,\theta_b,\phi_b) =$$
$$= \frac{U}{2}N(N-1)\left(2x_a^2 + 1 - 2x_a\right) - 2JN\sqrt{x_a(1-x_a)}\cos(\phi_a-\theta_a) +$$
$$+\frac{U}{2}M(M-1)\left(2x_b^2 + 1 - 2x_b\right) - 2JM\sqrt{x_b(1-x_b)}\cos(\phi_b-\theta_b) +$$
$$+WNM\left[2x_ax_b + 1 - x_a - x_b\right]$$

In order to minimize E, we look for stationary points, namely we solve

$$\frac{\partial E}{\partial x_a} = 0, \qquad \frac{\partial E}{\partial x_b} = 0, \qquad \frac{\partial E}{\partial(\phi_a - \theta_a)} = 0, \qquad \frac{\partial E}{\partial(\phi_b - \theta_b)} = 0.$$

From the last two equations one deduces that the minimum-energy configuration is obtained for $\phi_a = \theta_a$ and $\phi_b = \theta_b$. Substituting this information in the first two equations, one gets:

$$\sqrt{x_a}\left(-UN^2 + 2NMWx_b - NMW + NU\right) + x_a^{3/2}\left(2N^2U - 2NU\right) + \\ + \frac{3NJx_a}{2} - NJ = 0$$

$$\sqrt{x_b}\left(-UM^2 + 2NMWx_a - NMW + MU\right) + x_b^{3/2}\left(2M^2U - 2MU\right) + \\ + \frac{3MJx_b}{2} - MJ = 0$$

Since x_a and x_b are $\ll 1$, we perform a Taylor expansion and we neglect all the terms whose order is bigger than 1/2. Eventually, we get:

$$\sqrt{x_a}\left(-UN^2 - NMW + NU\right) - NJ = 0$$

$$\sqrt{x_b}\left(-UM^2 - NMW + MU\right) - MJ = 0$$

The minimum-energy configuration is therefore reached for $\phi_a = \theta_a$, $\theta_b = \phi_b$ and

$$x_a = \frac{J^2}{(NU - U + MW)^2}, \qquad x_b = \frac{J^2}{(MU - U + NW)^2}.$$

These formulas give the fraction of bosons characterizing the minority component and, correctly, give zero in the limit $W \to -\infty$.

2. Demixing (repulsive cat). If the interspecies repulsion ($W/J > 0$) is large enough, the two condensed species separate in different wells. Similarly to what explained in the previous paragraph, the ground state features a two-sided cat-like structure, because left (right) well can indistinctly host species A (B). Hence, the quantum state consists of an equally-weighted superposition of the two possible arrangements

$$|\Psi\rangle = \frac{1}{\sqrt{2}}\Big[|\mathrm{Loc}\rangle_{a,L}|\mathrm{Loc}\rangle_{b,R} + |\mathrm{Loc}\rangle_{a,R}|\mathrm{Loc}\rangle_{b,L}\Big] =$$
$$= \frac{1}{\sqrt{2}}\Big[|\lambda_a,\eta_a\rangle|\eta_b,\lambda_b\rangle + |\eta_a,\lambda_a\rangle|\lambda_b,\eta_b\rangle\Big],$$

where λ_c, η_c are such that $|\eta_c|^2 \ll |\lambda_c|^2$ and (obviously) $|\lambda_c|^2 + |\eta_c|^2 = 1$, with $c = a,b$. Following the variational approach described in the previous paragraph, and adopting the same conventions, we obtain that the variational energy

$$E(x_a,\theta_a,\phi_a,x_b,\theta_b,\phi_b) =$$
$$= \frac{U}{2}N(N-1)\left(2x_a^2+1-2x_a\right) - 2JN\sqrt{x_a(1-x_a)}\cos(\phi_a-\theta_a)+$$
$$+\frac{U}{2}M(M-1)\left(2x_b^2+1-2x_b\right) - 2JM\sqrt{x_b(1-x_b)}\cos(\phi_b-\theta_b)+$$
$$+WNM\left[x_a+x_b-2x_ax_b\right]$$

is minimized for $\theta_a = \phi_a$, $\theta_b = \phi_b$ and

$$x_a = \frac{J^2}{(NU-U-MW)^2}, \qquad x_b = \frac{J^2}{(MU-U-NW)^2}$$

Parameters x_a and x_b represent the fractions of bosons which do not aggregate with the others and thus make the "demixed phase" not ideal. Notice that, correctly, if $W \to +\infty$, then $x_{a,b} \to 0$, i.e. the demixing gets more and more complete.

Both for the supermixing and for the demixing scenario, after computing the fraction of bosons in each well, it is possible to reconstruct the cat state by superimposing two coherent states. This procedure, described in the next subsection, allows one to analytically compute the EE between left-well and right-well bosons [193].

3.4.1 Entanglement entropy and coherent states

On the basis of the coherent-state approach derived in Section 3.4 and in the same spirit of Reference [193], we compute the entanglement entropy between left-well bosons and right-well bosons. To begin, let us define $\rho_{n,m}(i)$ as the probability of having n bosons of species A and m bosons of species B at site i. The normalization of probability requires that

$$\sum_{n=0}^{N}\sum_{m=0}^{M}\rho_{n,m}(i)=1$$

where N is the total number of bosons of species A and M is the total number of bosons of species B. Let us define the single site entropy S_i as follows:

$$S_i=-\sum_{n=0}^{N}\sum_{m=0}^{M}\rho_{n,m}(i)\,\log_2\rho_{n,m}(i)$$

Neglecting the possible presence of cat states (a situation that will be re-inserted a posteriori), a generic coherent state can be written in the factorized form

$$|\Psi\rangle=\left[\frac{1}{\sqrt{N!}}\left(\xi_L A_L^\dagger+\xi_R A_R^\dagger\right)^N|0\rangle\right]\left[\frac{1}{\sqrt{M!}}\left(\nu_L B_L^\dagger+\nu_R B_R^\dagger\right)^M|0\rangle\right]$$

Of course the normalization conditions $|\xi_L|^2+|\xi_R|^2=1,\quad|\nu_L|^2+|\nu_R|^2=1$ must hold. State $|\Psi\rangle$ can be recast into the form

$$\begin{aligned}|\Psi\rangle&=\left[\sum_{n=0}^{N}\frac{\sqrt{N!}}{n!\,(N-n)!}\xi_L^n\left(A_L^\dagger\right)^n\xi_R^{N-n}\left(A_R^\dagger\right)^{N-n}|0\rangle\right]\cdot\\&\cdot\left[\sum_{m=0}^{M}\frac{\sqrt{M!}}{m!\,(M-m)!}\nu_L^m\left(B_L^\dagger\right)^m\nu_R^{M-m}\left(B_R^\dagger\right)^{M-m}|0\rangle\right]=\\&=\left[\sum_{n=0}^{N}\frac{\sqrt{N!}}{\sqrt{n!}\sqrt{(N-n)!}}\xi_L^n\xi_R^{N-n}|n,N-n\rangle_a\right]\cdot\\&\cdot\left[\sum_{m=0}^{M}\frac{\sqrt{M!}}{\sqrt{m!}\sqrt{(M-m)!}}\nu_L^m\nu_R^{M-m}|m,M-m\rangle_b\right]\end{aligned}$$

We calculate the reduced density matrix ρ partitioning the system into two subsystems (left-well bosons and right-well bosons) and tracing out the degrees of freedom relevant to one of them. For example

$$\rho=\sum_{n=0}^{N}\sum_{m=0}^{M}{}_R\langle n,m|\Psi\rangle\langle\Psi|n,m\rangle_R$$

Taking into account the orthogonality of the states, the reduced density matrix which originates from a coherent state can be written as

$$\rho_{n,m} = \frac{N!M!}{n!m!(N-n)!(M-m)!}\xi_L^n \xi_R^{(N-n)} \nu_L^m \nu_R^{(M-m)} (\xi_L^*)^n (\xi_R^*)^{(N-n)} (\nu_L^*)^m (\nu_R^*)^{(M-m)} =$$

$$= \left[\binom{N}{n} |\xi_L|^{2n} (1-|\xi_L|^2)^{(N-n)}\right] \left[\binom{M}{m} |\nu_L|^{2m} (1-|\nu_L|^2)^{(M-m)}\right]$$

where the expressions of coefficients $\xi_L = \xi_L(J,U,W)$, $\xi_R = \xi_R(J,U,W)$, $\nu_L = \nu_L(T,U,W)$ and $\nu_R = \nu_R(T,U,W)$ can be computed within the variational approach. In passing, notice that the probability distribution is correctly normalized, i.e. $\sum_{n=0}^{N}\sum_{m=0}^{M} \rho_{n,m} = 1$. The Von Neumann entropy of the reduced sub-system can be thus computed as

$$S = -\sum_{n=0}^{N}\sum_{m=0}^{M} \rho_{n,m} \log_2 \rho_{n,m}$$

This quite general procedure needs to be slightly modified in case one is considering cat states. In fact, the reduced density matrix must take into account the two-sided nature of a cat state and so it must be written as the average of the densities matrices relevant to simple coherent states, namely

$$\rho_{\text{side L}_{n,m}} = \left[\binom{N}{n} |\xi_L|^{2n} (1-|\xi_L|^2)^{(N-n)}\right] \left[\binom{M}{m} |\nu_L|^{2m} (1-|\nu_L|^2)^{(M-m)}\right]$$

$$\rho_{\text{side R}_{n,m}} = \left[\binom{N}{n} |\xi_L|^{2(N-n)} (1-|\xi_L|^2)^{n}\right] \left[\binom{M}{m} |\nu_L|^{2(M-m)} (1-|\nu_L|^2)^{m}\right]$$

implying

$$\rho_{\text{cat}_{n,m}} = \frac{1}{2}\left[\rho_{\text{side L}_{n,m}} + \rho_{\text{side R}_{n,m}}\right]$$

As shown in Figure 3.4, the result perfectly matches the numerical EE, of course in the validity range of this approximation, i.e. in the whole range of $|W|/J$ except the central region (mixed phase) between the two critical values.

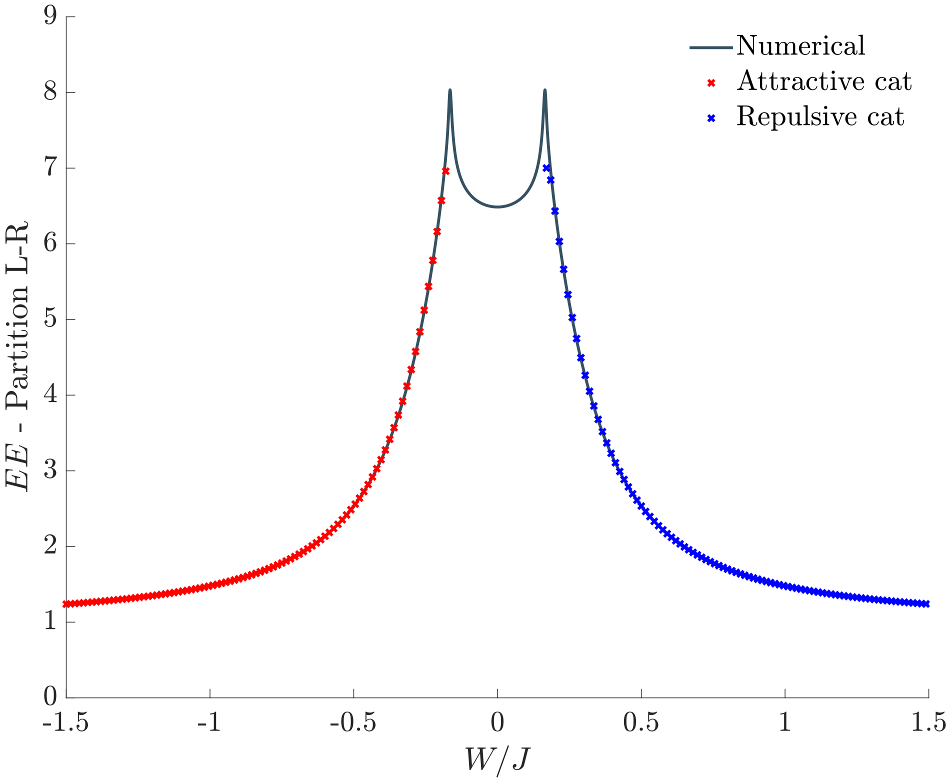

Figure 3.4: Entanglement entropy between left-well bosons and right-well bosons: comparison between the results derived within the coherent-state approach and the numerical ones.

3.5 Conclusions

In this Chapter, we have investigated the effectiveness of the bipartite Von Neumann entanglement entropy (EE) in detecting the occurrence of mixing-demixing (or localization-delocalization) transitions in a two-species Bose-Hubbard dimer.

In Section 3.2 we have introduced the model and highlighted the importance of W (the interspecies repulsion) in determining the quantum phase of the system (supermixed for $W/J \ll 0$, mixed for small $|W|/J$ and demixed for $W/J \gg 0$, where J represents the hopping amplitude).

Section 3.3 has been devoted to the analysis of the EE for three different partition schemes. We have evidenced the fact that different ways of partitioning the system into two sub-systems, correspond to different kinds of entanglement entropies. In all three cases, EE features discontinuities where the localization-delocalization phase transitions occur and quasi-plateaus where two dominating macroscopic configurations emerge. Interestingly, we have evidenced that *i)* a non-zero hopping J causes a non-zero entanglement between spatial modes, *ii)* the intraspecies interaction U contributes to the entanglement between momentum modes, and *iii)* the interspecies interaction W is responsible for the entanglement between species modes.

In Section 3.4, we have introduced su(2) coherent states and developed a fully-analytic variational approach apt to describe the supermixed and the demixed phases which, in turn, feature cat-like ground states. The superposition of two such coherent states has provided a good approximation of the ground state of the system in a non-small range of W/J, as demonstrated by the comparison with the numerical results.

Chapter 4

The mixing demixing phase diagram of bosonic mixtures in a ring trimer

4.1 Introduction

In this Chapter[1], we derive the complete mixing-demixing quantum phase diagram relevant to a (possibly asymmetric) bosonic binary mixture confined in a ring trimer and modeled within the Bose-Hubbard picture. We show how the fragmented character of the confining potential, together with the competition between intra- and interspecies interactions, give place to a number of different quantum phases, which differ in the degree of mixing of the two quantum fluids. The latter is quantified by means of a specific indicator imported from Statistical Thermodynamics and originally devised in order to evaluate and monitor the miscibility of different chemical compounds. In spite of the large number of parameters appearing in the original quantum model, the resulting quantum phase diagram is shown to be spanned by just *two* effective parameters: the ratio between the interspecies and the (geometric average of the) intraspecies repulsions, and another effective variable incorporating the asymmetry between the heteronuclear species. In view of

---

[1] Note to the reader: part of the content of this Chapter has been published in [176, 206, 207].

the collaboration with the experimental quantum-gas group from Hannover University, and to closely match the conditions available within their setup, our study is extended also beyond the pointlike approximation of potential wells. This is done by describing the system in terms of two coupled Gross-Pitaevskii equations and making use of the specific model parameters of the mixture ^{23}Na - ^{39}K, the two elements that can be Bose-condensed by the Hannover group. The resulting mean-field analysis confirms the rich scenario of mixing-demixing transitions exhibited by the mixture and also constitutes an effective springboard towards a viable experimental realization. Eventually, in the twin-species case, we present a number of genuinely quantum indicators capable of detecting the occurrence of critical phenomena, including but not limited to the energy spectrum (whose collapse at two critical points heralds the onset of as many quantum phase transitions), the ground-state energy (which features non-analiticities when sweeping a control parameter), the bipartite Von Neumann Entanglement Entropy (whose reliability as critical indicator has been discussed in Chapter 3 for the double-well system), and the ground state tomography. It is important to notice that the mixed phase gives the way to the demixed one when the interspecies-to-intraspecies ratio exceeds the same critical value which was determined in Chapter 2 in relation to the stability of Bogoliubov excitation spectrum. Eventually, we anticipate that the analysis of the quantum phase diagram relevant to mixtures featuring *attractive* interspecies interactions will be carried on in Chapter 6.

4.2 The model

The model describing a repulsive binary mixture in a triple well is effectively represented by two Bose-Hubbard Hamiltonians, each one associated to a single component and depending on three spatial boson modes, and by the density-density interspecies coupling of the two components. This has the form

$$\hat{H} = -T_a \sum_{j=1}^{3} \left(A_{j+1}^\dagger A_j + A_j^\dagger A_{j+1} \right) + \frac{U_a}{2} \sum_{j=1}^{3} N_j (N_j - 1) -$$

$$-T_b \sum_{j=1}^{3} \left(B_{j+1}^\dagger B_j + B_j^\dagger B_{j+1} \right) + \frac{U_b}{2} \sum_{j=1}^{3} M_j (M_j - 1) +$$

$$+ W \sum_{j=1}^{3} N_j \, M_j \tag{4.1}$$

where $j = 4 \equiv 1$ due to the periodic boundary conditions determined by the ring geometry, T_a and T_b are the hopping amplitudes, U_a and U_b the *intra*-species repulsive interactions, and W represents the *inter*-species repulsion. A_j and B_j are standard bosonic operators, having commutators $[A_j, A_k^\dagger] = \delta_{j,k} = [B_j, B_k^\dagger]$, and $[A_j, B_k^\dagger] = 0$. After defining number operators $N_j = A_j^\dagger A_j$ and $M_j = B_j^\dagger B_j$, we recall that total boson numbers $N = \sum_{j=1}^3 N_j$ and $M = \sum_{j=1}^3 M_j$ of both species represent conserved quantities, namely, $[\hat{H}, N] = [\hat{H}, M] = 0$.

Semiclassical approach towards demixing. The Continuous Variable Picture (CVP), originally introduced to investigate the spatial fragmentation of a condensate in a two-well potential [208], is a semi-classical approximation scheme based on the replacement of the inherently discrete quantum numbers associated to the Fock-state basis with continuous variables (see Appendix B for an exhaustive description of this approximation scheme). This technique has proved to be particularly effective in capturing the essential critical behaviour of complex many-body systems [209–211]. It also allows one to derive an effective semi-classical Hamiltonian H_{eff} which well reproduces the low-energy physics of the original quantum model [175, 212, 213] and to turn the search for the ground state thereof into that of the global minimum of the potential V included in H_{eff}. In the current case, the CVP associates to Hamiltonian (4.1) the potential

$$\begin{aligned} V = -2N_aT_a\left(\sqrt{x_1x_2} + \sqrt{x_2x_3} + \sqrt{x_3x_1}\right) - 2N_bT_b\left(\sqrt{y_1y_2} + \sqrt{y_2y_3} + \sqrt{y_3y_1}\right) + \\ + \frac{U_aN_a^2}{2}\left(x_1^2 + x_2^2 + x_3^2\right) + \frac{U_bN_b^2}{2}\left(y_1^2 + y_2^2 + y_3^2\right) + \\ + WN_aN_b\left(x_1y_1 + x_2y_2 + x_3y_3\right) \end{aligned} \tag{4.2}$$

which comes with the two constraints $\sum_{i=1}^3 x_i = \sum_{i=1}^3 y_i = 1$, enforcing particle number conservation in both condensed species. Notice that variables $x_i := n_i/N_a$ and $y_i := m_i/N_b$ represent normalized boson populations and are regarded as *continuous* in view of the fact that the total numbers of bosons N_a and N_b are assumed to be large.

4.3 Miscibility properties

We discuss the ground-state properties of a (possibly asymmetric) bosonic binary mixture in a ring trimer, showing that they can be conveniently represented by means of a two-dimensional phase diagram which is, in turn, spanned by two specific effective variables representing functions of the original-model parameters. Each phase features a characteristic boson-population distribution, which results in a different degree of mixing and in a different functional dependence of the ground-state energy on the aforementioned effective variables.

The phase diagram. The presence of four different phases emerges in a crystal-clear way when one considers the large-populations limit (this can be seen as sort of thermodynamic limit according to the scheme highlighted in [175]), i.e. when ratios U_aN_a/T_a and U_bN_b/T_b are big enough to make hopping terms negligible. In this limit, in fact, the (rescaled version of) effective potential (4.2), namely $V/(U_aN_a^2)$, reduces to

$$\mathcal{V} = \frac{1}{2}\left(x_1^2 + x_2^2 + x_3^2\right) + \frac{\beta^2}{2}\left(y_1^2 + y_2^2 + y_3^2\right) + \alpha\beta\left(x_1y_1 + x_2y_2 + x_3y_3\right), \tag{4.3}$$

an expression including only *two* effective parameters,

$$\alpha = \frac{W}{\sqrt{U_aU_b}}, \qquad \beta = \frac{N_b}{N_a}\sqrt{\frac{U_b}{U_a}}. \tag{4.4}$$

The former corresponds to the ratio between the inter-species and the (geometric average of) the intra-species repulsive interactions while the latter accounts for the degree of asymmetry between the two species. This reduced set of parameters proves to be the most natural one to investigate the occurrence of mixing-demixing transitions in the system and is therefore employed to build the phase diagram. In this regard, the region $\mathcal{D} = \{(\alpha,\beta) : 0 \leq \alpha \leq 3,\ 0 \leq \beta \leq 1\}$, which is depicted in Fig. 4.1 already includes all four phases that the system's ground state can exhibit (notice, in fact, that if $\beta > 1$, one can swap species labels a and b and therefore come back to region $\mathcal{D}$). In each phase, the configuration $(\vec{x}, \vec{y})$ which minimizes effective potential (4.3) is marked by a specific dependence on the effective model parameters (4.4). Analytic expressions $x_j(\alpha,\beta)$ and $y_j(\alpha,\beta)$ have been derived by means of an exhaustive exploration of the polytope-like domain of function (4.3)

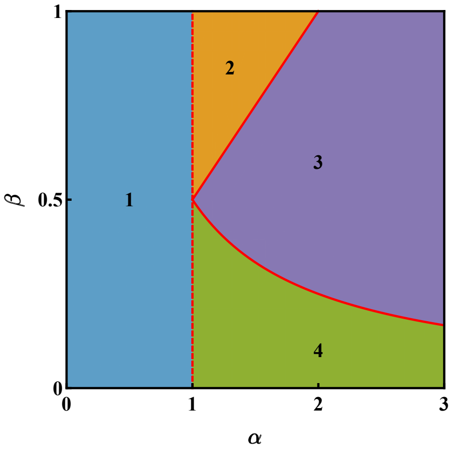

Figure 4.1: Phase diagram of a binary mixture in a ring trimer. Each of the four phases corresponds to a different functional relationship between the minimum-energy configuration and effective model parameters (4.4). This circumstance has a direct impact on the mixing properties of the system and on its ground-state energy. Red dashed (solid) line represents a mixing-demixing transition across which the components x_j and y_j of the minimum-energy configuration feature a jump discontinuity (are continuous). The plot has been obtained by means of a fully-analytic minimization of potential (4.3) under the constraints $\sum_{j=1}^{3} x_j = \sum_{j=1}^{3} y_j = 1$. See Appendix B.2 for an exhaustive description of the methodology employed to explore the domain of function $\mathcal{V}$ and its boundary.

(see Appendix B.2 for a detailed description of the method), and are presented here, together with the essential features of the associated phase:

1. In phase 1, being $\alpha < 1$, the inter-species repulsion is too small to trigger spatial phase separation and the two species are uniformly distributed among the three wells, i.e. $x_j = y_j = 1/3$, $\forall j = 1,2,3$.

2. Phase 2 occurs for $1 < \alpha < 2\beta$, that means for intermediate values of α and not too asymmetric species. In this region, one has complete demixing in two wells and mixing in the remaining one. The explicit expression of the minimum-energy configuration as functions of model parameters (4.4) reads

$$x_1 = 0, \qquad x_2 = \frac{\alpha^2 - \alpha\beta - 2}{\alpha^2 - 4}, \qquad x_3 = \frac{\alpha\beta - 2}{\alpha^2 - 4},$$

$$y_1 = \frac{\alpha^2\beta - \alpha - 2\beta}{(\alpha^2 - 4)\beta}, \qquad y_2 = 0, \qquad y_3 = \frac{\alpha - 2\beta}{(\alpha^2 - 4)\,\beta}.$$

3. Phase 3, occurring for sufficiently high values of α and not too asymmetric species (more specifically, for $1/(2\alpha) < \beta < \alpha/2$), features a completely demixed scenario, such that species b clots in one well, while species a equally spreads in the other two sites:
$$x_1 = 0, \quad x_2 = \frac{1}{2}, \quad x_3 = \frac{1}{2},$$
$$y_1 = 1, \quad y_2 = 0, \quad y_3 = 0.$$
4. Phase 4 occurs for sufficiently high values of α and sufficiently asymmetric species (i.e. for $\alpha > 1$ and $\beta < 1/(2\alpha)$). A good degree of asymmetry can be achieved, for example, if species b constitutes an impurity with respect to the majoritarian species a, meaning that $N_b \ll N_a$. The hallmark of this phase is that species b clots in one site, while species a spreads in all three sites, but in different proportions:
$$x_1 = \frac{1}{3}(1-2\alpha\beta), \quad x_2 = \frac{1}{3}(1+\alpha\beta), \quad x_3 = \frac{1}{3}(1+\alpha\beta),$$
$$y_1 = 1, \quad y_2 = 0, \quad y_3 = 0.$$

An illustrative summary of all presented minimum-energy configurations is provided in Fig. 4.2. Concerning the ones discussed at points 2, 3 and 4, we remark that, due to the Z_3 symmetry of the system, they are not unique and that other isoenergetic configurations can be obtained by permutations of site indexes. Quantum-mechanically, the ground state is degenerate only in the infinite-population limit because, as soon as they come into play, hopping terms lift the degeneracy and the ground state's structure gets that of a Schrödinger cat [201, 204, 206, 210] (see, in this regard, Figure 3.2 where the energy gap between the ground and the first excited level is illustrated in the case of a two-well potential). For example, in phase 3, the ground-state is of the type

$$|E_0\rangle \approx \frac{1}{\sqrt{3}}\left(\left|0,\frac{1}{2},\frac{1}{2}\right\rangle_a |1{,}0{,}0\rangle_b + \left|\frac{1}{2},0,\frac{1}{2}\right\rangle_a |0{,}1{,}0\rangle_b + \left|\frac{1}{2},\frac{1}{2},0\right\rangle_a |0{,}0{,}1\rangle_b \right),$$

an expression where symbol "≈" reminds that minor contributions coming from Fock states with different boson distributions and activated by the non-zero hopping

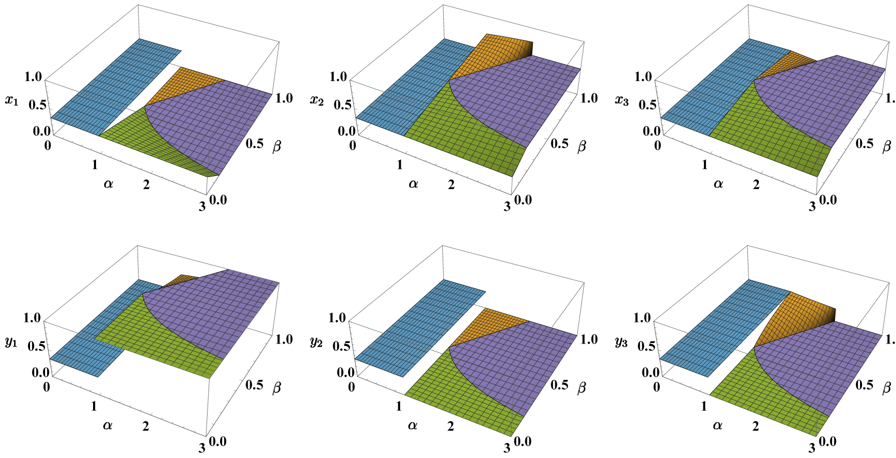

Figure 4.2: Summary of the configurations $(\vec{x}, \vec{y})$ which minimize effective potential (4.3) (under the constraints $\sum_j x_j = \sum_j y_j = 1$) in the four phases. Phase 1 (in blue) features perfect demixing; phase 2 (in orange) features demixing in two out of three sites and mixing in the third one; phase 3 (in purple) is the fully-demixed one; phase 4 (in green) is the one where species b clots in a site while species a spreads in all three sites, but in different proportions.

amplitudes have been understood.

As clearly illustrated in Fig. 4.2, for $\beta < 1$, the minimum-energy configuration $(\vec{x}, \vec{y})$, as a function of model parameters α and β, is discontinuous at transitions 1-2 and 1-4 while it is continuous at transitions 2-3 and 3-4. Nevertheless, in the case of perfectly symmetric species, a circumstance implying $\beta = 1$, the system gains an additional symmetry [consisting in the interchangeability of species' labels in formulas (4.1) - (4.3)] and a further discontinuity at transition 2-3 appears. The twin-species limit, widely discussed in Section 4.5, therefore features a qualitatively different critical behavior.

Phases and degree of mixing. An effective indicator to quantify the degree of mixing of two different species in discretized domains is the entropy of mixing (S_{mix}). Originally introduced in the context of macromolecular simulations [168], this measure has been recently introduced in the realm of ultracold atoms in order to investigate the link between chaotic dynamical regimes and mixing properties of a bosonic binary mixture in a ring trimer [214] (see Chapter 5). According to the definition given in [168] (see also Appendix C for its mathematical derivation), the entropy of mixing associated to a certain minimum-energy configuration $(\vec{x}, \vec{y})$ reads

$$S_{mix} = -\frac{1}{2}\sum_{j=1}^{3}\left(x_j \log\frac{x_j}{x_j+y_j} + y_j \log\frac{y_j}{x_j+y_j}\right). \tag{4.5}$$

This formula is based on *normalized* populations x_j and y_j and is therefore suited to describe binary mixtures where the species feature a particle-number imbalance (moreover the contribution of each site j to the total entropy of mixing is not fixed, but it is weighted by the fractions of particles present therein). As shown in Fig. 4.3, S_{mix} is zero in phase 3 (perfect demixing) while achieves the maximum possible value, $\log 2 \approx 0.69$ in phase 1 (perfect mixing). More generally, S_{mix}, as a function of model parameters α and β, mirrors the criticalities exhibited by the minimum-energy configuration, i.e. it is discontinuous at transition 1-2 and 1-3 while it is continuous at transitions 2-3 (apart from the special case $\beta = 1$) and 3-4. For this reason, it constitutes a valid indicator to capture the occurrence of mixing-demixing transitions. Note that S_{mix} is particularly advantageous in that it allows one to represent the system critical behavior by avoiding its description in terms of six boson populations x_j and y_j.

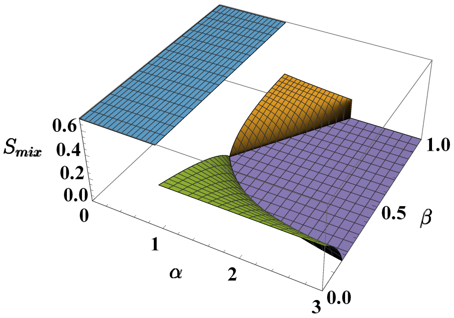

Figure 4.3: Entropy of mixing, S_{mix}, in the four phases. Phase 1 (in blue) features perfect mixing and S_{mix} takes the biggest possible value, i.e. $\log 2 \approx 0.69$. Conversely, phase 3 (in purple) features perfect demixing and S_{mix} is therefore zero.

Phases and free energy. Being the temperature zero, the free energy $F = E - TS$ coincides with the internal energy E, i.e. the ground-state energy. The latter, within the CVP approach, can be computed by means of the effective potential (4.3) which, for the four boson distributions corresponding to the four phases, exhibits a specific dependence law on model parameters α and β given by

$$\mathcal{V}_{*,1} = \frac{1}{6}\left(2\alpha\beta + \beta^2 + 1\right), \qquad \mathcal{V}_{*,2} = \frac{\left(\alpha^2 - 2\right)\beta^2 + \alpha^2 - 2\alpha\beta - 2}{2\left(\alpha^2 - 4\right)},$$

$$\mathcal{V}_{*,3} = \frac{1}{4}\left(2\beta^2 + 1\right), \qquad \mathcal{V}_{*,4} = \frac{1}{6}\left[\beta\left(-2\alpha^2\beta + 2\alpha + 3\beta\right) + 1\right].$$

The graphic representation of these expressions (see first panel of Fig. 4.4), shows that $\mathcal{V}_*$ is indeed continuous everywhere and, in particular, across the transitions. Nevertheless, in agreement with the previous mixing-entropy analysis, the non-analytic character of the ground-state energy does emerge if one computes the first and the second derivative of $\mathcal{V}_*$ with respect to α, which is regarded as a control parameter. As depicted in the second and in the third panel of the aforementioned figure, in fact, at transitions 1-2 and 1-4, the first derivative is discontinuous, while at transitions 2-3 and 3-4, the first derivative is continuous but the second one is discontinuous (except for the special case $\beta = 1$, where the first derivative is discontinuous at transition 2-3).

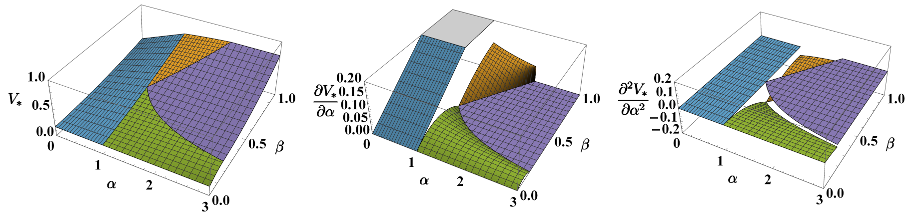

Figure 4.4: Effective potential (4.3) (first panel) and its first and second derivative with respect to α (second and third panel) relevant to the minimum-energy configuration as functions of model parameters parameters α and β.

4.3.1 Finite-size effects on the mixing-demixing transitions

As already mentioned, the four different phases emerge at their clearest in the large-populations limit, i.e. when $U_a N_a / T_a \to \infty$ and $U_b N_b / T_b \to \infty$. Such phases are still recognizable also in the more realistic case of finite-size systems (i.e. systems with limited numbers of atoms and featuring non-vanishing hopping terms), although the phase diagram presented in Fig. 4.1 gets blurred and deformed. The effects of finite ratios U_aN_a/T_a and U_bN_b/T_b can be summarized as follows:

- The minimum-energy configuration $(\vec{x},\vec{y})$, regarded as a function of model parameters $\alpha \in (0{,}3)$ and $\beta \in (0{,}1)$, is continuous and, as a consequence, so is the entropy S_{mix} (comparing Fig. 4.3 and Fig. 4.5, one can notice that the jump discontinuities give way to smooth junctions).
- The fully-mixed phase is favored by the presence of non-negligible hopping amplitudes, its border being given by the inequality

  $$\alpha < \sqrt{\left(1+\frac{9}{2}\frac{T_a}{U_aN_a}\right)\left(1+\frac{9}{2}\frac{T_b}{U_bN_b}\right)}. \tag{4.6}$$

  The latter represents the condition under which the Hessian matrix associated to effective potential (4.2) (and evaluated at point $x_j = y_j = 1/3$, with $j = 1,\,2,\,3$) is positive definite. Walking away from the large-populations limit, the right-hand term rises above the value 1, thus determining an enlargement of phase 1 at the expenses of the neighboring phases (see the enlargement of the blue region in Fig. 4.5 moving from the left panel to the right panel). It is worth mentioning that (the twin-species limit of) condition (4.6) was found to define the region of parameters' space where the spectrum of Bogoliubov quasiparticles is well-defined and not degenerate (see formula (2.23) in Chapter 2).
- As intuition suggests, the fully demixed phase is mined by the presence of hopping processes between the wells and therefore occurs for higher values of α (see the shrinking of the purple region in Fig. 4.5 moving from the left panel to the right panel).
- Interestingly, increasing the hopping amplitudes, phase 4 not only enlarges, but invades the $\beta > 1/2$ region, crushing and shrinking phases 2 and 3 (moving from the left to the right panel of Fig. 4.5, one can see that the green region enlarges at the expenses of the orange and of the purple regions).

4.3.2 Quantum results

The CVP approach can be safely applied when the number of particles is large enough, i.e. when it is possible to replace quantum mechanical operators with their

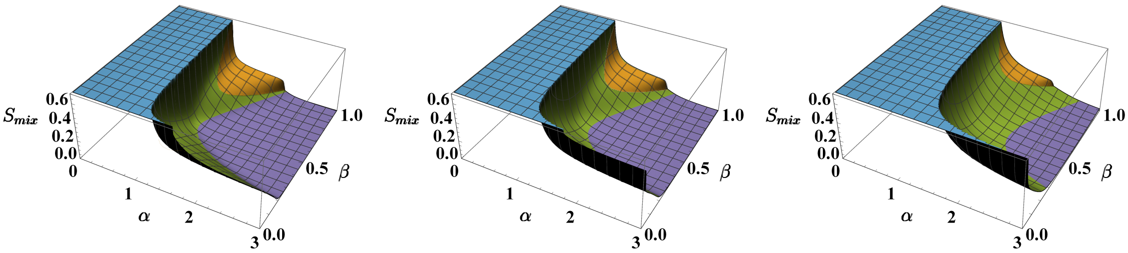

Figure 4.5: Entropy of mixing associated to the configurations $(\vec{x}, \vec{y})$ which minimize effective potential (4.2) sweeping model parameters α and β. The following values/intervals have been chosen: $U_a = U_b = 1$, $N_a = 15$, $N_b \in [0,15] \Rightarrow \beta \in [0,1]$, $W \in [0,3] \Rightarrow \alpha \in [0,3]$, $T_a = T_b = T$, where $T = 0.1$, 0.2, 0.5 in the left, central and right panel respectively. Colors have been employed as a guide to the eye: blue is used when $S_{mix} = \log 2$, purple when $S_{mix} < 0.05$, green for all intermediate values except the dome corresponding to phase 2 and therefore colored in orange.

$\mathbb{C}$-number counterpart. Conversely, for small boson populations, the adoption of this approximation scheme is less justified, and a fully quantum approach is needed. Such approach, involving the exact numerical diagonalization of Hamiltonian (4.1), can be computationally demanding since the dimension

$$D = \frac{(N_a + 2)!}{N_a!\, 2!} \frac{(N_b + 2)!}{N_b!\, 2!}$$

of the fixed-boson-number Hilbert space of states (the latter being of the type $|\vec{n}, \vec{m}\rangle := |n_1, n_2, n_3, m_1, m_2, m_3\rangle$), rapidly increases with increasing number of particles. Devoting the necessary attention to the numerical protocol [215], one can still handle the matrix representation of Hamiltonian (4.1) when $N_a = N_b = 15$ and therefore accomplish its *exact diagonalization*, thus obtaining the energy levels $E_i = \langle \psi_i | \hat{H} | \psi_i \rangle$ and the energy eigenstates $|\psi_i\rangle$. From these outputs, one can build several indicators which, in spite of the still small numbers of employed particles, already highlight the occurrence of the same critical phenomena and mixing-demixing transitions predicted within the CVP scheme. Among the various possibilities, and in order to offer a direct comparison with its CVP-counterpart, we introduce the quantum version of the entropy of mixing,

$$\tilde{S}_{mix} := \sum_{\vec{n},\vec{m}}^{D} |c(\vec{n},\vec{m})|^2 S_{mix}(\vec{n},\vec{m}), \tag{4.7}$$

where coefficients $c(\vec{n},\vec{m}) = \langle \vec{n},\vec{m}|\psi_0\rangle$ are the components of the ground state $|\psi_0\rangle$ with respect to the Fock basis and $S_{mix}(\vec{n},\vec{m})$ is the entropy of mixing associated to Fock state $|\vec{n},\, \vec{m}\rangle$, computed by means of formula (4.5) upon substitutions $n_i/N_a \to x_i$ and $m_i/N_b \to y_i$. Sweeping [216] model parameters W and U_b, one can effectively reconstruct the behaviour of $\tilde{S}_{mix}$ in the $(\alpha,\, \beta)$-plane. The result, illustrated in Fig. 4.6, witnesses the presence of the discussed four quantum phases also in this purely quantum scenario and, being in great agreement with its CVP-counterpart (compare with Fig. 4.5), validates the predictions given by the semiclassical approximation scheme. In particular, the latter proves to be rather accurate already with quite limited numbers of particles ($N_a = N_b = 15$).

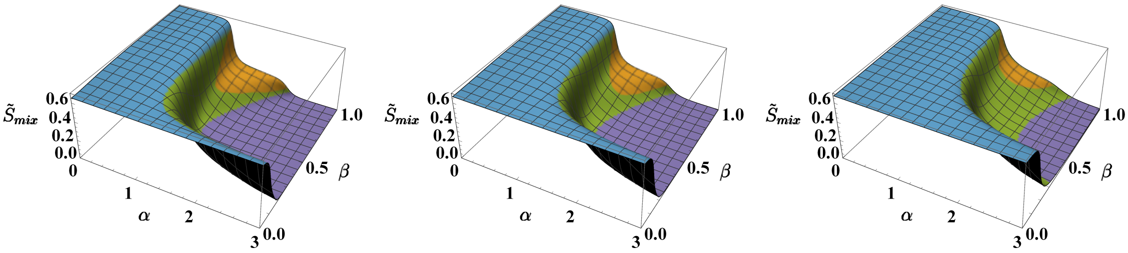

Figure 4.6: Entropy of mixing associated to the ground state $|\psi_0\rangle$, obtained by means of formula (4.7) sweeping model parameters α and β. The following values/intervals have been chosen: $U_a = 1$, $U_b \in [0{,}1]$, $N_a = N_b = 15 \Rightarrow \beta \in [0{,}1]$, $W \in [0{,}3] \Rightarrow \alpha \in [0{,}3]$, $T_a = T_b = T$, where $T = 0.1,\, 0.2,\, 0.5$ in the left, central and right panel respectively. Colors have been employed as a guide to the eye: blue is used when $S_{mix} \approx \log 2$, purple when $S_{mix} < 0.05$, green for all intermediate values except the dome corresponding to phase 2 and therefore colored in orange.

4.4 Toward an experimental realization: a "real" mixture and beyond point-like potential wells

In the previous sections of this Chapter we have discussed the mixing properties of an asymmetric binary mixture within the Bose-Hubbard model and within the continuous variable picture. In order to get closer to an experimental realization, one has to consider also the non-pointlike character of potential wells and the actual tunability of the scattering lengths in atomic systems.

In Chapter 7, we present an experimental proposal devised in collaboration with the Hannover Institute of Quantum Optics and which is based on a Sodium-Potassium mixture confined in an effective three-well potential by means of a system of optical tweezers.

From now on, therefore, the formulas and the simulations that we will present will be strictly linked with the real experimental setup and labels a and b will stand for *sodium* and *potassium* respectively. Parameters $m_a = 22.99$ u and $m_b = 39.10$ u are therefore the atomic masses of such elements, where u stands for unified atomic mass unit.

Validity of the point-like approximation of potential wells. By means of a mean-field treatment of the problem, we will show that, for the examined values of experimentally-available parameters, the phase separation mechanism of the realistic bosonic binary mixture is such that it takes place *inter*-well and not *intra*-well. This important circumstance justifies the usage of the Bose-Hubbard model (and of the associated CVP) and determines experimentally-accessible results which are in great agreement with the discussed previsions. In this regard, we want to stress the fact that, if the mean-field treatment of the problem had revealed an *intra*-well phase separation mechanism, the point-like approximation of potential wells [an approximation which is inherently present in the Bose-Hubbard model (4.1) and in its CVP (4.2)] would have been completely unjustified and the phase diagram illustrated in Fig. 4.1 would have been different.

Tunability of the scattering lengths. In the discussion developed in the previous sections of this chapter, the interspecies coupling W and the intraspecies interactions U_a and U_b are regarded as *independent* knobs. In Chapter 7, we will see that this is not the case in a real experimental setup, as the one engineered by the Hannover group. Namely, the intra- and interspecies scattering lengths present in the expressions of g_{ab}, g_a and g_b (the mean-field counterparts of W, U_a and U_b respectively) feature a specific functional dependence on the applied magnetic field, which is therefore the actual control knob which allows one to travel along *pathways* in the phase diagram of Fig. 4.1.

4.4.1 Mean-field approach to the simulation of real system

In pursuing an actual experimental realization, one must interface the rather essential Bose-Hubbard-like model (4.1) described within the CVP [see effective potential (4.2)] with experimentally-accessible parameters and measurable quantities. The bridge between theory and experiment is provided by a mean-field treatment of the problem. This approach also comes with a number of improvements to the CVP and, while confirming the fundamental results obtained therein, shines light on some possibly tricky aspects which were set aside by the pointlike approximation of potential wells and inherently present both in the Bose-Hubbard model and in the CVP.

In the mean-field picture, the system under analysis can be effectively modeled by two stationary Gross-Pitaevskii equations

$$-\frac{\hbar^2}{2m_a}\nabla^2\varphi_a + g_a|\varphi_a|^2\varphi_a + g_{ab}|\varphi_b|^2\varphi_a + V_{ext,a}\varphi_a = \mu_a\varphi_a \tag{4.8}$$

$$-\frac{\hbar^2}{2m_b}\nabla^2\varphi_b + g_b|\varphi_b|^2\varphi_b + g_{ab}|\varphi_a|^2\varphi_b + V_{ext,b}\varphi_b = \mu_b\varphi_b \tag{4.9}$$

with normalization conditions

$$\int_{-\infty}^{+\infty} |\varphi_a|^2 \, \mathrm{d}^3x = N_a, \qquad \int_{-\infty}^{+\infty} |\varphi_b|^2 \, \mathrm{d}^3x = N_b \tag{4.10}$$

enforcing particle-number conservation in both atomic species. Formulas

$$g_a = \frac{4\pi\hbar^2 a_a}{m_a} = 1.01\times 10^{-50} J \qquad \text{and} \qquad g_b = \frac{4\pi\hbar^2 a_b}{m_b} \in [8.67,\, 9.20]\times 10^{-52} J$$

give the intra-species interactions and

$$g_{ab} = \frac{2\pi\hbar^2 a_{ab}}{\mu_{ab}} \in [1.57,\, 7.44] \times 10^{-51} J$$

the inter-species coupling being $\mu_{ab} = (m_a^{-1} + m_b^{-1})^{-1}$ the reduced mass. These last two quantities can be tuned by means of the applied magnetic field B, which, acting on scattering lengths a_b and a_{ab}, therefore plays the role of the effective control parameter, capable of triggering the mixing-demixing transitions. Here we use $a_a = 52\, a_0$, $a_b \in [7.6{,}8.1]\, a_0$ and $a_{ab} \in [10.2{,}48.5]\, a_0$. Term $V_{ext}(\vec{x})$ represents the optical potential corresponding to the ring-trimer geometry (see Figure 4.7). One can generate (experimentally achievable) parameters' vectors $(N_a,\, N_b,\, g_a,\, g_b,\, g_{ab})$ both by tuning the magnetic field B (the latter has an impact on ratios g_{ab}/g_b and g_b/g_a) and by setting the boson population asymmetry N_b/N_a. On the basis of such sets of parameters, we determined (see Appendix D for details concerning the numerical simulation) the eigenfunctions of coupled, non-linear, eigenvalue problems (4.8) and

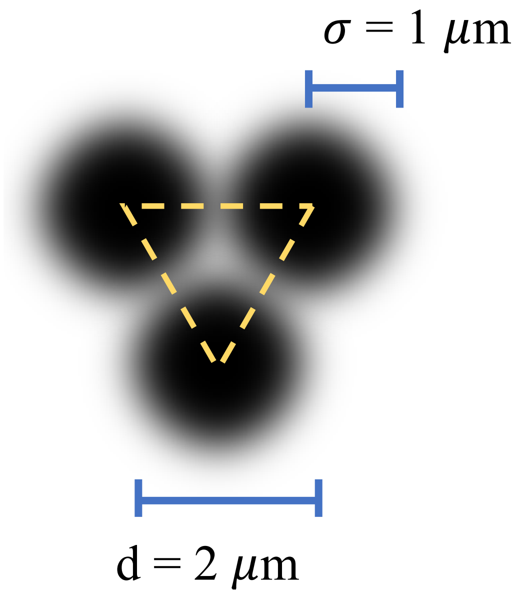

Figure 4.7: Schematic representation of the three Gaussian traps constituting the ring-trimer potential. Yellow dashed line represents the equilateral triangle formed by the trap's center. Such triangle can be associated to the curvilinear abscissa x present in equations (4.8) and (4.9) (and therefore automatically endowed with periodic boundary conditions).

(4.9), which minimize the Hamiltonian functional

$$\mathcal{H}[\varphi_a,\varphi_b]=\int\varphi_a^*\left[-\frac{\hbar^2}{2m_a}\nabla^2+V_{ext,a}\right]\varphi_a\,\mathrm{d}^3x+\frac{g_a}{2}\int|\varphi_a|^4\,\mathrm{d}^3x+$$

$$+\int\varphi_b^*\left[-\frac{\hbar^2}{2m_b}\nabla^2+V_{ext,b}\right]\varphi_b\,\mathrm{d}^3x+\frac{g_b}{2}\int|\varphi_b|^4\,\mathrm{d}^3x+g_{ab}\int|\varphi_a|^2|\varphi_b|^2\,\mathrm{d}^3x,\quad(4.11)$$

representing, in turn, the total energy of the system. Being qualitatively different, such minimum-energy solutions can be classified into four categories which indeed correspond to the already discussed four phases. In order to better appreciate the great agreement between the results obtained by means of the CVP and those obtained within the mean-field treatment, a representative of each of these categories is shown in Fig. 4.8. With reference to such figure, the first panel represents the category of ground-states belonging to phase 1, the one exhibiting perfect mixing.

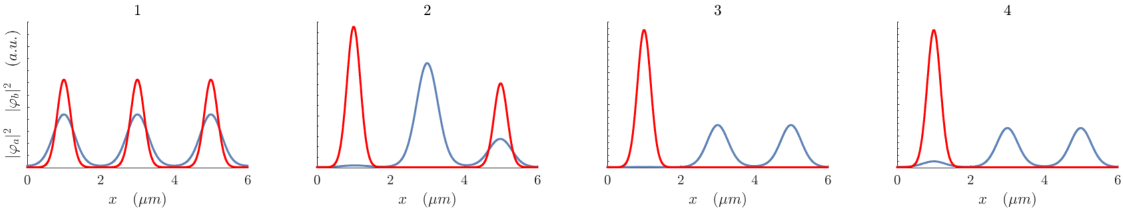

Figure 4.8: Graphical representation of four qualitatively different eigensolutions of equations (4.8) and (4.9) which minimize Hamiltonian functional (4.11). Blue (red) line corresponds to $|\varphi_a|^2$ ($|\varphi_b|^2$). The horizontal axis constitutes the arc length associated to the perimeter of the equilateral triangle formed by the traps' centers (see yellow line in Fig. 4.7) and therefore it comes with periodic boundary conditions (see Appendix D for details concerning the numerical simulation). The specific model parameters that have been used in each simulation are given in the form (N_a, N_b, g_a, g_b, g_{ab}). Panel 1: (200, 600, $52\times(4\pi\hbar^2 a_0)/m_a$, $8.1\times(4\pi\hbar^2 a_0)/m_b$, $10.2\times(2\pi\hbar^2 a_0)/\mu_{ab}$); Panel 2: (200, 600, $52\times(4\pi\hbar^2 a_0)/m_a$, $7.6\times(4\pi\hbar^2 a_0)/m_b$, $28.4\times(2\pi\hbar^2 a_0)/\mu_{ab}$); Panel 3: (200, 220, $52\times(4\pi\hbar^2 a_0)/m_a$, $7.8\times(4\pi\hbar^2 a_0)/m_b$, $48.5\times(2\pi\hbar^2 a_0)/\mu_{ab}$); Panel 4: (200, 220, $52\times(4\pi\hbar^2 a_0)/m_a$, $7.7\times(4\pi\hbar^2 a_0)/m_b$, $23.0\times(2\pi\hbar^2 a_0)/\mu_{ab}$). All panels: the ring-trimer geometry is realized by means of three Gaussian traps, whose centers lie on the vertexes of an equilateral triangle with edge $d=2\mu m$, whose width is $\sigma=1\mu m$ and whose depths are $P_a=4.44\times10^{-30}$ J $=322\times k_B$ nK for sodium and $P_b=1.16\times10^{-29}$ J $=840\times k_B$ nK for potassium being k_B the Boltzmann constant (see Methods). The energy of each of the four depicted solutions, together with their positions within the phase diagram spanned by effective parameters $g_{ab}/\sqrt{g_a g_b}$ and $N_b/N_a\sqrt{g_b/g_a}$ is shown in Fig. 4.9.

The two condensates, in fact, clearly overlap in each of the three wells and both boson distributions share the same Z_3 symmetry of the system. Notice also that, correctly, sodium (depicted in blue), being lighter, is more delocalized with respect to potassium (depicted in red) which, being heavier, is more strongly confined. The second panel depicts a ground-state belonging to phase 2, where one has demixing in two wells and mixing in the remaining one. Notice, in fact, that the first (second) well includes just potassium (sodium), while the third well includes both. The third panel shows a fully-demixed ground state, i.e. a representative of phase 3: potassium occupies the first well while sodium spread in the second and in the third one. Eventually, the fourth panel shows a representative of phase 4, the one characterized by the clotting of potassium in a single well and by the presence of a non-zero fraction of sodium therein.

Importantly, for all parameters' sets used in our numerical simulations, we observed that the phase separation mechanism is such that the two condensates redistribute *among* the wells and not *within* the wells (namely, an interwell and not an intrawell phase separation mechanism). Nevertheless, since in a single harmonic trap different phase separation mechanisms (e.g. hemispheric-like or spherical-shell-like) can be triggered by different potential and interaction strengths[80], we expect the interplay of these parameters to play an even more crucial role in multiple-trap systems. Due to its remarkable complexity, the analysis of this phenomenology will be investigated in future.

It is worth noticing that, when trap parameters and interaction strengths are such that phase separation does occur via an among-well boson redistribution, the terms proportional to g_a, g_b and g_{ab} in energy functional (4.11) quite naturally exhibit the same structure of the terms proportional to U_a, U_b and W in effective potential (4.2). In this sense, parameters α and β [see formulas (4.4)] correspond to, respectively, quantities $g_{ab}/\sqrt{g_a g_b}$ and $N_b/N_a\sqrt{g_b/g_a}$, and therefore span the mean-field counterpart of the phase diagram of Fig. 4.1. To link the phase diagram to experimental accessible parameters, in Fig. 4.9 we also plot the four phases by mapping β into N_b/N_a and α to the magnetic field B thanks to the known functional dependence of scattering lengths on the latter (see Fig. 7.1 in Chapter 7). Accordingly, gray lines in the both left panels of Fig. 4.9 play the role of the red boundaries separating the four phases in Fig. 4.1.

As g_b and g_{ab} depend on the applied magnetic field B, by sweeping the latter, one can generate pathways through the phase diagram. Moreover, one can vertically translate them simply by tuning the ratio N_b/N_a. For many such pathways, practically constituting extended sets of n-tuples $(N_a,\ N_b,\ g_a,\ g_b,\ g_{ab})$, we found the solutions of equations (4.8) and (4.9) which minimize energy functional (4.11). Two examples of this analysis are shown in Fig. 4.9, where we plot the ground state energy $E_0 := \mathcal{H}[\varphi_{a,0}, \varphi_{b,0}]$ as a function of the actual control parameter B along two specific pathways through the phase diagram. In remarkable analogy with the discussion relevant to effective potential (4.3) within the CVP, it is clear that E_0 is a continuous function of B and that its first derivative $\mathrm{d}E_0/\mathrm{d}B$ is discontinuous across transitions 1-2 and 1-4 (see rectangular markers in Fig. 4.9). Moreover, although not visually obvious, one can verify that the *second* derivative $\mathrm{d}^2E_0/\mathrm{d}B^2$ is discontinuous at transitions 2-3 and 3-4 (see circular markers in Fig. 4.9). Correctly, one does not observe phase transitions exactly at gray boundaries shown in the phase diagrams. This is due to the presence of non-zero hopping terms which smooths and deforms the zero-hopping phase diagram. On the right panels of Fig. 4.9 we plot the the mixing entropy S_{mix} relative to the two paths previously considered and the presence of different mix/demix phases is confirmed. This is very promising in the outlook of an experimental realization as S_{mix} represents a very versatile quantity, easily obtainable from the measured atom number in each well, irrespective of the observed permutation. We associate the presence of small fluctuations at small values of S_{mix} in both panels to numerical resolution resulting from the strong demixing and the consequent very small atom number in the wells. One could consider these fluctuations as a statistical error on the simulations in that range of magnetic field strength.

Upon the associations $\alpha \leftrightarrow g_{ab}/\sqrt{g_a g_b}$ and $\beta \leftrightarrow N_b/N_a\sqrt{g_b/g_a}$, our mean-field analysis, based on realistic model parameters involving sodium and potassium atoms, has therefore led to the same phases and the same mixing-demixing transitions evidenced within the CVP and thus corroborates, both qualitatively and quantitatively, the predictions about the phase-separation mechanism obtained therein, offering, also, a viable path towards an actual experimental realization.

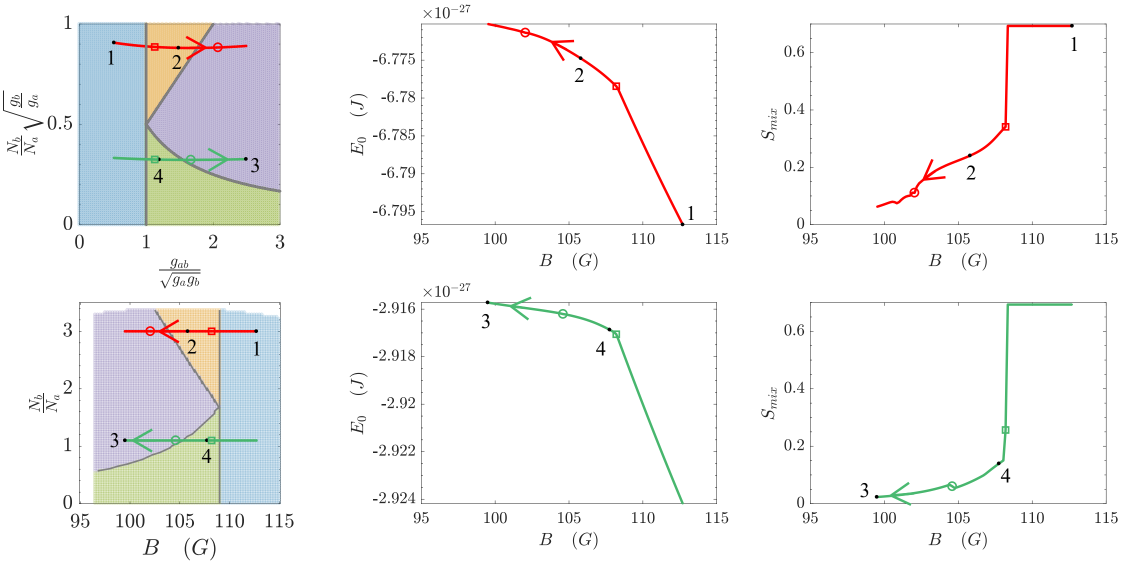

Figure 4.9: Upper left panel: two pathways in the mean-field counterpart of the phase diagram shown in Fig. 4.1. One can show, in fact, that parameter α and β of Fig. 4.1 play the role of $g_{ab}/\sqrt{g_a g_b}$ and $N_b/N_a\sqrt{g_b/g_a}$. Lower left panel: experimental counterpart of the phase diagram, the actual control parameters being the applied magnetic field B and the ratio N_b/N_a. Notice that curved pathways in the upper left panel are here horizontal. Each pathway is obtained by sweeping the applied magnetic field B. The upper red (lower green) pathway is obtained for $N_a = 200$ and $N_b = 600$ ($N_b = 220$). Central column's panels: ground state energy computed along each pathway [more specifically, they are computed by plugging the solutions of equations (4.8) and (4.9) into functional (4.11)]. Rectangular (circular) markers indicate the points where the first (second) derivative of E_0 with respect to B is discontinuous. Numbers 1-4 not only refer to the phase crossed by the pathway but specifically correspond to the minimum-energy solutions 1-4 illustrated in Fig. 4.8. Right column's panels: entropy of mixing computed along each pathway. Normalized boson populations appearing in formula (4.5) are computed by integrating the (square modulus of) the solutions of equations (4.8) and (4.9) in the three spatial domains associated to the potential wells.

4.5 Twin species

In this Section, we come back to the framework of the Bose-Hubbard model (and of its CVP) and consider the special but interesting case of twin species, namely the case of $U_a = U_b = U$, $N_a = N_b$ [entailing $\beta = 1$ according to formula (4.4)] and

$T_a = T_b = T$. In this circumstance, Hamiltonian (4.1) reads

$$\hat{H} = -T \sum_{j=1}^{3} \left(A_{j+1}^{\dagger} A_j + A_j^{\dagger} A_{j+1} + B_{j+1}^{\dagger} B_j + B_j^{\dagger} B_{j+1} \right) + \\ + \frac{U}{2} \sum_{j=1}^{3} \left[N_j (N_j - 1) + M_j (M_j - 1) \right] + \\ + W \sum_{j=1}^{3} N_j \, M_j \tag{4.12}$$

As already mentioned, under these conditions, the system gains an additional symmetry [i.e. the interchangeability of species' labels in formulas (4.1) - (4.3)] and a further discontinuity at transition 2-3 appears. The main effect analyzed in this Section, the two-step process where two different mixing-demixing phase transitions are triggered by a change in W/U, is

- Investigated within the CVP and by means of exact diagonalization of Hamiltonian (4.12);
- Shown to be related to the collapse and rearrangement of the energy spectrum of Hamiltonian (4.12);
- Characterized in terms of quantum-correlation properties (entanglement entropy) between two parts of the systems.

4.5.1 Semiclassical approach to the demixing

In the same spirit of Section 4.2, it is advantageous to investigate spatial phase separation by reformulating Hamiltonian (4.12) within the CVP (see Appendix B). According to this approximation scheme, it is possible to reduce the search for the ground state of Hamiltonian (4.12) to the one for the global minimum of the following effective potential:

$$V = -2NT \left(\sqrt{x_1 x_2} + \sqrt{x_2 x_3} + \sqrt{x_3 x_1} + \sqrt{y_1 y_2} + \sqrt{y_2 y_3} + \sqrt{y_3 y_1} \right) + \\ \frac{UN^2}{2} \left(x_1^2 + x_2^2 + x_3^2 + y_1^2 + y_2^2 + y_3^2 \right) + WN^2 \left(x_1 y_1 + x_2 y_2 + x_3 y_3 \right) \tag{4.13}$$

where variables x_i and y_i ($i = 1,2,3$) are normalized boson numbers, entailing that x_i, $y_i \in [0,1]$ and that $z_1 + z_2 + z_3 = 1$, ($z = x$, y) due to particle number conservation and $T_a = T_b =: T$, $U_a = U_b =: U$. Notice that only many-body states with the same fixed number $N = M$ of bosons for the two species are considered. The configuration $(\vec{x}, \vec{y})$ which minimizes the effective potential V is determined, at first, when the tunnelling processes are negligible if compared to onsite intra- and interspecies interactions. In this circumstance, in fact, it is possible to carry out a fully analytic study (see Appendix B.2) based on the exhaustive exploration of the domain of function (4.13) and capable of illustrating the physics of the problem in a particularly simple and effective way. The results, sketched in Fig. 4.10, can be summarized as follows:

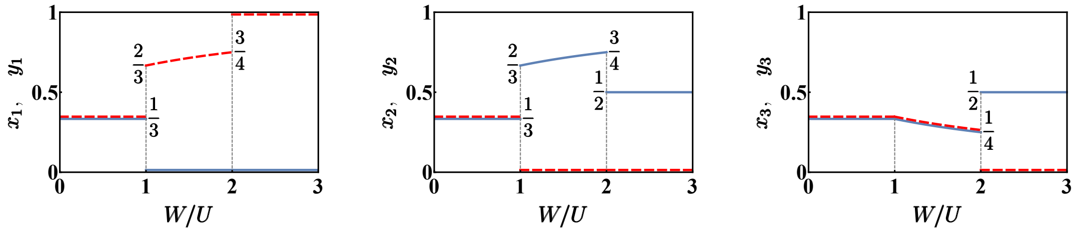

Figure 4.10: Normalized semiclassical bosonic populations in each of the three wells for varying W/U and for $T = 0$. Each panel corresponds to a site of the trimer, while blue solid (red dashed) lines are associated to bosonic species a (b). (Notice that, wherever two lines overlapped, they have been slightly displaced for purely graphical reasons). One can recognize the presence of three different quantum phases: i) for $W/U \in [0,1)$ the two condensates are fully mixed and completely delocalized; ii) for $W/U \in (1,2)$ they are separated in two out of the three wells while they coexist in the third one; iii) for $W/U > 2$ the demixing is complete, meaning that one species conglomerates in a well, while the other species distributes in the remaining two wells. It is clear that $W/U = 1,2$ represent critical values where two different mixing-demixing phase transitions occur. Data have been obtained by means of a fully analytic study of the global minimum of effective potential (B.4) (see Methods section).

1. For small W/U values (more specifically, if $W/U \in [0,1)$), the two species are delocalized and uniformly distributed in the trimer, thus entailing a perfect mixing.
2. For moderate W/U values (namely, if $W/U \in (1,2)$), the demixing occurs in two out of the three wells, while, in the third well, the species are still mixed.

Of course, due to the symmetry of the trimer system, no well is favoured compared to the others, and, as a consequence, there are three configurations $(\vec{x}, \vec{y})$ which minimize the effective potential V. Among such configurations, which are equal up to a permutation of the site labels, the one that we have illustrated in Fig. 4.10 is

$$\begin{array}{l|l|l} x_1 = 0 & x_2 = \frac{1+\frac{W}{U}}{2+\frac{W}{U}} & x_3 = \frac{1}{2+\frac{W}{U}} \\ y_1 = \frac{1+\frac{W}{U}}{2+\frac{W}{U}} & y_2 = 0 & y_3 = \frac{1}{2+\frac{W}{U}} \end{array}$$

Quantum-mechanically, the degeneracy associated to the six minimum-energy configurations leads to the formation of a non-degenerate ground state $|\Psi_0\rangle$ which is a six-sided Schrödinger cat, i.e. a state of the type

$$|\Psi_0\rangle = \frac{1}{\sqrt{6}} \sum_{j=1}^{6} |\psi_j\rangle \tag{4.14}$$

where each $|\psi_j\rangle$ corresponds to a different macroscopic configuration. Our analysis, which is semiclassical, breaks the symmetry of the problem and considers just one side of the cat, the one defined above and sketched in Fig. 4.10. It is interesting to observe that, crossing the critical point $W/U = 1$, the populations of site 1 and site 2 exhibit discontinuities, i.e. jumps from the uniform configuration $x_1 = y_1 = x_2 = y_2 = 1/3$ to the characteristic values $2/3$ and 0. Conversely, functions $x_3(W/U)$ and $y_3(W/U)$ are continuous in $W/U = 1$. Increasing the ratio W/U from 1 to 2, the third site (where the two bosonic species coexist) gradually looses bosons, while the first and the second site (each one hosting just one species) become increasingly populated. For $W/U \to 2^-$, the first well hosts $3/4$ of species-b bosons, while the second well hosts $3/4$ of species-a bosons. The remaining parts coexist in the third well in equal measure.

3. For big W/U values (i.e., for $W/U > 2$), the two species completely demix. One of them conglomerates in one site, while the other one spreads on the remaining two sites. This situation corresponds to 6 possible scenarios, i.e. to 6 configurations $(\vec{x}, \vec{y})$ minimizing the effective potential V. In fact, if configuration $(\vec{x}^*, \vec{y}^*)$ is a minimum for V, also the two configurations obtained

by permutations of the site labels are minima for V. Moreover, as the species we are considering feature the same hopping amplitude T and the same on-site repulsion U, the configurations where species-a conglomerates must not be favoured to the configurations where it is species-b the one that conglomerates. In other words, the energy of the system remains equal after the exchanges $x_i \leftrightarrow y_i$ ($i = 1,2,3$). The presence of 6 minimum-energy configurations in the classical analysis corresponds to a quantum ground state $|\Psi_0\rangle$ which is a six-faced Schrödinger cat, i.e. a state of the type (4.14) where each $|\psi_j\rangle$ is a state corresponding to a certain macroscopic configuration. In Fig. 4.10 we have broken such symmetry and plotted just one of the 6 possible configurations.

Finite-size effects. As illustrated in Fig. 4.11, for non-zero values of the ratio $T/(UN)$, the critical points move rightward (i.e., the transitions occur at bigger values of W/U). It is possible to show with a fully analytic computation based on the request that Hessian matrix (see matrix (B.8) in Appendix B.2) must be

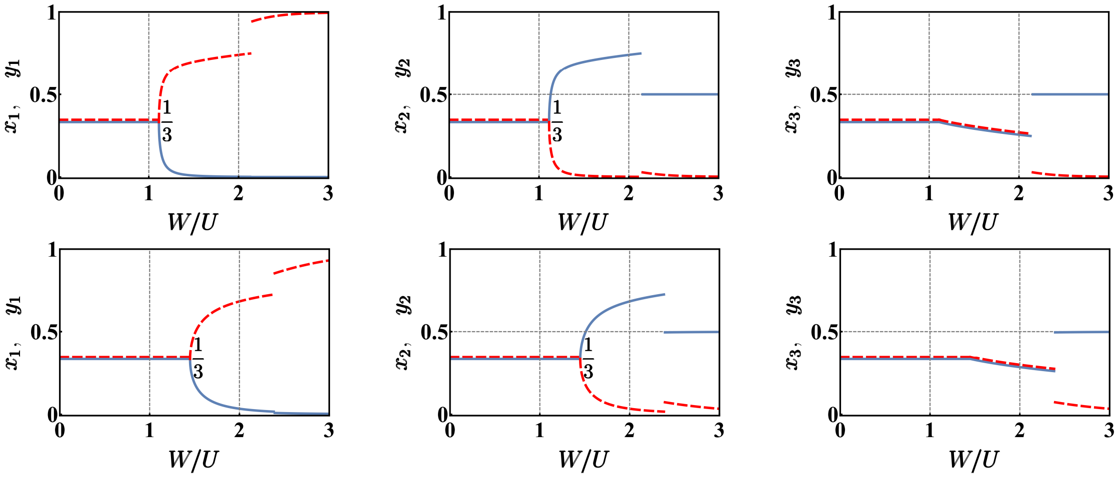

Figure 4.11: Normalized semiclassical bosonic populations in each of the three wells for varying W/U and for $N = 50$. First row corresponds to $T/U = 1.25$, second row to $T/U = 5$; Each panel corresponds to a site of the trimer, while blue solid (red dashed) lines are associated to bosonic species a (b). The presence of a non-zero T is responsible for the rightward translation of the two critical points. Data correspond to a particular branch of solutions (determined numerically) of system (B.7).

positive definite, that the first mixing-demixing phase transition onsets at

$$\frac{W}{U} = 1 + \frac{9}{2}\frac{T}{UN}, \tag{4.15}$$

a value which is greater than 1, mirroring the fact that tunnelling T favors the mixed phase and delays the occurrence of the first demixing. On the other hand, one can notice that the effect of T is smaller and smaller as the number of bosons, N, increases and, in the thermodynamic limit [175], it becomes negligible. In such limit, the scenario is again the one depicted in Fig. 4.10. It is also important to notice that equation (4.15) was found to determine the occurrence of the spectral collapse of Bogoliubov quasi-particle frequencies (see inequality (2.23) in Section 2.6), a circumstance that we will be further discussed in Section 4.5.2. We observe, also, that equation 4.15 represents the twin-species limit of equation (4.6) which was derived in the context of asymmetric mixtures.

The activation of the hopping amplitude T makes the model more realistic but does not upsets the scenario, which is still marked by two critical points. From a technical point of view, the search for the minimum energy configuration is simpler because T constitutes a regularizing term for function (4.13) since it prevents the points of minimum from falling on the boundary of the domain of function (4.13) itself. The exploration of such domain boundary (see Appendix B.2 for the description of this geometric approach) is therefore no longer necessary and it is enough to look just for *local* points of minimum in the interior of the domain. This conceptual simplification comes with the impossibility of analytically solving the resulting system of equations (B.7). With reference to Fig. 4.11, where numerical results are plotted, one can observe that bigger W/U values are needed to trigger the demixing transitions which, in turn, are less abrupt.

Semiclassical vs quantum results. To test its reliability, we have compared CVP's predictions to the results obtained by means of exact numerical diagonalization. Fig. 4.12 shows that the two mixing-demixing phase transitions occur at the same critical values of W/U and, more generally, that the semiclassical approach and the purely quantum scenario are in good agreement. Notice that we chose not to plot the expectation values of boson populations in the ground state (e.g. $\langle \Psi_0 | N_j | \Psi_0 \rangle$) because one would obtain the *average* over the different macroscopic configurations constituting the cat-states and, therefore, the constant value $N/3$, irrespective of the ratio W/U. Instead, we have determined, sweeping the parameter W/U, the *most probable configuration* i.e. the Fock state associated to the biggest (square modulus of the) coefficient in the decomposition of the ground state. It is interesting to notice that function (4.13) features a unique minimum in the uniform and fully mixed phase and six isoenergetic points of minimum in the intermediate and in the fully demixed phase. These degeneracies in the semi-classical energy landscape are resolved, quantum mechanically, with the formation of cat-states of the type (4.14).

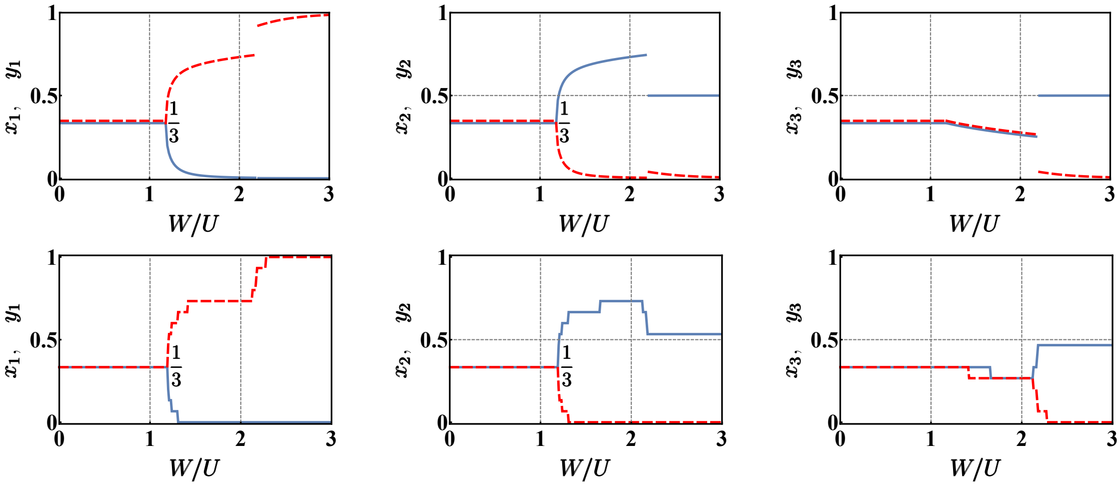

Figure 4.12: Upper row: a branch of solutions predicted by the CVP approach. Lower row: the corresponding branch of most probable Fock states present in the ground states $|\Psi_0\rangle$. The latter have been determined by means of an exact numerical diagonalization. In both cases parameters $N = 15$, $U = 1$, $T = 0.6$ have been chosen. Each panel corresponds to a site of the trimer, while blue solid (red dashed) lines are associated to bosonic species a (b).

Different families of minimum-energy solutions in the parameters space. Fig. 4.13 illustrates, for three different values of N (namely, for three different values of the ratio $T/(UN)$) how the three different families of solutions represent minimum-energy configurations in the parameters space. Basically, if one considers a certain point $(W/U, T/U)$ in the parameters space, varying N, the family of solutions associated to the lowest value of the energy can change. The borders illustrated in Fig. 4.13 have determined numerically solving systems (B.7) and

(B.9), and checking that the obtained stationary point actually is a minimum point for effective potential (4.13). Purple solid lines represent critical condition (4.15) derived analytically while no analytic expression can be found to define the orange dashed lines due to the complex nonlinear character of equations (B.7).

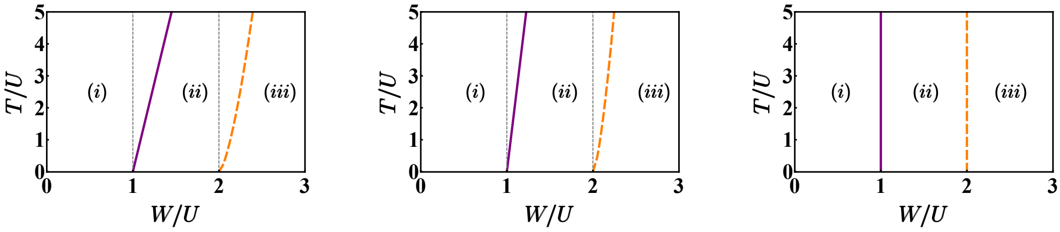

Figure 4.13: Subdivision of the parameters space in regions corresponding to different families of minimum-energy configurations, for $N = 50$, $N = 100$, $N \to +\infty$ (thermodynamic limit). Purple solid lines correspond to critical condition (4.15); orange dashed lines corresponds to those solutions of system (B.9) which are no longer minimum points for (4.13). Label (i) indicates the uniform and fully mixed phase, region (ii) is the intermediate phase and, eventually, label (iii) denotes the fully demixed phase. Notice that, as N increases, the role of T becomes more and more negligible.

4.5.2 Energy-spectrum collapse and demixing transitions

The double critical behaviour exhibited by the system upon a variation of W/U can be evidenced also from the energy-spectrum standpoint [167]. As shown in Fig. 4.14, whose data have been obtained by means of an exact (numerical) diagonalization of Hamiltonian (4.12), the energy levels tend to collapse in the neighborhood of the two critical points and have different arrangements in the three phases. One can recognize, for example, families of energy levels which are clearly distinct in the first two phases while tend to overlap in the third one. Approaching the limiting case $T/(UN) \to 0$, the collapses are more and more evident and the points where they take place tend to $W/U = 1$ and $W/U = 2$. The low-energy excitations spectrum of a binary mixture in the uniform and completely mixed phase was determined for a generic $L-$site ring by means of a group-theoretic approach combined with Bogoliubov scheme (see Chapter 2). Choosing $L = 3$ sites, the condition corresponding to the collapse of a Bogoliubov frequency [see equation (2.23)] exactly reproduces equation (4.15), which gives the onset of the first mixing-demixing phase transition.

One can thus appreciate the fact that the range of validity of the quasi-particles Bogoliubov spectrum exactly corresponds to the region of parameters space where the system is in the uniform and fully mixed phase.

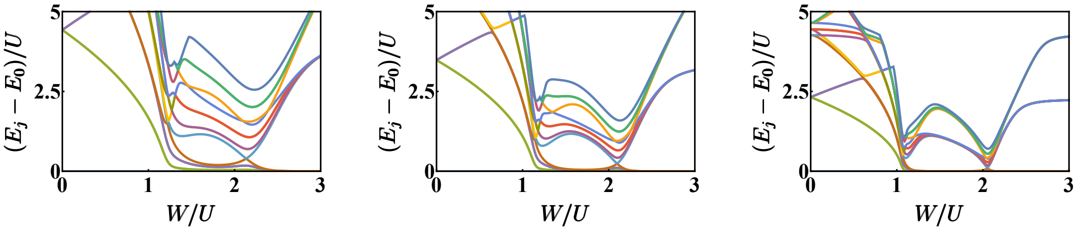

Figure 4.14: First 16 energy levels obtained for $N = 15$, $T/U = 0.6$, 0.4, and 0.2 respectively. The smaller T/U, the more evident the rearrangement and the collapse of the spectrum at the critical points. Data have been obtained by means of an exact diagonalization of Hamiltonian (4.12). Notice that the first panel (the one obtained for $T = 0.6$) can be compared with boson populations depicted in Fig. 4.12.

Ground state energy. The analysis of the energy spectrum is confirmed by the behaviour of the ground state energy $E_0 = \langle\psi_0|\hat{H}|\psi_0\rangle$ of Hamiltonian (4.12). E_0 has been numerically evaluated as a function of parameter W/U, for different values of $T/(UN)$. The results, illustrated in Fig. 4.15, show, for $T/(UN) \to 0$, the emergence of two critical points at $W/U = 1$ and $W/U = 2$. In such points, the ground state energy features discontinuities in the first derivative, a circumstance which suggests the onset of a quantum phase transition.

4.5.3 Entanglement and demixing

Quantities traditionally belonging to quantum information theory have been used to highlight the occurrence of quantum phase transitions [193, 217–221]. As explained in Chapter 3, among the others, the bipartite Von Neumann entanglement entropy (EE) is an indicator capable of quantifying the quantum correlation between two parts of a physical system through the Von Neumann entropy of a suitably defined sub-system[201, 222]. In our case, the physical system is of course the binary mixture, the two parts have been chosen to correspond to the two different atomic species and, therefore, the EE describes the quantum correlation between them (see the following paragraph for a detailed mathematical definition).

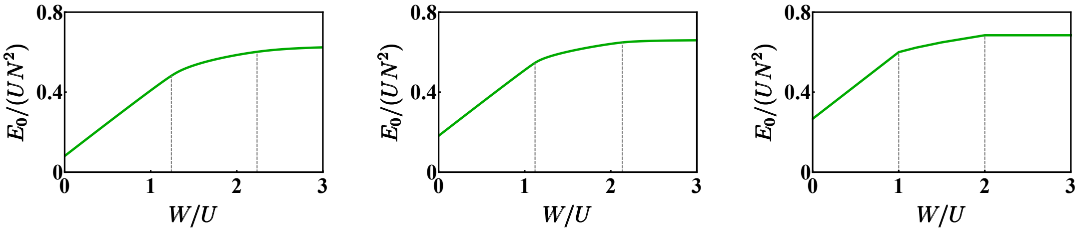

Figure 4.15: Normalized ground state energy vs W/U for $N = 15$ bosons. In each panel, the ratio T/U has been set to 0.8, 0.4 and 0 respectively. One can observe that, for non-zero T (first and second panel), the function is differentiable everywhere, while, for $T/U \to 0$ (third panel), the function is not differentiable at the two critical points. Gray dashed lines have been drawn where the CVP approach predicts the change of the the minimum-energy solution family (notice that they move leftward for $T/U \to 0$). Data have been obtained by means of an exact diagonalization of Hamiltonian (4.12).

As shown in Fig. 4.16, this indicator strongly depends on the specific phase of the system which, in turn, is determined by the ratio W/U. In the completely

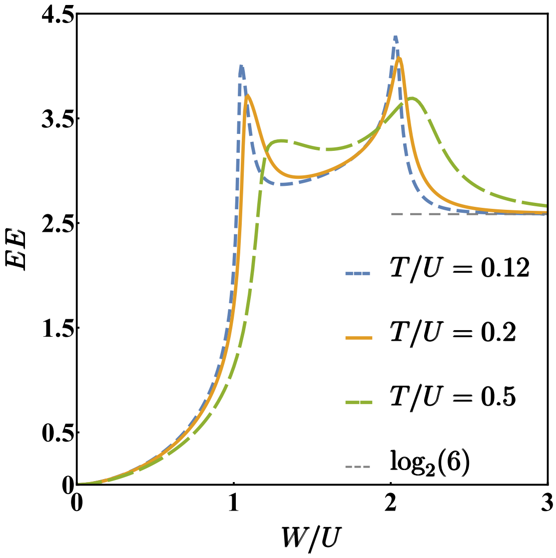

Figure 4.16: Entanglement entropy between the two atomic species for different values of T/U and for $N = 15$. Notice that, the smaller the ratio T/U, the sharper the peaks. Data have been obtained by means of an exact diagonalization of Hamiltonian (4.12).

mixed phase, i.e. for W/U smaller than the critical value (4.15), the EE steadily increases as W/U increases, despite the fact that semiclassical boson populations remain constant (uniformly distributed on the three wells). Notice that EE → 0 for $W/U \to 0$ because, in this limit, the species are decoupled. At the two critical values of W/U, the EE features peaks, which not only indicate that the two mixtures are strongly entangled, but also allow to clearly distinguish the three different phases. Such peaks are sharper if T/U is smaller, that means that the effect of the hopping amplitude is to smooth the mixing-demixing transition. For W/U greater than the second critical value, the demixing gets more and more complete and the EE approaches the limiting value $\log_2(6)$. According to standard notions of Quantum Information Theory and to applications thereof in the field of ultracold bosons [195, 201], the emergence of this value can be appreciated by recalling that there are 6 possible ways of realizing a completely demixed semiclassical configuration which, in turn, equally contribute to the formation of a unique quantum ground state of the type (4.14).

Entanglement Entropy between the atomic species. We give the mathematical definition of the kind of entanglement investigated in this section and illustrated in Figure 4.16. Let us consider the system ground state, $|\psi_0\rangle$ and let us choose, as a basis, the set $|n_1, n_2, N - n_1 - n_2, m_1, m_2, M - m_1 - m_2\rangle$ [notice that, for the sake of clarity, N (M) indicates the total number of bosons of species a (b)]. It is therefore possible to expand $|\psi_0\rangle$ with respect to this basis:

$$|\psi_0\rangle = \sum_{i=0}^{N} \sum_{j=0}^{N-i} \sum_{k=0}^{M} \sum_{l=0}^{M-k} C_{i,j,k,l}\, |i, j, N - i - j, k, l, M - k - l\rangle$$

where

$$C_{i,j,k,l} = \langle i, j, N - i - j, k, l, M - k - l|\psi_0\rangle.$$

As a consequence, the density matrix associated to the system ground state reads:

$$\hat{\rho}_0 = |\psi_0\rangle\langle\psi_0| =$$

$$= \sum_{i=0}^{N} \sum_{j=0}^{N-i} \sum_{k=0}^{M} \sum_{l=0}^{M-k} \sum_{i'=0}^{N} \sum_{j'=0}^{N-i'} \sum_{k'=0}^{M} \sum_{l'=0}^{M-k'} C_{i,j,k,l}\, C^*_{i',j',k',l'} \cdot$$

$$\cdot |i, j, N - i - j, k, l, M - k - l\rangle\langle i', j', N - i' - j', k', l', M - k' - l'|.$$

This is the density matrix of a *pure state* and so one can check that it is Hermitian, it has unitary trace, it is equal to its square, and its eigenvalues are all zero except for one which is 1.

A possible and quite natural way to sub-divide the system into two partitions leads to consider the entanglement between the two condensed species. The basis relevant to the sub-system “species A" is $\{|n_1, n_2, N - n_1 - n_2\rangle\}$ while the basis relevant to the sub-system “species B" is $\{|m_1, m_2, M - m_1 - m_2\rangle\}$. It is possible to compute the reduced density matrix relevant to the “species A" by tracing out the degrees of freedom relevant to “species B"

$$\hat{\rho}_{0,a} = \mathrm{Tr}_b\,(\hat{\rho}_0) = \sum_{p=0}^{M} \sum_{q=0}^{M-p} \langle p, q, M-p-q|\; \hat{\rho}_0\; |p, q, M-p-q\rangle = \tag{4.16}$$

$$= \sum_{i=0}^{N} \sum_{j=0}^{N-i} \sum_{i'=0}^{N} \sum_{j'=0}^{N-i'} M_{i,j,i',j'} |i, j, N-i-j\rangle\; \langle i', j', N-i'-j'|$$

where

$$M_{i,j,i',j'} = \sum_{k=0}^{M} \sum_{l=0}^{M-k} C_{i,j,k,l}\, C^*_{i',j',k,l}.$$

This is the reduced density matrix of a *mixed state*, whose Von Neumann entropy

$$EE = -\mathrm{Tr}(\hat{\rho}_{0,a}\, \log_2 \hat{\rho}_{0,a}) = -\sum_{j=0} \lambda_j\, \log_2 \lambda_j \tag{4.17}$$

(where $\lambda_j' s$ are the eigenvalues of $\hat{\rho}_{0,a}$) corresponds to the EE between the two parts of the global system.

4.6 Conclusions

In this Chapter, we have investigated the miscibility properties of a (possibly asymmetric) bosonic binary mixture loaded in a three-well potential (ring trimer). The fragmented character of the confining potential, together with the competition between inter- and intraspecies repulsions, in fact, give rise to a rich mixing-demixing phase diagram. The latter is spanned by two effective variables, $\alpha = W/\sqrt{U_a U_b}$, which accounts for the ratio between inter- and intraspecies repulsions, and $\beta = N_b/N_a\sqrt{U_b/U_a}$, which incorporates the asymmetry between the two species. Each phase features a specific functional dependence of the internal energy and of the entropy of mixing (an indicator imported from Statistical Thermodynamics and devised for quantifying the degree of mixing) on α and β.

To closely match the experimental conditions available within the setup engineered by the Hannover group, our analysis has been extended also beyond the pointlike approximation of potential wells (an approximation which is inherently present both in the second-quantized Bose-Hubbard model and in its continuous variable picture). We therefore employed two coupled Gross-Pitaevskii equations, where the confining-potential term V_{ext} represents the array of three Gaussian traps implementing the ring-trimer potential and where all model parameters are referred to the experimentally available mixture of sodium and potassium. The resulting mean-field analysis, based on the study of the minimum-energy solutions of the Gross-Pitaevskii equations, confirms the rich scenario of mixing-demixing transitions exhibited by the mixture and also constitutes an effective springboard towards a viable experimental realization.

Eventually, in the twin-species case (a circumstance implying $\beta = 1$), we develop a fully quantum analysis, showing that a number of genuinely quantum indicators (e.g. the energy spectrum, the bipartite Von Neumann Entanglement Entropy and the ground state tomography) witness the occurrence of critical phenomena even when a limited number of particles (e.g. $N = 15$) is present in the system.

Chapter 5

Phase separation can be stronger than chaos

5.1 Introduction

In this Chapter[1], we focus on the dynamical properties of a bosonic binary mixture loaded in a ring trimer, with particular reference to the persistence of demixing. The degree of spatial phase separation of the two quantum fluids is monitored by means of the Entropy of Mixing, an indicator borrowed from Statistical Thermodynamics and already introduced in Chapter 4. After mapping the original quantum model into a suitable set of discrete nonlinear Schrödinger equations, we identify three classes of demixed stationary configurations (which are *not* necessarily minimum-energy states). Their energetic and linear stability are carefully analyzed and extended sets of trajectories originating in the vicinity of these fixed points are explicitly simulated. Interestingly, we find both *regular* and *chaotic* dynamical regimes, i.e. regimes where the first Lyapunov exponent [223, 224] is bigger than zero. Chaos is shown to arise according to three different mechanisms, involving the *commensurability* of certain characteristic frequencies, the *size* of regular islands, and the presence of *unstable* fixed points. By analyzing many trajectories in phase space and by monitoring the time evolution of the Entropy of Mixing, we show that chaos could not able to disrupt the order imposed

---

[1] Note to the reader: part of the content of this Chapter has been published in [207, 214].

by phase separation, i.e. boson populations, despite evolving in a chaotic fashion, do not mix. This circumstance is explained either with energetic considerations (mixed states lie outside the constant-energy hypersurface determined by the initial condition) or in terms of dynamical restrictions (mixed states do lie on the constant-energy hypersurface determined by the initial condition, but their are encapsulated by regular islands where the chaotic trajectory cannot penetrate). The analysis developed in this Chapter is thus meant to go beyond the one developed in Chapter 4 (which was restricted to ground-state configurations) as it aims at clarifying the miscibility properties of excited states and the dynamical robustness of spatial phase separation.

5.2 A binary mixture in a ring trimer

As already discussed in Chapter 4 (see formula 4.1), the second-quantized Hamiltonian describing a bosonic mixture of two atomic species in a three-well potential (with periodic boundary conditions) is

$$\begin{aligned} \hat{H} = -T_a \sum_{j=1}^{3} \left(\hat{a}_{j+1}^\dagger \hat{a}_j + \hat{a}_j^\dagger \hat{a}_{j+1} \right) + \frac{U_a}{2} \sum_{j=1}^{3} \hat{n}_j (\hat{n}_j - 1) \\ -T_b \sum_{j=1}^{3} \left(\hat{b}_{j+1}^\dagger \hat{b}_j + \hat{b}_j^\dagger \hat{b}_{j+1} \right) + \frac{U_b}{2} \sum_{j=1}^{3} \hat{m}_j (\hat{m}_j - 1) \\ + W \sum_{j=1}^{3} \hat{n}_j \, \hat{m}_j \end{aligned} \tag{5.1}$$

where $j = 4 \equiv 1$ due to the ring geometry. This is a typical Bose-Hubbard Hamiltonian, where T_a and T_b are the tunnelling amplitudes, U_a and U_b represent *intra*-species repulsive interactions and W corresponds to the *inter*-species repulsion. Creation and destruction operators satisfy usual bosonic commutators, namely $[\hat{a}_i, \hat{a}_j^\dagger] = [\hat{b}_i, \hat{b}_j^\dagger] = \delta_{i,j}$ and $[\hat{a}_i, \hat{b}_j] = [\hat{a}_i, \hat{b}_j^\dagger] = 0$. $\hat{n}_j = \hat{a}_j^\dagger \hat{a}_j$ and $\hat{m}_j = \hat{b}_j^\dagger \hat{b}_j$ are number operators and their sums, $\hat{N} = \sum_{j=1}^{3} \hat{n}_j$ and $\hat{M} = \sum_{j=1}^{3} \hat{m}_j$ respectively, constitute two independent conserved quantities, being $[\hat{N}, \hat{H}] = [\hat{M}, \hat{H}] = 0$. Provided that the number of bosons is sufficiently high [225], it is possible to replace field operators in Hamiltonian (5.1) with local order parameters, [226, 227]. Such substitutions, which explicitly read

$$\hat{a}_j \quad \to \quad a_j, \qquad \hat{b}_j \quad \to \quad b_j,$$

allow one to cast the quantum dynamics generated by Hamiltonian (5.1) in a classical form, that is

$$i\hbar\dot{a}_j = -T_a(a_{j-1} + a_{j+1}) + a_j\left(U_a|a_j|^2 + W|b_j|^2\right)$$

$$i\hbar\dot{b}_j = -T_b(b_{j-1} + b_{j+1}) + b_j\left(U_b|b_j|^2 + W|a_j|^2\right).$$

It is convenient to express local order parameters in terms of number of bosons and local phase [198, 225], i.e. $a_j = \sqrt{n_j}e^{i\phi_j}$ and $b_j = \sqrt{m_j}e^{i\psi_j}$. One thus obtain the following classical Hamiltonian

$$\begin{aligned} H = -2T_a\left(\sqrt{n_2 n_1}\cos(\phi_2-\phi_1) + \sqrt{n_3 n_2}\cos(\phi_3-\phi_2) + \sqrt{n_1 n_3}\cos(\phi_1-\phi_3)\right) \\ -2T_b\left(\sqrt{m_2 m_1}\cos(\psi_2-\psi_1) + \sqrt{m_3 m_2}\cos(\psi_3-\psi_2) + \sqrt{m_1 m_3}\cos(\psi_1-\psi_3)\right) \\ +\frac{U_a}{2}\left(n_1^2+n_2^2+n_3^2\right) + \frac{U_b}{2}\left(m_1^2+m_2^2+m_3^2\right) \\ + W(n_1 m_1 + n_2 m_2 + n_3 m_3) \end{aligned} \tag{5.2}$$

which, in turn, after setting $\hbar = 1$, entails the following motion equations

$$\dot{\phi}_j = \frac{\partial H}{\partial n_j}, \qquad \dot{n}_j = -\frac{\partial H}{\partial \phi_j}, \tag{5.3}$$

$$\dot{\psi}_j = \frac{\partial H}{\partial m_j}, \qquad \dot{m}_j = -\frac{\partial H}{\partial \psi_j}. \tag{5.4}$$

because of the canonical structure $\{\phi_j, n_j\} = \delta_{i,j}$ and $\{\psi_j, m_j\} = \delta_{i,j}$.

5.3 Notable demixed stationary configurations

The exhaustive study of all possible stationary configurations (i.e. configurations having a trivial time dependence) which the system admits goes beyond the scope of this study, as the scenario is extraordinarily branched and rich. Already with a single condensed species confined in a ring trimer, several classes of stationary states (e.g. vortex, π and dimerlike states) have been evidenced [228].

In this study, we put the focus onto the miscibility properties of the two condensed species, and we start our analysis from some notable stationary configurations which feature phase separation. According to the theory of discrete nonlinear Schrödinger equations [162], substitutions $\phi_j \to \Phi_j + \lambda_a t$ and $\psi_j \to \Psi_j + \lambda_b t$, where λ_a and λ_b represent collective angular frequencies of condensates' phases, constitute a preliminary step in the search for stationary configurations [the presence of two independent collective frequencies λ_a and λ_b, follows from the density-density form of the interspecies interaction of Hamiltonian (5.1)]. These substitutions, in fact, allow one to recast Hamilton equations (5.3) and (5.4) into the following dynamical system

$$\begin{cases} \begin{gathered} \dot{\Phi}_j = U_a n_j + W m_j - \lambda_a + \\ -T_a\left[\sqrt{\frac{n_{j-1}}{n_j}}\cos(\Phi_{j-1}-\Phi_j) + \sqrt{\frac{n_{j+1}}{n_j}}\cos(\Phi_{j+1}-\Phi_j)\right] \end{gathered} \\ \\ \begin{gathered} \dot{\Psi}_j = U_b m_j + W n_j - \lambda_b + \\ -T_b\left[\sqrt{\frac{m_{j-1}}{m_j}}\cos(\Psi_{j-1}-\Psi_j) + \sqrt{\frac{m_{j+1}}{m_j}}\cos(\Psi_{j+1}-\Psi_j)\right] \end{gathered} \\ \\ \dot{n}_j = 2T_a\left[\sqrt{n_{j-1}n_j}\sin(\Phi_{j-1}-\Phi_j) + \sqrt{n_j n_{j+1}}\sin(\Phi_{j+1}-\Phi_j)\right] \\ \\ \dot{m}_j = 2T_b\left[\sqrt{m_{j-1}m_j}\sin(\Psi_{j-1}-\Psi_j) + \sqrt{m_j m_{j+1}}\sin(\Psi_{j+1}-\Psi_j)\right] \end{cases} \tag{5.5}$$

with $j = 1,2,3$. Looking for fixed points (FPs) of the latter [which therefore correspond to stationary solutions of equations (5.3) and (5.4)], together with the two constraints $\sum_{j=1}^{3} n_j = N$ and $\sum_{j=1}^{3} m_j = M$, one finds three classes of configurations which, in the limit $T_a, T_b \to 0$, feature perfect demixing (meaning that the presence of a condensate in a well implies the absence of the other condensate in the same well). They are schematically illustrated in Figure 5.1 (upper row) and described below:

1. *Dimer - Soliton:* Condensate A is equally subdivided in two wells, the phases therein being the same, while the third well contains all the condensate B.

$$\begin{aligned} n_1 &= N/2, \quad & n_2 &= 0, \quad & n_3 &= N/2, \quad & \lambda_a &= NU_a/2, \\ m_1 &= 0, \quad & m_2 &= M, \quad & m_3 &= 0, \quad & \lambda_b &= MU_b. \end{aligned}$$

2. *Single Depleted Well (SDW) - Soliton:* Condensate A is equally subdivided in two wells but, contrary to the previous case, the relative phase $\Phi_3 - \Phi_1$ between such wells is π. The third well contains all the condensate B.

3. *Soliton - Soliton:* One well contains all the condensate A while an other well contains all the condensate B.

$$\begin{aligned} n_1 &= N, \quad n_2 = 0, \quad n_3 = 0, \quad \lambda_a = NU_a, \\ m_1 &= 0, \quad m_2 = M, \quad m_3 = 0, \quad \lambda_b = MU_b. \end{aligned}$$

Upon activation of hopping amplitudes T_a and T_b, FPs slightly deviate from the aforementioned ones, as some bosons move from the macroscopically occupied wells to neighbouring ones. The new scenario of FPs, thus moderately blurred by the presence of non-zero tunnelling processes, is pictorially sketched in the lower row of Figure 5.1 and fully discussed in Appendix E.1.

In the following, we shall assume that the two condensates feature the same dynamical parameters, i.e. $U_a = U_b =: U$, $T_a = T_b =: T$ and $N = M$. Nevertheless, we note in advance that the presence of small deviation $T_a \neq T_b$, $U_a \neq U_b$ and $N \neq M$, from the previous ideal conditions (deviations which could be present in a real experimental setup), have been proved (by means of numerical simulations) not to significantly affect the developed analysis and the dynamical scenario discussed in the following. Both the hopping amplitudes and the interaction strengths depend on the lattice constants and on the scattering length [229], which are tunable parameters of the experimental setups mentioned in the introduction. In particular, interaction strengths can be controlled by means of Feshbach resonances [17, 230].

5.4 Stability of stationary demixed states

Energetic-stability and linear-stability analysis are standard but powerful tools to investigate the qualitative dynamical behaviour of the system in the vicinity of a FP [231, 232]. In view of an experimental realization, the developed analysis plays an important role, since it is impossible to prepare the system in a state which *exactly* coincides to one of the aforementioned stationary configurations.

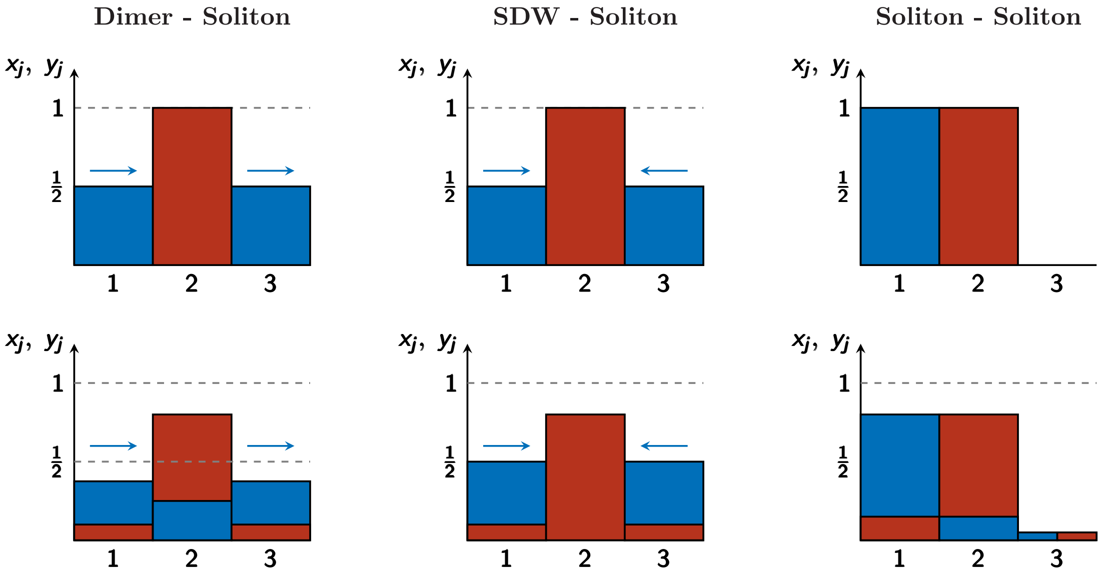

Figure 5.1: The three families of stationary, demixed, configurations for zero (upper row) and non-zero (lower row) hopping amplitudes T_a and T_b. Lower row displays in an exaggerate but illustrative manner the deviations from the zero-tunnelling scenario. Numbers on the horizontal axis correspond to wells' labels, while the height of the histograms represents normalized populations $x_j = n_j/N$ and $y_j = m_j/M$. Parallel (antiparallel) arrows stand for “in-phase" (antiphase) condensates. Wherever not explicitly defined, condensate phases assume different values according to different choices of model parameters (see Appendix E.1).

Preliminary, it is convenient to introduce vector

$$\vec{z} = (\Phi_1,\, \Phi_2,\, \Phi_3,\, \Psi_1,\, \Psi_2,\, \Psi_3,\, n_1,\, n_2,\, n_3,\, m_1,\, m_2,\, m_3)\,,$$

and to write dynamical system (5.5) in the compact form

$$\dot{\vec{z}} = \mathbb{E}\vec{\nabla}\tilde{H} \tag{5.6}$$

where

$$\mathbb{E} = \begin{pmatrix} 0_6 & \mathbb{I}_6 \\ -\mathbb{I}_6 & 0_6 \end{pmatrix}$$

is the standard symplectic matrix,

$$\tilde{H} = H - \lambda_a \sum_{j=1}^{3} n_j - \lambda_b \sum_{j=1}^{3} m_j \tag{5.7}$$

is the effective Hamiltonian and $\vec{\nabla}\tilde{H} = (\partial_{\Phi_1}\tilde{H} \ldots, \partial_{m_3}\tilde{H})$.

5.4.1 Energetic stability

An effective way to determine whether a FP $\vec{z}_*$ is energetically stable or not is to study the signature of the relevant Hessian matrix

$$\mathbb{H}_{i,j}(\vec{z}_*) = \left.\frac{\partial^2 \tilde{H}}{\partial z_i \partial z_j}\right|_{\vec{z}_*} . \tag{5.8}$$

According to Lagrange-Dirichlet Theorem, a FP $\vec{z}_*$ is energetically stable if $\mathbb{H}(\vec{z}_*)$ is positive or negative definite [232] (to be more precise, in the same spirit of [198], one has to exclude the pair of vanishing eigenvalues corresponding to the two conserved quantities or, equivalently, consider a 8×8 Hessian matrix obtained after explicitly introducing constraints $\Phi_1 = \Psi_1 = 0$, $n_1 = N - n_2 - n_3$ and $m_1 = M - m_2 - m_3$). A point exhibiting energetic instability is therefore neither a local minimum nor a local maximum of the energy function $\tilde{H}$ [198]. With reference to the first row of Figure 5.2, one can observe that no FP of the class “SDW - Soliton" is energetically stable, each of them being a multidimensional-saddle point for Hamiltonian function $\tilde{H}$ (see second panel). Interestingly, the energetically-stable region relevant to FPs of the class “Dimer - Soliton" (see first panel) exactly corresponds to the demixed phase (i.e. to one of the three kinds of ground states) that was found and discussed in Section 4.5. In fact, all FPs $\vec{z}_*$ in such region (depicted in green) are indeed global minima of function $\tilde{H}$ or, in other words, ground states of Hamiltonian (5.1). Eventually, observing the third panel, one can recognize the presence of an energetically-stable region for moderately low values of W/U (depicted in blue). In this region, FPs $\vec{z}_*$ are local maxima of function $\tilde{H}$. White regions in Figure 5.2 correspond to those values of W/U and $T/(UN)$ for which FPs belonging to a given class do not exist. Such regions stand in between different sub-classes which differ in the relative phases $\Phi_j - \Phi_{j-1}$ between the wells. Each sub-class is a portion of parameters' space where stationary configurations share common features (e.g.

the relative phases) and which are delimited by white regions. Fox example, the first class includes three sub-classes which, in turn, include points 1A, 1B and 1C respectively.

5.4.2 Linear stability

The linear stability (also called dynamical stability [198]) of a FP $\vec{z}_*$ of motion equations (5.6), (i.e. a configuration such that $\dot{\vec{z}}_* = 0$) is determined by the eigenvalues of Jacobian matrix [231]

$$\mathbb{J}_{i,j}(\vec{z}_*) = \left. \frac{\partial \dot{z}_i}{\partial z_j} \right|_{\vec{z}_*} . \tag{5.9}$$

More precisely, as dynamical system (5.6) is a Hamiltonian one, a FP $\vec{z}_*$ is said to be linearly stable (or elliptic) if all eigenvalues of $\mathbb{J}_{i,j}(\vec{z}_*)$ are purely imaginary; conversely, it is said to be linearly unstable if at least one (pair of) eigenvalues of matrix (5.9) has non-zero real part. In the second row of Figure 5.2, obtained by sweeping model parameters W/U and $T/(UN)$, we have represented, for each of the three classes of stationary points characterized by demixing, the largest real part among the eigenvalues of matrix (5.9). One can notice wide regions of the parameters' space where FPs of the class "Dimer - Soliton" are linearly stable (represented in dark blue). Interestingly, while in the first sub-class (the one including point 1A), all FPs are linearly stable, in the remaining two sub-classes (respectively including points 1B and 1C) there are regions featuring linear stability and regions featuring linear instability. FPs of the class "SDW - Soliton" (see second panel), are mostly linearly unstable, excepts for a tiny triangular-like region existing only for $W/U > 2$ (notice that FPs obtained in the unphysical situation $T = 0$ are linearly stable too). As shown in the third panel, the vast majority of FPs belonging to the class "Soliton - Soliton" are linearly stable, except for those ones in a narrow band confining with the white region and those ones in a needle-like region present for $W/U \approx 2$ and moderately high values of $T/(UN)$.

5.4.3 Scope of the energetic- and the linear-stability analysis

If a trajectory moves away from a FP, the energetic- and the linear-stability analysis thereof are of little use. For this reason, one should employ other indicators such as the first Lyapunov exponent, which is the gold standard to distinguish regular and chaotic trajectories. A further limitation affecting the energetic- and the linear-stability analysis comes from their *local* character. More specifically, also in view of an experimental realization, one should pay particular attention to the *size* of the FP's neighborhood where they are valid. Both aspects are discussed in Section 5.5.

An important remark is in order concerning the traditional criterion to evaluate the linear stability of a FP (i.e. all eigenvalues λ_j's of matrix (5.9) must be purely imaginary). Interestingly, the latter fails when the characteristic frequencies $\omega_j = \mathcal{I}\{\lambda_j\}$ satisfy a certain *commensurability condition*, essentially represented by a Diophantine equation (see [232] for details, in particular for the procedure which is used to determine their sign). In this case, in fact, a so-called "elliptic" FP ceases to be the center of an elliptic island and turns unstable. More specifically, it has been proven by Moser [232] that, if the initial configuration $\vec{z}(t=0) =: \vec{z}_0$ is sufficiently close to a linearly stable FP $\vec{z}_*$, solutions of the actual non linear system (5.6) *almost always* depart from those of the linearized one only extremely slowly, if at all. Nevertheless, this is true only if characteristic frequencies ω_j's, properly taken with a certain sign, do not satisfy the aforementioned commensurability condition. The frequency vectors $\vec{\omega}$ which satisfy such condition constitute a dense set, although of measure zero, excepts in the positive ($\omega_j > 0\ \forall j$) and negative ($\omega_j < 0\ \forall j$) quadrants of space $\vec{\omega}$. These two quadrants exactly corresponds to the regions where energetic stability holds.

5.5 Regular and chaotic oscillations of boson populations

For each of the 102729 pairs of model parameters $(W/U, T/(UN))$, a starting point $\vec{z}_0$ very close to the relevant FP $\vec{z}_*$ is chosen in such a way that the relative difference between the vector components of $\vec{z}_0$ and the corresponding ones of $\vec{z}_*$

is from 2% to 5% thus emulating what could be achieved in a real experimental set up [105, 190, 233, 234]. Then motion equations (5.6) are numerically solved [216] for a series of consecutive time intervals and the first Lyapunov exponent is iteratively computed according to the standard scheme described in [223]. The comparison between the results (see third row of Figure 5.2) and the previously discussed linear-stability analysis (see second row of Figure 5.2) indeed shows that if a FP $\vec{z}_*$ is linearly unstable, than a trajectory starting from a point $\vec{z}_0$ close to it is chaotic, i.e. it is associated to a non-zero Lyapunov exponent. Note to the reader: in the following, labels 1A,...,3C are indistinctly used to indicate both a FP or a trajectory starting in a neighborhood thereof. Likewise, the vast majority of FPs featuring linear stability is such that the trajectory originating from a point $\vec{z}_0$ close to it is regular. Actually, for a limited number of FPs this is not true. For example, with reference to the central column of 5.2, the tiny linearly stable region present in the second row has no counterpart in the third row, all the trajectories therein represented being chaotic. This circumstance can be interpreted in terms of *size* of the elliptic islands centered around an elliptic FP. As already evidenced in Figure 7 of reference [228], such elliptic islands are very small when their center is a FP of the class “SDW - Soliton" and so the distance $|\vec{z}_0 - \vec{z}_*|$, despite chosen to be small, is already greater than the islands' characteristic radius. Moreover, it is worth noticing the presence of curved lines featuring a large Lyapunov exponent [e.g., in the first panel of the third row of Figure 5.2, the curve whose bounds are points (0.5,0.075) and (2,0) in parameters' space $(W/U, T/(UN))$] which are expected to correspond to linearly stable FPs (see first panel of the second row). The seed of chaotic behavior is, in this case, the commensurability of characteristic frequencies ω_j's, which are the imaginary parts of the eigenvalues of Jacobian (5.9) (see [232] for details, in particular for the procedure which is used to determine their sign). In fact, one can verify that all FPs constituting the aforementioned curve are such that $\omega_1 = -2\omega_2$.

5.6 How to quantify mixing and demixing of boson populations

Looking at the first row of Figure 5.1, one can recognize that the three presented configurations feature perfect demixing, as the presence of a condensed species in a certain well always implies the *complete* absence of the other species. In the second row of the same figure, where the aforementioned ideal configurations are blurred by the activation of tunnelling processes, the two species, despite being still overall separated, feature a small degree of mixing. In fact, in whichever well a certain species is macroscopically present, the other one is *nearly* absent, yet non zero. In the following we will make use of the same indicator presented in Chapter 4, the Entropy of Mixing,

$$S_{mix} = -\frac{1}{2}\sum_{j=1}^{3}\left(x_j \log\frac{x_j}{x_j+y_j} + y_j \log\frac{y_j}{x_j+y_j}\right), \qquad \text{where} \quad x_j = \frac{n_j}{N}, \quad y_j = \frac{m_j}{M}, \tag{5.10}$$

whose role is to *quantify* the degree of separation or, to be more precise, the degree of mixing of the two atomic species (see also Appendix C for its detailed mathematical justification). As already discussed in the previous Chapter, the Entropy of Mixing is a standard indicator commonly used in Statistical Thermodynamics when investigating miscibility properties of chemical compounds [168, 235, 236] whose role, in the present work, is played by quantum gases.

From the definition itself of S_{mix}, two important properties, which serve to highlight the lower and the upper bounds of this indicator, emerge: i) The entropy of mixing of any perfectly demixed configuration, as the ones depicted in the upper row of Figure 5.1, is zero; ii) The entropy of mixing of a uniform configuration (i.e. any configuration $\vec{z}_{un}$ such that $n_j = m_j = N/3$, for $j = 1,2,3$) features the maximum possible entropy of mixing, which reads

$$S_{mix}(\vec{z}_{un}) = \log 2 \approx 0.6931. \tag{5.11}$$

In passing, we observe that the relative phases between the wells play no role in the computation of S_{mix}, but are crucial for its time evolution. The fourth row of Figure 5.2 shows the value of the entropy of mixing for all FPs belonging to the three classes discussed in Section 5.3. As expected, we observe that S_{mix} steadily increases with $T/(UN)$, since a bigger hopping amplitude blurs the fully demixed configurations depicted in the upper row of Figure 5.1. Contrary to expectations, there are regions where S_{mix} increases for increasing inter-species repulsion W/U (to be more specific, the region featuring $1 < W/U < 2$ in the first panel, the region for $0 < W/U < 2$ in the second panel and the region featuring $0 < W/U < 1$ in the third panel). This circumstance looks counter intuitive, but it is easily explained by recalling that FPs are not necessarily minimum-energy configurations. As illustrated in the second row of Figure 5.2 and discussed in Section 5.4.1, in fact, a FP can also be a local maximum or a saddle point for effective Hamiltonian (5.7). In the third panel, moreover, we observe that there are values of W/U and $T/(UN)$ for which S_{mix} tends to the maximum value $\log 2$. This happens because FPs of the class “Soliton - Soliton" have been so blurred by the activation of the hopping amplitude T, that they have almost lost their identifying aspect and turned into a uniform configurations of the type $\vec{z}_{un}$ (as shown in Figure E.3, notice that the stationary configuration continuously varies with respect to model parameters W/U and $T/(UN)$).

5.7 Competition between phase separation and chaotic behaviour

In the same spirit of Section 5.5, we have numerically solved motion equations (5.6) choosing, for each parameters' pair $(W/U, T/(UN))$, a starting point $\vec{z}_0$ close to the corresponding FP $\vec{z}_*$. The choice has been made in such a way that the difference between the vector components of $\vec{z}_*$ and those of $\vec{z}_0$ is from 2% to 5%. The knowledge of the time evolution of boson populations $n_j(t)$ and $m_j(t)$ allows one to readily compute $S_{mix}(t)$ and so to monitor the mixing properties of the atomic species.

If the initial configuration $\vec{z}_0$ lies within a regular island centered around a linearly stable FP $\vec{z}_*$ (and the characteristic frequencies thereof do not match Moser's commensurability condition [232]), the motion consists in small oscillations around $\vec{z}_*$. Therefore, the entropy of mixing $S_{mix}(t)$ features small oscillations around the constant values $S_{mix}(\vec{z}_*)$ which, in turn, is very low for the vast majority of FPs $\vec{z}_*$ belonging to the three classes of notable stationary demixed configurations under

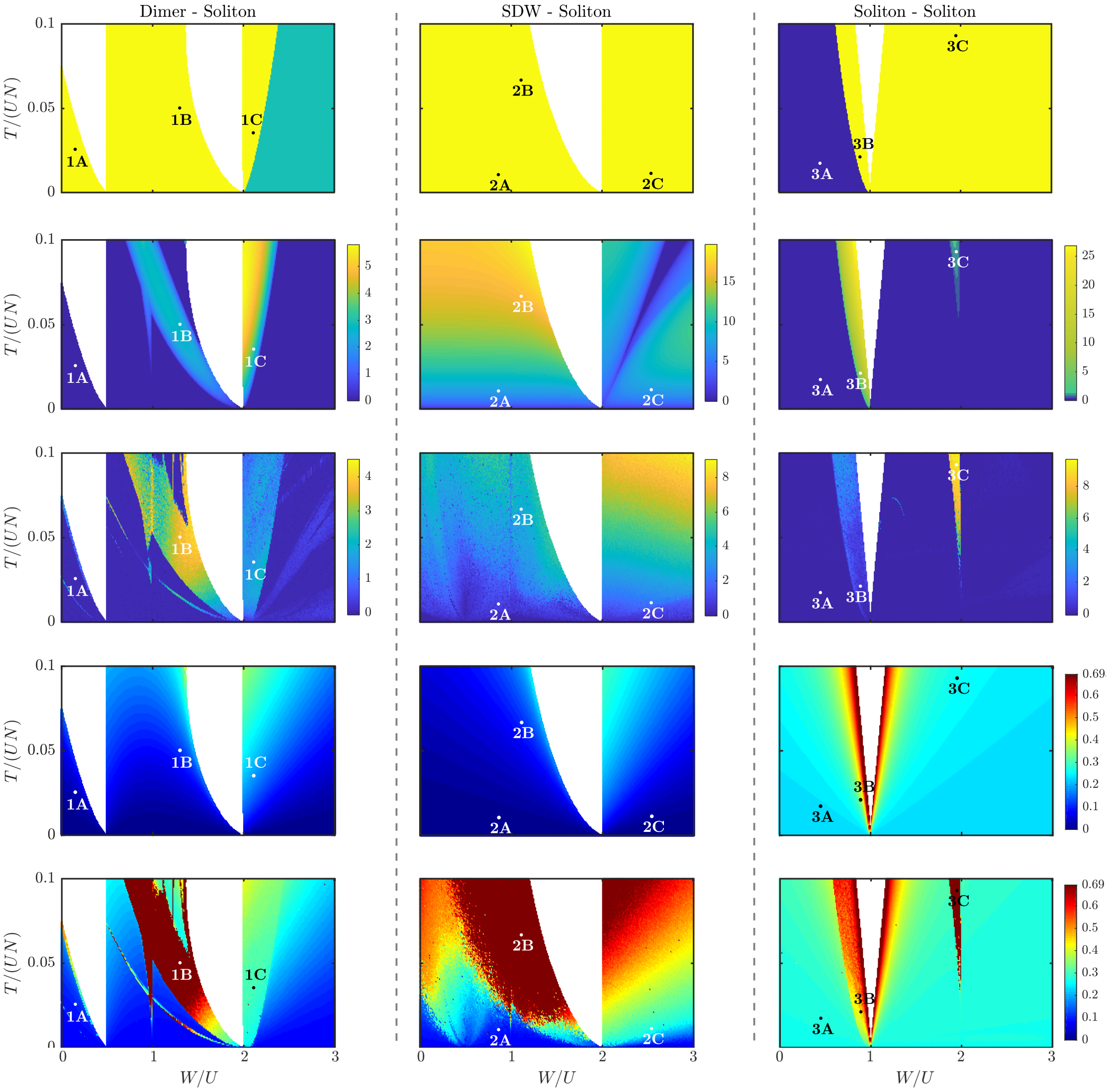

Figure 5.2: **First row**: Energetic-stability analysis of FPs $\vec{z}_*$. Green and blue correspond to energetically stable regions, as they represent, respectively, minima and maxima of Hamiltonian (5.7). Yellow refers to energetically unstable regions, i.e. to saddle points of Hamiltonian (5.7). **Second row:** Linear-stability analysis of FPs $\vec{z}_*$. The color corresponds to $\max_j\{\mathcal{R}\{\lambda_j\}\}$ where λ_j's are the eigenvalues of matrix (5.9). Dark blue represents linearly stable FPs. **Third row:** First Lyapunov exponent associated to trajectories starting close to FPs $\vec{z}_*$. Dark blue (yellow) corresponds to regular motions (highly chaotic trajectories). **Fourth row:** FPs' entropy of mixing, i.e. $S_{mix}(\vec{z}_*)$. Blue (red) represents a remarkable phase separation (an high degree of mixing). **Fifth row:** Maximum entropy of mixing, i.e. $\max_{0<t<50}\{S_{mix}(t)\}$ relevant to trajectories starting close to FPs $\vec{z}_*$. Blue corresponds to trajectories which feature a very small degree of mixing S_{mix} throughout all the simulated dynamics. Conversely, red is associated to trajectories which, one or more times during the time evolution, feature complete mixing. **All panels:** White regions correspond to model parameters W/U and $T/(UN)$ for which no stationary solutions of the type defined in the column's title exist. In each panel, three points have been highlighted in order to facilitate the discussion. Model parameters $N = 50$ and $U = 1$ have been chosen.

considerations (recall the fourth row of Figure 5.2). On the other hand, if $\vec{z}_0$ lies outside regular islands, the motion is chaotic, as discussed in Section 5.5. In these circumstances, one would expect the two condensed species to fully mix and thus to quickly loose memory of their initial, demixed character. We show that this is not always the case, as demixing and chaos can coexist indeed. To this purpose, for each simulated trajectory, we have recorded $\max_t\{S_{mix}(t)\}$, where t ranges from $t = 0s$ to $t = 50s$, a time interval whose width is three orders of magnitudes larger than the smallest characteristic period of populations' oscillations. Overall, 102729 trajectories have been simulated, each one starting from an initial condition $\vec{z}_0$ which, in turn, is close to a FP $\vec{z}_*$. The result is shown in the fifth row of Figure 5.2.

In the attempt to facilitate the comparison among the info provided by the linear-stability analysis (second row of Figure 5.2), by the computation of the first Lyapunov exponent (third row), by the evaluation of $S_{mix}(\vec{z}_*)$ (fourth row) and of $\max_t\{S_{mix}(t)\}$ (fifth row), we highlight and analyze some notable dynamical regimes and we explicitly illustrate them in Figures 5.3-5.5. We group them according to the regularity of the motion and to the persistence of demixing during the dynamics. We remind that labels 1A,...,3C are indistinctly used to indicate either a FP or a trajectory starting in a neighborhood thereof.

- *Regular oscillations of demixed species.* The regimes represented in the first column of Figure 5.3 and in the first column of Figure 5.5 are regular, i.e. they feature a vanishing Lyapunov exponent. The initial states ($t = 0$) lie in elliptic islands centered around linearly stable FPs $1A$ and $3A$, respectively (and their characteristic frequencies do not match Moser's commensurability condition [232]). The time evolution of boson populations consists in small oscillations around FPs. As a consequence, $S_{mix}(t)$ slightly oscillates around constant values $S_{mix}(1A) \approx 0.08$ and $S_{mix}(3A) \approx 0.25$ respectively, thus witnessing the persistence of a remarkable demixing.

- *Fully developed mixing.* The regimes illustrated in the second column of Figure 5.3, second column of Figure 5.4 and third column of Figure 5.5 are chaotic, i.e. they are associated to a non-zero Lyapunov exponent. The initial configurations lies in the vicinity of linearly unstable FPs. The onset of chaos completely destroys the original, demixed configurations whose entropies of mixing are approximately equal to the ones relevant to the corresponding FPs, i.e. $S_{mix}(1B) \approx 0.15$, $S_{mix}(2B) \approx 0.13$ and $S_{mix}(3C) \approx 0.23$ respectively. As a consequence, in all three cases, $S_{mix}(t)$ repeatedly reaches the maximum possible value of ≈ 0.69 which, in turn, witnesses the full mixing of the bosonic species.

- *Persistent demixing despite chaos.* The dynamical regimes depicted in the first column of Figure 5.4 and in the second column of Figure 5.5 consist in small chaotic oscillations around the FPs 2A and 3B respectively. Chaos develops because the initial conditions already lie in the chaotic sea which, in turn, has been shown to surround linearly unstable FPs. However, despite the occurrence of chaos, not only the demixing of bosonic species persists, but also the macroscopic structure of the initial configurations remains unchanged during the dynamics. As a consequence, the oscillations of $S_{mix}(t)$ are chaotic but their amplitude is small, namely it never exceeds critical values ≈ 0.10 and ≈ 0.44 respectively.

  The dynamical regimes illustrated in the third column of Figure 5.3 and in the third column of Figure 5.4 are chaotic as well, but much less shrunken. It is a fact that, also in these cases, despite the presence of chaos, the two atomic species feature a low degree of mixing for all the simulated dynamics (in fact $S_{mix}(t)$ remains smaller than ≈ 0.29 and ≈ 0.27 respectively). Nevertheless, contrary to trajectories 2A and 3B (which consist in small chaotic oscillations around the equilibrium points), in these cases, chaos disrupts the structure of the original configurations, repeatedly triggering *populations inversions*. In other words, for what concerns trajectories 1C and 2C, as time goes by, boson populations in each well severely change but always in such a way to preserve the (low) degree of mixing.

Table 5.1 is intended to summarize the aforementioned results.

Interestingly, we observe that the persistence of spatial phase separation marks extended bundles of chaotic trajectories, i.e. chaotic trajectories involving wide patches of starting points and rather extended ranges of model parameters. Such a persistence can be explained either in terms of energy conservation or by recalling the presence of regular islands where chaotic trajectories cannot enter (see Figure 5.6).

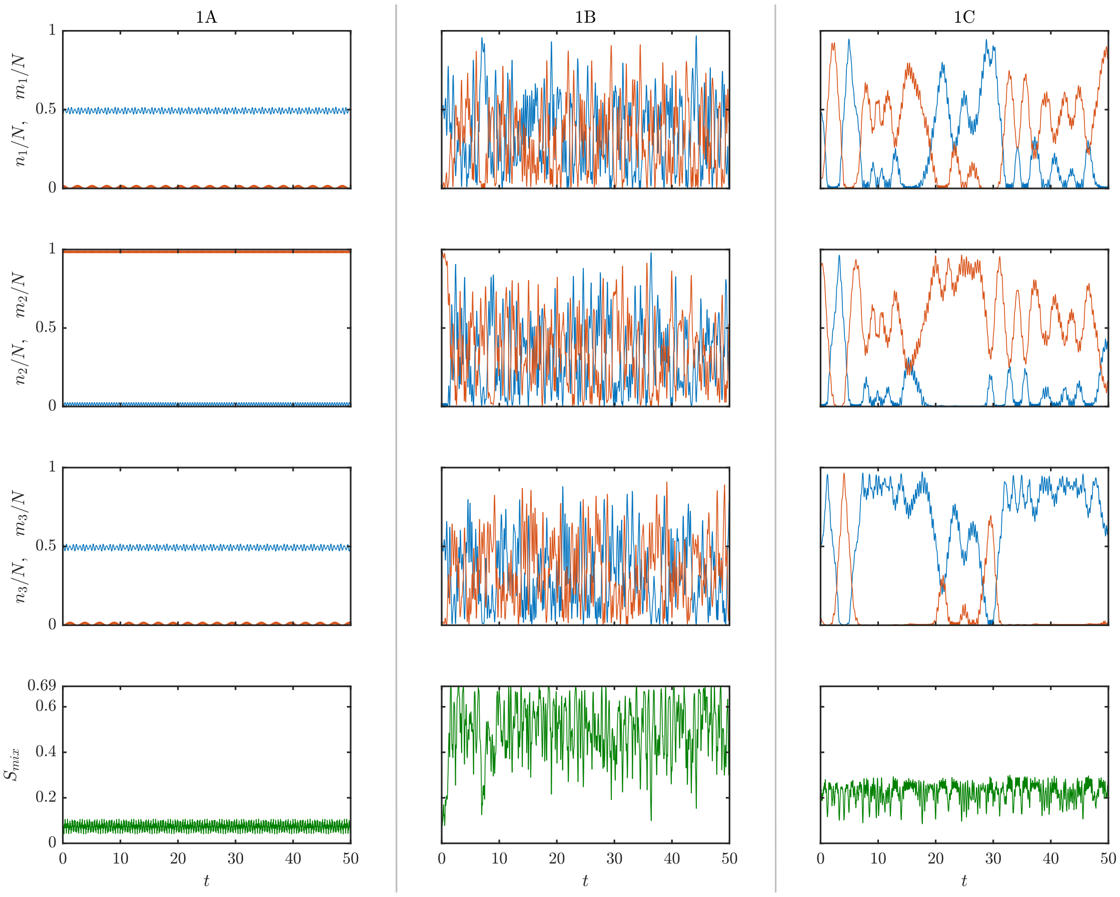

Figure 5.3: Time evolution of normalized boson populations and of entropy of mixing S_{mix}. The results have been obtained numerically solving equations 5.6. Blue (red) denote species-A (B) bosons. Each column corresponds to the dynamics originating from three different starting points $\vec{z}_0$ which, in turn, are chosen in the vicinity of FPs 1A, 1B and 1C respectively.

Concerning the energy-conservation argument, we remind that the choice of a certain $\vec{z}_0$ automatically fixes the trajectory and the constant-energy hypersurface Γ where the trajectory will be confined. Then, we analytically determine the maximum value of the entropy of mixing over the entire Γ, $\bar{S}_{mix}$, and note that the entropy of mixing along the trajectory, $S_{mix}(t)$, will never exceed $\bar{S}_{mix}$ at any time. In other words, (see also Appendix E.3, where we comment on the structure of phase space), the trajectory will wander wide regions of Γ but, if $\bar{S}_{mix}$ is small enough, it will never visit highly-mixed configurations. The values $\bar{S}_{mix}$ are determined over surfaces Γ by maximizing the objective function S_{mix} under the constraints

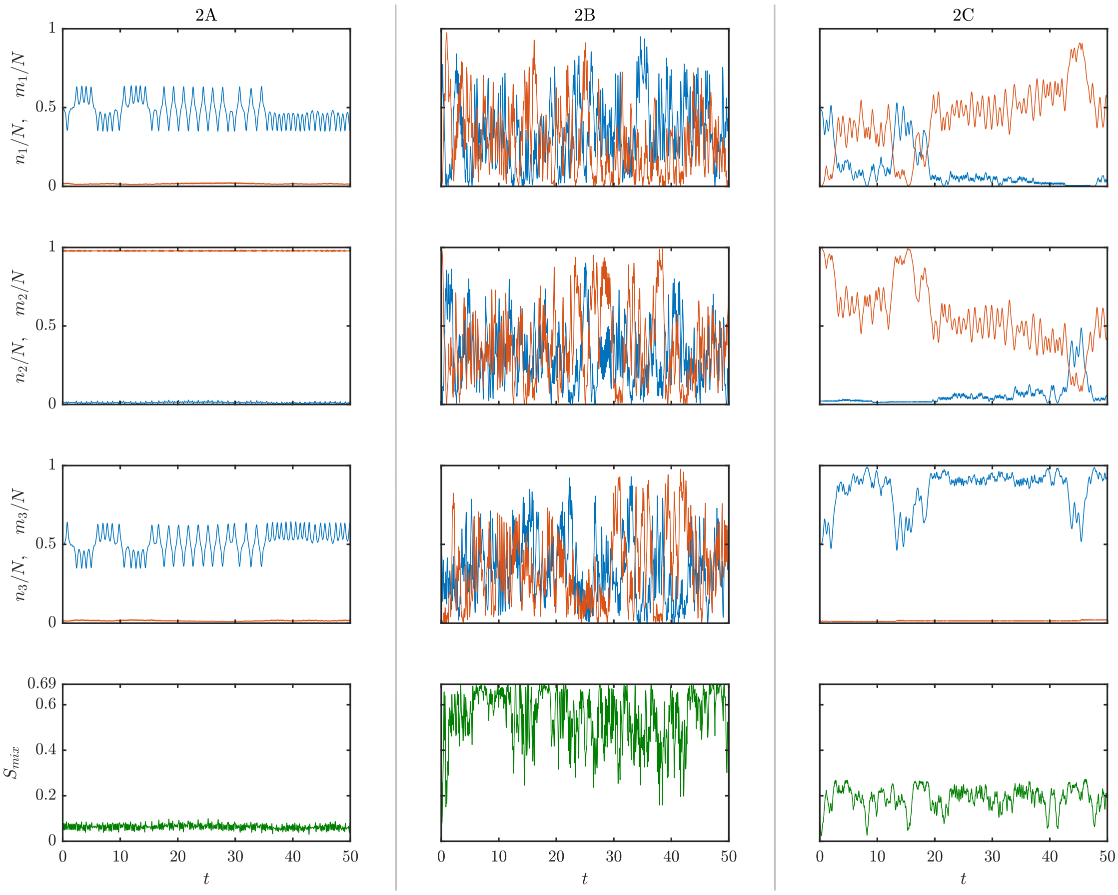

Figure 5.4: Time evolution of normalized boson populations and of entropy of mixing S_{mix}. The results have been obtained numerically solving equations 5.6. Blue (red) denote species-A (B) bosons. Each column corresponds to the dynamics originating from three different starting points $\vec{z}_0$ which, in turn, are chosen in the vicinity of FPs 2A, 2B and 2C respectively.

$\sum_j n_j = N$, $\sum_j m_j = N$ and $H = H(\vec{z}_0)$, for each initial state $\vec{z}_0$. Such computation of $\bar{S}_{mix}$ as a function of model parameters is based on the well-known method of Lagrange multipliers. The result is shown figure 5.7. As an example, compare the green domain around point 1C in Figure 5.7 (witnessing persistent spatial phase phase separation) with the light-blue domain around point 1C in the third row of Figure 5.2 (displaying a manifestly chaotic behaviour). The same reasoning holds also for point 2C.

Concerning the regular-islands argument, the latter is suggested by several examples of trajectories which, despite exhibiting a chaotic behaviour together with

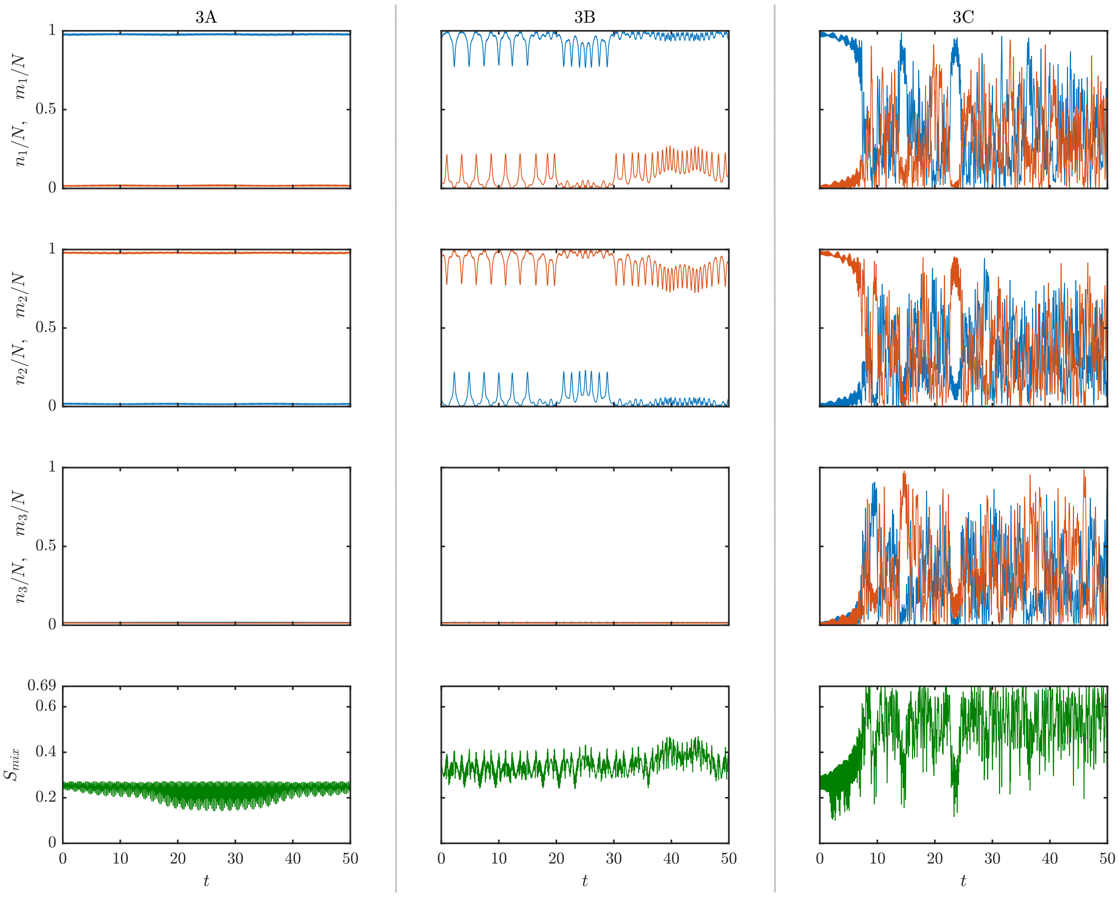

Figure 5.5: Time evolution of normalized boson populations and of entropy of mixing S_{mix}. The results have been obtained numerically solving equations 5.6. Blue (red) denote species-A (B) bosons. Each column corresponds to the dynamics originating from three different starting points $\vec{z}_0$ which, in turn, are chosen in the vicinity of FPs 3A, 3B and 3C respectively.

persistent spatial phase separation, are associated to the maximum possible (i.e. energetically accessible) value of $\bar{S}_{mix} := \max_\Gamma \{S_{mix}\}$. For example, the trajectory 3B is of this type since, as shown in Figure 5.7, the constant-energy hypersurface Γ where it is embedded, features the biggest possible entropy of mixing, $\log 2$ (depicted in dark red). A reasonable interpretation of this apparent mismatch is linked to the possible presence of regular islands on Γ [237] (see also Appendix E.3). If $\bar{S}_{mix}$ lies inside such islands, in fact, chaotic trajectories will never have the chance to visit highly-mixed configurations. This interpretation can be applied also to point 2A. A detailed analysis to ascertain the presence of mixed configurations

	Energetic stability	Linear stability	Chaotic/ regular	Initial demixing	Persistent demixing	Energetically immiscible
1A	✗	✓	Regular	✓	✓	✗
1B	✗	✗	Chaotic	✓	✗	✗
1C	✗	✗	Chaotic	✓	✓	✓
2A	✗	✗	Chaotic	✓	✓	✗
2B	✗	✗	Chaotic	✓	✗	✗
2C	✗	✗	Chaotic	✓	✓	✓
3A	✓	✓	Regular	✓	✓	✓
3B	✗	✗	Chaotic	✓	✓	✗
3C	✗	✗	Chaotic	✓	✗	✗

Table 5.1: Summary of the most important static and dynamical features for each of the nine representative cases.

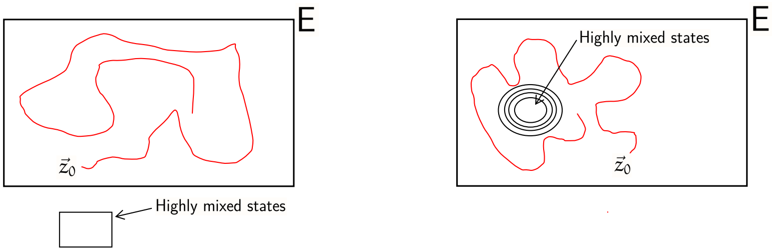

Figure 5.6: Pictorial representation of the two arguments behind the occurrence of persisting demixing in spite of chaos. E represents the constant-energy manifold, $\vec{z}_0$ a generic initial condition. **Left panel:** "energetic argument" - highly mixed states lie outside the constant energy hypersurface and are therefore inaccessible, no matter the degree of chaoticity of the trajectory. **Right panel:** "dynamical argument" - highly mixed states, although being energetically accessible, are encapsulated within regular islands and cannot be visited by chaotic trajectories originating out of them.

inside regular islands requires an extended work that will be developed elsewhere.

5.8 Conclusions

We have investigated the dynamics of a bosonic binary mixture loaded in a three-well potential with periodic boundary conditions, its relation with the entropy of mixing and the robustness of spatial phase separation. In general, the developed analysis, even if focused on some particular classes of configurations, has provided

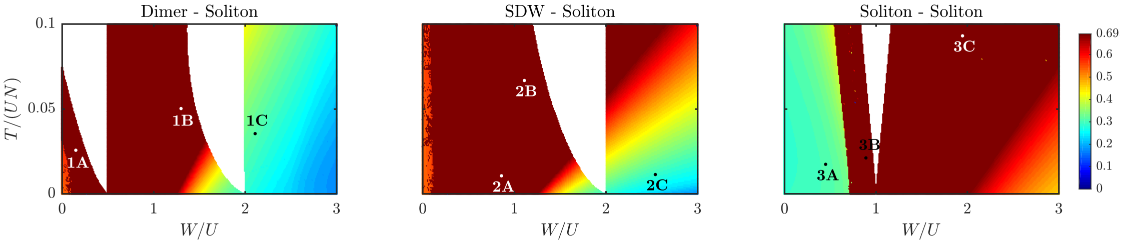

Figure 5.7: Maximum entropy of mixing $\bar{S}_{mix}$ over constant-energy hypersurfaces Γ's which, in turn, are well specified by choosing an initial condition $\vec{z}_0$ and a pair of model parameters $(W/U, T/(UN))$. The maximum value of the entropy of mixing over an hypersurface Γ, $\bar{S}_{mix}$, is computed according to the standard method of Lagrange multipliers, a technique which allows to find the maximum of a certain objective function in presence of one or more constraints. White regions correspond to model parameters W/U and $T/(UN)$ for which no stationary solutions of the type defined in the column's title exist. In each panel, three points have been highlighted in order to facilitate the discussion. Model parameters $N = 50$ and $U = 1$ have been chosen.

a considerable amount of information about dynamical regimes characterized by regular and chaotic behaviours.

In Section 5.2, we have introduced the model describing the mixture in the ring trimer and derived the corresponding semiclassical motion equations. Section 5.3 has been devoted to the presentation of the three notable classes of stationary configurations featuring demixing, "Dimer - Soliton", "SDW - Soliton" and "Soliton - Soliton". In Section 5.4, we have developed the energetic- and the linear-stability analysis of the previously identified stationary configurations, highlighting their scope and limitations. In Section 5.5, we have explicitly computed the first Lyapunov exponent along 102729 trajectories starting in the vicinity of as many FPs thus clearly identifying regular and chaotic regimes. We have observed that chaos can originate in three different ways: 1) When the trajectory starts in the vicinity of a linearly unstable FP; 2) When the trajectory starts in the neighbourhood of an elliptic FP such that its characteristic frequencies match Moser's commensurability condition [232]; 3) When the initial configuration lies outside the regular island centered around a linearly stable FP. In Section 5.6, we have recalled the entropy of mixing S_{mix}, borrowed from Statistical Thermodynamics [168], to quantify and monitor the degree of mixing between the two condensed species.

Eventually, in Section 5.7 we have shown that the chaotic motion of boson populations and demixing can coexist or, in other words, that chaos, despite present, may not be able to completely disrupt the order imposed by phase separation. Such coexistence can occur either because highly mixed states lie in regular islands where the chaotic trajectory cannot penetrate or because the constant-energy hypersurface does not contain mixed states at all.

Chapter 6

Pathway towards the formation of supermixed states in optical lattices

6.1 Introduction

In this Chapter[1], we investigate the mechanism of formation of supermixed soliton-like states in bosonic binary mixtures loaded in ring lattices. We evidence the presence of a common pathway which, irrespective of the number of lattice sites and upon variation of the interspecies attraction, leads the system from a mixed and delocalized phase to a supermixed and localized one, passing through an intermediate phase where the supermixed soliton progressively emerges. The degree of mixing, localization and quantum correlation of the two condensed species, quantified by means of suitable indicators commonly used in Statistical Thermodynamics and Quantum Information Theory, allow one to reconstruct a bi-dimensional mixing-supermixing quantum phase diagram featuring two characteristic critical lines and three different phases. In spite of the large number of parameters characterizing the original quantum model, we show that the phase diagram is spanned by only two effective parameters, incorporating the competition between inter- and intraspecies

---

[1] Note to the reader: part of the content of this Chapter has been published in [238].

repulsions and accounting for the possible asymmetry between the species.

Our analysis is initially developed within a semiclassical framework, capable of capturing the essential features of the phase diagram and the analogies between systems featuring a different number of potential wells. We then develop a fully-quantum approach, which corroborates and validates the sketched scenario. This is done by presenting a number of genuinely quantum indicators, including but not limited to the quantum versions of the Entropy of Mixing and of the Entropy of Location, the Entanglement between the species, the ground-state energy and, more in general, the energetic fingerprint of the mixture in the different quantum phase. This Chapter therefore aims at extending the analysis developed in Chapter 4 to the case of *attractive* interspecies couplings and to the case of a many-site ring lattice. Eventually, we provide a fully-analytic treatment of the energy-level structure in the supermixed phase (the phase where both species tend to occupy the same site). We, in fact, develop a Bogoliubov approximation scheme based on the macroscopic occupation of *site* modes (and therefore conceptually different from the one developed in Chapter 2 which, being referred to the uniform and mixed phase, was based on the macroscopic occupation of *momentum* modes) which well captures the linear dependence of the energy levels on the control parameter.

6.2 The model

6.2.1 The quantum model

Let us consider a two-component bosonic mixture loaded in L-site potentials. As explained in Chapter 2 [see Hamiltonian (2.1)], the genuinely quantum features of such system can be effectively captured by the second-quantized Hamiltonian

$$\begin{aligned} H = -T_a \sum_{j=1}^{L} \left(a_{j+1}^\dagger a_j + a_j^\dagger a_{j+1} \right) + \frac{U_a}{2} \sum_{j=1}^{L} n_j (n_j - 1) \\ -T_b \sum_{j=1}^{L} \left(b_{j+1}^\dagger b_j + b_j^\dagger b_{j+1} \right) + \frac{U_b}{2} \sum_{j=1}^{L} m_j (m_j - 1) \\ + W \sum_{j=1}^{L} n_j \, m_j , \end{aligned} \tag{6.1}$$

an extended version of the well-known Bose-Hubbard model whose last term accounts for the *attractive* interaction between the species. Operator a_i (b_i) destroys a species a (species b) boson in the $i-$th site. Notice that $i \in \{1, \dots, L\}$ and that, for $L > 2$, the trapping potential is assumed to feature a ring geometry, a circumstance which results in the periodic boundary conditions $i = L + 1 \equiv 1$. As a consequence of the bosonic character of the trapped particles, the following commutation relations hold: $[a_i, b_\ell^\dagger] = 0$, $[a_i, a_\ell^\dagger] = [b_i, b_\ell^\dagger] = \delta_{i,\ell}$. The definition of number operators, $n_i = a_i^\dagger a_i$ and $m_i = b_i^\dagger b_i$, allows one to evidence two independent conserved quantities, namely $N_a = \sum_{i=1}^L n_i$ and $N_b = \sum_{i=1}^L m_i$. Concerning model parameters, T_a and T_b represent the tunnelling energy of the two species, $U_a > 0$ and $U_b > 0$ their *intra*-species *repulsive* interactions, and $W < 0$ the *inter*-species *attractive* coupling.

6.2.2 A Continuous-Variable-Picture approach for the detection of different quantum phases

As explained in Chapter 4 speaking of *repulsive* bosonic binary mixtures on a ring trimer, an effective way to determine the ground state structure of multi-mode Bose-Hubbard Hamiltonians consists in approximating the inherently discrete single-site occupation numbers n_j and m_j with continuous variables $x_j = n_j/N_a$ and $y_j = m_j/N_b$ [167, 175, 176, 206, 208, 210]. Provided that the overall boson populations, $N_a = \sum_{j=1}^L n_j$ and $N_b = \sum_{j=1}^L m_j$, are large enough, the application of this approximation scheme (see also Appendix B for a detailed description thereof) to a second-quantized Hamiltonian of the type (6.1) allows one to associate it to the following effective potential

$$V = -2N_a T_a \sum_{j=1}^{L} \sqrt{x_j x_{j+1}} - 2N_b T_b \sum_{j=1}^{L} \sqrt{y_j y_{j+1}}$$
$$+\frac{U_a N_a^2}{2} \sum_{j=1}^{L} x_j (x_j - \epsilon_a) + \frac{U_b N_b^2}{2} \sum_{j=1}^{L} y_j (y_j - \epsilon_b)$$
$$+ W N_a N_b \sum_{j=1}^{L} x_j y_j \tag{6.2}$$

which therefore represents the generalization of effective potential (6.4) to the case of L sites. As explained in Chapter 4, potential V provides a remarkably effective way to investigate the ground state structure of Hamiltonian (6.1) as a function of model parameters. To be more clear, the $2L$-tuples $(\vec{x}, \vec{y})$ which minimize function V on its domain

$$\mathcal{R} = \left\{ (\vec{x}_j, \vec{y}_j) \,:\, 0 \le x_j,\, y_j \le 1, \quad \sum_{j=1}^{L} x_j = \sum_{j=1}^{L} y_j = 1 \right\}$$

correspond to those Fock states $|\vec{n}, \vec{m}\rangle$ featuring the largest weights $|c(\vec{n}, \vec{m})|^2$ in the expansion of the ground state, i.e. in $|\psi_0\rangle = \sum_{\vec{n},\vec{m}}^{Q} c(\vec{n}, \vec{m})|\vec{n},\, \vec{m}\rangle$, where the superscript Q recalls that

$$Q = \frac{(N_a + L - 1)!}{N_a!(L-1)!}\frac{(N_b + L - 1)!}{N_b!(L-1)!} \tag{6.3}$$

is the dimension of the constant-boson-number subspace contained in the Hilbert space of states associated to Hamiltonian (6.1).

The determination of the minimum points of potential V is of particular interest when $T_a/(U_a N_a) \to 0$ and $T_b/(U_b N_b) \to 0$. These limiting conditions, in fact, can be regarded as a thermodynamic limit according to the statistical-mechanical approach discussed in [175, 239] and, when they hold, the different phases of the quantum system (6.1) emerge at their clearest [176, 206]. In this limit, generalized potential (6.2) can be conveniently recast as

$$\mathcal{V} \approx \frac{V}{U_a N_a^2} = \frac{1}{2}\sum_{j=1}^{L} x_j^2 + \frac{\beta^2}{2}\sum_{j=1}^{L} y_j^2 + \alpha\beta\sum_{j=1}^{L} x_j y_j, \tag{6.4}$$

an expressions which generalizes formula (4.3) to the case of L sites which corresponds to a new (rescaled) effective potential which depends only on two effective parameters

$$\alpha = \frac{W}{\sqrt{U_a U_b}}, \qquad \beta = \frac{N_b}{N_a}\sqrt{\frac{U_b}{U_a}}. \tag{6.5}$$

The former constitutes the ratio between the interspecies attractive coupling and the (geometric average of) the intraspecies repulsions, while the latter corresponds to the degree of asymmetry between species a and species b condensates. Notice, in particular, that $\beta \to 1$ in the twin-species scenario, while $\beta \to 0$ when species b represents an impurity with respect to species a. In the following, we will assume $\beta \in [0,1]$ without loss of generality, as one can always swap species labels in order for β to fall in this interval.

Effective model parameters α and β have already proved to be the most natural ones to describe the occurrence of mixing-demixing transitions in ultracold binary mixtures loaded in ring-trimer geometries (see Chapter 4) and, in the present case, constitute the most effective variables to capture the formation of supermixed solitons. Parameters α and β span, in fact, a two-dimensional phase diagram where the various phases included therein correspond to different functional dependencies of the minimum-energy configuration $(\vec{x}_*, \vec{y}_*)$ and of the relevant energy

$$\mathcal{V}_* := \mathcal{V}(\vec{x}_*, \vec{y}_*) := \min_{(\vec{x},\vec{y})\in\mathcal{R}} \mathcal{V}(\vec{x}, \vec{y}) \tag{6.6}$$

on α and β themselves. The presence of different functional dependencies of $\mathcal{V}_*$ on model parameters α and β results in the presence of borders on the (α, β) plane where function $\mathcal{V}_*$ is not analytic, a circumstance which constitutes the signature of quantum phase transitions [240].

The search for the configuration $(\vec{x}_*, \vec{y}_*)$ which minimizes function $\mathcal{V}$ on its closed domain $\mathcal{R}$ can be carried out in a fully analytic way. Nevertheless, the complexity of such analysis increases with increasing lattice size L, not only because the *interior* of region $\mathcal{R}$ gets bigger and bigger but also (and above all) because the *boundary* of $\mathcal{R}$ gets increasingly complex and branched. Indeed, for wide regions of the (α, β) plane, it is on the boundary of $\mathcal{R}$ that $\mathcal{V}_*$ falls, a circumstance which makes its complete exploration necessary [see Appendix B.2 for further details on the systematic analysis of the closed $(2L-2)-$polytope representing the domain $\mathcal{R}$].

6.3 The mixing-supermixing phase diagram

The search for the configuration $(\vec{x}, \vec{y})$ minimizing effective potential (6.4), on its domain $\mathcal{R}$ has been developed according to the fully-analytic scheme sketched in Chapter 4 and thoroughly described in Appendix B.2 for the case of a twin-species mixture on a ring trimer. Interestingly, our analysis has highlighted the presence of a common phase diagram for systems featuring $L = 2$ (dimer), $L = 3$ (trimer) and

$L = 4$ (tetramer). Such a phase diagram is illustrated in Figure 6.1 and includes three phases:

i) Phase M (Mixed) occurs for $\alpha > -1$ and features uniform boson distribution among the L wells and mixing of the two species;

ii) Phase PL (Partially Localized), present for $\alpha < -1$ and $\beta < -1/\alpha$, is such that the minority species, i.e. species b (since $N_b\sqrt{U_b} < N_a\sqrt{U_a}$), conglomerates and forms a soliton, while the majority species, i.e. species a, occupies all available wells, even if not in a uniform way;

iii) Phase SM (SuperMixed) is marked by the presence of a supermixed soliton (and full localization), meaning that both species conglomerate in the same well.

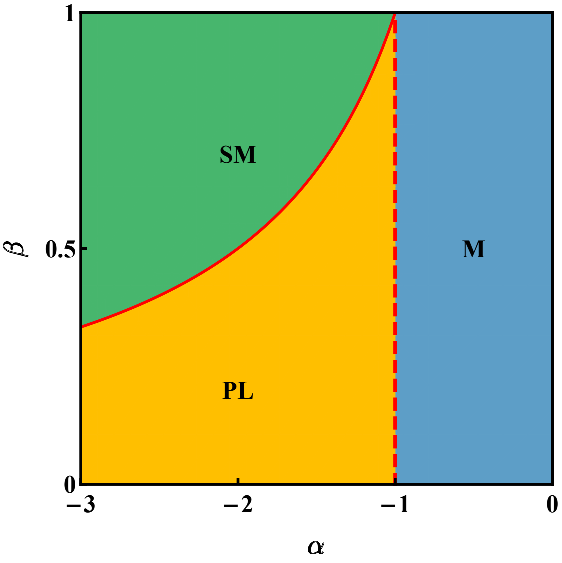

Figure 6.1: Phase diagram of a bosonic binary mixture featuring *attractive* inter-species coupling and confined in a generic $L-$site potential. Each of the three phases is associated to a specific functional dependence of the minimum-energy configuration $(\vec{x}_*, \vec{y}_*)$ and of $\mathcal{V}_*$ [see relations (6.6)] on parameters (6.5). Phase M is the uniform and mixed one, phase PL features a soliton just in the minority species, while phase SM exhibits the presence of a supermixed soliton. Red dashed (solid) line corresponds to a phase transition where the first (second) derivative of $\mathcal{V}_*$ with respect to α is discontinuous.

These three systems therefore feature a common pathway which, upon variation of control parameters α and β, leads from the uniform and mixed configuration (phase M) to the supermixed soliton (phase SM), through the intermediate phase (phase PL), characterized by partial localization, i.e already showing the seed of the soliton, whose emergence, in turn, is due to the localizing effect of the interspecies attraction. For this reason, we conjecture that the mechanism of formation of supermixed solitons is the same regardless of the value of L. To better connote the three presented phases, in Table 6.1 we give the explicit expressions of $(\vec{x}_*, \vec{y}_*)$ as functions of model parameters α and β, together with the relevant value of $\mathcal{V}_*$ [recall relations (6.6)], in each of the three phases. We remark that the results listed in Table 6.1 have been derived in an analytic way [and numerically checked by means of a brute-force minimization of potential (6.4)] for $L = 2$, 3, 4 while it is quite natural to conjecture the validity of these results also for $L \geq 5$. To corroborate our conjecture, it is worth observing that, for any L, $\mathcal{V}_* = \mathcal{V}_*(\alpha, \beta)$ is continuous everywhere in the half-plane $\{(\alpha,\, \beta)\, :\, \alpha \leq 0 \text{ and } 0 \leq \beta \leq 1\}$. In particular, equations

Phase	$(\vec{x}_*, \vec{y}_*)$	$\mathcal{V}_*$
M	$x_{*,j} = 1/L \quad \forall j$ $y_{*,j} = 1/L \quad \forall j$	$\mathcal{V}_*^{\mathrm{M}} = \frac{1}{2L}(\beta^2 + 2\alpha\beta + 1)$
PL	$x_{*,i} = [1-(L-1)\alpha\beta]/L$ $x_{*,j} = [1+\alpha\beta]/L \quad \forall j \neq i$ $y_{*,i} = 1,\ \ y_{*,j} = 0\ \forall j \neq i$	$\mathcal{V}_*^{\mathrm{PL}} = \frac{1}{2L}[1 + 2\alpha\beta$ $+\beta^2(L-(L-1)\alpha^2)]$
SM	$x_{*,i} = 1$ $x_{*,j} = 0 \quad \forall j \neq i$ $y_{*,i} = 1,\ \ y_{*,j} = 0\ \forall j \neq i$	$\mathcal{V}_*^{\mathrm{SM}} = \frac{1}{2}(\beta^2 + 2\alpha\beta + 1)$

Table 6.1: Summary of the different functional dependencies of the minimum-energy configuration and of the relevant value of the effective potential [see relations (6.6)] in each of the three phases.

$$\mathcal{V}_*^{\mathrm{M}}(\alpha = -1, \beta) = \mathcal{V}_*^{\mathrm{PL}}(\alpha = -1, \beta)$$

and

$$\mathcal{V}_*^{\mathrm{PL}}(\alpha, \beta = -1/\alpha) = \mathcal{V}_*^{\mathrm{SM}}(\alpha, \beta = -1/\alpha)$$

hold, respectively, at phase M-PL and phase PL-SM borders. On the other hand, one can easily realize that the *first* derivative $\partial \mathcal{V}_*/\partial \alpha$ is discontinuous at $\alpha = -1$ while the *second* derivative $\partial^2 \mathcal{V}_*/\partial \alpha^2$ is discontinuous at $\beta = -1/\alpha$, regardless of the specific value of L (see the first panel of Figure 6.3). This difference in the non-analyticity properties of $\mathcal{V}_*$ at the two phase boundaries is a direct consequence of the specific functional dependence of $x_{*,j}$'s and $y_{*,j}$'s on model parameters α and β in each of the three phases (see second column of Table 6.1). The minimum energy configuration $(\vec{x}_*, \vec{y}_*)$, in fact, features a jump discontinuity at transition M-PL while it is continuous at transition PL-SM. In this regard, one can notice that $(\vec{x}_*, \vec{y}_*)$ exhibits the same Z_L symmetry of the trapping potential just in phase M. By making the control parameter α more negative, one crosses the M-PL border and such symmetry *suddenly* breaks. A soliton starts to emerge in a certain well, although the remaining $L-1$ wells still include part of the majority species (i.e. species a). Further increasing $|\alpha|$, the soliton emerges in a clearer and sharper way, since all the remaining wells are gradually emptied by the localizing effect of the interspecies attraction. At border PL-SM, the latter has become so strong that both species are fully localized in a certain well, leaving all the remaining ones empty: the supermixed soliton is now completely formed and a further increase of $|\alpha|$ has no effect on the minimum energy configuration $(\vec{x}_*, \vec{y}_*)$. This scenario is pictorially illustrated in Figure 6.2 for the case $L = 3$. We recall that generalized potentials (6.2) and (6.4) have been derived under the assumption that overall boson populations N_a and N_b are large enough (see Section 6.2.2 and Appendix B). If this is not the case, the introduction of continuous variables is no longer legitimate and, for small or zero values of T_a and T_b, the formation of the supermixed solitons will not occur in a continuous way with respect to the variation of a control parameter. On the contrary, in phase PL, the soliton will form and enlarge by incorporating one boson at a time. This phenomenology, whose inherently discretized essence is closely connected with the emergence of the Mott-insulator phase, is currently under investigation.

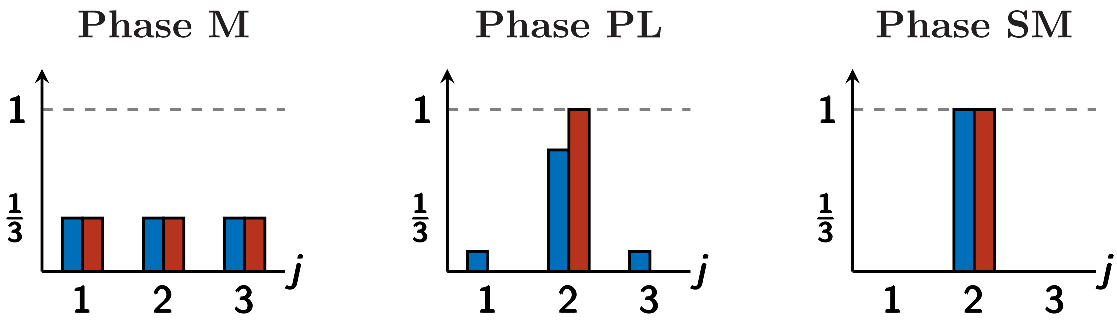

Figure 6.2: Pictorial representation of the minimum-energy configurations for phases M, PL and SM, in a 3-well system. Vertical axis represent normalized populations $x_{*,j}$ and $y_{*,j}$ for the ground state, while numbers 1, 2, 3 label the three wells. The majority (minority) species is depicted in blue (red) and corresponds to the left (right) columns of the histograms in each panel. In phase M the two species are uniformly distributed in the three wells; in phase PL the minority species forms a soliton while the majority species still occupies all available sites; in phase SM the interspecies attraction is so strong that a supermixed soliton is formed.

6.3.1 Entropy of mixing and Entropy of location as critical indicators

Already introduced in Chapter 4 in order to quantify the degree of mixing of the two species constituting the mixture, two indicators that are well-known in Statistical Thermodynamics and Physical Chemistry [168, 236], can be conveniently used to detect the occurrence of phase transitions in the class of systems that we are investigating. The Entropy of mixing and the Entropy of location are respectively defined as follows (see also Appendix C for their mathematical derivation):

$$S_{mix} = -\frac{1}{2}\sum_{j=1}^{L}\left(x_j \log \frac{x_j}{x_j+y_j} + y_j \log \frac{y_j}{x_j+y_j}\right) \tag{6.7}$$

$$S_{loc} = -\sum_{j=1}^{L} \frac{x_j+y_j}{2} \log \frac{x_j+y_j}{2}. \tag{6.8}$$

They provide complementary information about the degree of non-homogeneity present in the system. Namely, the former quantifies the degree of mixing while the latter measures the spatial localization of the particles irrespective of their species.

By plugging the expressions of $x_{*,j}$'s and $y_{*,j}$'s associated to each of the three phases (see second column of Table 6.1) into formulas (6.7) and (6.8), one can obtain particularly simple expressions for S_{mix} and S_{loc} in phase M and in phase SM, which read

$$S_{mix,\mathrm{M}} = \log 2, \qquad S_{loc,\mathrm{M}} = \log L,$$

$$S_{mix,\mathrm{SM}} = \log 2, \qquad S_{loc,\mathrm{SM}} = 0.$$

Interestingly, S_{mix} is the same both in phase M and in phase SM. This indicator, in fact, gives information just about the degree of mixing of the two atomic species, which is indeed the same both in the mixed and in the supermixed phase. Nevertheless, the profound difference between such phases can be appreciated by the combined use of S_{mix} and S_{loc}, as the latter quantifies the degree of spatial delocalization of the atomic species among the wells. In phase PL, the analytic expressions of these indicators are rather complex (although straightforward to find) and, for the sake of clarity, we prefer to give their extreme values:

$$\min_{(\alpha,\beta)\in \mathrm{PL}} S_{mix} = \frac{1}{2L}\left[L \log\left(1+\frac{1}{L}\right) + \log\left(1+L\right)\right]$$

$$\max_{(\alpha,\beta)\in \mathrm{PL}} S_{mix} = \log 2 \equiv S_{mix,\mathrm{SM}}$$

$$\min_{(\alpha,\beta)\in \mathrm{PL}} S_{loc} = 0 \equiv S_{loc,\mathrm{SM}}$$

$$\max_{(\alpha,\beta)\in \mathrm{PL}} S_{loc} = \log(2L) - \frac{L+1}{2L}\log(L+1),$$

which are found on the PL-SM border and on the line $\beta = 0$. The complete scenario on the (α, β)-plane is illustrated (for $L = 3$ sites) in the second and in the third panel of Figure 6.3, where the presence of three qualitatively different regions is evident.

6.4 The delocalizing effect of tunnelling

As already mentioned, the presence of well-recognizable phases in the plane (α, β) sharply emerges when $T_a/(U_a N_a) \to 0$ and $T_b/(U_b N_b) \to 0$, two conditions that can be regarded as a thermodynamic limit, according to the statistical-mechanical scheme developed in [175, 239]. Moving away from these limits (either because the numbers of particles N_a and N_b are not large enough or because the hopping amplitudes T_a and T_b have a non-negligible weight in the overall energy

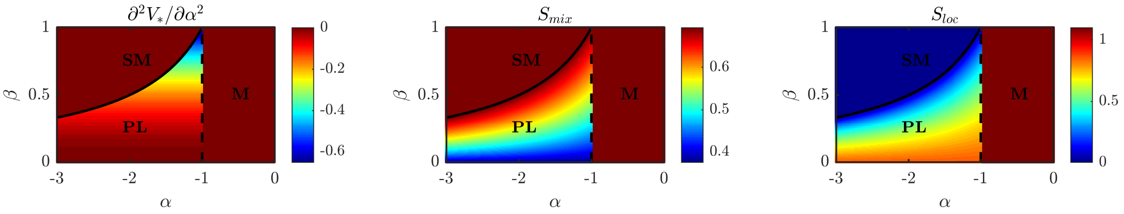

Figure 6.3: Some critical indicators witnessing the presence of three different phases in an ($L = 3$)-site potential (trimer) for $T_a/(U_a N_a) \to 0$ and $T_b/(U_b N_b) \to 0$. First panel: second derivative of functions $\mathcal{V}_*^{\mathrm{M}}$, $\mathcal{V}_*^{\mathrm{PL}}$ and $\mathcal{V}_*^{\mathrm{SM}}$ (see third column of Table 6.1) with respect to control parameter α for $L = 3$. One can appreciate that it is discontinuous both at border PL-SM and at border M-PL (in the latter border the *first* derivative $\partial\mathcal{V}_*/\partial\alpha$ is already discontinuous). Second and third panel: critical indicators (6.7) and (6.8) associated to the minimum-energy configuration $(\vec{x}_*, \vec{y}_*)$ (obtained, in turn, setting $L = 3$ in the second column of Table 6.1).

balance of the system), the phase diagram illustrated in Figure 6.1 and discussed in Section 6.3 gets smoothed and deformed, but it is still recognizable. The changes are essentially due to the delocalizing effect of tunnelling terms, which hinder the formation of localized configurations, i.e. of solitons (compare Figures 6.2 and 6.4).

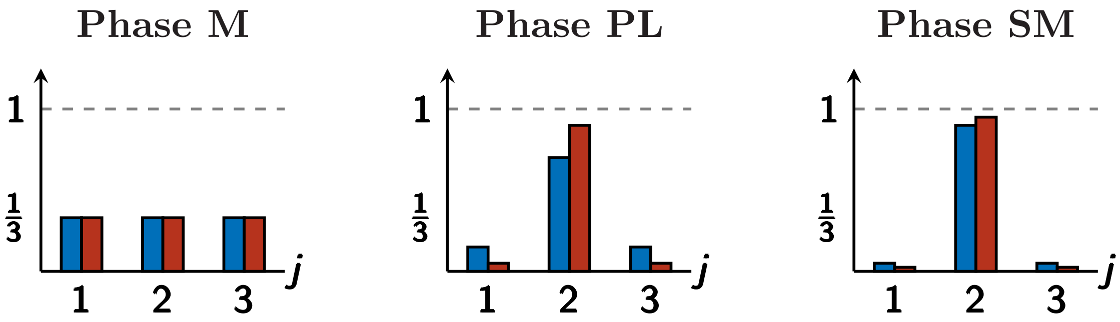

Figure 6.4: Pictorial representation of the minimum-energy configurations for a 3-well system where the tunnelling processes are present. Vertical axis represent normalized populations $x_{*,j}$ and $y_{*,j}$ for the ground state, while numbers 1, 2, 3 label the three wells. The majority (minority) species is depicted in blue (red) and corresponds to the left (right) columns of the histograms in each panel. Non-zero tunnelling processes determine the presence of residual tails at the two sides of the soliton but they do not significantly modify the scenario depicted in Figure 6.2.

In a mathematical perspective, the presence of non-zero tunnelling terms has a regularizing effect on the generalized potential (6.2), whose global minimum can be determined with less effort than in the vanishing-tunnelling case, since such minimum always falls in the *interior* of domain $\mathcal{R}$ and never on its *boundary*. One therefore needs to look for the minimum-energy solution of equations $\nabla V = 0$, the gradient being computed with respect to the $2L-2$ independent variables x_j, y_j where $j = 1, 2, \dots L-1$ due to particle-number-conservation constraints.

We have fully developed this analysis for $L = 2$ (dimer), $L = 3$ (trimer) and $L = 4$ (tetramer). Although we refer to Figure 6.5 (obtained setting $L = 3$) for the sake of clarity, the following observations have been proved to hold for $L = 2, 3, 4$ and are conjectured to be still valid also for $L \geq 5$:

- Contrary to the zero-tunneling case, critical indicators S_{mix} and S_{loc} are continuous functions of model parameters α and β. This circumstance is due to the fact that normalized boson populations x_j's and y_j's themselves no longer feature jump discontinuities. Nevertheless, both indicators are still able to witness the presence of three qualitatively different regions in the (α, β) plane.

- Supported by tunneling processes, the mixed phase survives beyond the border $\alpha = -1$, provided that $\beta = N_b\sqrt{U_b}/(N_a\sqrt{U_a})$ is small enough. In this case, in fact, the interspecies attraction is hindered by the delocalizing effect of T_a and T_b so much that it is unable to trigger soliton formation. Interestingly, by resorting to the Hessian matrix associated to effective potential (6.2), it is possible to derive inequality

$$\alpha > -\sqrt{\left(1+\frac{9}{2}\frac{T_a}{U_a N_a}\right)\left(1+\frac{9}{2}\frac{T_b}{U_b N_b}\right)} \tag{6.9}$$

  giving the region of parameters' space where the uniform configuration is the least energetic one, i.e. where the configuration $x_j = y_j = 1/3$ represents not only *a local* but also *the global* (constrained) minimum of function (6.2). This region, whose border is depicted with dashed lines in Figure 6.5, coincides (in the limit $N_a = N_b$, $T_a = T_b$, $U_a = U_b$) with the portion of parameters' space where Bogoliubov quasi-particle frequencies (2.18)-(2.19), which were found assuming the macroscopic occupation of the *momentum* mode $k = 0$ (see Section 2.5), are well defined.

- The formation of a supermixed soliton, the configuration for which $S_{loc} = 0$, is only slightly hindered by the presence of tunnelling processes. The latter tend to delocalize the atomic species among the wells and are responsible for the survival of non-zero tails in wells far from the supermixed soliton. Nevertheless, such tails, which are fully reabsorbed by the soliton only in the limit $\alpha \to -\infty$, do not significantly affect the solitonic structure of the minimum-energy configuration (see third panel of Figure 6.4). This circumstance is witnessed by the fact that, in the upper left part of the phase diagram, S_{loc} is only slightly lower than $\log L$ (see second row of Figure 6.5).

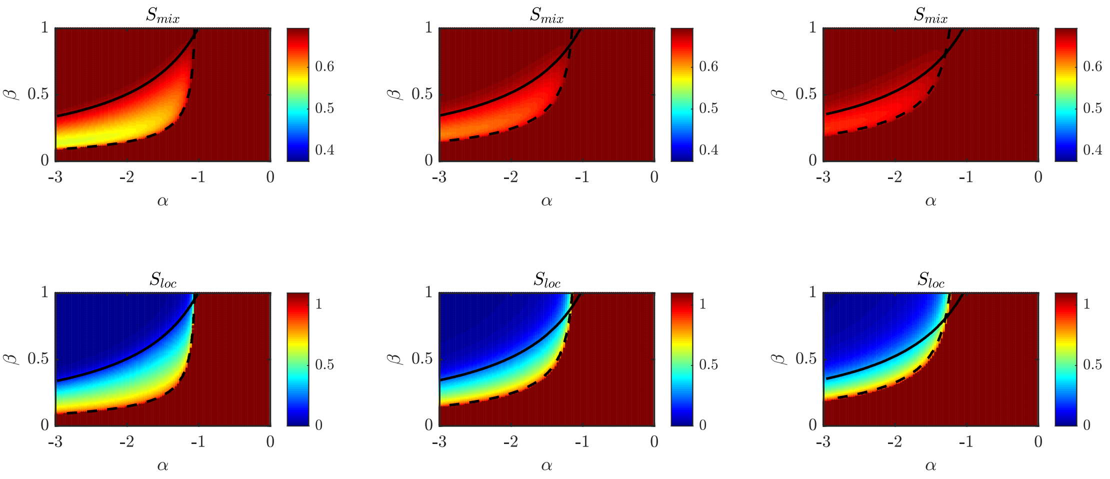

Figure 6.5: Entropy of mixing and Entropy of location associated to the configuration $(\vec{x}, \vec{y})$ minimizing potential (6.2), where $L = 3$, $N_a = N_b = 15$, $U_a = 1$, $U_b \in [0{,}1]$ and $W \in [-3{,}0]$. From left to right, $T_a = T_b$ have been set, respectively, to 0.2, 0.5 and 0.8. The dashed lines represent the border of the region where the uniform solution $x_j = y_j = 1/3$ constitutes the minimum-energy configuration and where Bogoliubov frequencies, computed assuming the macroscopic occupation of a *momentum* mode, are well defined. Their analytic expression is given by inequality (6.9). The solid lines constitute the border of the region where Bogoliubov frequencies, computed assuming the macroscopic occupation of a *site* mode, are well defined. Their analytical expression is given by formula (6.22). The comparison with Figure 6.3 shows that the phase diagram is modified by the presence of tunnelling processes, but it is not disrupted by them.

With reference to Figure 6.5, we remark that, along the dashed lines [representing the border between phase M and phase PL and given by formula (6.9)], the Bogoliubov frequencies computed assuming the macroscopic occupation of a *momentum* mode vanish (see Section 2.5). Conversely, along the solid lines [representing the border between phase PL and phase SM and given by formula (6.22)], the Bogoliubov frequencies computed assuming the macroscopic occupation of a *site* mode vanish (see Section 6.6).

6.4.1 Uniform configuration for a generic L-site potential

It is possible to analytically derive the counterpart of inequality (6.9), which holds for $L = 3$, both for the dimer ($L = 2$) and for the tetramer ($L = 4$). These inequalities, ensuing from the condition that the Hessian matrix associated to generalized potential (6.2) and evaluated at point $x_j = y_j = 1/L$ is positive definite, respectively read

$$\alpha > -\sqrt{\left(1+2\frac{T_a}{U_aN_a}\right)\left(1+2\frac{T_b}{U_bN_b}\right)} \tag{6.10}$$

and

$$\alpha > -\sqrt{\left(1+4\frac{T_a}{U_aN_a}\right)\left(1+4\frac{T_b}{U_bN_b}\right)}. \tag{6.11}$$

It is worth mentioning that their twin-species limits (i.e. their expression when $N_a \to N_b$, $U_a \to U_b$ and $T_a \to T_b$) coincide with the inequalities giving the regions of parameters' space where Bogoliubov quasi-particle frequencies are well defined. The latter have been derived, assuming the macroscopic occupation of a *momentum* mode, for the dimer in Reference [167] and in Section 2.5, thanks to the dynamical algebra method, for a ring lattice. In view of these results and of the rather general formulas giving the condition for the collapse of Bogoliubov frequencies in a generic ($L \geq 3$)-site ring lattice (see Section 2.5), it is quite natural to conjecture that, for a generic L-site potential and for $T_a \neq T_b$, $U_a \neq U_b$ and $N_a \neq N_b$, inequality

$$\alpha > -\sqrt{\left[1+C_L\frac{T_aL}{U_aN_a}\right]\left[1+C_L\frac{T_bL}{U_bN_b}\right]}, \tag{6.12}$$

where $C_L = 1 - \cos(2\pi/L)$, gives the region of parameters' space where the uniform solution $x_j = y_j = 1/L$ is the least energetic one. Conversely, going out of region (6.12), the uniform solution ceases to be a local (and also the global) minimum of function (6.2), a circumstance which corresponds to the onset of the transition between phase M and phase PL. Remarkably, in the limit $T_a/(U_aN_a) \to 0$ and $T_b/(U_bN_b) \to 0$, inequalities (6.9), (6.10), (6.11) and (6.12) reduce to $\alpha > -1$, the condition which was shown to constitute the border between phase M and PL in the thermodynamic limit (see Figure 6.1). In passing, one can observe that, for $L = 2$, the mismatch between inequalities (6.12) and (6.10) is only apparent, in that the former is referred to a system inherently featuring the ring geometry which is absent in the dimer.

6.5 Quantum critical indicators

The mechanism of formation of supermixed solitons presented in Section 6.3 and 6.4 by means of a semiclassical approach capable of highlighting, in a rather transparent way, the presence of three different phases in the plane (α, β), is fully confirmed by genuinely quantum indicators. To develop the quantum analysis, one has to perform the exact numerical diagonalization [216] of Hamiltonian (6.1) in order to determine the ground state

$$|\psi_0\rangle = \sum_{\vec{n},\,\vec{m}}^{Q} c(\vec{n},\, \vec{m})|\vec{n}, \vec{m}\rangle, \tag{6.13}$$

the associated energy

$$E_0 = \langle\psi_0|H|\psi_0\rangle \tag{6.14}$$

and the first excited levels

$$E_i = \langle\psi_i|H|\psi_i\rangle. \tag{6.15}$$

Of particular importance for the current investigation are coefficients $c(\vec{n}, \vec{m})$ appearing in expansion (6.13) and defined as

$$c(\vec{n}, \vec{m}) = \langle\vec{n}, \vec{m}|\psi_0\rangle \tag{6.16}$$

which will be used to introduce the quantum counterparts of indicators (6.7) and (6.8). The diagonalization of Hamiltonian (6.1) is carried out for extended sets of model parameters, in such a way to explore vast regions of the $(\alpha,\, \beta)$-plane [recall formulas (6.5)], also in relation with the presence of non-negligible hoppings T_a and T_b. This analysis allows one to appreciate the dependence of some genuinely quantum indicators on model parameters and, above all, their being critical along the same curves of the $(\alpha,\, \beta)$-plane where the semiclassical approach predicts the occurrence of mixing-supermixing transitions. For the sake of clarity, we will refer to Figure 6.6, whose rows correspond to different quantum indicators and whose columns to different values of the hopping amplitude $T := T_a = T_b$. Going from left to right, it reads

$$T = 0.2,\ 0.5,\ 0.8 \tag{6.17}$$

respectively. In general, the same observations that we made in Section 6.4 concerning the delocalizing effect of tunnelling and the impact thereof on S_{mix} and on S_{loc}, hold also within this purely quantum scenario. In particular, one can notice that:

- All quantum indicators are continuous functions of model parameters α and β;
- The mixed phase is supported by tunnelling processes;
- The formation of supermixed solitons occurs for large values of $|\alpha|$ and moderate values of β.

The quantum critical indicators which have been scrutinized in relation to the mixing-supermixing transitions are the following:

Ground-state energy. Observing indicator (6.14), regarded as a function of effective model parameters α and β, one can appreciate the presence of three different phases (corresponding to the already discussed phase M, phase PL and phase SM). To be more clear, function $E_0(\alpha,\,\beta)$ is everywhere continuous in the $(\alpha,\,\beta)$-plane, but it features non analiticities, either in its first or in its second derivative, along two specific lines of the phase diagram which, in turn, divide the latter into three separate regions. The functional dependence of E_0 in each of the three regions is different, that means that the slope $\partial E_0/\partial\alpha$ and the concavity $\partial^2 E_0/\partial\alpha^2$ exhibit different behaviours.

This circumstance is well illustrated in the first row of Figure 6.6, where we have plotted $\partial^2 E_0/\partial\alpha^2$ (the logarithmic scale has been adopted just for graphical purposes) for three different values of the hopping amplitude. The left panel, obtained for $T/U_a = 0.2$, allows one to recognize two regions (in green), well separated by an intermediate region (in red-orange) which intercalates between them. In the central and in the right panels, which feature bigger hopping amplitudes ($T/U_a = 0.5$ and

0.8 respectively), the presence of the intermediate phase (phase PL) is still evident, although it turns out to be slightly deformed and its borders less sharp.

Entropy of mixing. In Section 6.3, we employed indicator (6.7), (already introduced in Section 4.3), and discussed its ability to quantify the degree of mixing of a semiclassical configuration $(\vec{x},\, \vec{y})$. Its quantum mechanical version has already been introduced in Section 4.3.2 [see formula (4.7)]. We recall that it is constructed as follows: after determining the complete decomposition (6.13) of the system's ground state $|\psi_0\rangle$ and, in particular, the full list of coefficients (6.16) [the cardinality of this set being given by formula (6.3)], one can evaluate the entropy of mixing of $|\psi_0\rangle$ by defining

$$\tilde{S}_{mix} := \sum_{\vec{n},\vec{m}}^{Q} |c(\vec{n},\vec{m})|^2 S_{mix}(\vec{n},\vec{m}), \tag{6.18}$$

where $S_{mix}(\vec{n},\vec{m})$ is the entropy of mixing of the state $(\vec{n},\vec{m})$ of the Fock basis, computed by means of formula (6.7) (with the obvious identifications $x_j = n_j/N_a$ and $y_j = m_j/N_b$).

The indicator thus obtained is illustrated, as a function of model parameters α and β, in the second row of Figure 6.6 for the three choices (6.17). Especially for small hoppings, one can observe the presence of an intermediate phase (phase PL) which stands in between phase SM and phase M. Increasing the tunnelling, the inter-phase borders tend to get less sharp and the distinction between the phases gets decreasingly evident. Interestingly, the results given by quantum indicator (6.18), whose employment requires the knowledge of the full list of coefficients (6.16), are in very good agreement with those ones obtained within the CVP (compare the panels in the first row of Figure 6.5 with the corresponding ones in the the second row of Figure 6.6, obtained for the same model parameters).

Entropy of location. With a similar reasoning, one can define the quantum counterpart of classical indicator (6.8), i.e.

$$\tilde{S}_{loc} := \sum_{\vec{n},\vec{m}}^{Q} |c(\vec{n},\vec{m})|^2 S_{loc}(\vec{n},\vec{m}), \tag{6.19}$$

where coefficients $c(\vec{n},\vec{m})$ are given by formula (6.16) and $S_{loc}(\vec{n},\vec{m})$ is the entropy of location associated to the state $(\vec{n},\vec{m})$ of the Fock basis and computed by means of formula (6.8) (with the obvious identifications $x_j = n_j/N_a$ and $y_j = m_j/N_b$). The behaviour of indicator $\tilde{S}_{loc}$ in the (α, β)-plane is illustrated in the third row of Figure 6.6. In the three panels corresponding to values (6.17), similar to the case of $\tilde{S}_{mix}$, it is possible to identify phase M (in red), phase SM (in blue), and the intermediate one (where $\tilde{S}_{loc}$ varies between ≈ 0 and $\approx \log L = \log 3$).

Its remarkable specificity and sensitivity, together with the non-small extent of its range, make this indicator particularly suitable for the detection of soliton-like configurations. It is worth mentioning that the results obtained within a purely quantum treatment [i.e. numerically diagonalize Hamiltonian (6.1), obtain coefficients (6.16) and plug them into formula (6.19)] well match those obtained within the semiclassical CVP approach (compare the panels in the second row of Figure 6.5 with the corresponding ones in the third row of Figure 6.6, which share the same model parameters).

Entropy of Entanglement (EE). The degree of quantum correlation between two partitions of its can effectively mirror the structure of a given ground state $|\psi_0\rangle$, which, in turn, can radically change upon variation of model parameters. The validity of the EE as a critical indicator has been illustrated in Chapter 3 for a binary mixture in a two-well potential (and for different partition schemes) and in Section 4.5.3 for a symmetric binary mixture in a three-well potential. Among various possibilities, we have focused on the entropy of entanglement between species a and species b. As a consequence, the entanglement between the two atomic species is given by

$$EE = -\mathrm{Tr}_a(\hat{\rho}_a \, \log_2 \hat{\rho}_a), \tag{6.20}$$

an expression corresponding to the Von Neumann entropy of the reduced density matrix

$$\hat{\rho}_a = \mathrm{Tr}_b \left(\hat{\rho}_0 \right) . \tag{6.21}$$

The latter can be obtained, in turn, by tracing out the degrees of freedom of species b from the ground state's density matrix $\hat{\rho}_0 = |\psi_0\rangle\langle\psi_0|$. The fourth row of Figure 6.6 illustrates indicator EE as a function of α and β for the three values (6.17).

One can notice that, when $\alpha \to 0$, then $EE \to 0$ since in this limit the two species do not interact. Increasing $|\alpha|$, EE features a sharp peak exactly where the transition between phase M and phase PL takes place, a circumstance which has been already noticed in relation to mixing-demixing transitions (see Figure 4.16). Further increasing $|\alpha|$, a plateau is reached, wherein the EE stabilizes to the limiting value of $\log L = \log_2 3 \approx 1.59$. The argument of the logarithm (which is set to $L = 3$ in the example shown in Figure 6.6), corresponds to the number of semiclassical configurations minimizing potential (6.4) and which are quantum-mechanically reabsorbed in the formation of a unique non-degenerate ground state. In other words, the L-fold degeneracy of the semiclassical configuration corresponding to the presence of a supermixed soliton in one of the L wells is lifted by the presence of tunnelling, which therefore determines the formation of a L-faced Schrödinger cat.

Energy spectrum. The computation of the first excited energy levels of the system [see formula (6.15)] as a function of control parameter α can give an additional physical insight and a further confirmation of the presence of three qualitatively different phases. Figure 6.7 illustrates the energy fingerprint of a $L = 3$ system, for $\beta = 0.6$ and the usual values (6.17). With reference to the left panel, the one featuring the smallest value of T/U_a, it is possible to distinguish three different regions wherein the energy-levels arrangement is qualitatively different. For small values of $|\alpha|$, the levels can be shown to well match Bogoliubov quasi-particles frequencies (2.18)-(2.19) which were, in turn, derived in Section 2.5 assuming the macroscopic occupation of momentum mode $k = 0$. At $\alpha \approx -1$ all these levels collapse, thus signing the end of phase M and, further increasing $|\alpha|$ they manifestly rearrange (it is worth mentioning that, for $\alpha < -1$ some excited levels seem to coincide with the lowest one, but, actually, this overlap is just apparent and merely due to the scale used for the vertical axis). Further increasing $|\alpha|$ down to $\alpha \approx -1.7$, another qualitative change of the energy levels' structure is met, which constitutes the border between phase PL and phase SM. At such value of α, in fact, the energy levels, although they do not collapse, assume a distinctly-linear functional dependence on α, a circumstance which will be mathematically justified in the next Section. The presence of three regions where the energy fingerprint is qualitatively different can be noticed also in the central and in the right panel of Figure 6.7, although the critical behaviours (namely the spectral collapse and the onset of the linear ramp) are smoothed down by the delocalizing effect of tunnelling. In this regard, one can observe that tunnelling is responsible also for the leftward translation of the collapse point [see formula (6.9) and the discussion thereof].

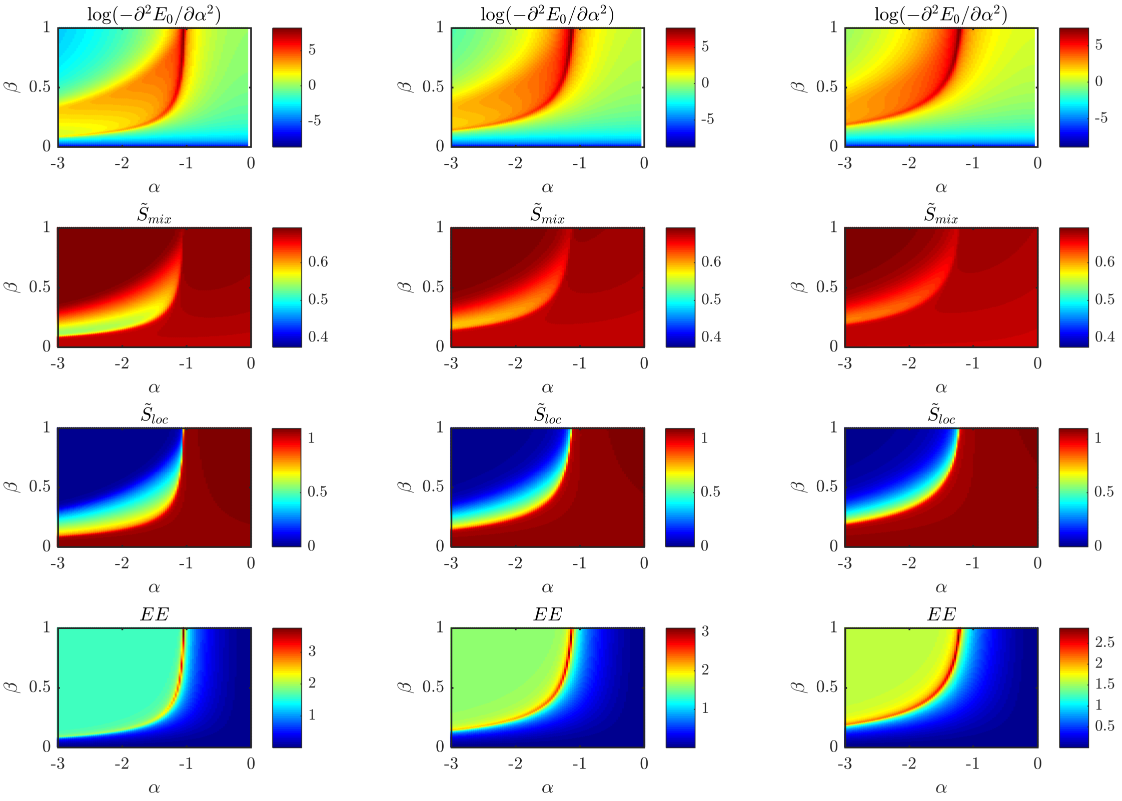

Figure 6.6: Each row illustrates the behaviour of a genuinely quantum indicator as a function of model parameters α and β. Each column corresponds to a different value of the ratio T/U_a, where $T := T_a = T_b$ (from left to right, $T/U_a = 0.2$, 0.5, 0.8). First row: second derivative of the ground-state energy E_0 (see formula 6.14) with respect to α. The logarithmic scale is used in order to better visualize the presence of three qualitatively different regions. Second row: quantum version of the entropy of mixing, $\tilde{S}_{mix}$ (see formula 6.18). Third row: quantum version of the entropy of location $\tilde{S}_{loc}$ (see formula 6.19). Fourth row: entanglement between the two condensed species, EE [see formula (6.20)]. Model parameters $L = 3$, $N_a = N_b = 15$, $U_a = 1$, $U_b \in [0,1]$ and $W \in [-3,0]$ have been used.

6.6 Analytical approach to the energy spectrum

In this Section, we derive, by means of a modified version of the Bogoliubov approximation scheme (see Chapter 2), the analytical expression of quasiparticles' frequencies of a $L = 3$-system when its ground state exhibits a supermixed soliton-like structure (namely, when it belongs to phase SM). In this circumstance, in fact,

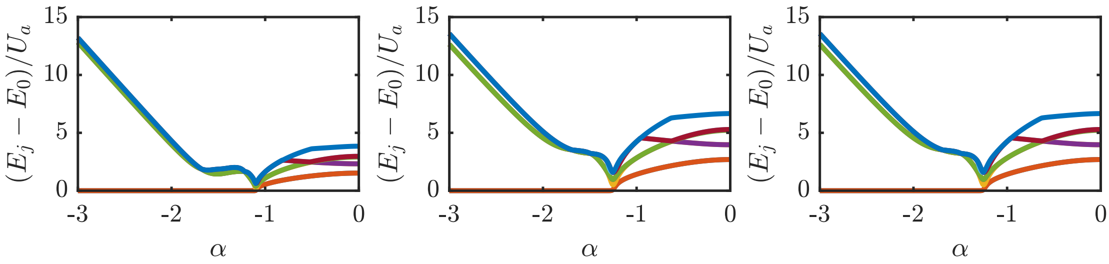

Figure 6.7: First 8 excited energy levels, obtained by means of an exact numerical diagonalization of Hamiltonian (6.1), for a $L = 3$-system and for $T := T_a = T_b = 0.2, 0.5, 0.8$ in the left, central and right panel, respectively. Model parameters $N_a = N_b = 15$, $U_a = 1$, $U_b = 0.36$ and $W \in [-1.8,0]$ have been chosen.

one can recognize that there are two site modes, a_1, b_1, that are macroscopically occupied (contrarily to the assumptions made in Chapter 2, where the *momentum* mode $k = 0$ was the one macroscopically occupied), namely $n_1 \approx N_a - n_2 - n_3$ and $m_1 \approx N_b - m_2 - m_3$ while the microscopically occupied ones are a_2, a_3, b_2 and b_3. With these substitutions in mind, one can derive $H^{(2)}$, the quadratic approximation of the original Hamiltonian (6.1), which reads

$$H^{(2)} \approx -T_a(a_3^\dagger a_2 + a_2^\dagger a_3) - (U_a N_a + N_b W)(n_2 + n_3)$$

$$-T_b(b_3^\dagger b_2 + b_2^\dagger b_3) - (U_b N_b + N_a W)(m_2 + m_3).$$

Notice that we have neglected not only higher-order terms but also linear terms, since the latter contribute just to the ground-state energy but do not affect the characteristic frequencies and, in general, they can be removed by a suitable unitary transformation.

Recognizing that terms

$$J_+ = a_2 a_3^\dagger, \qquad J_- = a_2^\dagger a_3, \qquad J_3 = \frac{1}{2}(n_3 - n_2)$$

constitute the two-boson realization of algebra su(2), one can easily diagonalize $H^{(2)}$ enacting the unitary transformation $U_\varphi = e^{\frac{\varphi}{2}(J_+ - J_-)}$ which gives

$$U_\varphi (J_+ + J_-) U_\varphi^\dagger = 2J_3 \sin\varphi + (J_+ + J_-)\cos\varphi.$$

Treating in the same way terms b_j's, it is straightforward to derive diagonal Hamiltonian

$$H_D = n_2(T_a - U_a N_a - N_b W) + n_3(-T_a - U_a N_a - N_b W)$$

$$+m_2(T_b - U_b N_b - N_a W) + m_3(-T_b - U_b N_b - N_a W),$$

an expression where the coefficients of number operators constitute the Bogoliubov quasiparticles' frequencies, namely $H_D = \omega_2 n_2 + \omega_3 n_3 + \Omega_2 m_2 + \Omega_3 m_3$. As illustrated in Figure 6.8, the agreement between the spectrum envisaged by this approximation scheme and the exact one, obtained numerically, is good, not only qualitatively (same linear behaviour) but also quantitatively ($< 10\%$ of difference if $|\alpha|$ is large enough). This agreement rapidly improves as soon as the numbers of particles N_a and N_b increase.

Interestingly, the simultaneous validity of conditions

$$\omega_2 > 0, \quad \omega_3 > 0, \quad \Omega_2 > 0, \quad \Omega_3 > 0 \tag{6.22}$$

gives the region of parameters' space where Hamiltonian H_D is lower bounded, i.e. the region where the supermixed soliton-like configuration is estimated to be stable. The border of this region corresponds to the solid lines present in Figure 6.5 which, in turn, stand where indicators S_{mix} and S_{loc} illustrated therein feature criticalities.

In conclusion, we remark that the approximation scheme developed in this Section is based on the assumption of macroscopic occupation of *site* modes (one for each component) and that it is able to estimate the energy spectrum for large values of $|\alpha|$, i.e. in phase SM. This scheme is therefore fundamentally different from the one developed in Chapter 2 and linked to condition (6.9), since the latter was based on the assumption of macroscopic occupation of momentum mode $k = 0$ and was therefore intended to approximate the energy spectrum for small values of $|\alpha|$ (a circumstance corresponding, in turn, to uniform boson configuration, i.e. to phase M).

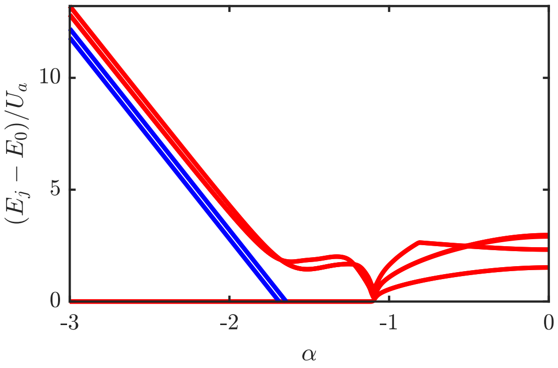

Figure 6.8: Red lines: first excited levels of the exact spectrum obtained by means of numerical diagonalization of Hamiltonian (6.1). Blue lines: Bogoliubov characteristic frequencies present in diagonal Hamiltonian H_D. The following model parameters have been chosen: $L = 3$, $T_a = T_b = 0.2$, $U_a = 1$, $U_b = 0.36$, $N_a = N_b = 15$, $W \in [-1.8, 0]$.

6.7 Conclusions

In this Chapter, we have investigated the mechanism of soliton formation in bosonic binary mixtures loaded in ring-lattice potentials. Our analysis has evidenced that all these systems, irrespective of the number sites, share a common mixing-demixing phase diagram. The latter is spanned by two effective parameters, α and β, the first one representing the ratio between the interspecies attraction and the (geometric average of) the intraspecies repulsions, the second one accounting for the degree of asymmetry between the species. Such phase diagram includes three different regions, differing in the degree of mixing and localization. The first phase, occurring for sufficiently small $|\alpha|$, is the mixed one (phase M) and it is such that the atomic species are perfectly mixed and uniformly distributed among the wells. The second phase (phase PL) occurs for moderate values of $|\alpha|$ and sufficiently asymmetric species. It includes the seed of localized soliton-like states, although the latter are not developed in a full way. Eventually, the third phase (phase SM), occurring for sufficiently large values of $|\alpha|$, corresponds to states such that both atomic species clot in the same unique well, hence the name supermixed solitons.

After introducing the quantum model and its representation in the CVP, in Section 6.3, the mixing-supermixing transitions are derived within such semiclassical approximation scheme which transparently shows the emergence of a bi-dimensional phase diagram. The three phases therein not only feature specific functional dependences of the ground-state energy on model parameters, but also are characterized in terms of two critical indicators imported from Statistical Thermodynamics, the entropy of mixing and the entropy of location.

Section 6.4 is devoted to the analysis when the ratio $T/(UN)$ is small but non-zero, i.e. how the phase diagram changes and gets blurred if one walks away from the thermodynamic limit (in the sense specified within the statistical mechanical approach developed in [175, 239]). The delocalizing effect of tunneling is shown to favor the mixed phase and to hinder the formation of solitons but not to upset the presented phase diagram. Quantum indicators are presented in Section 6.5, whose critical behaviour along certain lines of the phase diagram (α, β) corroborates the scenario that emerged from the semiclassical treatment of the problem.

In conclusion, we note that the methodology on which our analysis relies, together with the classical and quantum indicators used to detect critical phenomena, can be easily applied to systems with more complex lattice topologies, interactions and tunnelling processes [193, 241–243]. In view of this, and considering the increasing interest for multicomponent condensates [244–247], our future work will aim to extend the presented analysis to the soliton formation's mechanism in complex lattices and in presence of multiple condensed species.

Chapter 7

A remark on some experimental aspects

7.1 Introduction

Although this Thesis mainly focuses on various *theoretical* aspects of bosonic binary mixtures trapped in ring-lattice and in few-site potentials, in this Chapter[1], we would like to make some remarks on the *experimental* feasibility of the systems investigated in the previous sections. At first, we present an experimental proposal devised in collaboration with the Institute of Quantum Optics of Hannover University which, although specifically focused on the observability of the mixing-demixing transitions investigated in Chapter 4 in the case of a three-well potential, can be extended, with the due care, to the case of the two-well potential examined in Chapter 3. Then, we broaden our discussion to the case of many lattice sites and review some published experiments where the ring geometry was indeed produced, a circumstance which offers a viable pathway towards the realization of the models treated in Chapters 2 and 6. Further details concerning Bose-Bose mixtures can be found in Chapter 1, more specifically in Section 1.1.2.

---

[1] Note to the reader: part of the content of this Chapter has been published in [176].

7.2 A proposal to realize the ring-trimer system

We present an experimental proposal devised in collaboration with the Institute of Quantum Optics of Hannover University. This proposal (see Reference [176]) is based on a realistic optical-tweezers system and on a mixture of bosonic ^{23}Na and ^{39}K atoms, two condensed species that, thanks to the remarkable tunability of their intra- and inter-species scattering lengths, offer the possibility to explore a number of different regimes. Such a tunability is made possible by magnetic Feshbach resonances [52], although one cannot trim intra- and inter-species scattering lengths in an independent way.

One should recall that, nowadays, many bosonic binary mixtures can be doubly Bose-condensed (see Section 1.1.2), but some of them have extremely large background scattering lengths [248], very narrow resonances far beyond experimental magnetic field stability [248], overlapping resonances [51], and promising broad inter-species resonances where, however, the inter-species scattering length is excessively large or has the wrong sign [79]. Conversely, the mixture $|f=1,m_f=-1\rangle_{\mathrm{Na}}+|f=1,m_f=-1\rangle_{\mathrm{K}}$ (where f is the atomic total angular momentum and m_f is its projection on the quantization axis), which has been recently doubly Bose-condensed, exhibits a favorable window of magnetic field (from 90 to 150 G) where the combination of two intra- and one inter-species resonances allows for a smooth tuning of the scattering lengths [51] (see Figure 7.1). Additionally, in this range of magnetic field, three-body losses [249] are limited thanks to the small value of $a_{\mathrm{Na,K}}$. In our case, varying the magnetic field corresponds to tune g_a, g_b and g_{ab}, and therefore to walk along a line in the phase diagram illustrated in Figure 4.9. As already explained, this diagram is spanned by effective variables α and β which, in turn, are suitable functions of the mean-field parameters (i.e. $\alpha=g_{ab}/\sqrt{g_a g_b}$ and $\beta=N_b/N_a\sqrt{g_b/g_a}$, see also Section 4.4.1 for further details). In the region of interest for our investigation, the scattering lengths of sodium and potassium are almost constant and the corresponding lines in the $(\alpha,\,\beta)$-plane will be almost horizontal. Of course their position in the phase diagram, i.e. their β-coordinate can be easily tuned via the atom-number ratio N_b/N_a.

Recent developments in single-site resolution detection of single atoms and the realization of diffraction limited potentials have pushed forward the capabilities of handling few atoms in tweezers systems [250]. The trimer potential consists (see

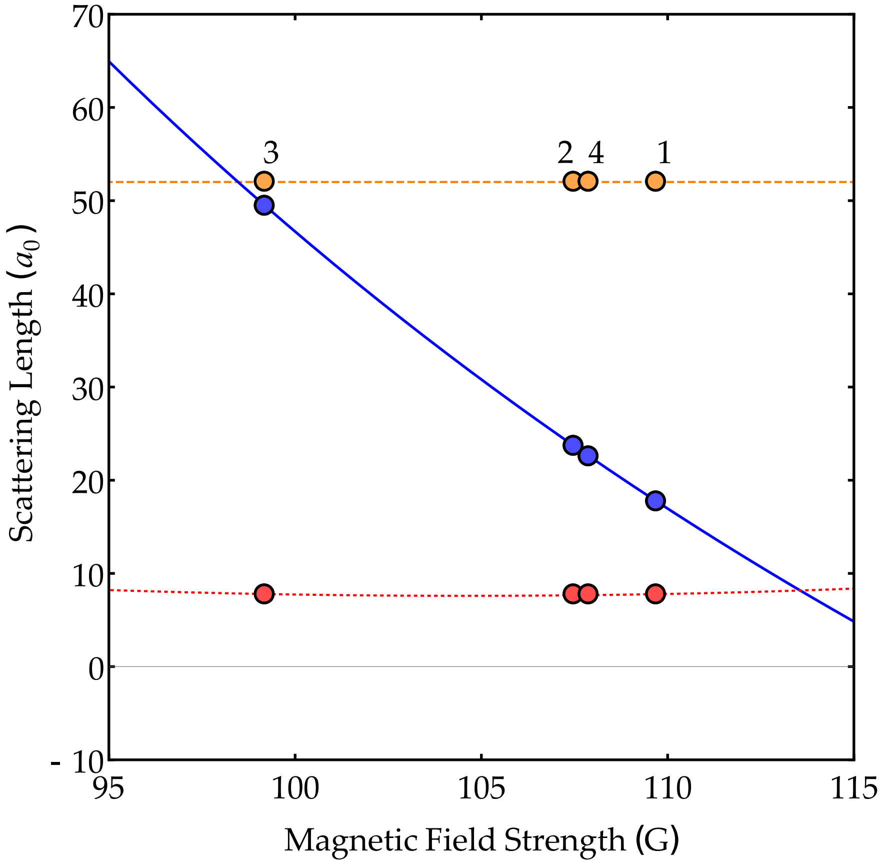

Figure 7.1: Intra- and inter-species scattering lengths for $|f=1, m_f=-1\rangle_{^{23}\mathrm{Na}} + |f=1, m_f=-1\rangle_{^{39}\mathrm{K}}$ mixture given in the Bohr radii a_0. Yellow dashed, red dotted and blue continuous line refer to sodium a_{Na}, potassium a_{K} and sodium-potassium $a_{\mathrm{Na,K}}$ scattering lengths. Labels refer to points considered in Section 4.4. Note the approximately constant intra-species scattering lengths and the inter-species $a_{\mathrm{Na,K}}$ varying from $< a_{\mathrm{K}}$ to $> a_{\mathrm{Na}}$.

Figure 4.7) of three Gaussian traps whose centers correspond to the vertexes of an equilateral triangle with edge d. The realization of such a potential is based on the projection of three dipole-trap beams from the vertical direction of our experimental apparatus which features a large numerical aperture objective with demonstrated high resolution capability [251]. Being the wavelength 1064 nm, we consider realistic values for the width of the three beams ($\sigma = 1{,}00\,\mu m$) and for the distance of their centers, $d = 2\,\mu m$. For simplicity, we consider monochromatic tweezers, despite the large difference between sodium and potassium trap frequencies resulting from the different atomic polarizability. A bichromatic sheet of light on the horizontal direction or a time-averaged light potential provide confinement in the vertical direction and compensate for the presence of a gravitational sag.

Experimental sequence. To strengthen the feasibility of our proposal, we consider also a possible experimental sequence and problems related to the limited lifetime of the sample because of three-body losses.

The starting point of the experimental sequence will be the creation of the degenerate samples in a cross dipole trap [51] at a magnetic field of about 154 G and the following ramp of the magnetic field to the zero of the inter-species scattering length at 117 G. This allows one to maximize the lifetime of the sample against three-body losses. The mixture can be adiabatically loaded into the trimer potential by rising the intensity of the tweezers and decreasing the intensity of the crossed dipole trap. A ramp of the magnetic-field strength to the target value follows, and the system is let mix/demix. After a fast ramp up of the tweezers intensity to stop hopping between the wells, the tweezers will be separated and the atom number of each species in the three wells will be detected with absorption imaging after a short time of flight. We expect that, at each single realization, the system will lie in one of the possible permutations of the typical boson distributions. Post analysis is carried on by plugging the measured occupation numbers into Equation (4.5), thus obtaining the entropy of mixing associated to the probed state. Mixing/demixing will be thus pointed out depending on the applied magnetic field.

Eventually, one should notice that, once the interaction parameters have been set, the miscibility properties of the mixture do not depend on the *absolute* number of atoms but just on their *ratio*, through the effective variable $\beta = N_b/N_a\sqrt{g_b/g_a}$. On the other hand, and in view of an experimental realization, the numbers of atoms do play a crucial role, as they appear with the third power in the formula for three-body recombination [13], from which one can extract the expected lifetime of the mixture in the tweezers' wells. The model parameters employed in Section 4.4.1 and, specifically, the numbers of atoms present in the system, were chosen in such a way that the lifetime exceeds the smallest of the two hopping times (< 20 ms) of an order of magnitude. In particular, we have computed three-body densities from Gross-Pitaevskii simulations (see Figure 4.8) and assumed three-body loss-rate coefficients to be of the order of 10^{-41} m^6/s, a value taken from the experimental measurements performed in the Hannover setup and compatible with literature values [13].

The optical potential. Acousto-optical modulators will generate the three beams and particular attention will be devoted to the calibration of the three wells in order to verify their being identical. To this end, the use of modern digital mirror devices can be useful to compensate for possible aberrations and defects in the potentials, as already shown in other experiments [252].

We consider, also, the possibility to realize three-well potentials by means of triangular optical lattices. In this case, nevertheless, the tighter confinement suggests that a much smaller number of atoms per site must be considered. Species-specific trap frequencies are considered in the calculations as well as the different hopping rates coming from the different heights of the inter-well barriers. These correspond to $\omega_a \approx 2\pi \times 5600$ Hz, $\omega_b \approx 2\pi \times 6900$ Hz. The depth of the wells is chosen to allow the hopping times $\{1/T_a, 1/\ T_b\}$ to be smaller than 20 ms for both species; estimated hopping rate are evaluated by calculating overlap integrals and one has $\{T_a, T_b\} \approx 2\pi \times \{1000,50\}$ Hz. Excessively large hopping rates would smooth out the phases discussed in Section 4.3, while too small ones will not allow the system to mix/demix in a time shorter than the mixture lifetime. Real hopping rates will be experimentally determined to overcome limitations coming from the simple overlap-integral approximation.

Experimental stability. One needs a remarkable experimental stability of the three quantities involved in the mixing-demixing process. These are the atom number (preparation and detection), the trimer potential depth and the magnetic field strength. The accuracy of the latter is below 30 mG in the Hannover setup [253] and therefore allows a smooth tuning of the scattering lengths, up to a precision well within the resolution requested to observe the phase transition shown in Figure 4.9. The optical-potential stability can be assured by advanced feedback techniques [254] while the stability of the atom number by real-time analysis [255].

7.3 Ring lattices

Ring-lattice potentials featuring a relatively high number of sites are within the reach of current experimental apparatuses [256–261]. Among the rest, this kind of confining potentials has played a central role in the emerging field of "Atomtronics" [262–266], a term which encompasses a broad range of topics featuring *guided* atomic matter waves [256, 267] and which focuses on the design of atomic systems that emulate standard solid-state devices, such as transistors [264] and qubits [258]. These atomic equivalents of standard semiconductor devices, in fact, often feature the ring-lattice geometry [188, 239, 243, 268–274], or its natural extension to ring-ladder [177, 275–277] systems.

In Reference [258], the authors reported on the creation of such an optical potential by means of a liquid crystal on silicon spatial light modulator, a device which allows one to controllably imprint a phase onto a well-collimated laser beam. The latter, generated by a diode-pumped solid state laser, has a wavelength of 532 nm. The spatial light modulator plays the role of a programmable phase array and, locally modulating the phase of the impinging laser beam, allows one to create arbitrary 2D optical potentials. The light which is diffracted from the computer-generated phase hologram thus gives place to the desired intensity pattern, exactly in the focal plane of an optical apparatus. The obtained ring-lattice potential, including up to 20 lattice sites, can be easily rescaled by means of a suitable microscope objective and the final ring radius can range from 90 μm to 5–10 μm. The laser power which comes into play is of the order of 50 mW and, interestingly, the height of the potential barriers between the wells can be tuned in a very precise way and also in a dynamical manner [258].

7.4 Conclusions

In this Chapter, we have commented on the *experimental* feasibility of some physical systems and phenomena discussed, from a *theoretical* viewpoint, in the previous chapters of this Thesis. In Section 7.2, by describing the experimental proposal that the group I belong to has developed in collaboration with the Institute of Quantum Optics of Hannover University, we have shown that the mixing-demixing quantum phase transitions predicted in Chapter 4 (see also the relevant phase diagram of Figure 4.1) are indeed observable. In this regard, a Bose-Bose mixture of ^{23}Na and ^{39}K atoms featuring tunable intra- and interspecies interactions has been described, together with an array of optical tweezers realizing the tree-well potential, the experimental protocol to prepare, manipulate and probe the mixture, and other details concerning the stability and the robustness of the discussed phenomenology against three-body losses. In Section 7.3, we have extended our discussion to ring lattices including more than three sites and summarized the recent work of the Singapore group, which has reported on the creation of annular, fragmented, optical potentials by means of a rather complex apparatus based on a spatial light modulator. This circumstance should strengthen the interest towards the systems and the phenomenology discussed in Chapters 2 and 6.

Appendix A

Algebraic diagonalization

Let us consider Hamiltonian (2.5)

$$\hat{H}_k = 2\gamma_k(A_3 + B_3) + u(A_+ + A_- + B_+ + B_-) + u_{ab}(K_+ + K_- + S_+ + S_-)$$

obtained in Section 2.2 within the Bogoliubov approximation scheme. For simplicity, in the following, we will omit the index k. It is convenient to consider $\hat{H}$ as a vector of a 10-dimensional vector space (recall that the dimension of the dynamical algebra so(2,3) which $\hat{H}$ belongs to is 10 and see Figure 2.1 for a pictorial representation). By making use of the well-known Baker–Campbell–Hausdorff formula, one can prove that for any two operator $\hat{x}$, $\hat{y}$, it holds that

$$e^{\hat{x}}\,\hat{y}\,e^{-\hat{x}} = \sum_{k=0}^{+\infty} \frac{1}{k!}[\hat{x}, \hat{y}]_k.$$

Our purpose, here, is to employ suitable unitary transformations in order to diagonalize $\hat{H}$. In this regard, recall that only operators A_3 and B_3 are diagonal in the Fock-state basis (see formulas 2.4). In general, if $\mathcal{A}$ is a Lie algebra and $\mathcal{G} = \exp[i\mathcal{A}]$ is the associated group, one can verify that

$$\forall\, a \,\in\, \mathcal{A}, \forall\, g \,\in\, \mathcal{G} \Rightarrow g\,a\,g^{\dagger} = a' \,\in\, \mathcal{A},$$

an expression meaning that an element of the group associated to a certain algebra generates an endomorphism of the algebra itself. In the following, the unitary transformations employed to diagonalize $\hat{H}$, i.e. to reduce the latter to a linear combination of operators A_3 and B_3, will be frequently called "rotations", in view of the geometric structure that can be associated to the algebra (see Figure 2.1 for a pictorial representation). In the following we will prove that the unitary transformation (2.6), whose explicit expression is

$$U = e^{\frac{\varphi}{2}(S_- - S_+)} e^{\frac{\theta_a}{2}(A_- - A_+)} e^{\frac{\theta_b}{2}(B_- - B_+)}$$

(where the index k has been dropped for simplicity) can indeed diagonalize $\hat{H}$ upon properly choosing angles φ, θ_a and θ_b.

Let us start to rotate $\hat{H}$ around $S_2 = \frac{S_+ - S_-}{2i}$:

$$e^{i\varphi S_2} \hat{H} e^{-i\varphi S_2} = e^{\frac{\varphi}{2}(S_+ - S_-)} \hat{H} e^{-\frac{\varphi}{2}(S_+ - S_-)}$$

Here we compute the various parts:

$$e^{\frac{\varphi}{2}(S_+ - S_-)}\, A_3\, e^{-\frac{\varphi}{2}(S_+ - S_-)} = A_3 + \left(\frac{\cos\varphi - 1}{2}\right) S_3 - \frac{1}{4}\sin\varphi (S_+ + S_-)$$

$$e^{\frac{\varphi}{2}(S_+ - S_-)}\, B_3\, e^{-\frac{\varphi}{2}(S_+ - S_-)} = B_3 + \left(\frac{1 - \cos\varphi}{2}\right) S_3 + \frac{1}{4}\sin\varphi (S_+ + S_-)$$

$$e^{\frac{\varphi}{2}(S_+ - S_-)}\, (A_+ + A_-)\, e^{-\frac{\varphi}{2}(S_+ - S_-)} =$$

$$= \left(\frac{1 + \cos\varphi}{2}\right)(A_+ + A_-) + \left(\frac{1 - \cos\varphi}{2}\right)(B_+ + B_-) - \frac{1}{2}\sin\varphi (K_+ + K_-)$$

$$e^{\frac{\varphi}{2}(S_+ - S_-)}\, (B_+ + B_-)\, e^{-\frac{\varphi}{2}(S_+ - S_-)} =$$

$$= \left(\frac{1 - \cos\varphi}{2}\right)(A_+ + A_-) + \left(\frac{1 + \cos\varphi}{2}\right)(B_+ + B_-) + \frac{1}{2}\sin\varphi (K_+ + K_-)$$

$$e^{\frac{\varphi}{2}(S_+ - S_-)}\, (S_+ + S_-)\, e^{-\frac{\varphi}{2}(S_+ - S_-)} = 2\sin\varphi S_3 + \cos\varphi (S_+ + S_-)$$

$$e^{\frac{\varphi}{2}(S_+ - S_-)}\, (K_+ + K_-)\, e^{-\frac{\varphi}{2}(S_+ - S_-)} =$$

$$= \sin\varphi (A_+ + A_-) - \sin\varphi (B_+ + B_-) + \cos\varphi (K_+ + K_-)$$

After putting together the various terms, one obtains that:

$$e^{i\varphi S_2} \hat{H} e^{-i\varphi S_2} = 2\gamma\,(A_3 + B_3) + u\,(A_+ + A_- + B_+ + B_-) +$$

$$+ u_{ab}\Big[2\sin\varphi S_3 + \cos\varphi (S_+ + S_-) + \sin\varphi (A_+ + A_-) - \sin\varphi (B_+ + B_-) + \cos\varphi (K_+ + K_-)\Big]$$

One thus discovers that it is possible to get rid of non-diagonal terms $(S_+ + S_-)$ and $(K_+ + K_-)$ by choosing $\varphi = \frac{\pi}{2}$. With such a substitution Hamiltonian turns:

$$\hat{H}' = e^{i\varphi S_2} \hat{H} e^{-i\varphi S_2} =$$

$$= 2\gamma\,(A_3 + B_3) + u\,(A_+ + A_- + B_+ + B_-) + u_{ab}\Big[2(A_3 - B_3) + (A_+ + A_-) - (B_+ + B_-)\Big]$$

Collecting similar terms:

$$\hat{H}' = A_3(2\gamma + 2u_{ab}) + B_3(2\gamma - 2u_{ab}) + (A_+ + A_-)(u + u_{ab}) + (B_+ + B_-)(u - u_{ab})$$

At this point, we can further rotate $\hat{H}'$ around $A_2 := \frac{A_+ - A_-}{2i}$:

$$\hat{H}'' = e^{\frac{\theta_a}{2}(A_+ - A_-)} \hat{H}' e^{-\frac{\theta_a}{2}(A_+ - A_-)}$$

The various addends transform as follows:

$$e^{\frac{\theta_a}{2}(A_+ - A_-)} A_3 e^{-\frac{\theta_a}{2}(A_+ - A_-)} = \cosh\theta_a A_3 - \frac{1}{2}\sinh\theta_a (A_+ + A_-)$$

$$e^{\frac{\theta_a}{2}(A_+ - A_-)} B_3 e^{-\frac{\theta_a}{2}(A_+ - A_-)} = B_3$$

$$e^{\frac{\theta_a}{2}(A_+ - A_-)}\,(A_+ + A_-)\,e^{-\frac{\theta_a}{2}(A_+ - A_-)} = -2\sinh\theta_a\,A_3 + \cosh\theta_a\;(A_+ + A_-)$$

$$e^{\frac{\theta_a}{2}(A_+ - A_-)}(B_+ + B_-)e^{-\frac{\theta_a}{2}(A_+ - A_-)} = (B_+ + B_-)$$

Putting together the transformed addends, one obtains

$$\hat{H}'' = A_3\Big[\cosh\theta_a(2\gamma + 2u_{ab}) - 2\sinh\theta_a(u + u_{ab})\Big] +$$

$$+ (A_+ + A_-)\Big[-\sinh\theta_a(\gamma + u_{ab}) + \cosh\theta_a(u + u_{ab})\Big] +$$

$$+ B_3(2\gamma - 2u_{ab}) + (B_+ + B_-)(u - u_{ab})$$

Non-diagonal term $(A_+ + A_-)$ cancels if one chooses

$$\theta_a = \operatorname{arctanh}\left(\frac{u + u_{ab}}{\gamma + u_{ab}}\right)$$

Hamiltonian $\hat{H}''$ thus reduces to:

$$\hat{H}'' = 2A_3\sqrt{(\gamma - u)(\gamma + u + 2u_{ab})} + B_3(2\gamma - 2u_{ab}) + (B_+ + B_-)(u - u_{ab})$$

Eventually we rotate $\hat{H}''$ around $B_2 = \frac{B_+ - B_-}{2i}$:

$$\hat{H}_d = e^{\frac{\theta_b}{2}(B_+ - B_-)}\hat{H}'' e^{-\frac{\theta_b}{2}(B_+ - B_-)}$$

The addends transform as follows:

$$e^{\frac{\theta_b}{2}(B_+ - B_-)}A_3 e^{-\frac{\theta_b}{2}(B_+ - B_-)} = A_3$$

$$e^{\frac{\theta_b}{2}(B_+ - B_-)}B_3 e^{-\frac{\theta_b}{2}(B_+ - B_-)} = \cosh\theta_b B_3 - \frac{1}{2}\sinh\theta_b(B_+ + B_-)$$

$$e^{\frac{\theta_b}{2}(B_+ - B_-)}(B_+ + B_-) e^{-\frac{\theta_b}{2}(B_+ - B_-)} = -2\sinh\theta_b B_3 + \cosh\theta_b(B_+ + B_-)$$

Putting the transformed addends together, one obtains that

$$\hat{H}_d = 2A_3\sqrt{(\gamma - u)(\gamma + u + 2u_{ab})} +$$

$$+ B_3\Big[\cosh\theta_b(2\gamma - 2u_{ab}) - 2\sinh\theta_b(u - u_{ab})\Big] +$$

$$+ (B_+ + B_-)\Big[-\sinh\theta_b(\gamma - u_{ab}) + \cosh\theta_b(u - u_{ab})\Big]$$

Non-diagonal term $(B_+ + B_-)$ cancels upon setting:

$$\theta_b = \operatorname{arctanh}\left(\frac{u - u_{ab}}{\gamma - u_{ab}}\right)$$

Eventually, the diagonal Hamiltonian reads:

$$\hat{H}_d = 2A_3\sqrt{(\gamma - u)(\gamma + u + 2u_{ab})} + 2B_3\sqrt{(\gamma - u)(\gamma + u - 2u_{ab})}$$

Appendix B

The continuous variable picture

An effective study of the ground state configuration of multimode Bose-Hubbard Hamiltonians can be carried out by reformulating single-site boson populations N_j and M_j in terms of continuous variables $x_j = N_j/N$ and $y_j = M_j/M$ [167, 175, 208, 210, 278]. This approximation, valid if the numbers of bosons $N = \sum_{j=1} N_j$ and $M = \sum_{j=1} M_j$ are large enough, allows one to associate a certain Fock state $|\vec{N}, \vec{M}\rangle = |N_1, \dots, N_L, M_1, \dots, M_L\rangle$ to state $|\vec{x}, \vec{y}\rangle = |x_1, \dots, x_L, y_1, \dots, y_L\rangle$, i.e. to identify integer quantum numbers N_j, $M_j \in \mathbb{N}$ with real numbers x_j, $y_j \in [0,1]$. In this perspective, creation and annihilation processes $N_j \to N_j \pm 1$ ($M_j \to M_j \pm 1$) correspond to small variations $x_j \to x_j \pm \epsilon_a$ ($y_j \to y_j \pm \epsilon_b$), where $\epsilon_a = 1/N \ll 1$ ($\epsilon_b = 1/M \ll 1$). This scheme leads to a new effective Hamiltonian written in terms of coordinates x_j, y_j and of their generalized conjugate momenta [175]. Interestingly, through study of the associated effective potential, one can obtain valuable info concerning the ground-state structure and shine light on the occurrence of mixing-demixing (or localization-delocalization) transitions.

In this Appendix[1], we illustrate this versatile approximation scheme in depth.

---

[1] Note to the reader: part of the content of this Appendix has been published in [206, 238].

Setting the stage: the Bose-Hubbard Hamiltonian. Let us start from the Bose-Hubbard Hamiltonian corresponding to a two-species mixture on a trimer.

$$H = -T_a(A_2^\dagger A_1 + A_1^\dagger A_2 + A_3^\dagger A_2 + A_2^\dagger A_3 + A_1^\dagger A_3 + A_1 A_3^\dagger)+$$

$$+\frac{U_a}{2}\left(A_1^\dagger A_1^\dagger A_1 A_1 + A_2^\dagger A_2^\dagger A_2 A_2 + A_3^\dagger A_3^\dagger A_3 A_3\right) -$$

$$-T_b(B_2^\dagger B_1 + B_1^\dagger B_2 + B_3^\dagger B_2 + B_2^\dagger B_3 + B_1^\dagger B_3 + B_1 B_3^\dagger)+$$

$$+\frac{U_b}{2}\left(B_1^\dagger B_1^\dagger B_1 B_1 + B_2^\dagger B_2^\dagger B_2 B_2 + B_3^\dagger B_3^\dagger B_3 B_3\right) +$$

$$+U_{ab}(N_1 M_1 + N_2 M_2 + N_3 M_3)$$

One should take into account the following two constraints, one for each bosonic species:

$$N_1 + N_2 + N_3 = N$$

$$M_1 + M_2 + M_3 = M$$

The most general state of such a system is a superposition of Fock states:

$$|\psi\rangle = \sum_{N_1}\sum_{N_2}\sum_{N_3}^{*}\sum_{M_1}\sum_{M_2}\sum_{M_3}^{*} C(N_1, N_2, N_3, M_1, M_2, M_3)\ |N_1, N_2, N_3, M_1, M_2, M_3\rangle$$

where symbol $*$ on the summations reminds that one has to respect the two constraints. For simplicity, in the following, we will adopt the convention

$$\vec{N} := (N_1,\, N_2,\, N_3), \qquad \vec{M} := (M_1,\, M_2,\, M_3)$$

Revisiting the eigenvalue problem. The eigenvalue equation which gives stationary solutions is:

$$H|\psi\rangle = E|\psi\rangle$$

Substituting the general expression of $|\psi\rangle$ one obtains a system of coupled algebraic equations for the various C's. For example, recalling that, in general

$$a^\dagger|n\rangle = \sqrt{n+1}|n+1\rangle$$

$$a|n\rangle = \sqrt{n}|n-1\rangle$$

one has that

$$H|\vec{N},\,\vec{M}\rangle = H|N_1,N_2,N_3,M_1,M_2,M_3\rangle =$$

$$= -T_a\Bigg[\sqrt{(N_2+1)N_1}|N_1-1,N_2+1,N_3,M_1,M_2,M_3\rangle +$$

$$+\cdots+$$

$$+\sqrt{(N_3+1)N_1}|N_1-1,N_2,N_3+1,M_1,M_2,M_3\rangle\Bigg]+$$

$$-T_b\Bigg[\sqrt{(M_2+1)M_1}|N_1,N_2,N_3,M_1-1,M_2+1,M_3\rangle +$$

$$+\cdots+$$

$$+\sqrt{(M_3+1)M_1}|N_1,N_2,N_3,M_1-1,M_2,M_3+1\rangle\Bigg]+$$

$$+\frac{U_a}{2}\sum_{j=1}^{3}N_j(N_j-1)|\vec{N},\,\vec{M}\rangle + \frac{U_b}{2}\sum_{j=1}^{3}M_j(M_j-1)|\vec{N},\,\vec{M}\rangle +$$

$$+U_{ab}\sum_{j=1}^{3}N_jM_j|\vec{N},\,\vec{M}\rangle$$

At this point one must remember that there is a multiple summation and that the target is to collect all the coefficients of ket-state $|\vec{N},\,\vec{M}\rangle = |N_1,N_2,N_3,M_1,M_2,M_3\rangle$. To this purpose, let us notice that while on-site repulsion terms U_a, U_b and U_{ab} do not modify the state (because they are diagonal in the Fock-states basis), tunnelling terms modify the ket-state. So one has to proceed the other way around: looking for all Fock states that, after the action of tunnelling term, become equal to $|\vec{N},\,\vec{M}\rangle$:

$$A_2^\dagger A_1|N_1+1,N_2-1,N_3,M_1,M_2,M_3\rangle = \sqrt{(N_1+1)N_2}|\vec{N},\,\vec{M}\rangle$$

$$\cdots$$

$$A_3^\dagger A_1|N_1+1,N_2,N_3-1,M_1,M_2,M_3\rangle = \sqrt{(N_1+1)N_3}|\vec{N},\,\vec{M}\rangle$$

and the same reasoning also holds for the tunnelling of the second bosonic species:

$$B_2^\dagger B_1|N_1,N_2,N_3,M_1+1,M_2-1,M_3\rangle = \sqrt{(M_1+1)M_2}|\vec{N},\,\vec{M}\rangle$$

$$\cdots$$

$$B_3^\dagger B_1|N_1, N_2, N_3, M_1+1, M_2, M_3-1\rangle = \sqrt{(M_1+1)M_3}|\vec{N},\, \vec{M}\rangle$$

In conclusion, one can say that the eigenvalue equation $H|\psi\rangle = E|\psi\rangle$ turns into a system of many algebraic equations, one for each ket vector $|\vec{N},\, \vec{M}\rangle$. Notice that the original equation can be split in a system of equations because the various ket vectors, being Fock-states, are orthogonal, and so the equation must be satisfied for each vector. In conclusion, the equation that holds for the coefficients of $|\vec{N},\, \vec{M}\rangle$ is:

$$\begin{gathered}
-T_a\Bigg[\sqrt{(N_1+1)N_2}\; C(N_1+1, N_2-1, N_3, M_1, M_2, M_3)+ \\
+\sqrt{(N_2+1)N_1}\; C(N_1-1, N_2+1, N_3, M_1, M_2, M_3)+ \\
+\sqrt{(N_2+1)N_3}\; C(N_1, N_2+1, N_3-1, M_1, M_2, M_3)+ \\
+\sqrt{(N_3+1)N_2}\; C(N_1, N_2-1, N_3+1, M_1, M_2, M_3)+ \\
+\sqrt{(N_3+1)N_1}\; C(N_1-1, N_2, N_3+1, M_1, M_2, M_3)+ \\
+\sqrt{(N_1+1)N_3}\; C(N_1+1, N_2, N_3-1, M_1, M_2, M_3)\Bigg]- \\
-T_b\Bigg[\sqrt{(M_1+1)M_2}\; C(N_1, N_2, N_3, M_1+1, M_2-1, M_3)+ \\
+\sqrt{(M_2+1)M_1}\; C(N_1, N_2, N_3, M_1-1, M_2+1, M_3)+ \\
+\sqrt{(M_2+1)M_3}\; C(N_1, N_2, N_3, M_1, M_2+1, M_3-1)+ \\
+\sqrt{(M_3+1)M_2}\; C(N_1, N_2, N_3, M_1, M_2-1, M_3+1)+ \\
+\sqrt{(M_3+1)M_1}\; C(N_1, N_2, N_3, M_1-1, M_2, M_3+1)+ \\
+\sqrt{(M_1+1)M_3}\; C(N_1, N_2, N_3, M_1+1, M_2, M_3-1)\Bigg]+ \\
+\frac{U_a}{2}\sum_{j=1}^{3} N_j(N_j-1)C(\vec{N},\, \vec{M}) + \frac{U_b}{2}\sum_{j=1}^{3} M_j(M_j-1)C(\vec{N},\, \vec{M})+
\end{gathered}$$

$$+U_{ab}\sum_{j=1}^{3} N_j M_j C(\vec{N},\,\vec{M}) = E\;C(\vec{N},\,\vec{M})$$

This methodology was first discussed in [212].

B.1 From discrete to continuous variables

Under the assumptions that the numbers of bosons in the system are large enough (i.e. $N,\,M \gg 1$), one can perform a second-order Taylor expansion for the C's. In general one has that:

$$f(x_0+\Delta x, y_0+\Delta y) \approx f(x_0,y_0) + \left.\frac{\partial f}{\partial x}\right|_{(x_0,y_0)} \Delta x + \left.\frac{\partial f}{\partial y}\right|_{(x_0,y_0)} \Delta y +$$

$$+\frac{1}{2}\left.\frac{\partial^2 f}{\partial x^2}\right|_{(x_0,y_0)} (\Delta x)^2 + \left.\frac{\partial^2 f}{\partial x \partial y}\right|_{(x_0,y_0)} \Delta x\,\Delta y + \frac{1}{2}\left.\frac{\partial^2 f}{\partial y^2}\right|_{(x_0,y_0)} (\Delta y)^2$$

So, one can approximate the various coefficients (see [213]) as follows

$$C(N_1+1, N_2-1, N_3, M_1, M_2, M_3) \approx C(\vec{N},\,\vec{M}) +$$

$$+\left[+\frac{\partial C}{\partial N_1} - \frac{\partial C}{\partial N_2} + \frac{1}{2}\frac{\partial^2 C}{\partial N_1^2} - \frac{\partial^2 C}{\partial N_1 \partial N_2} + \frac{1}{2}\frac{\partial^2 C}{\partial N_2^2}\right]$$

$$C(N_1-1, N_2+1, N_3, M_1, M_2, M_3) \approx C(\vec{N},\,\vec{M}) +$$

$$+\left[-\frac{\partial C}{\partial N_1} + \frac{\partial C}{\partial N_2} + \frac{1}{2}\frac{\partial^2 C}{\partial N_1^2} - \frac{\partial^2 C}{\partial N_1 \partial N_2} + \frac{1}{2}\frac{\partial^2 C}{\partial N_2^2}\right]$$

$$\dots$$

$$C(N_1, N_2, N_3, M_1+1, M_2, M_3-1) \approx C(\vec{N},\,\vec{M}) +$$

$$+\left[-\frac{\partial C}{\partial M_3} + \frac{\partial C}{\partial M_1} + \frac{1}{2}\frac{\partial^2 C}{\partial M_3^2} - \frac{\partial^2 C}{\partial M_3 \partial M_1} + \frac{1}{2}\frac{\partial^2 C}{\partial M_1^2}\right]$$

Terms including square roots can be simplified as follows

$$\sqrt{(N_1+1)N_2} = \sqrt{N_1 N_2 + N_2} = \sqrt{N_1 N_2\left(1+\frac{1}{N_1}\right)} =$$

$$= \sqrt{N_1 N_2}\sqrt{1+\frac{1}{N_1}} \approx \sqrt{N_1 N_2}\left(1+\frac{1}{2N_1}\right) = \sqrt{N_1 N_2} + \frac{1}{2}\sqrt{\frac{N_2}{N_1}}$$

Now we are ready to introduce normalized quantities:

$$\vec{x} = (x_1,\, x_2,\, x_3) = \frac{1}{N}(N_1,\, N_2,\, N_3) = \frac{\vec{N}}{N}$$

$$\vec{y} = (y_1,\, y_2,\, y_3) = \frac{1}{M}(M_1,\, M_2,\, M_3) = \frac{\vec{M}}{M}$$

Of course the two constraints, i.e. the conservation of the total numbers of bosons read:

$$\sum_{j=1}^{3} N_j = N \qquad \Rightarrow \qquad \sum_{j=1}^{3} x_j = 1$$

$$\sum_{j=1}^{3} M_j = M \qquad \Rightarrow \qquad \sum_{j=1}^{3} y_j = 1$$

Let us study, e.g. the effect of these variable substitutions on the first term:

$$C(\vec{N},\, \vec{M}) + \left[\frac{\partial C}{\partial N_1} - \frac{\partial C}{\partial N_2} + \frac{1}{2}\frac{\partial^2 C}{\partial N_1^2} - \frac{\partial^2 C}{\partial N_1 \partial N_2} + \frac{1}{2}\frac{\partial^2 C}{\partial N_2^2}\right]$$

$$\Downarrow$$

$$C(\vec{x},\, \vec{y}) + \frac{1}{N}\left[\frac{\partial C}{\partial x_1} - \frac{\partial C}{\partial x_2}\right] + \frac{1}{N^2}\left[\frac{1}{2}\frac{\partial^2 C}{\partial x_1^2} - \frac{\partial^2 C}{\partial x_1 \partial x_2} + \frac{1}{2}\frac{\partial^2 C}{\partial x_2^2}\right]$$

Square-root-like terms transform as follows:

$$\sqrt{N_1 N_2} + \frac{1}{2}\sqrt{\frac{N_2}{N_1}} = N\sqrt{x_1 x_2} + \frac{1}{2}\sqrt{\frac{x_2}{x_1}}$$

$$\sqrt{N_1 N_2} + \frac{1}{2}\sqrt{\frac{N_1}{N_2}} = N\sqrt{x_1 x_2} + \frac{1}{2}\sqrt{\frac{x_1}{x_2}}$$

Putting all the terms together, one obtains:

$$\left(N\sqrt{x_1 x_2} + \frac{1}{2}\sqrt{\frac{x_2}{x_1}}\right) \times$$

$$\times\left[C(\vec{x},\,\vec{y})+\frac{1}{N}\left(\frac{\partial C}{\partial x_1}-\frac{\partial C}{\partial x_2}\right)+\frac{1}{N^2}\left(\frac{1}{2}\frac{\partial^2 C}{\partial x_1^2}-\frac{\partial^2 C}{\partial x_1\partial x_2}+\frac{1}{2}\frac{\partial^2 C}{\partial x_2^2}\right)\right]+$$

$$+\left(N\sqrt{x_1x_2}+\frac{1}{2}\sqrt{\frac{x_1}{x_2}}\right)\times$$

$$\times\left[C(\vec{x},\,\vec{y})+\frac{1}{N}\left(\frac{\partial C}{\partial x_2}-\frac{\partial C}{\partial x_1}\right)+\frac{1}{N^2}\left(\frac{1}{2}\frac{\partial^2 C}{\partial x_1^2}-\frac{\partial^2 C}{\partial x_1\partial x_2}+\frac{1}{2}\frac{\partial^2 C}{\partial x_2^2}\right)\right]=$$

$$\approx 2N\sqrt{x_1x_2}\;C+\frac{1}{2N}\left(\sqrt{\frac{x_2}{x_1}}-\sqrt{\frac{x_1}{x_2}}\right)\left(\frac{\partial C}{\partial x_1}-\frac{\partial C}{\partial x_2}\right)+$$

$$+\frac{1}{N}\sqrt{x_1x_2}\left(\frac{\partial^2 C}{\partial x_1^2}-2\frac{\partial^2 C}{\partial x_1\partial x_2}+\frac{\partial^2 C}{\partial x_2^2}\right)$$

Check. It corresponds to formula

$$(\partial_r-\partial_s)\,\sqrt{x_rx_s}(\partial_r-\partial_s)=$$

presented in [167], in fact:

$$(\partial_r-\partial_s)\,\sqrt{x_rx_s}(\partial_r-\partial_s)=$$

$$=\frac{1}{2}\left(\sqrt{\frac{x_s}{x_r}}-\sqrt{\frac{x_r}{x_s}}\right)(\partial_r-\partial_s)+\sqrt{x_rx_s}\left(\frac{\partial^2}{\partial x_r^2}-2\frac{\partial^2}{\partial x_r\partial x_s}+\frac{\partial^2}{\partial x_s^2}\right)$$

Of course the first addend, $2N\sqrt{x_1x_2}C$, does not belong to the generalized Laplacian but must be moved to the generalized potential.

Effective equation. The final equation reads:

$$(D+V)C=E\;C \tag{B.1}$$

where the generalized Laplacian reads

$$D=-\frac{T_a}{N}\sum_{j=1}^{3}\Big[(\partial_j-\partial_{j+1})\sqrt{x_jx_{j+1}}(\partial_j-\partial_{j+1})\Big]+$$

$$-\frac{T_b}{M}\sum_{j=1}^{3}\Big[(\partial_j-\partial_{j+1})\sqrt{y_j y_{j+1}}(\partial_j-\partial_{j+1})\Big]$$

and where the generalized potential reads

$$V=-2NT_a\sum_{j=1}^{3}\sqrt{x_j x_{j+1}}-2MT_b\sum_{j=1}^{3}\sqrt{y_j y_{j+1}}+$$
$$+\frac{U_aN^2}{2}\sum_{j=1}^{3}x_j(x_j-\epsilon_a)+\frac{U_bM^2}{2}\sum_{j=1}^{3}y_j(y_j-\epsilon_b)+$$
$$+U_{ab}NM\sum_{j=1}^{3}x_j y_j. \tag{B.2}$$

B.2 The role of the effective potential

If one wants to determine the system ground state, eigenvalue problem (B.1) can be reduced to the search for the global minimum of effective potential V [see formula (B.2)], provided that the minimum-energy solution $C(\vec{x},\,\vec{y})$ is well localized in the global minimum of V itself. This is certainly the case if boson populations N and M are large enough, the central hypothesis under which the CVP approximation scheme can be safely applied. Notice, in this regard that the generalized Laplacian D goes as N_c^{-1} while the effective potential V goes as N_c^2, with $c=a,\,b$ (as already noticed in Reference [175]).

In the following, we focus on effective potential (B.2) and we use it in order to obtain meaningful information about the ground-state structure as a function of the model parameters. Preliminarily, one should notice that, in the CVP framework, expressions $N=\sum_{j=1}^{3}N_j$ and $M=\sum_{j=1}^{3}M_j$, giving the particle numbers conservation, read $1=\sum_{i=1}^{3}x_i$ and $1=\sum_{j=1}^{3}y_j$ respectively. This circumstance entails that the two terms proportional to ϵ_a and ϵ_b represent constant quantities and can therefore be neglected. In the following, we will show how to determine the global minimum of V in the simple case of twin species, i.e. by setting $T_a=T_b=:T$, $U_a=U_b=:U$ and $N=M$ in expression (B.2):

$$V=-2NT\left(\sqrt{x_1x_2}+\sqrt{x_2x_3}+\sqrt{x_3x_1}+\sqrt{y_1y_2}+\sqrt{y_2y_3}+\sqrt{y_3y_1}\right)+$$

$$
+\frac{UN^2}{2}\left(x_1^2+x_2^2+x_3^2+y_1^2+y_2^2+y_3^2\right)+
$$

$$
+\,WN^2\left[x_1y_1+x_2y_2+x_3y_3\right] \tag{B.3}
$$

Of course the case of asymmetric species (discussed in Section 4.2-4.3) can be investigated in the same way, although the analytic computations get more cumbersome.

Minimum-energy configuration for $T=0$: need for an exhaustive exploration of a polytope-like domain. If the tunnelling is suppressed, effective potential (B.3) simplifies as follows

$$
\mathcal{V}=\frac{UN^2}{2}\left(x_1^2+x_2^2+x_3^2+y_1^2+y_2^2+y_3^2\right)+WN^2\left(x_1y_1+x_2y_2+x_3y_3\right), \tag{B.4}
$$

where $x_3=1-x_1-x_2$ and $y_3=1-y_1-y_2$ are, actually, dependent variables. The minimum-energy configuration corresponds to the global minimum of $\mathcal{V}(x_1,x_2,y_1,y_2)$, which is a function $\mathcal{V}:\mathcal{D}\subset\mathbb{R}^4\to\mathbb{R}$. The domain $\mathcal{D}$ is a 4-polytope, consisting in the direct product of two triangular regions in $\mathbb{R}^2$, as shown in Fig. B.1 (left panel). Computing the gradient with respect to the four independent variables, one finds that the only stationary point is the one associated to the uniform configuration, i.e $x_1=x_2=y_1=y_2=1/3$, corresponding to

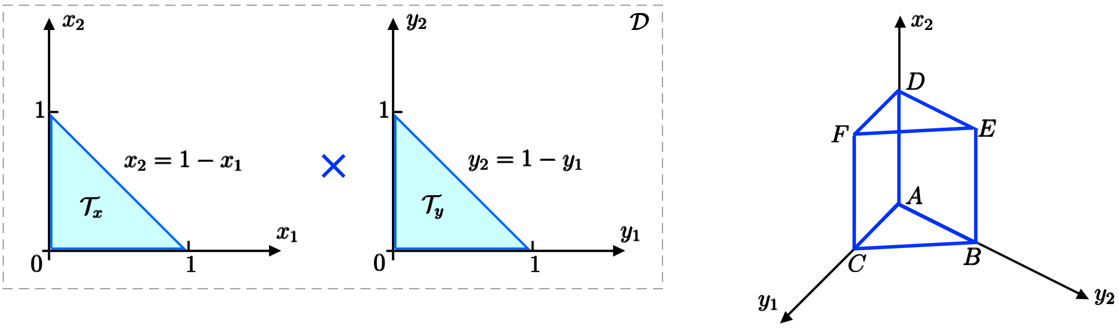

Figure B.1: Left panel: the domain of function $\mathcal{V}$ is the direct product of two triangular bi-dimensional regions. Right panel: one of the three-dimensional objects which constitutes the boundary of the 4-polytope $\mathcal{D}$.

$$
\mathcal{V}\left(\frac{1}{3},\frac{1}{3},\frac{1}{3},\frac{1}{3}\right)=\frac{N^2}{3}(U+W). \tag{B.5}
$$

The eigenvalues of the associated Hessian matrix show that this stationary point is a minimum provided that $W < U$. Notice that, in general, computing the stationary points does not necessarily give the *global* minimum. The latter, in fact, can live on the boundary of the domain $\mathcal{D}$, in a point where the four-dimensional gradient is not well defined. So, one has to compare the value of $\mathcal{V}$ at the local minimum, i.e. $N^2(U+W)/3$, with the values of $\mathcal{V}$ at the boundary of $\mathcal{D}$.

The exhaustive exploration of the domain boundary is a fortiori necessary when $W > U$ i.e. when the stationary point $x_1 = x_2 = y_1 = y_2 = 1/3$ is no longer a minimum, a circumstance which entails that the global minimum lives on the domain boundary. The complexity of our problem is due to the fact that the domain of $\mathcal{V}$ is four-dimensional and so its boundary is the union of six three-dimensional objects of the type sketched in Fig. B.1 (right panel). Each of them corresponds to a Cartesian product $I'_j \times \mathcal{T}_x$ and $I_j \times \mathcal{T}_y$ (where I_j and I'_j, with $j = 1, 2, 3$ are the edges of triangles $\mathcal{T}_x$ and $\mathcal{T}_y$, respectively) and constitutes the domain of a 3-variable function obtained by introducing an additional constraint in formula (B.4). In the same spirit, the global minimum of these constrained functions must be searched not only in the interior of their domain (imposing the stationarity of a three-dimensional gradient), but also on their boundaries, by means of an exhaustive exploration thereof. One therefore iterates this process looking for stationary points, at first inside the *volume*, then on the *faces*, on the *edges* (employing, at each step, a lower-dimensional gradient) and, eventually, evaluates the function at the *vertices* of this 3D region. The resulting set of candidates for the global minimum is such that each local minimum is linked to an existence condition (typically, an inequality in the one-dimensional space W/U) on the subdomain where it was found. The global minimum, in each interval of the space W/U, is determined by comparing all the possible candidates. In the following we sketch the application of this rather general scheme to our problem.

We start fixing $x_1 = 0$. Notice that the other possible ways of fixing the first variable, i.e. $x_2 = 0$, $x_2 = -x_1 + 1$, $y_1 = 0$, $y_2 = 0$ and $y_2 = -y_1 + 1$ would lead to minimum-energy configurations which are equivalent up to cyclic permutations of the indexes and/or species labels swapping. The resulting constrained function

$$\mathcal{V}_3 = \mathcal{V}(x_2, y_1, y_2\,; x_1 = 0) = UN^2(1 - x_2 + x_2^2 - y_1 + y_1^2 - y_2 + y_1 y_2 + y_2^2)+$$

$$+WN^2(-x_2+y_1+x_2y_1+2x_2y_2)$$

is defined on the *prism* represented in the right panel of Fig. B.1. The stationary point of this 3-variable function, computed imposing $\nabla_{x_2,y_1,y_2}\mathcal{V}_3=(0{,}0{,}0)$, is a local minimum of $\mathcal{V}_3$ if $W<U$ but it must be discarded because the corresponding value of $\mathcal{V}$ is greater than (B.5). Let us focus on the 5 *faces* of this prism. Each face is fixed by introducing an additional constraint. As an example, face ABC is the domain of function

$$\mathcal{V}_2=\mathcal{V}(y_1,\,y_2\,;\,x_1=0,\,x_2=0)=UN^2(1-y_1+y_1^2-y_2+y_1y_2+y_2^2)+$$

$$+WN^2(1-y_1-y_2)$$

Computing the gradient, ∇_{y_1,y_2} one finds that there is one stationary point, which is $\left(y_1=\frac{U+W}{3U},\,y_2=\frac{U+W}{3U}\right)$. This is a minimum (both eigenvalues of the Hessian matrix bigger than 0) in the domain of interest iff $W<U/2$. Nevertheless, the corresponding value of $\mathcal{V}$ is smaller than the uniform-configuration value (B.5) just for $W>U$. But, in this range, this stationary point is no longer a minimum, so it must be discarded. The analysis of the 5 faces, carried out according to this scheme, leads to the conclusion that, for $1<W/U<2$, there are 2 minimum-energy configurations

$$\Big(x_1=0,\quad x_2=\frac{U+W}{2U+W},\quad x_3=\frac{U}{2U+W},$$

$$y_1=\frac{U+W}{2U+W},\quad y_2=0,\quad y_3=\frac{U}{2U+W}\Big)\quad\leftarrow\quad\text{Face ACFD}$$

and

$$\Big(x_1=0,\quad x_2=\frac{U}{2U+W},\quad x_3=\frac{U+W}{2U+W},$$

$$y_1=\frac{U+W}{2U+W},\quad y_2=\frac{U}{2U+W},\quad y_3=0\Big)\quad\leftarrow\quad\text{Face CBEF.}$$

Notice that these two configurations are equivalent up to a permutation of site indexes. The first one has been plotted in Fig. 4.10.

The 9 *edges* of the solid of Fig. B.1 (right panel) are identified by fixing an additional constraint. Their analysis shows that local iso-energetic points of minimum are present in segments CB DF and CF. Such minimum energy configurations are equal up to permutation of site indexes and/or species labels swapping. For example, segment CB is the domain of function

$$\mathcal{V}_1 = \mathcal{V}(y_1\,;\, x_1 = 0,\, x_2 = 0,\, y_2 = 1 - y_1) = UN^2(1 - y_1 + y_1^2).$$

Computing the derivative, $\frac{d}{dy_1}$, one finds that there is only one stationary point, which is $y_1 = \frac{1}{2}$. Computing the second order derivative one can verify that this stationary point is always a local minimum in the physical interval [0,1]. The corresponding value $\frac{3}{4}UN^2$ of $\mathcal{V}$, is less than the one found in faces ACFD and CBEF provided that $W > 2U$. Eventually, the analysis of the 6 *vertices* does not give any further minimum-energy configuration.

The search for the minimum- energy configuration for $T \neq 0$. The minimum-energy configuration is the configuration $(\vec{x}, \vec{y}) = (x_1, x_2, x_3, y_1, y_2, y_3)$ which minimizes effective potential (B.3). The presence of a non-vanishing T constitutes a regularizing term which makes the exploration of the domain boundary no longer necessary. This fact, verified numerically, can be understood in physical terms because the presence of $T \neq 0$ makes configurations where one or more populations are exactly zero impossible. To compute the minimum-energy configuration, one therefore imposes stationary conditions for effective potential V in which $x_3 = 1-x_1-x_2$ and $y_3 = 1-y_1-y_2$ take into account the boson number conservation. The resulting system of equations is

$$\left(\frac{\partial V}{\partial x_1}, \frac{\partial V}{\partial x_2}, \frac{\partial V}{\partial y_1}, \frac{\partial V}{\partial y_2}\right) = (0,0,0,0) \tag{B.6}$$

and the explicit form thereof is

$$\begin{cases} -2NT\left(-\frac{x_2}{\sqrt{-x_2(x_1+x_2-1)}}+\sqrt{\frac{x_2}{x_1}}-\frac{2x_1+x_2-1}{\sqrt{-x_1(x_1+x_2-1)}}\right)+ \\ +2UN^2(2x_1+x_2-1)+2WN^2(2y_1+y_2-1)=0 \\ -2NT\left(-\frac{x_1}{\sqrt{-x_1(x_1+x_2-1)}}+\sqrt{\frac{x_1}{x_2}}-\frac{x_1+2x_2-1}{\sqrt{-x_2(x_1+x_2-1)}}\right)+ \\ +2UN^2(x_1+2x_2-1)+2WN^2(y_1+2y_2-1)=0 \\ -2NT\left(-\frac{y_2}{\sqrt{-y_2(y_1+y_2-1)}}+\sqrt{\frac{y_2}{y_1}}-\frac{2y_1+y_2-1}{\sqrt{-y_1(y_1+y_2-1)}}\right)+ \\ +2UN^2(2y_1+y_2-1)+2WN^2(2x_1+x_2-1)=0 \\ -2NT\left(-\frac{y_1}{\sqrt{-y_1(y_1+y_2-1)}}+\sqrt{\frac{y_1}{y_2}}-\frac{y_1+2y_2-1}{\sqrt{-y_2(y_1+y_2-1)}}\right)+ \\ +2UN^2(y_1+2y_2-1)+2WN^2(x_1+2x_2-1)=0. \end{cases} \tag{B.7}$$

In general, it is not possible to find all the possible solutions of this system in a closed form and one needs to resort to numerical methods. Boson populations shown in Fig. 4.11 not only fulfill system (B.7), but have been checked (by evaluating the eigenvalues of each associated Hessian matrix), to be minimum points of the effective potential (B.3). As already mentioned, Fig. 4.11 illustrates a particular *family* of solutions, meaning that those configurations which are obtained by means of cyclic permutations of site indexes and/or by species-labels swapping, are still solutions of system (B.7) and therefore points of minimum of (B.3).

It is worth noticing that a particularly simple and significant solution of system (B.7) is the one which corresponds to the uniform configuration $x_1 = x_2 = y_1 = y_2 = 1/3$. This stationary point is a minimum of (B.3) provided that the associated Hessian matrix

$$\boldsymbol{H} = N^2 \begin{pmatrix} \frac{9T}{N}+2U & \frac{9T}{2N}+U & 2W & W \\ \frac{9T}{2N}+U & \frac{9T}{N}+2U & W & 2W \\ 2W & W & \frac{9T}{N}+2U & \frac{9T}{2N}+U \\ W & 2W & \frac{9T}{2N}+U & \frac{9T}{N}+2U \end{pmatrix} \tag{B.8}$$

is definite positive, a condition which is verified iff $W/U < 1 + (9T)/(2UN)$. This argument proves the correctness of critical value (4.15), presented in the main text and corresponding to purple solid lines in Fig. 4.13.

An effective way to reduce the complexity of system (B.6) (and possibly simplify its numerical solution) comes from the symmetry which marks the boson populations when the system is in phase (ii) (see central regions of Fig. 4.11 panels). In such phase, i.e. for moderate W/U values, one can notice, in fact, that $y_2 = x_1$ and $y_1 = x_2$, two constraints that allow to rewrite system (B.6) as

$$\begin{cases} -2NT\left(-\frac{x_2}{\sqrt{-x_2(x_1+x_2-1)}}+\sqrt{\frac{x_2}{x_1}}-\frac{2x_1+x_2-1}{\sqrt{-x_1(x_1+x_2-1)}}\right)+ \\ +2UN^2(2x_1+x_2-1)+2WN^2(x_1+2x_2-1)=0 \\ -2NT\left(-\frac{x_1}{\sqrt{-x_1(x_1+x_2-1)}}+\sqrt{\frac{x_1}{x_2}}-\frac{x_1+2x_2-1}{\sqrt{-x_2(x_1+x_2-1)}}\right)+ \\ +2UN^2(x_1+2x_2-1)+2WN^2(2x_1+x_2-1)=0. \end{cases} \tag{B.9}$$

The orange dashed lines in Fig. 4.13, which constitute the border between the intermediate and the fully demixed phase, have no analytical expression and correspond to those solutions of system (B.9) which are no longer minimum points for effective potential (B.3), i.e. to stationary points for which at least one Hessian-matrix eigenvalue vanishes. Incidentally, critical condition (4.15), obtained “from the left" by means of Hessian matrix (B.8), can be obtained “from the right" also. This can be understood by linearizing equations (B.9) around the known solution $\left(x_1 = \frac{1}{3}, x_2 = \frac{1}{3}\right)$. Substituting $x_1 = \frac{1}{3} - \epsilon_1$ and $x_2 = \frac{1}{3} + \epsilon_2$ and expanding up to the first order for $\epsilon_1 \to 0$ and $\epsilon_2 \to 0$, one gets

$$\begin{cases} \epsilon_1(-9NT-2UN^2-WN^2)+\epsilon_2\left(\frac{9NT}{2}+UN^2+2WN^2\right)=0 \\ \epsilon_1\left(-\frac{1}{2}9NT-UN^2-2WN^2\right)+\epsilon_2(9NT+2UN^2+WN^2)=0. \end{cases}$$

This linear system admits non-trivial solutions provided that the determinant is zero, a condition which leads, again, to critical value (4.15).

Appendix C

Entropy of mixing and entropy of location

Along the same lines of [168], we present a rigorous mathematical derivation, which relies on information entropy, of two indicators used, in this thesis, to quantify the mixing and the localization of quantum fluids, namely the entropy of mixing and the entropy of location. The motivation for using Shannon entropy is that the latter naturally follows from some axioms, called Khinchin axioms, a set of properties that a good measure of entropy should posses:

1. It should depend on a certain probability distribution p only;
2. The lowest entropy value (zero, in our case) is obtained when one of the ps is 1 and all the other ps are 0;
3. The highest entropy values is obtained when all the ps are equal to each other;
4. The entropy should be additive with respect to partitions of the outcomes;

In the following, we adopt a classical perspective and consider the bosons as classical particles that can be placed in 3 different boxes (of course, the generalization to $L > 3$ sites is straightforward). n_j (m_j) will be the number of species-a (specie-b) bosons in the j-th site (with $j = 1, 2, 3$). The total number of species-a (specie-b) bosons is $\sum_{j=1}^{3} n_j = N$ ($\sum_{j=1}^{3} m_j = M$). Let us start by introducing normalized local populations:

$$x_j = \frac{n_j}{N}, \qquad y_j = \frac{m_j}{M}$$

and let us introduce the joint probability of finding a fraction of species c, where $c = \{n, m\}$ in site j:

$$p_{c,j} = \frac{c_j}{2C}$$

So, practically:

$$p_{n,j} = \frac{n_j}{2N}, \qquad p_{m,j} = \frac{m_j}{2M}.$$

Notice that this probability distribution is well normalized, in fact:

$$\sum_{j=1}^{3} (p_{n,j} + p_{m,j}) = \frac{N}{2N} + \frac{M}{2M} = 1.$$

Then, using Bayes theorem, we factor this joint probability:

$$p_{c,j} = p_{c|j}\, p_j$$

where

$$p_{n|j} = \frac{\frac{n_j}{N}}{\frac{n_j}{N} + \frac{m_j}{M}}, \qquad p_{m|j} = \frac{\frac{m_j}{M}}{\frac{n_j}{N} + \frac{m_j}{M}}$$

and

$$p_j = \frac{\frac{n_j}{N} + \frac{m_j}{M}}{2}$$

One can notice that p_j is correctly normalized, in fact:

$$\sum_{j=1}^{3} p_j = \frac{\frac{N}{N} + \frac{M}{M}}{2} = 1.$$

Also the conditional probability distribution is well normalized, in fact, it is clear that:

$$p_{n|j} + p_{m|j} = \frac{\frac{n_j}{N} + \frac{m_j}{M}}{\frac{n_j}{N} + \frac{m_j}{M}} = 1, \qquad \forall j.$$

The total entropy of the system is defined as

$$S = -\sum_{c=\{n,m\}} \sum_{j=1}^{3} p_{c,j} \log p_{c,j}$$

Substituting Bayes' factorization, one gets:

$$S = -\sum_{c=\{n,m\}} \sum_{j=1}^{3} p_{c|j} p_j \log \left(p_{c|j} p_j \right) =$$

$$= -\sum_{j=1}^{3} \left[p_{n|j} p_j \log \left(p_{n|j} p_j \right) + p_{m|j} p_j \log \left(p_{m|j} p_j \right) \right] =$$

$$= -\sum_{j=1}^{3} p_j \left(p_{n|j} \log p_{n|j} + p_{m|j} \log p_{m|j} \right) - \sum_{j=1}^{3} (p_{n|j} + p_{m|j}) p_j \log p_j$$

Recalling that $p_{n|j} + p_{m|j} = 1$, $\forall j$, one obtains that

$$S = -\sum_{j=1}^{3} p_j \left(p_{n|j} \log p_{n|j} + p_{m|j} \log p_{m|j} \right) - \sum_{j=1}^{3} p_j \log p_j$$

The first part goes under the name of entropy of mixing

$$S_{mix} = -\sum_{j=1}^{3} p_j \left(p_{n|j} \log p_{n|j} + p_{m|j} \log p_{m|j} \right) =$$

$$= -\sum_{j=1}^{3} \left(\frac{n_j}{2N} + \frac{m_j}{2M} \right) \left(\frac{\frac{n_j}{N}}{\frac{n_j}{N} + \frac{m_j}{M}} \log \frac{\frac{n_j}{N}}{\frac{n_j}{N} + \frac{m_j}{M}} + \frac{\frac{m_j}{M}}{\frac{n_j}{N} + \frac{m_j}{M}} \log \frac{\frac{m_j}{M}}{\frac{n_j}{N} + \frac{m_j}{M}} \right),$$

an expression which, after some algebra, reads

$$S_{mix} = -\frac{1}{2} \sum_{j=1}^{3} \left(\frac{n_j}{N} \log \frac{\frac{n_j}{N}}{\frac{n_j}{N} + \frac{m_j}{M}} + \frac{m_j}{M} \log \frac{\frac{m_j}{M}}{\frac{n_j}{N} + \frac{m_j}{M}} \right).$$

The second part gives the entropy relevant to the boson distributions among the wells and goes under the name of entropy of location:

$$S_{loc} = -\sum_{j=1}^{3} p_j \log p_j = -\sum_{j=1}^{3} \frac{\frac{n_j}{N} + \frac{m_j}{M}}{2} \log \left(\frac{\frac{n_j}{N} + \frac{m_j}{M}}{2} \right).$$

The total entropy of the system can be therefore written as the sum of the entropy of mixing and the entropy of location:

$$S = S_{mix} + S_{loc}.$$

Appendix D

Numerical solution of stationary Gross-Pitaevskii equations

Let us consider[1] the following non-linear, coupled, eigenvalue problem:

$$-\frac{\hbar^2}{2m_a}\nabla^2\varphi_a + g_a|\varphi_a|^2\varphi_a + g_{ab}|\varphi_b|^2\varphi_a + V_{ext,a}\varphi_a = \mu_a\varphi_a$$

$$-\frac{\hbar^2}{2m_b}\nabla^2\varphi_b + g_b|\varphi_b|^2\varphi_b + g_{ab}|\varphi_a|^2\varphi_b + V_{ext,b}\varphi_b = \mu_b\varphi_b$$

with normalization conditions

$$\int_{-\infty}^{+\infty} |\varphi_a|^2 \,\mathrm{d}^3x = N_a, \qquad \int_{-\infty}^{+\infty} |\varphi_b|^2 \,\mathrm{d}^3x = N_b$$

Our aim is to find the eigensolutions φ_a and φ_b which minimize the energy functional

$$\mathcal{H}[\varphi_a, \varphi_b] = \int \varphi_a^* \left[-\frac{\hbar^2}{2m_a}\nabla^2 + V_{ext,a}\right] \varphi_a \,\mathrm{d}^3x + \frac{g_a}{2}\int |\varphi_a|^4 \,\mathrm{d}^3x +$$

---

[1] Note to the reader: part of the content of this Appendix has been published in [176].

$$+\int \varphi_b^* \left[-\frac{\hbar^2}{2m_b}\nabla^2 + V_{ext,b}\right]\varphi_b \,\mathrm{d}^3x + \frac{g_b}{2}\int |\varphi_b|^4 \,\mathrm{d}^3x + g_{ab}\int |\varphi_a|^2|\varphi_b|^2 \,\mathrm{d}^3x,$$

We solve this problem by means of a numerical technique based on the damped oscillating particle method [66]. Preliminary, in order to lighten the computational burden, we enact a dimensional reduction (in the spirit of the scheme discussed in [279, 280]) to turn the original genuinely 3D problem into a 1D one. This is obtained by means of factorizations

$$\psi_a = \psi_a(x,y,z) = \psi_{a,x}(x)\psi_{a,y,z}(y,z) = \psi_{a,x}(x)\frac{1}{\sqrt{L_y}}\frac{1}{\sqrt{L_z}}$$

$$\psi_b = \psi_b(x,y,z) = \psi_{b,x}(x)\psi_{b,y,z}(y,z) = \psi_{b,x}(x)\frac{1}{\sqrt{L_y}}\frac{1}{\sqrt{L_z}}$$

where ψ_a and ψ_b are such that

$$\varphi_a = \sqrt{N_a}\psi_a, \qquad \varphi_b = \sqrt{N_b}\psi_b$$

and are therefore normalized to unity, as a consequence of normalization conditions (4.10). These substitutions lead to equations

$$-\frac{\partial^2}{\partial x^2}\psi_a + \gamma_a|\psi_a|^2\psi_a + \gamma_{ab}|\psi_b|^2\psi_a + \tilde{V}_{ext,a}\psi_a = \tilde{\mu}_a\psi_a \tag{D.1}$$

$$-\frac{\partial^2}{\partial x^2}\psi_b + \gamma_b|\psi_b|^2\psi_b + \gamma_{ba}|\psi_a|^2\psi_b + \tilde{V}_{ext,b}\psi_b = \tilde{\mu}_b\psi_b \tag{D.2}$$

(notice that wave functions labels "a, x" and "b, x" are understood) whose effective parameters are

$$\gamma_a = \frac{2m_a g_a N_a}{L_y L_z \hbar^2}, \qquad \gamma_{ab} = \frac{2m_a g_{ab} N_b}{L_y L_z \hbar^2}, \qquad \tilde{\mu}_a = \frac{2m_a}{\hbar^2}\mu_a,$$

$$\gamma_b = \frac{2m_b g_b N_b}{L_y L_z \hbar^2}, \qquad \gamma_{ba} = \frac{2m_b g_{ab} N_a}{L_y L_z \hbar^2}, \qquad \tilde{\mu}_b = \frac{2m_b}{\hbar^2}\mu_b.$$

where L_y and L_z are chosen in a such a way that $L_y \approx L_z \approx 2\sigma \approx 2\mu m$. Moreover, the optical-potential terms read:

$$\tilde{V}_{ext,a} = -\frac{2m_a}{\hbar^2} P_a \sum_{i=1}^{3} e^{-\frac{2(x-x_i)^2}{\sigma^2}}, \qquad \tilde{V}_{ext,b} = -\frac{2m_b}{\hbar^2} P_b \sum_{i=1}^{3} e^{-\frac{2(x-x_i)^2}{\sigma^2}}$$

where x_i's are the positions of the centers of each Gaussian trap, expressed in terms of the curvilinear abscissa describing the perimeter of the equilateral triangle formed by the x_i's themselves (see yellow line in Fig. 4.7).

Resorting to the damped oscillating particle method [66], one can turn the search for the ground state of stationary non linear Schrödinger equations (D.1) and (D.2) into the steady-state solution of the following damped oscillators:

$$\frac{\partial^2 \psi_a}{\partial \tau^2} + \eta \frac{\partial \psi_a}{\partial \tau} = \frac{\partial^2}{\partial x^2}\psi_a - \gamma_a |\psi_a|^2 \psi_a - \gamma_{ab} |\psi_b|^2 \psi_a - \tilde{V}_{ext,a}\psi_a + \tilde{\mu}_a \psi_a \tag{D.3}$$

$$\frac{\partial^2 \psi_b}{\partial \tau^2} + \eta \frac{\partial \psi_b}{\partial \tau} = \frac{\partial^2}{\partial x^2}\psi_b - \gamma_b |\psi_b|^2 \psi_b - \gamma_{ba} |\psi_a|^2 \psi_b - \tilde{V}_{ext,b}\psi_b + \tilde{\mu}_b \psi_b \tag{D.4}$$

where the possible differences between left and right members of equations (D.1) and (D.2) act as forcing terms, and where the presence of a non-zero damping η guarantees the convergence to a steady-state solution. Upon recasting equations (D.3) and (D.4) into pairs of first-order equations by means of substitutions

$$q_a = \psi_a, \qquad p_a = \frac{\partial \psi_a}{\partial \tau}, \qquad q_b = \psi_b, \qquad p_b = \frac{\partial \psi_b}{\partial \tau},$$

one can solve the resulting dynamical system with standard finite difference methods[281]. More specifically, we made use of the leapfrog integrator [282], iterating it until equations (D.1) and (D.2) are satisfied up to *relative* errors $< 10^{-3}$ (in order to quantify the mismatch between left and right members, the 2-norm has been employed). It is important to remember that the solutions produced by this method may be false minimum-energy solutions, i.e. solutions of equations (D.3) and (D.4) which do *not* minimize energy functional $\mathcal{H}$. In this case, in fact, the fictitious trajectory of ψ_a and ψ_b in the associated functional space falls and gets stuck at a local minimum of $\mathcal{H}$ but not at its global one. In order to avoid this possible problem, every eigenvalue problem is solved starting from 10 different initial conditions, comparing the energy $\mathcal{H}$ of the resulting eigensolutions and then choosing the ones associated to the lowest value of the energy $\mathcal{H}$.

Appendix E

Demixed stationary configurations and some dynamical remarks

In this Appendix [1] we show how fixed points of motion equations (5.5) modify upon the activation of tunneling processes. Moreover, we make some general remarks on the dynamical properties of the system, which directly affect the miscibility properties of the quantum mixture.

E.1 Stationary configurations featuring demixing

As explained in Section 5.3, the stationary solutions of motion equations (5.3) and (5.4), [corresponding to the FPs of dynamical system (5.5)] which, for $T = 0$, feature perfect demixing, slightly change upon activation of tunnelling processes (compare upper and lower row of Figure 5.1). On top of that, such solutions do not exist at all in certain regions of the parameters space $(W/U, T/(UN))$.

Figures E.1-E.3 show in detail how the stationary configuration changes in a non-narrow range of model parameters. They account both for the variations of boson populations n_j, m_j (different color shades) and for the relative phase between the

---

[1] Note to the reader: part of the content of this Chapter has been published in [214].

wells (numbers within the various regions). Notice that white areas, representing the absence of a certain class of FPs, stand in between different sub-classes. The latter differ in the relative phases between the wells and are three in the "Dimer - Soliton" case, two in the "SDW - Soliton" case and in the "Soliton - Soliton" case as well (see figures 5.3, 5.4 and 5.5 respectively). We conclude by observing that the collective phase difference between the two condensed species play no role in the dynamics of the system [see Hamiltonian (5.2)], so figures 5.3-5.5 have been drawn arbitrarily setting $\Phi_1 = \Psi_1 = 0$.

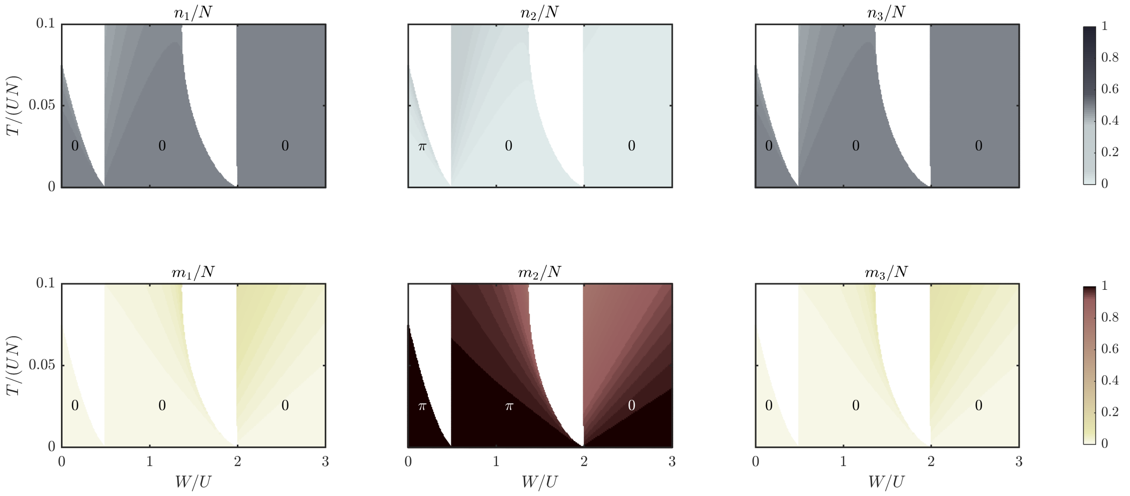

Figure E.1: Class of FPs of the type Dimer - Soliton. Each column corresponds to a well while each row to a different condensed species. The color corresponds to the fraction of bosons hosted by the well (see color bars) while numbers 0 and π indicate the phase shift with respect to the first well. In the white regions, this kind of stationary configuration does not exist.

E.2 Remarks on the dynamical behaviour of trajectories starting close to a fixed point

In the following, we describe the qualitative behaviour of a trajectory which, at $t = 0$, starts from a point $\vec{z}_0$ very close to a FP $\vec{z}_*$. To this end we consider 4 different kinds of FPs $\vec{z}^*$ corresponding to different kinds of stability/instability.

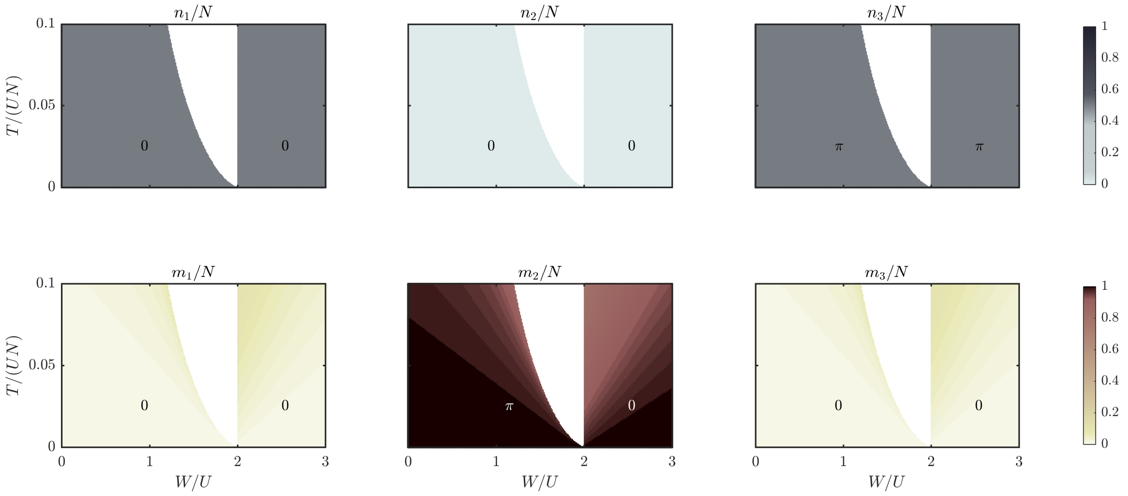

Figure E.2: Class of FPs of the type SDW - Soliton. Each column corresponds to a well while each row to a different condensed species. The color corresponds to the fraction of bosons hosted by the well (see color bars) while numbers 0 and π indicate the phase shift with respect to the first well. In the white region, this kind of stationary configuration does not exist.

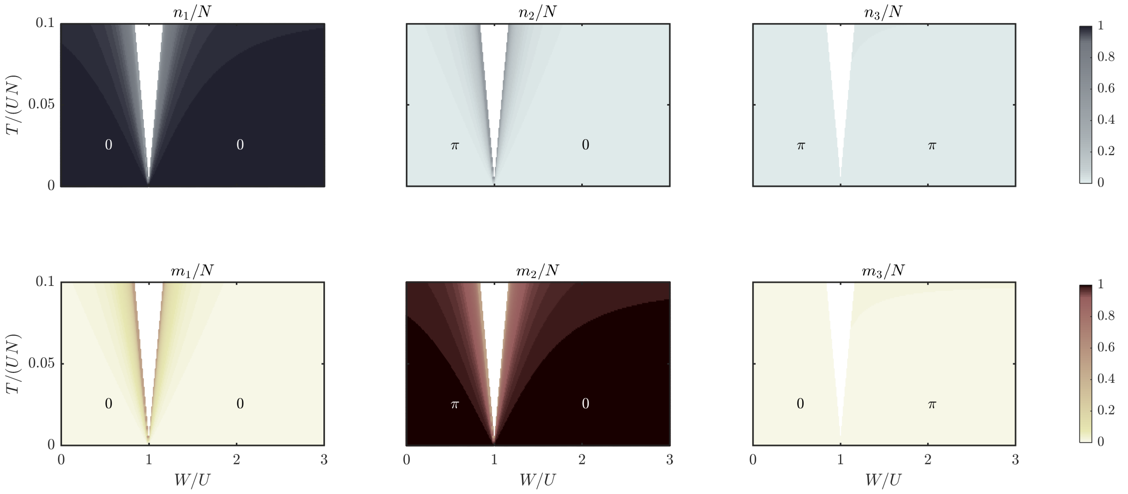

Figure E.3: Class of FPs of the type Soliton - Soliton. Each column corresponds to a well while each row to a different condensed species. The color corresponds to the fraction of bosons hosted by the well (see color bars) while numbers 0 and π indicate the phase shift with respect to the first well. In the white region, this kind of stationary configuration does not exist.

Linearly-stable FP. The solutions of the linearized system of differential equations $\dot{\vec{y}} = \mathbb{J}(\vec{z}_*)\,\vec{y}$ induced by matrix (5.9) correspond to small oscillations around a given equilibrium point $\vec{z}_*$ [231], the characteristic frequencies thereof being $\omega_j = \mathcal{I}\{\lambda_j\}$, where λ_j's are the eigenvalues of matrix (5.9). The effectiveness of the solutions of the linearized equations in representing those of the actual non-linear equations has been discussed in Section 5.4.3.

Energetically-stable FP. Energetic stability is stronger than linear stability, as one can prove that if the initial configuration $\vec{z}_0$ is sufficiently close to FP $\vec{z}_*$, solutions of the actual non linear system (5.6) remain arbitrarily close to those of the linearized one *for all times* and, moreover, there are no issues associated to the commensurability of characteristic frequencies ω_j's.

Linearly-unstable FP. A point of linear instability (also called dynamic instability [198]) is such that almost every trajectory will depart from it. For a generic (i.e. non necessarily Hamiltonian) dynamical system, a trajectory starting close to an unstable FP can have any sort of behaviour (e.g. fall towards a FP, towards a periodic orbit, become chaotic, etc.). Since we are dealing with an *Hamiltonian* system, one knows a priori that the relevant flow in the phase space is incompressible, so the number of possible alternatives decreases. Despite not rigorously proven [2], as the number of effective degrees freedom is relatively high ($D = 4$), one can expect that linearly unstable FPs are surrounded by chaos (see Appendix E.3). The validity of this reasonable ansatz is confirmed by the explicit calculation of the first Lyapunov exponent along trajectories starting close to FPs $\vec{z}_*$ (compare second and third row of Figure 5.2).

Energetically-unstable FP. An energetically-unstable FP can be linearly stable (but not viceversa), so the qualitative behaviour of a trajectory starting from its neighborhood strongly depends on the linear stability of $\vec{z}_*$ and, as already discussed, on the possible commensurability of characteristic frequencies ω_j's. Although we have restricted our analysis to isolated systems at zero temperature, it is worth mentioning that, if dissipation is introduced or in presence of thermalization

---

[2] Consider, as a counter example, a particle in a one-dimensional double-well-like potential centered at $x = 0$. Of course the local maximum present at $x = 0$ is a linearly unstable FP. Nevertheless trajectories starting in a neighborhood thereof are regular.

processes, an energetically-unstable system will tend to decay to an energetically-stable state [268].

E.3 On the structure of phase space

The phase space associated to Hamiltonian dynamical system 5.6 seems to be 12-dimensional as, for each of the two condensed species and for each of the three wells, there are two canonically conjugate dynamic variables: local boson number n_j (m_j) and local phase Φ_j (Ψ_j). As discussed in Section 5.3, the relative phase between the two condensed species play no role in the dynamics [see Hamiltonian (5.2)] so one can arbitrarily fix $\Phi_1 = \Psi_1 = 0$. Moreover, as the total number of bosons $N = \sum_{j=1}^{3} n_j$ and $M = \sum_{j=1}^{3} m_j$ constitute two independent conserved quantities, one can substitute $n_1 = N - n_2 - n_3$ and $m_1 = M - m_2 - m_3$. Therefore, the number of effective dynamical variables is 8, which correspond to $D = 4$ degrees of freedom. It is well known, also in the field of ultracold atoms [198], that there is a profound difference between systems featuring $D = 2$ and $D > 2$ degrees of freedom [283]. Only in the first case, the three-dimensional space corresponding to the constant-energy ($\tilde{H} = E$) hypersurface can be divided by the relevant two-dimensional KAM tori into separated regions. Chaotic trajectories, if present, are therefore always topologically confined by KAM tori. For $D > 2$, instead, the latter cannot divide the phase space into separated regions (in the same way as a circumference cannot divide the euclidean space $\mathbb{R}^3$ into two parts). All chaotic regions are therefore interconnected by a very slow percolation-like phenomenon which goes under the name of Arnold diffusion [198, 283]. Nevertheless, they do not occupy the whole constant-energy space, since regular islands are still present (e.g. the neighbourhoods of energetically-stable FPs), the relative measure thereof being still an open problem [237]. In passing, we mention that, when the number of degrees of freedom of a non linear dynamical system tends to infinite, the measure of regular islands tends to zero and so the constant-energy hypersurface gets completely chaotic, thus justifying the ergodic hypothesis and a microcanonical approach to the problem [237].

Bibliography

1. Pitaevskii, L. & Stringari, S. *Bose-Einstein condensation and Superfluidity* (Oxford University Press, 2016).
2. Penrose, O. & Onsager, L. Bose-Einstein Condensation and Liquid Helium. *Phys. Rev.* **104,** 576 (1956).
3. Esslinger, T. *Experimental and Theoretical Aspects of Quantum Gases* (Lecture notes, 2017).
4. Cohen-Tannoudji, C. N. Nobel Lecture: Manipulating atoms with photons. *Rev. Mod. Phys.* **70,** 707 (1998).
5. Phillips, W. D. Nobel Lecture: Laser cooling and trapping of neutral atoms. *Rev. Mod. Phys.* **70,** 721 (1998).
6. Anderson, M. H., Ensher, J. R., Matthews, M. R., Wieman, C. E. & Cornell, E. A. Observation of Bose-Einstein condensation in a dilute atomic vapor. *science,* 198 (1995).
7. Davis, K. B. *et al.* Bose-Einstein Condensation in a Gas of Sodium Atoms. *Phys. Rev. Lett.* **75,** 3969 (1995).
8. Bradley, C. C., Sackett, C. A., Tollett, J. J. & Hulet, R. G. Evidence of Bose-Einstein Condensation in an Atomic Gas with Attractive Interactions. *Phys. Rev. Lett.* **75,** 1687 (1995).
9. Fried, D. G. *et al.* Bose-Einstein Condensation of Atomic Hydrogen. *Phys. Rev. Lett.* **81,** 3811 (1998).
10. Pereira Dos Santos, F. *et al.* Bose-Einstein Condensation of Metastable Helium. *Phys. Rev. Lett.* **86,** 3459 (2001).

11. Robert, A. *et al.* A Bose-Einstein condensate of metastable atoms. *Science* **292,** 461 (2001).
12. Modugno, G. *et al.* Bose-Einstein condensation of potassium atoms by sympathetic cooling. *Science* **294,** 1320 (2001).
13. Zaccanti, M. *et al.* Observation of an Efimov spectrum in an atomic system. *Nat. Phys.* **5,** 586 (2009).
14. Ketterle, W. Nobel lecture: When atoms behave as waves: Bose-Einstein condensation and the atom laser. *Rev. Mod. Phys.* **74,** 1131 (2002).
15. Pethick, C. J. & Smith, H. *Bose–Einstein condensation in dilute gases* (Cambridge university press, 2008).
16. Griffin, A., Snoke, D. W. & Stringari, S. *Bose-Einstein condensation* (Cambridge University Press, 1996).
17. Dalfovo, F., Giorgini, S., Pitaevskii, L. P. & Stringari, S. Theory of Bose-Einstein condensation in trapped gases. *Rev. Mod. Phys.* **71,** 463 (3 1999).
18. Leggett, A. J. Bose-Einstein condensation in the alkali gases: Some fundamental concepts. *Rev. Mod. Phys.* **73,** 307 (2001).
19. Fetter, A. L. Rotating trapped Bose-Einstein condensates. *Rev. Mod. Phys.* **81,** 647 (2009).
20. Hutson, J. M. Ultracold chemistry. *Science* **327,** 788 (2010).
21. Bloch, I., Dalibard, J. & Nascimbène, S. Quantum simulations with ultracold quantum gases. *Nat. Phys.* **8,** 267 (2012).
22. Gross, C. & Bloch, I. Quantum simulations with ultracold atoms in optical lattices. *Science* **357,** 995 (2017).
23. Chien, C. C., Peotta, S. & Di Ventra, M. Quantum transport in ultracold atoms. *Nat. Phys.* **11,** 998 (2015).
24. Cabrera, C. *et al.* Quantum liquid droplets in a mixture of Bose-Einstein condensates. *Science* **359,** 301 (2018).
25. Myatt, C. J., Burt, E. A., Ghrist, R. W., Cornell, E. A. & Wieman, C. E. Production of Two Overlapping Bose-Einstein Condensates by Sympathetic Cooling. *Phys. Rev. Lett.* **78,** 586 (1997).

26. Ho, T.-L. & Shenoy, V. B. Binary Mixtures of Bose Condensates of Alkali Atoms. *Phys. Rev. Lett.* **77,** 3276 (1996).
27. Hall, D. S., Matthews, M. R., Ensher, J. R., Wieman, C. E. & Cornell, E. A. Dynamics of Component Separation in a Binary Mixture of Bose-Einstein Condensates. *Phys. Rev. Lett.* **81,** 1539 (1998).
28. Stenger, J. *et al.* Spin domains in ground-state Bose–Einstein condensates. *Nature* **396,** 345 (1998).
29. Stamper-Kurn, D. M. *et al.* Optical Confinement of a Bose-Einstein Condensate. *Phys. Rev. Lett.* **80,** 2027 (1998).
30. Maddaloni, P., Modugno, M., Fort, C., Minardi, F. & Inguscio, M. Collective Oscillations of Two Colliding Bose-Einstein Condensates. *Phys. Rev. Lett.* **85,** 2413 (2000).
31. Esry, B. D., Greene, C. H., Burke Jr., J. P. & Bohn, J. L. Hartree-Fock Theory for Double Condensates. *Phys. Rev. Lett.* **78,** 3594 (1997).
32. Timmermans, E. Phase Separation of Bose-Einstein Condensates. *Phys. Rev. Lett.* **81,** 5718 (1998).
33. Pu, H. & Bigelow, N. P. Properties of Two-Species Bose Condensates. *Phys. Rev. Lett.* **80,** 1130 (1998).
34. Tojo, S. *et al.* Controlling phase separation of binary Bose-Einstein condensates via mixed-spin-channel Feshbach resonance. *Phys. Rev. A* **82,** 033609 (2010).
35. Modugno, G., Modugno, M., Riboli, F., Roati, G. & Inguscio, M. Two Atomic Species Superfluid. *Phys. Rev. Lett.* **89,** 190404 (2002).
36. Molony, P. K. *et al.* Creation of Ultracold ^{87}Rb^{133}Cs Molecules in the Rovibrational Ground State. *Phys. Rev. Lett.* **113,** 255301 (2014).
37. Guo, M. *et al.* Creation of an Ultracold Gas of Ground-State Dipolar ^{23}Na^{87}Rb Molecules. *Phys. Rev. Lett.* **116,** 205303 (2016).
38. Will, S. A., Park, J. W., Yan, Z. Z., Loh, H. & Zwierlein, M. W. Coherent Microwave Control of Ultracold ^{23}Na^{40}K Molecules. *Phys. Rev. Lett.* **116,** 225306 (2016).

39. Thalhammer, G. *et al.* Double Species Bose-Einstein Condensate with Tunable Interspecies Interactions. *Phys. Rev. Lett.* **100,** 210402 (2008).

40. McCarron, D. J., Cho, H. W., Jenkin, D. L., Köppinger, M. P. & Cornish, S. L. Dual-species Bose-Einstein condensate of ^{87}Rb and ^{133}Cs. *Phys. Rev. A* **84,** 011603 (2011).

41. Pasquiou, B. *et al.* Quantum degenerate mixtures of strontium and rubidium atoms. *Phys. Rev. A* **88,** 023601 (2013).

42. Ni, K.-K. *et al.* A high phase-space-density gas of polar molecules. *Science* **322,** 231 (2008).

43. Krems, R., Friedrich, B. & Stwalley, W. C. *Cold molecules: theory, experiment, applications* (CRC press, 2009).

44. Kotochigova, S. & Tiesinga, E. Ab initio relativistic calculation of the RbCs molecule. *J. Chem. Phys.* **123,** 174304 (2005).

45. Deiglmayr, J., Aymar, M., Wester, R., Weidemüller, M. & Dulieu, O. Calculations of static dipole polarizabilities of alkali dimers: Prospects for alignment of ultracold molecules. *J. Chem. Phys.* **129,** 064309 (2008).

46. Semeghini, G. *et al.* Self-Bound Quantum Droplets of Atomic Mixtures in Free Space. *Phys. Rev. Lett.* **120,** 235301 (2018).

47. Micheli, A., Pupillo, G., Büchler, H. P. & Zoller, P. Cold polar molecules in two-dimensional traps: Tailoring interactions with external fields for novel quantum phases. *Phys. Rev. A* **76,** 043604 (2007).

48. Lahaye, T., Menotti, C., Santos, L., Lewenstein, M. & Pfau, T. The physics of dipolar bosonic quantum gases. *Rep. Prog. Phys.* **72,** 126401 (2009).

49. Gorshkov, A. V. *et al.* Tunable Superfluidity and Quantum Magnetism with Ultracold Polar Molecules. *Phys. Rev. Lett.* **107,** 115301 (2011).

50. Baranov, M. A., Dalmonte, M., Pupillo, G. & Zoller, P. Condensed matter theory of dipolar quantum gases. *Chem. Rev.* **112,** 5012 (2012).

51. Schulze, T. A. *et al.* Feshbach spectroscopy and dual-species Bose-Einstein condensation of ^{23}Na$-^{39}$K mixtures. *Phys. Rev. A* **97,** 023623 (2018).

52. Chin, C., Grimm, R., Julienne, P. & Tiesinga, E. Feshbach resonances in ultracold gases. *Rev. Mod. Phys.* **82,** 1225 (2010).

53. Papp, S. B., Pino, J. M. & Wieman, C. E. Tunable Miscibility in a Dual-Species Bose-Einstein Condensate. *Phys. Rev. Lett.* **101,** 040402 (2008).
54. Sugawa, S., Yamazaki, R., Taie, S. & Takahashi, Y. Bose-Einstein condensate in gases of rare atomic species. *Phys. Rev. A* **84,** 011610 (2011).
55. Ronen, S., Bohn, J. L., Halmo, L. E. & Edwards, M. Dynamical pattern formation during growth of a dual-species Bose-Einstein condensate. *Phys. Rev. A* **78,** 053613 (2008).
56. Hoefer, M. A., Chang, J. J., Hamner, C. & Engels, P. Dark-dark solitons and modulational instability in miscible two-component Bose-Einstein condensates. *Phys. Rev. A* **84,** 041605 (2011).
57. Hamner, C., Chang, J., Engels, P. & Hoefer, M. Generation of dark-bright soliton trains in superfluid-superfluid counterflow. *Phys. Rev. Lett.* **106,** 065302 (2011).
58. De, S. *et al.* Quenched binary Bose-Einstein condensates: Spin-domain formation and coarsening. *Phys. Rev. A* **89,** 033631 (2014).
59. Beattie, S., Moulder, S., Fletcher, R. J. & Hadzibabic, Z. Persistent Currents in Spinor Condensates. *Phys. Rev. Lett.* **110,** 025301 (2013).
60. Smyrnakis, J. *et al.* Mixtures of Bose Gases Confined in a Ring Potential. *Phys. Rev. Lett.* **103,** 100404 (2009).
61. Anoshkin, K., Wu, Z. & Zaremba, E. Persistent currents in a bosonic mixture in the ring geometry. *Phys. Rev. A* **88,** 013609 (2013).
62. Yakimenko, A. I., Isaieva, K. O., Vilchinskii, S. I. & Weyrauch, M. Stability of persistent currents in spinor Bose-Einstein condensates. *Phys. Rev. A* **88,** 051602 (2013).
63. Wu, Z. & Zaremba, E. Mean-field yrast spectrum of a two-component Bose gas in ring geometry: Persistent currents at higher angular momentum. *Phys. Rev. A* **88,** 063640 (2013).
64. Abad, M., Sartori, A., Finazzi, S. & Recati, A. Persistent currents in two-component condensates in a toroidal trap. *Phys. Rev. A* **89,** 053602 (2014).
65. Wu, Z. *et al.* Mean-field yrast spectrum and persistent currents in a two-component Bose gas with interaction asymmetry. *Phys. Rev. A* **92,** 033630 (2015).

66. Sandin, P., Ögren, M. & Gulliksson, M. Numerical solution of the stationary multicomponent nonlinear Schrödinger equation with a constraint on the angular momentum. *Phys. Rev. E* **93,** 033301 (2016).

67. Kasamatsu, K., Tsubota, M. & Ueda, M. Quadrupole and scissors modes and nonlinear mode coupling in trapped two-component Bose-Einstein condensates. *Phys. Rev. A* **69,** 043621 (2004).

68. Lee, K. L. & Proukakis, N. P. Non-equilibrium atomic condensates and mixtures: collective modes, condensate growth and thermalisation. *J. Phys. B* **49,** 214003 (2016).

69. Ao, P. & Chui, S. T. Binary Bose-Einstein condensate mixtures in weakly and strongly segregated phases. *Phys. Rev. A* **58,** 4836 (1998).

70. Esry, B. D. & Greene, C. H. Spontaneous spatial symmetry breaking in two-component Bose-Einstein condensates. *Phys. Rev. A* **59,** 1457 (1999).

71. Trippenbach, M., Goral, K., Rzazewski, K., Malomed, B. & Band, Y. Structure of binary Bose-Einstein condensates. *J. Phys. B* **33,** 4017 (2000).

72. Shi, H., Zheng, W.-M. & Chui, S.-T. Phase separation of Bose gases at finite temperature. *Phys. Rev. A* **61,** 063613 (2000).

73. Ma, H. & Pang, T. Path-integral quantum Monte Carlo study of a mixture of Bose–Einstein condensates. *Phys. Lett. A* **351,** 92 (2006).

74. Sakhel, A. R., DuBois, J. L. & Glyde, H. R. Condensate depletion in two-species Bose gases: A variational quantum Monte Carlo study. *Phys. Rev. A* **77,** 043627 (2008).

75. Jain, P. & Boninsegni, M. Quantum demixing in binary mixtures of dipolar bosons. *Phys. Rev. A* **83,** 023602 (2011).

76. Svidzinsky, A. A. & Chui, S. T. Symmetric-asymmetric transition in mixtures of Bose-Einstein condensates. *Phys. Rev. A* **67,** 053608 (2003).

77. Riboli, F. & Modugno, M. Topology of the ground state of two interacting Bose-Einstein condensates. *Phys. Rev. A* **65,** 063614 (2002).

78. Jezek, D. M. & Capuzzi, P. Interaction-driven effects on two-component Bose-Einstein condensates. *Phys. Rev. A* **66,** 015602 (2002).

79. Lee, K. L. *et al.* Phase separation and dynamics of two-component Bose-Einstein condensates. *Phys. Rev. A* **94,** 013602 (2016).
80. Cikojevic, V., Markic, L. V. & Boronat, J. Harmonically trapped bose-bose mixtures: A quantum monte carlo study. *New J. Phys.* **20,** 85002 (2018).
81. Becker, C. *et al.* Oscillations and interactions of dark and dark–bright solitons in Bose–Einstein condensates. *Nat. Phys.* **4,** 496 (2008).
82. Middelkamp, S. *et al.* Dynamics of dark–bright solitons in cigar-shaped Bose–Einstein condensates. *Phys. Lett. A* **375,** 642 (2011).
83. Busch, T. & Anglin, J. R. Dark-Bright Solitons in Inhomogeneous Bose-Einstein Condensates. *Phys. Rev. Lett.* **87,** 010401 (2001).
84. Perez Garcia, V. M. & Beitia, J. B. Symbiotic solitons in heteronuclear multicomponent Bose-Einstein condensates. *Phys. Rev. A* **72,** 033620 (2005).
85. Law, K. J. H., Kevrekidis, P. G. & Tuckerman, L. S. Stable Vortex–Bright-Soliton Structures in Two-Component Bose-Einstein Condensates. *Phys. Rev. Lett.* **105,** 160405 (2010).
86. Mukherjee, K., Mistakidis, S., Kevrekidis, P. & Schmelcher, P. Quench induced vortex-bright-soliton formation in binary Bose-Einstein condensates. *arXiv preprint arXiv:1904.06208* (2019).
87. Pola, M., Stockhofe, J., Schmelcher, P. & Kevrekidis, P. G. Vortex–bright-soliton dipoles: Bifurcations, symmetry breaking, and soliton tunneling in a vortex-induced double well. *Phys. Rev. A* **86,** 053601 (2012).
88. Richaud, A., Penna, V., Guilleumas, M. & Mayol, R. Massive vortices in a binary mixture of Bose-Einstein condensates. *arXiv preprint arXiv:1908.06668* (2019).
89. Petrov, D. S. Quantum Mechanical Stabilization of a Collapsing Bose-Bose Mixture. *Phys. Rev. Lett.* **115,** 155302 (2015).
90. Cappellaro, A., Macri, T., Bertacco, G. F. & Salasnich, L. Equation of state and self-bound droplet in Rabi-coupled Bose mixtures. *Sci. Rep.* **7,** 13358 (2017).
91. Lee, T. D., Huang, K. & Yang, C. N. Eigenvalues and Eigenfunctions of a Bose System of Hard Spheres and Its Low-Temperature Properties. *Phys. Rev.* **106,** 1135 (1957).

92. Salasnich, L. Beyond mean-field theory for attractive bosons under transverse harmonic confinement. *J. Phys. B* **39,** 1743 (2006).
93. Dalfovo, F. & Stringari, S. Helium nanodroplets and trapped Bose–Einstein condensates as prototypes of finite quantum fluids. *J. Chem. Phys.* **115,** 10078 (2001).
94. Barranco, M. *et al.* Helium nanodroplets: An overview. *J. Low Temp. Phys.* **142,** 1 (2006).
95. Kadau, H. *et al.* Observing the Rosensweig instability of a quantum ferrofluid. *Nature* **530,** 194 (2016).
96. Ferrier-Barbut, I., Kadau, H., Schmitt, M., Wenzel, M. & Pfau, T. Observation of Quantum Droplets in a Strongly Dipolar Bose Gas. *Phys. Rev. Lett.* **116,** 215301 (2016).
97. Ferrier-Barbut, I., Schmitt, M., Wenzel, M., Kadau, H. & Pfau, T. Liquid quantum droplets of ultracold magnetic atoms. *J. Phys. B* **49,** 214004 (2016).
98. Schmitt, M., Wenzel, M., Böttcher, F., Ferrier-Barbut, I. & Pfau, T. Self-bound droplets of a dilute magnetic quantum liquid. *Nature* **539,** 259 (2016).
99. Wenzel, M., Bottcher, F., Langen, T., Ferrier-Barbut, I. & Pfau, T. Striped states in a many-body system of tilted dipoles. *Phys. Rev. A* **96,** 053630 (2017).
100. Chomaz, L. *et al.* Quantum-Fluctuation-Driven Crossover from a Dilute Bose-Einstein Condensate to a Macrodroplet in a Dipolar Quantum Fluid. *Phys. Rev. X* **6,** 041039 (2016).
101. Bloch, I. Ultracold quantum gases in optical lattices. *Nat. Phys.* **1,** 23 (2005).
102. Feynman, R. P. Quantum mechanical computers. *Opt. News* **11,** 11 (1985).
103. Feynman, R. P. Quantum mechanical computers. *Found. Phys.* **16,** 507 (1986).
104. Cataliotti, F. *et al.* Josephson junction arrays with Bose-Einstein condensates. *Science* **293,** 843 (2001).
105. Albiez, M. *et al.* Direct Observation of Tunneling and Nonlinear Self-Trapping in a Single Bosonic Josephson Junction. *Phys. Rev. Lett.* **95,** 010402 (2005).
106. Javanainen, J. Oscillatory exchange of atoms between traps containing Bose condensates. *Phys. Rev. Lett.* **57,** 3164 (1986).

107. Jack, M. W., Collett, M. J. & Walls, D. F. Coherent quantum tunneling between two Bose-Einstein condensates. *Phys. Rev. A* **54,** 4625 (6 1996).

108. Zapata, I., Sols, F. & Leggett, A. J. Josephson effect between trapped Bose-Einstein condensates. *Phys. Rev. A* **57,** 28 (1998).

109. Milburn, G. J., Corney, J., Wright, E. M. & Walls, D. F. Quantum dynamics of an atomic Bose-Einstein condensate in a double-well potential. *Phys. Rev. A* **55,** 4318 (1997).

110. Smerzi, A., Fantoni, S., Giovanazzi, S. & Shenoy, S. R. Quantum Coherent Atomic Tunneling between Two Trapped Bose-Einstein Condensates. *Phys. Rev. Lett.* **79,** 4950 (1997).

111. Raghavan, S., Smerzi, A., Fantoni, S. & Shenoy, S. R. Coherent oscillations between two weakly coupled Bose-Einstein condensates: Josephson effects, π oscillations, and macroscopic quantum self-trapping. *Phys. Rev. A* **59,** 620 (1999).

112. Franzosi, R., Penna, V. & Zecchina, R. Quantum dynamics of coupled bosonic wells within the Bose-Hubbard picture. *Int. J. Mod. Phys. B* **14,** 943 (2000).

113. Bloch, I., Dalibard, J. & Zwerger, W. Many-body physics with ultracold gases. *Rev. Mod. Phys.* **80,** 885 (2008).

114. Fisher, M. P. A., Weichman, P. B., Grinstein, G. & Fisher, D. S. Boson localization and the superfluid-insulator transition. *Phys. Rev. B* **40,** 546 (1989).

115. Jaksch, D., Bruder, C., Cirac, J. I., Gardiner, C. W. & Zoller, P. Cold Bosonic Atoms in Optical Lattices. *Phys. Rev. Lett.* **81,** 3108 (1998).

116. Greiner, M., Mandel, O., Esslinger, T., Hänsch, T. W. & Bloch, I. Quantum phase transition from a superfluid to a Mott insulator in a gas of ultracold atoms. *Nature* **415,** 39 (2002).

117. Lewenstein, M. *et al.* Ultracold atomic gases in optical lattices: mimicking condensed matter physics and beyond. *Adv. Phys.* **56,** 243 (2007).

118. Simon, J. *et al.* Quantum simulation of antiferromagnetic spin chains in an optical lattice. *Nature* **472,** 307 (2011).

119. Langen, T., Geiger, R., Kuhnert, M., Rauer, B. & Schmiedmayer, J. Local emergence of thermal correlations in an isolated quantum many-body system. *Nat. Phys.* **9,** 640 (2013).

120. Langen, T. *et al.* Experimental observation of a generalized Gibbs ensemble. *Science* **348,** 207 (2015).

121. Kaufman, A. M. *et al.* Quantum thermalization through entanglement in an isolated many-body system. *Science* **353,** 794 (2016).

122. Choi, J.-y. *et al.* Exploring the many-body localization transition in two dimensions. *Science* **352,** 1547 (2016).

123. Catani, J., De Sarlo, L., Barontini, G., Minardi, F. & Inguscio, M. Degenerate Bose-Bose mixture in a three-dimensional optical lattice. *Phys. Rev. A* **77,** 011603 (2008).

124. Bruderer, M., Klein, A., Clark, S. R. & Jaksch, D. Polaron physics in optical lattices. *Phys. Rev. A* **76,** 011605 (2007).

125. Damski, B. *et al.* Creation of a Dipolar Superfluid in Optical Lattices. *Phys. Rev. Lett.* **90,** 110401 (2003).

126. Kuklov, A. B. & Svistunov, B. V. Counterflow Superfluidity of Two-Species Ultracold Atoms in a Commensurate Optical Lattice. *Phys. Rev. Lett.* **90,** 100401 (2003).

127. Daley, A. J., Fedichev, P. O. & Zoller, P. Single-atom cooling by superfluid immersion: A nondestructive method for qubits. *Phys. Rev. A* **69,** 022306 (2004).

128. Roscilde, T. & Cirac, J. I. Quantum Emulsion: A Glassy Phase of Bosonic Mixtures in Optical Lattices. *Phys. Rev. Lett.* **98,** 190402 (2007).

129. Buonsante, P., Giampaolo, S. M., Illuminati, F., Penna, V. & Vezzani, A. Mixtures of Strongly Interacting Bosons in Optical Lattices. *Phys. Rev. Lett.* **100,** 240402 (2008).

130. Gavish, U. & Castin, Y. Matter-Wave Localization in Disordered Cold Atom Lattices. *Phys. Rev. Lett.* **95,** 020401 (2005).

131. Paredes, B., Verstraete, F. & Cirac, J. I. Exploiting Quantum Parallelism to Simulate Quantum Random Many-Body Systems. *Phys. Rev. Lett.* **95,** 140501 (2005).

132. Gadway, B., Pertot, D., Reeves, J., Vogt, M. & Schneble, D. Glassy Behavior in a Binary Atomic Mixture. *Phys. Rev. Lett.* **107,** 145306 (2011).

133. Kramer, B. & MacKinnon, A. Localization: theory and experiment. *Rep. Prog. Phys.* **56,** 1469 (1993).

134. Guglielmino, M., Penna, V. & Capogrosso-Sansone, B. Mott-insulator–to–superfluid transition in Bose-Bose mixtures in a two-dimensional lattice. *Phys. Rev. A* **82,** 021601 (2010).

135. Duan, L.-M., Demler, E. & Lukin, M. D. Controlling Spin Exchange Interactions of Ultracold Atoms in Optical Lattices. *Phys. Rev. Lett.* **91,** 090402 (2003).

136. Ehud, A., Walter, H., Eugene, D. & Mikhail, D. L. Phase diagram of two-component bosons on an optical lattice. *New J. Phys.* **5,** 113 (2003).

137. Isacsson, A., Cha, M.-C., Sengupta, K. & Girvin, S. M. Superfluid-insulator transitions of two-species bosons in an optical lattice. *Phys. Rev. B* **72,** 184507 (2005).

138. Kuklov, A., Prokof'ev, N. & Svistunov, B. Commensurate Two-Component Bosons in an Optical Lattice: Ground State Phase Diagram. *Phys. Rev. Lett.* **92,** 050402 (2004).

139. Lingua, F., Guglielmino, M., Penna, V. & Capogrosso Sansone, B. Demixing effects in mixtures of two bosonic species. *Phys. Rev. A* **92,** 053610 (2015).

140. Ziegler, K. Two-component Bose gas in an optical lattice at single-particle filling. *Phys. Rev. A* **68,** 053602 (2003).

141. Krutitsky, K. V. & Graham, R. Spin-1 bosons with coupled ground states in optical lattices. *Phys. Rev. A* **70,** 063610 (2004).

142. Gadway, B., Pertot, D., Reimann, R. & Schneble, D. Superfluidity of Interacting Bosonic Mixtures in Optical Lattices. *Phys. Rev. Lett.* **105,** 045303 (2010).

143. Mathey, L. Commensurate mixtures of ultracold atoms in one dimension. *Phys. Rev. B* **75,** 144510 (2007).

144. Argüelles, A. & Santos, L. Mott-insulator phases of nonlocally coupled one-dimensional dipolar Bose gases. *Phys. Rev. A* **75,** 053613 (2007).

145. Moore, M. G. & Sadeghpour, H. R. Controlling two-species Mott-insulator phases in an optical lattice to form an array of dipolar molecules. *Phys. Rev. A* **67,** 041603 (2003).
146. Guglielmino, M., Penna, V. & Capogrosso-Sansone, B. Ising antiferromagnet with ultracold bosonic mixtures confined in a harmonic trap. *Phys. Rev. A* **84,** 031603 (2011).
147. Mishra, T., Pai, R. V. & Das, B. P. Phase separation in a two-species Bose mixture. *Phys. Rev. A* **76,** 013604 (2007).
148. Hu, A. *et al.* Counterflow and paired superfluidity in one-dimensional Bose mixtures in optical lattices. *Phys. Rev. A* **80,** 023619 (2009).
149. Suthar, K. & Angom, D. Optical-lattice-influenced geometry of quasi-two-dimensional binary condensates and quasiparticle spectra. *Phys. Rev. A* **93,** 063608 (2016).
150. Nakano, Y. *et al.* Finite-temperature phase diagram of two-component bosons in a cubic optical lattice: Three-dimensional t-J model of hard-core bosons. *Phys. Rev. A* **85,** 023617 (2012).
151. Lingua, F., Capogrosso-Sansone, B., Minardi, F. & Penna, V. Thermometry of bosonic mixtures in Optical Lattices via Demixing. *Sci. Rep.* **7,** 5105 (2017).
152. Xu, X.-Q., Lu, L.-H. & Li, Y.-Q. Stability and dynamical property for two-species ultracold atoms in double wells. *Phys. Rev. A* **78,** 043609 (2008).
153. Wang, C., Kevrekidis, P., Whitaker, N. & Malomed, B. Two-component nonlinear Schrödinger models with a double-well potential. *Physica D* **237,** 2922 (2008).
154. Satija, I. I. *et al.* Symmetry-breaking and symmetry-restoring dynamics of a mixture of Bose-Einstein condensates in a double well. *Phys. Rev. A* **79,** 033616 (2009).
155. Mazzarella, G., Moratti, M., Salasnich, L., Salerno, M. & Toigo, F. Atomic Josephson junction with two bosonic species. *J. Phys. B* **42,** 125301 (2009).
156. Mazzarella, G., Moratti, M., Salasnich, L. & Toigo, F. Nonlinear quantum model for atomic Josephson junctions with one and two bosonic species. *J. Phys. B* **43,** 65303 (2010).

157. Zhang, D.-W., Fu, L.-B., Wang, Z. D. & Zhu, S.-L. Josephson dynamics of a spin-orbit-coupled Bose-Einstein condensate in a double-well potential. *Phys. Rev. A* **85,** 043609 (2012).

158. Garcia-March, M. A. *et al.* Josephson physics of spin-orbit-coupled elongated Bose-Einstein condensates. *Phys. Rev. A* **89,** 063607 (2014).

159. Citro, R. & Naddeo, A. Spin-orbit coupled Bose-Einstein condensates in a double well. *The European Physical Journal Special Topics* **224,** 503 (2015).

160. Wang, W.-Y., Cao, H., Zhu, S.-L., Liu, J. & Fu, L.-B. Energy levels of a spin–orbit-coupled Bose–Einstein condensate in a double-well potential. *Laser Physics* **25,** 025501 (2014).

161. Julia-Diaz, B., Mele-Messeguer, M., Guilleumas, M. & Polls, A. Spinor Bose-Einstein condensates in a double well: Population transfer and Josephson oscillations. *Phys. Rev. A* **80,** 043622 (2009).

162. Kevrekidis, P. G. *The discrete nonlinear Schrödinger equation: Mathematical analysis, numerical computations and physical perspectives* (Springer Science & Business Media, 2009).

163. Naddeo, A. & Citro, R. Quantum Bose–Josephson junction with binary mixtures of BECs. *J. Phys. B* **43,** 135302 (2010).

164. Zin, P., Oles, B. & Sacha, K. Quantum particle-number fluctuations in a two-component Bose gas in a double-well potential. *Phys. Rev. A* **84,** 033614 (2011).

165. Lingua, F., Mazzarella, G. & Penna, V. Delocalization effects, entanglement entropy and spectral collapse of boson mixtures in a double well. *J. Phys. B* **49,** 205005 (2016).

166. Mujal, P., Julia-Diaz, B. & Polls, A. Quantum properties of a binary bosonic mixture in a double well. *Phys. Rev. A* **93,** 043619 (2016).

167. Lingua, F. & Penna, V. Continuous-variable approach to the spectral properties and quantum states of the two-component Bose-Hubbard dimer. *Phys. Rev. E* **95,** 062142 (2017).

168. Camesasca, M., Kaufman, M. & Manas-Zloczower, I. Quantifying fluid mixing with the Shannon entropy. *Macromol. Theory Simul.* **15,** 595 (2006).

169. Wang, W., Penna, V. & Capogrosso-Sansone, B. Inter-species entanglement of Bose-Bose mixtures trapped in optical lattices. *New J. Phys.* **18,** 63002 (2016).

170. Dell'Anna, L. Analytical approach to the two-site Bose-Hubbard model: From Fock states to Schrödinger cat states and entanglement entropy. *Phys. Rev. A* **85,** 053608 (2012).

171. Zhu, Q., Zhang, Q. & Wu, B. Extended two-site Bose–Hubbard model with pair tunneling: Spontaneous symmetry breaking, effective ground state and fragmentation. *J. Phys. B* **48,** 045301 (2015).

172. Bychek, A. A., Maksimov, D. N. & Kolovsky, A. R. NOON state of Bose atoms in the double-well potential via an excited-state quantum phase transition. *Phys. Rev. A* **97,** 063624 (2018).

173. Trombettoni, A. & Smerzi, A. Discrete Solitons and Breathers with Dilute Bose-Einstein Condensates. *Phys. Rev. Lett.* **86,** 2353 (11 2001).

174. Trombettoni, A., Smerzi, A. & Bishop, A. R. Superfluidity versus Disorder in the Discrete Nonlinear Schrodinger Equation. *Phys. Rev. Lett.* **88,** 173902 (2002).

175. Buonsante, P., Penna, V. & Vezzani, A. Dynamical bifurcation as a semiclassical counterpart of a quantum phase transition. *Phys. Rev. A* **84,** 061601 (2011).

176. Richaud, A., Zenesini, A. & Penna, V. The mixing-demixing phase diagram of ultracold heteronuclear mixtures in a ring trimer. *Sci. Rep.* **9,** 6908 (2019).

177. Richaud, A. & Penna, V. Quantum dynamics of bosons in a two-ring ladder: Dynamical algebra, vortexlike excitations, and currents. *Phys. Rev. A* **96,** 013620 (2017).

178. Penna, V. & Richaud, A. Two-species boson mixture on a ring: A group-theoretic approach to the quantum dynamics of low-energy excitations. *Phys. Rev. A* **96,** 053631 (2017).

179. Rasetti, M. Generalized definition of coherent states and dynamical groups. *Int. J. Theor. Phys.* **13,** 42 (1975).

180. Zhang, W.-M., Feng, D. H. & Gilmore, R. Coherent states: Theory and some applications. *Rev. Mod. Phys.* **62,** 867 (1990).

181. Kaushal, R. S. & Mishra, S. C. Dynamical algebraic approach and invariants for time-dependent Hamiltonian systems in two dimensions. *J. Math. Phys.* **34,** 5843 (1993).
182. Celeghini, E., Faoro, L. & Rasetti, M. Dynamical algebra of single and coupled Josephson junctions. *Phys. Rev. B* **62,** 3054 (2000).
183. Penna, V. Dynamics of the central-depleted-well regime in the open Bose-Hubbard trimer. *Phys. Rev. E* **87,** 052909 (2013).
184. Torrontegui, E., Martinez-Garaot, S. & Muga, J. G. Hamiltonian engineering via invariants and dynamical algebra. *Phys. Rev. A* **89,** 043408 (2014).
185. Rey, A. M. *et al.* Bogoliubov approach to superfluidity of atoms in an optical lattice. *J. Phys. B* **36,** 825 (2003).
186. Burnett, K., Edwards, M., Clark, C. W. & Shotter, M. The Bogoliubov approach to number squeezing of atoms in an optical lattice. *J. Phys. B* **35,** 1671 (2002).
187. Huang, H. & Li, S. Q. Factorizability of the two-component Bose-Einstein condensate ground state. *Chin. Phys. Lett.* **16,** 9 (1999).
188. Jack, M. W. & Yamashita, M. Bose-Hubbard model with attractive interactions. *Phys. Rev. A* **71,** 023610 (2005).
189. Van Hemmen, J. A note on the diagonalization of quadratic boson and fermion hamiltonians. *Z. Phys. B* **38,** 271 (1980).
190. Buonsante, P., Franzosi, R. & Penna, V. Dynamical Instability in a Trimeric Chain of Interacting Bose-Einstein Condensates. *Phys. Rev. Lett.* **90,** 050404 (2003).
191. Buonsante, P., Franzosi, R. & Penna, V. Control of unstable macroscopic oscillations in the dynamics of three coupled Bose condensates. *J. Phys. A* **42,** 285307 (2009).
192. Jason, P., Johansson, M. & Kirr, K. Quantum signatures of an oscillatory instability in the Bose-Hubbard trimer. *Phys. Rev. E* **86,** 016214 (2012).
193. Dell'Anna, L., Mazzarella, G., Penna, V. & Salasnich, L. Entanglement entropy and macroscopic quantum states with dipolar bosons in a triple-well potential. *Phys. Rev. A* **87,** 053620 (2013).

194. Bradly, C. J., Rab, M., Greentree, A. D. & Martin, A. M. Coherent tunneling via adiabatic passage in a three-well Bose-Hubbard system. *Phys. Rev. A* **85,** 053609 (2012).

195. Gallemí, A. *et al.* Fragmented condensation in Bose-Hubbard trimers with tunable tunnelling. *New J. Phys.* **17,** 73014 (2015).

196. Olsen, M. K. & Corney, J. F. Negative differential conductivity and quantum statistical effects in a three-site Bose-Hubbard model. *Phys. Rev. A* **94,** 033605 (2016).

197. Buonsante, P., Penna, V. & Vezzani, A. Quantum signatures of the self-trapping transition in attractive lattice bosons. *Phys. Rev. A* **82,** 043615 (2010).

198. Arwas, G., Vardi, A. & Cohen, D. Superfluidity and Chaos in low dimensional circuits. *Sci. Rep.* **5,** 13433 (2015).

199. Han, X. & Wu, B. Ehrenfest breakdown of the mean-field dynamics of Bose gases. *Phys. Rev. A* **93,** 023621 (2016).

200. Jason, P. & Johansson, M. Quantum signatures of charge flipping vortices in the Bose-Hubbard trimer. *Phys. Rev. E* **94,** 052215 (2016).

201. Lingua, F., Richaud, A. & Penna, V. Residual entropy and critical behavior of two interacting boson species in a double well. *Entropy* **20,** 84 (2018).

202. Buonsante, P. & Penna, V. Some remarks on the coherent-state variational approach to nonlinear boson models. *J. Phys. A* **41,** 175301 (2008).

203. Landau, L. D. & Lifshitz, E. M. *Quantum mechanics: non-relativistic theory* (Elsevier, 2013).

204. Wang, W., Penna, V. & Capogrosso-Sansone, B. Analysis and resolution of the ground-state degeneracy of the two-component Bose-Hubbard model. *Phys. Rev. E* **90,** 022116 (2014).

205. Nielsen, M. A. & Chuang, I. *Quantum Computation and Quantum Information* (Cambridge University Press, 2000).

206. Penna, V. & Richaud, A. The phase separation mechanism of a binary mixture in a ring trimer. *Sci. Rep.* **8,** 10242 (2018).

207. Penna, V. & Richaud, A. Spatial Phase Separation of a Binary Mixture in a Ring Trimer. *J. Phys. Conf. Ser.* **1206,** 10242 (2019).
208. Spekkens, R. W. & Sipe, J. E. Spatial fragmentation of a Bose-Einstein condensate in a double-well potential. *Phys. Rev. A* **59,** 3868 (1999).
209. Buonsante, P., Burioni, R., Vescovi, E. & Vezzani, A. Quantum criticality in a bosonic Josephson junction. *Phys. Rev. A* **85,** 043625 (2012).
210. Ho, T.-L. & Ciobanu, C. V. The Schrödinger Cat Family in Attractive Bose Gases. *J. Low Temp. Phys.* **135,** 257 (2004).
211. Ziń, P., Chwedeńczuk, J., Oleś, B., Sacha, K. & Trippenbach, M. Quantum phase transition and critical fluctuations of an attractive Bose gas in a double well potential. *arXiv preprint arXiv:0804.3705* (2008).
212. Javanainen, J. Phonon approach to an array of traps containing Bose-Einstein condensates. *Phys. Rev. A* **60,** 4902 (1999).
213. Mazzarella, G. & Penna, V. Localization-delocalization transition of dipolar bosons in a four-well potential. *J. Phys. B* **48,** 65001 (2015).
214. Richaud, A. & Penna, V. Phase separation can be stronger than chaos. *New J. Phys.* **20,** 105008 (2018).
215. Zhang, J. & Dong, R. Exact diagonalization: the Bose–Hubbard model as an example. *Eur. J. Phys.* **31,** 591 (2010).
216. *Computational resources provided by HPC@POLITO*
217. Mazzarella, G., Salasnich, L., Parola, A. & Toigo, F. Coherence and entanglement in the ground state of a bosonic Josephson junction: From macroscopic Schrödinger cat states to separable Fock states. *Phys. Rev. A* **83,** 053607 (2011).
218. Hines, A. P., McKenzie, R. H. & Milburn, G. J. Quantum entanglement and fixed-point bifurcations. *Phys. Rev. A* **71,** 042303 (2005).
219. Fu, L. & Liu, J. Quantum entanglement manifestation of transition to nonlinear self-trapping for Bose-Einstein condensates in a symmetric double well. *Phys. Rev. A* **74,** 063614 (2006).

220. Juliá-Díaz, B., Dagnino, D., Lewenstein, M., Martorell, J. & Polls, A. Macroscopic self-trapping in Bose-Einstein condensates: Analysis of a dynamical quantum phase transition. *Phys. Rev. A* **81,** 023615 (2010).

221. Viscondi, T. F., Furuya, K. & de Oliveira, M. C. Generalized purity and quantum phase transition for Bose-Einstein condensates in a symmetric double well. *Phys. Rev. A* **80,** 013610 (2009).

222. Amico, L., Fazio, R., Osterloh, A. & Vedral, V. Entanglement in many-body systems. *Rev. Mod. Phys.* **80,** 517 (2008).

223. Sprott, J. C. *Chaos and time-series analysis* (Citeseer, 2003).

224. Wimberger, S. Nonlinear Dynamics and Quantum Chaos. *Graduate Texts in Physics. Springer International Publishing (Cham)* (2014).

225. Kolovsky, A. R. Bose–Hubbard Hamiltonian: Quantum chaos approach. *Int. J. Mod. Phys. B* **30,** 1630009 (2016).

226. Ciuchi, S. & de Pasquale, F. Dynamical mean field theory of the CDW phase. *Le Journal de Physique IV* **08,** Pr6–99–Pr6–103 (1998).

227. Ellinas, D., Johansson, M. & Christiansen, P. L. Quantum nonlinear lattices and coherent state vectors. *Physica D* **134,** 126 (1999).

228. Franzosi, R. & Penna, V. Chaotic behavior, collective modes, and self-trapping in the dynamics of three coupled Bose-Einstein condensates. *Phys. Rev. E* **67,** 046227 (2003).

229. Gerbier, F. *et al.* Interference pattern and visibility of a Mott insulator. *Phys. Rev. A* **72,** 053606 (2005).

230. Yukalov, V. I. Principal problems in Bose-Einstein condensation of dilute gases. *Laser Phys. Lett.* **1,** 435 (2004).

231. Rota, G.-C. *Mathematical methods of classical mechanics* **1,** 135 (Springer Science & Business Media, 2005).

232. Moser, J. New aspects in the theory of stability of Hamiltonian systems. *Commun. Pure Appl. Math.* **11,** 81 (1958).

233. Anker, T. *et al.* Nonlinear Self-Trapping of Matter Waves in Periodic Potentials. *Phys. Rev. Lett.* **94,** 020403 (2005).

234. Mustecaplioglu, O. E., Zhang, W. & You, L. Quantum dynamics of a spin-1 condensate in a double-well potential. *Phys. Rev. A* **75,** 023605 (2007).

235. Gugan, D. *Equilibrium Thermodynamics* **9,** 379 (Cambridge University Press, 1969).

236. Brandani, G. B. *et al.* Quantifying disorder through conditional entropy: an application to fluid mixing. *PLOS ONE* **8,** e65617 (2013).

237. Kandrup, H. E., Sideris, I. V. & Bohn, C. L. Chaos, ergodicity, and the thermodynamics of lower-dimensional time-independent Hamiltonian systems. *Phys. Rev. E* **65,** 016214 (2001).

238. Richaud, A. & Penna, V. Pathway toward the formation of supermixed states in ultracold boson mixtures loaded in ring lattices. *Phys. Rev. A* **100,** 013609 (2019).

239. Oelkers, N. & Links, J. Ground-state properties of the attractive one-dimensional Bose-Hubbard model. *Phys. Rev. B* **75,** 115119 (2007).

240. George, B. & Scalettar, R. T. *Quantum phase transitions* ISBN: 9780191729515 (Cambridge university press, 2011).

241. Jason, P. & Johansson, M. Discrete breathers for a discrete nonlinear Schrödinger ring coupled to a central site. *Phys. Rev. E* **93,** 012219 (2016).

242. Chianca, C. & Olsen, M. Quantum dynamics of a four-well Bose-Hubbard model with two different tunneling rates. *Phys. Rev. A* **83,** 043607 (2011).

243. Cavaletto, S. M. & Penna, V. Spectral properties of attractive bosons in a ring lattice including a single-site potential. *J. Phys. B* **44,** 115308 (2011).

244. Fukuhara, T., Sugawa, S. & Takahashi, Y. Bose-Einstein condensation of an ytterbium isotope. *Phys. Rev. A* **76,** 051604 (2007).

245. Eto, M. & Nitta, M. Vortex trimer in three-component Bose-Einstein condensates. *Phys. Rev. A* **85,** 053645 (2012).

246. Fujimoto, K. & Tsubota, M. Spin-superflow turbulence in spin-1 ferromagnetic spinor Bose-Einstein condensates. *Phys. Rev. A* **90,** 013629 (2014).

247. Hartman, S., Erlandsen, E. & Sudbø, A. Superfluid drag in multicomponent Bose-Einstein condensates on a square optical lattice. *Phys. Rev. B* **98,** 024512 (2018).

248. Pilch, K. *et al.* Observation of interspecies Feshbach resonances in an ultracold Rb-Cs mixture. *Phys. Rev. A* **79,** 042718 (2009).
249. Weber, T., Herbig, J., Mark, M., Nägerl, H.-C. & Grimm, R. Three-Body Recombination at Large Scattering Lengths in an Ultracold Atomic Gas. *Phys. Rev. Lett.* **91,** 123201 (2003).
250. Kaufman, A. M., Lester, B. J. & Regal, C. A. Cooling a Single Atom in an Optical Tweezer to Its Quantum Ground State. *Phys. Rev. X* **2,** 041014 (2012).
251. Gempel, M. *et al.* An adaptable two-lens high-resolution objective for single-site resolved imaging of atoms in optical lattices. *Rev. Sci. Instrum.* **90,** 053201 (2019).
252. Zupancic, P. *et al.* Ultra-precise holographic beam shaping for microscopic quantum control. *Opt. Express* **24,** 13881 (2016).
253. Hartmann, T. *et al.* Feshbach resonances in $^{23}\mathrm{Na} +^{39}\mathrm{K}$ mixtures and refined molecular potentials for the NaK molecule. *Phys. Rev. A* **99,** 032711 (2019).
254. Blatt, S. *et al.* Low-noise optical lattices for ultracold ^{6}Li. *Phys. Rev. A* **92,** 021402 (2015).
255. Gajdacz, M. *et al.* Preparation of Ultracold Atom Clouds at the Shot Noise Level. *Phys. Rev. Lett.* **117,** 073604 (2016).
256. Amico, L., Osterloh, A. & Cataliotti, F. Quantum Many Particle Systems in Ring-Shaped Optical Lattices. *Phys. Rev. Lett.* **95,** 063201 (2005).
257. Franke-Arnold, S. *et al.* Optical ferris wheel for ultracold atoms. *Opt. Express* **15,** 8619 (2007).
258. Amico, L. *et al.* Superfluid qubit systems with ring shaped optical lattices. *Sci. Rep.* **4,** 4298 (2014).
259. Aghamalyan, D. *et al.* Coherent superposition of current flows in an atomtronic quantum interference device. *New J. Phys.* **17,** 045023 (2015).
260. Aghamalyan, D. *et al.* An atomtronic flux qubit: a ring lattice of Bose–Einstein condensates interrupted by three weak links. *New J. Phys.* **18,** 075013 (2016).

261. Haug, T. *et al.* Readout of the atomtronic quantum interference device. *Phys. Rev. A* **97,** 013633 (2018).

262. Olsen, M. K. & Bradley, A. S. Quantum ultracold atomtronics. *Phys. Rev. A* **91,** 043635 (2015).

263. Seaman, B. T., Krämer, M., Anderson, D. Z. & Holland, M. J. Atomtronics: Ultracold-atom analogs of electronic devices. *Phys. Rev. A* **75,** 023615 (2007).

264. Caliga, S. C., Straatsma, C. J., Zozulya, A. A. & Anderson, D. Z. Principles of an atomtronic transistor. *New J. Phys.* **18,** 1 (2016).

265. Pepino, R. A., Cooper, J., Anderson, D. Z. & Holland, M. J. Atomtronic Circuits of Diodes and Transistors. *Phys. Rev. Lett.* **103,** 140405 (2009).

266. Benseny, A. *et al.* Atomtronics with holes: Coherent transport of an empty site in a triple-well potential. *Phys. Rev. A* **82,** 013604 (2010).

267. Labouvie, R., Santra, B., Heun, S., Wimberger, S. & Ott, H. Negative Differential Conductivity in an Interacting Quantum Gas. *Phys. Rev. Lett.* **115,** 050601 (2015).

268. Paraoanu, G.-S. Persistent currents in a circular array of Bose-Einstein condensates. *Phys. Rev. A* **67,** 023607 (2003).

269. Buonsante, P., Penna, V. & Vezzani, A. Attractive ultracold bosons in a necklace optical lattice. *Phys. Rev. A* **72,** 043620 (2005).

270. Buonsante, P., Kevrekidis, P., Penna, V. & Vezzani, A. Ground-state properties of attractive bosons in mesoscopic 1D ring lattices. *J. Phys. B* **39,** S77 (2006).

271. Buonsante, P., Kevrekidis, P. G., Penna, V. & Vezzani, A. Ground-state properties of small-size nonlinear dynamical lattices. *Phys. Rev. E* **75,** 016212 (2007).

272. Nunnenkamp, A., Rey, A. M. & Burnett, K. Generation of macroscopic superposition states in ring superlattices. *Phys. Rev. A* **77,** 023622 (2008).

273. Nunnenkamp, A. & Rey, A. M. Macroscopic superposition states in rotating ring lattices. *J. Mod. Opt.* **55,** 3339 (2008).

274. Nunnenkamp, A., Rey, A. M. & Burnett, K. Superposition states of ultracold bosons in rotating rings with a realistic potential barrier. *Phys. Rev. A* **84,** 053604 (2011).

275. Aghamalyan, D., Amico, L. & Kwek, L. C. Effective dynamics of cold atoms flowing in two ring-shaped optical potentials with tunable tunneling. *Phys. Rev. A* **88,** 063627 (2013).

276. Haug, T., Amico, L., Dumke, R. & Kwek, L.-C. Mesoscopic Vortex–Meissner currents in ring ladders. *Quantum Sci. Technol.* **3,** 035006 (2018).

277. Victorin, N., Haug, T., Kwek, L.-C., Amico, L. & Minguzzi, A. Nonclassical states in strongly correlated bosonic ring ladders. *Phys. Rev. A* **99,** 033616 (2019).

278. Franzosi, R. & Penna, V. Spectral properties of coupled Bose-Einstein condensates. *Phys. Rev. A* **63,** 043609 (2001).

279. Salasnich, L., Parola, A. & Reatto, L. Effective wave equations for the dynamics of cigar-shaped and disk-shaped Bose condensates. *Phys. Rev. A* **65,** 043614 (2002).

280. Parola, A., Salasnich, L., Rota, R. & Reatto, L. Quantum phases of attractive matter waves in a toroidal trap. *Phys. Rev. A* **72,** 063612 (2005).

281. Hairer, E., Lubich, C. & Wanner, G. *Geometric Numerical Integration: Structure-Preserving Algorithms for Ordinary Differential Equations (Springer Series in Computational Mathematics)* 661 (Springer Science & Business Media, 2006).

282. Birdsall, C. *Plasma Physics via Computer Simulation* (CRC press, 2018).

283. Lichtenberg, A. & Liebermann, M. *Regular and Stochastic Motion. Applied Mathematics Series* 692 (Springer Science & Business Media, 1983).

“Tesi discussa per il conseguimento del titolo di dottore di ricerca in Fisica, svolta presso il corso di dottorato in Fisica (ciclo 32) del Politecnico di Torino”.

“Thesis discussed for the Ph.D title achievement in Physics, carried out in the Politecnico di Torino Ph.D program in Physics (cycle 32nd)”.